The Analysis of the Thermomechanical Coupling Effect on Fractured Solids by the Finite Element Method

Nansheng Sun

A Thesis

Submitted to the Faculty of Graduate Studies

in Partial Fulfillment of the Requirement

for the Degree of

Doctor of Philosophy

Department of Mechanical Engineering

University of Manitoba, Canada

April, 1991

ISBN 0-315-77011-2

THE ANALYSIS OF THE THERMOMECHANICAL COUPLING EFFECT ON FRACTURED SOLIDS BY THE FINITE ELEMENT METHOD

BY

NANSHENG SUN

A thesis submitted to the Faculty of Graduate Studies of the University of Manitoba in partial fulfillment of the requirements of the degree of

DOCTOR OF PHILOSOPHY

ABSTRACT

This thesis presents a new analytical model for the coupled thermomechanical analysis of fractured solids subjected to static or dynamic loading conditions. This model included the thermoelastic, the thermoplastic and thermofracture coupling effects which were expressed as three separate terms of the coupled heat conduction equation.

A finite element program for this model was developed. It included these four characteristics: (1) All nodes possess three degrees of freedom (the two displacement components and one temperature). (2) Singular elements are used. (3) Time integration was performed by using optimal collocation methods. (4) The mixed coupled-uncoupled algorithm was offered.

These coupling effects were demonstrated by measuring and calculating the temperature changes in the vicinity of crack tip of a double cantilever beam specimen subjected to an impulsive force.

The numerical and experimental studies indicated that the coupling effect on a fractured solid subjected to an impulsive force is indeed significant in comparison to the same effect on unfractured solids.

ACKNOWLEDGMENT

The author wishes to express his deepest gratitude to Dr. T. R. Hsu for the valuable advice and guidance throughout the course of the study. Sincere appreciation is also due to Dr. N. Popplewell, Dr. A. H. Shah of University of Manitoba and Dr. S. Sheppard of Stanford University for their valuable advice and suggestions.

Thanks are also extended to his colleagues and friends, Messrs. G. Pizey, G. G. Chen, Z. L. Gong and D. Kuss for their assistance and useful discussions.

The financial support by the Natural Science and Engineering Research Council of Canada is greatly acknowledged.

Above all, the author would like to thank his wife Ying for her patience during the long period of study and preparation of this dissertation. The author is indebted to his parents in China for their sincere support and encouragement.

Contents

List of Tables

Listing of Figures

Chapter 1

INTRODUCTION

1.1 Background

The mechanical field and thermal field within a solid body in a true sense are inseparable. The two field analyses therefore must be solved simultaneously. Although the concept of this coupling has been realized by researchers for many years, the relative theory is progressing rather slowly, and is not in parallel with the development of other branches of solid mechanics such as plasticity and fracture mechanics. The topic of coupled thermoelasticity is relatively well documented. However, little consistency appears to exist among the various published theoretical formulations of the subject of coupled thermoplasticity. Effective solution methods for coupled thermofracture problems are essentially lacking. This situation is due to the facts that: (a) this coupling effect makes the theoretical treatment of the problem extremely complicated; (b) such a coupling effect did not appear to be significant and important in the past when engineers seldom extend their design effort to

involve plasticity and dynamic fracture.

The development of modern computers and numerical methods such as the finite element method have resulted in problem-solving techniques which have reached a high level of accuracy and capability. Consequently, solutions of many stress analysis problems which involve more accurate modeling of the physical problems are now feasible.

Equally important, the significant shift in design requirements in recent years for high performance and efficient components in aerospace satellites and rockets, conventional power plants and engines as well as nuclear power stations has made thorough component design analysis a necessity. For most structures, in fact, the high performance requirement normally requires severe thermal and mechanical loads to be carried by lighter or nontraditional materials with high strength-to-weight ratios. Under these conditions, the structural integrity of the machine components has become a prime concern of designers, contractors and the general public, because the failure of a key component in modern industrial installations such as nuclear power stations may lead to disastrous consequences. The structural integrity is likely to be ensured by a sophisticated design which is based on temperature and stress analysis of the structure when it is in a severe service environment. Hence, the development of a more accurate method of stress analysis has received much attention in research activities.

In the field of thermomechanical stress analysis, a number of computer

codes based on the finite element method are now available. These codes have the capability of handling dynamic or quasi-static conditions. However, most of the codes require knowledge of the temperature distribution as an input of the stress analysis, i.e., they use the uncoupled analysis approach.

The coupled analysis approach can improve the mechanical and thermal analyses in some cases, such as the damping of a stress wave propagation, or dynamic fracture problems. The current interest in the study of thermomechanical coupling effect on fractured solid derives from this concept.

Before proceeding with further discussion, here is a brief review of the concept of the thermomechanical coupling effect and the relative coupled approach to thermomechanical stress analysis.

1.1.1 Thermomechanical coupling effect

The thermomechanical coupling effect is generally used to express an interaction between thermal and mechanical deformation fields in a solid. Not only does the thermal field in a solid affect the mechanical fields such as stress and strain of the solid, but also the mechanical deformation of a solid generates heat and hence heat conduction within the solid. In other words, the induced temperature change can cause the mechanical deformation, and vice versa. Therefore, these two field analyses should be solved simultaneously in a coupled manner.

If the mechanical deformation is in the elastic region, then the phenomenon is called the thermoelastic coupling effect. As a result of experi-

ments, this effect had been known for many years. Also it is well known that when a solid with a uniform initial temperature is subjected to cycles of elastic deformations in an adiabatic environment, then the solid returns to the initial temperature due to the cancellation of the coupling effect during the loading and unloading cycles. Therefore, the thermoelastic coupling effect behaves in a reversible or conservative way rather than in a dissipative way.

The thermoplastic coupling effect always behaves in a dissipative way. The experimental results of Tammann and Warrentrup [1] [1] proved that a sharp reversal in the direction of the temperature change was observed at the onset of plastic deformation of a material. Moreover, when the solid finished a cycle of plastic deformation, it did not return to its initial temperature, but always exhibited an increase in temperature. Based on this phenomenon, some coupled thermoelastic-plastic analysis methods were developed during recent years. Hsu, Banas and the author had further elaborated on their method of the coupled thermo-elasto-plastic effect in references [2,3].

It is known that the temperature rise in uncracked metals during plastic deformation under the conditions of infinitesimal deformation in an adiabatic environment is only of the order of a tenth of a degree Centigrade, or slightly more [3,4,36]. It is for this reason that most of commercial codes on thermal stress analysis employ the uncoupled approach which omits the thermo-elastic-plastic coupling effect.

[1]Complete reference listing is contained at the back of the thesis.

1.1.2 Thermomechanical coupling effect relating to fracture

Experimental results during recent years have proved that the temperature rise in a cracked solid seems more significant and local than that in uncracked solids. Thus, within a small region near the crack tip, significant heat generation and a temperature rise occurs. Indeed, temperatures as high as the melting point of metals was measured.

Several researchers reported measurement of a localized temperature rise caused by deformation of fractured solids : Weichert et al (1974, 1978) [5,6] , Schonert and Weichert (1969) [7] ,Kobayashi et al (1981) [8] , Fox and Soria-Ruitz (1970) [14] , Fuller et al (1975) [24] , Loose et al (1983) [9] , and Bryant et al(1986) [31] all reported a considerable temperature rise near the tip of cracks during fracture in either ductile or brittle materials. They found that the localized temperature rises to be in the order of 10 to $100^{o}C$, even more than $1000^{o}C$ for some brittle materials or even as high as the melting point of metals such as titanium alloys. This is particularly true during dynamic fracture.

These facts imply that there is a new kind of thermomechanical coupling effect. First, such a phenomenon of temperature rise, undoubtedly, should be considered as a thermomechanical coupling effect. Also, such a rise in temperature at a crack tip might be large enough to influence: (a) the stress and strain distribution in the vicinity of crack tip; (b) the properties of

materials, particularly of plastics which are temperature-sensitive; (c) the fracture behavior due to the changes of (a) and (b). Consequently, there is speculation that the distributions of temperature and stress as well as strain obtained by using the uncoupled approach to analysis of fractured solid may considerably deviate from the true fields. It is logical that a coupled approach should be applied to the analysis of this phenomenon. None of the reseachers mentioned above have done this. Indeed, this coupling effect has generally been omitted in common fracture analyses.

The coupled method enables one to simultaneously obtain the correct distributions of both temperature and strain fields. It will be possible to reexamine some fracture problems and then to improve on the fracture mechanics analysis based on these distributions. As a result, the role of the coupling effect in a cracked solid can be well understood. This should contribute to the thermomechanics theory on the coupling effect and its application to thermofracture problems. Therefore, a reliable analytical model that enables researchers and engineers to assess this effect is highly desirable.

1.1.3 The thermofracture coupling effect

A finite element model for assessing the coupling effect in a fractured solid should be the logical extension of both the in-house developed coupled thermo-elastic-plastic theory and the results of recent experiments on the temperature rises within fractured solids. In order to distinguish the coupling effect in a cracked solid from the foregoing thermo-elastic or thermo-elastic-plastic

coupling effect, it will be refered to it as thermofracture coupling effect (TFCE) in the subsequent development.

1.2 Objective

The objective of this research project is to develop a finite element model for analyzing the thermomechanical coupling effect during the fracture of engineering materials. This thesis describes the research effort which results in a coupled analysis methodology designed to treat the TFCE in a two-dimensional structure with a stationary crack subjected to static or dynamic load.

1. A coupled heat conduction equation involving TFCE is derived.

2. A finite element model to take account for the TFCE is developed. This model has the following unique features:

   - The coupled thermoelastic-plastic stress analysis under dynamic loading conditions can be carried out.
   - The TFCE of a solid with a stable crack under dynamic loading conditions can be predicted.

3. This work leads to an examination of how the TFCE affects the stress, strain and temperature distributions in a thin plate containing a line crack under dynamic loading.

4. An experiment for the measurement of the induced temperature rise near the crack tip in a thin plate subjected to impact load is carried out to test the validity of the proposed finite element model. Finally, application of the above methodology in engineering analysis is discussed.

1.3 Scope

The first part of this thesis is concerned with the derivations of the coupled analysis of the temperature and displacement fields in a cracked solid. This part is covered in the first three chapters.

The second part deals with the description of the finite element model, algorithm and code construction. This is described in Chapter 4.

The third part describes the experimental apparatus and procedure, numerical illustration and the comparison between the finite element analysis and the experimental results gven in Chapter 5 and 6.

The remaining parts include the conclusions and recommendations, computer programs and the appendices showing the detailed derivations of key mathematical formulas. A list of references is enclosed at the end of the thesis.

Chapter 2

BASIC COUPLED THERMOMECHANICAL ANALYSIS

2.1 Introduction

Thermomechanics, as clearly indicated by the name itself, is concerned with the effects of heat on the deformation and stresses in solid bodies. In the field of elasticity, the term refers to thermoelastic mechanics, and in the field of elasto- plasticity, the term refers to thermo-elastic-plastic mechanics.

It is well known in thermoelastic stress analysis that the stress-strain law in a general thermal environment is expressed as the general Duhamel-Neumann form of Hooke's law as follows [2,21,22]:

$$\sigma_{ij} = C_{ijkl}\varepsilon_{kl} - \beta_{ij}(T - T_o) \tag{2.1}$$

where σ_{ij} is the stress tensor, ε_{kl} is the strain tensor, C_{ijkl} is the elastic constant tensor, β_{ij} is the thermal modulus tensor, T_o is the temperature of

a reference state of the body and $(T - T_o)$ is the rise of temperature above the reference state. Eq. (2.1) states that a change of temperature of a body will cause the change of stress states within the body.

The usual approach to uncoupled thermomechanics analysis involves two steps [2,21,,22]:

(1) Solving $T(x, y, z, t)$ from the Fourier's heat conduction equation

$$(kT_{,i})_{,i} + Q_{in} = \rho C_v \dot{T} \tag{2.2}$$

where k is the thermal conductivity of material, C_v the specific heat, ρ the mass density, and Q_{in} the internal heat source.

(2) Substituting temperature change into the thermoelastic equation of motion

$$\frac{1}{2} C_{ijkl}(u_{k,l} + u_{l,k})_{,j} - \beta_{ij} T_{,j} + F_i = \rho \ddot{u}_i \tag{2.3}$$

and then conducting the usual mechanics analysis. In Eq. (2.3), u_i is the displacement vector, $u_{i,j}$ is the displacement gradient, $\ddot{u}_i$ is the acceleration vector, and F_i is the body force vector. The first step is independent of the second step. In other words, the deformation of a solid does not generate heat which changes the temperature field. Therefore, it is called uncoupled method. However, the effect of the temperature field on the deformation and stress field is not a one-way phenomenon. It is an experimental fact [2,21,22] that a deformation of the body produces changes in its temperature.

2.2 Coupled Thermoelastic Stress Analysis

It is a familiar fact that an adiabatic expansion of a gas is accompanied by a drop in its temperature. Similarly, a solid body should change its temperature when the state of strain of the body is altered adiabatically. Based on this idea, Lord Kelvin (Sir William Thomson, 1824-1907) derived the following formula for the change of temperature of an insulated elastic body due to a uniform strain: [22]

$$\dot{T} = -\frac{T}{\rho C_v}\beta_{ij}\dot{\varepsilon}_{ij} \tag{2.4}$$

which is the first equation of coupled heat conduction.

Later, the research of thermoelastic theory resulted in the other equation of coupled heat conduction [21]:

$$\left(kT_{,i}\right)_{,i} + Q_{in} - \beta_{ij}T_o\dot{u}_{i,j} = \rho C_v\dot{T} \tag{2.5}$$

Obviously, the above equation suggested that the process of heat conduction in elastic solids is conditioned not only by the existing differences of temperature, but also is a compound process in which the deformation field takes part and interacts with the temperature field. Equation (2.5), in which this interaction appears, is referred to as the heat conduction equation of the coupled theory of thermoelastic mechanics, or in short the coupled heat conduction equation. To solve the temperature and displacement fields, we require a combination of Eqs. (2.3) and Eqs. (2.5).

By applying the linear strain-displacement relations, Eqs. (2.3), results in the following equations:

$$u_{i,jj} + \frac{1}{1-2\nu} u_{j,ji} + \frac{\rho}{\mu} F_i - \frac{2(1+\nu)}{1-2\nu} \alpha T_{,i} = \frac{\rho}{\mu} \ddot{u}_i \tag{2.6}$$

where ν is the Poisson's ratio, μ iss the Lamé elastic constant, and α is the linear thermal expansion coefficient. Equations (2.5) and (2.6) are taken together to constitute the central equations of linear coupled thermoelastic stress analysis.

To solve these equations by using an analytical method is a very difficult task. Only a few initial boundary-value problems were solved by means of Laplace transform techniques. One of these initial boundary-value problems, now named the Sternberg- Chakravorty's problem, concerned a linear elastic half space subjected to a uniform sudden temperature change on its bounding plane. The plane was assumed to be traction-free. Sternberg and Chakravorty [48] developed the solution for this problem, including both the displacements and stresses. Numerical investigations into the Sternberg-Chakravorty's problem have been made by Nickell and Sackman [49]. These numerical results will be used to check the computer program developed in the present work. (See Section 4.9.)

For synthetic materials such as plastics, the effect of coupling may be considerable. Thermoelastic coupling also plays a significant role in the phenomenon of elastic wave propagation, where, because of the dissipation of heat, its presence contributes to the damping of a wave motion.

However, it should be pointed out here that it is usually permissible in many common practical applications to disregard the influence of thermoelastic coupling and hence to treat the thermoelastic problems as totally or partially uncoupled. This is the case because engineers usually deal with problems that involve elastic stress analyses as in common engineering applications. But, with the availability of sophisticated analytical tools such as the finite element method, demands for utilizing a material's strength beyond its elastic limit have been increasing steadily in recent years. The thermomechanical coupling effect has thus become an important factor in design analyses.

Tammann and Warrentrup [1] observed in their experiments on plastic deformation that a sharp reversal of the temperature variation begins at the plastic yield point of a material. Moreover, many examples, such as fault analysis of nuclear reactors, damping of stress wave propagation,and the deformation localization after bifurcation, have indicated that a coupling effect could become more noticeable when the material is loaded beyond its elastic limit. To analyze this phenomenon, Hsu [2], Dillon [36], Lehmann [50], for example, separately developed their own coupled thermoelastic-plastic stress algorithm. Because a unified and systematic approach to this problem has not been realized, some basic concepts of the analysis will be discussed in the next section, based on the references [2] and [3].

2.3 Coupled Thermoelastic-plastic Stress Analysis

The quasi-static coupled thermoelastic-plastic analysis will be highlighted in this section.

2.3.1 Theoretical background

The physical system under consideration consists of a structural component (or its part) made of a polycrystalline material and exposed to a thermal environment and a mechanical load. Heat and mechanical power fluxes are considered to be the only possible means of energy exchange with the surrounding. At the outset of the process the component material is in its virgin, stress- and strain-free state and remains in a thermal equilibrium state. The macroscopic deformation of the material remains infinitesimal in the sense that displacements of individual material points and displacement gradients remain infinitesimal during the evolution process. Under the above assumptions the task of modeling is approached from a purely phenomenological point of view.

In the thermomechanics approach to modelling, the classical irreversible thermodynamics and isotropic hardening plasticity theory offer the simplest mathematical model. Such an approach uses the balance principles of mass, energy, linear momentum, angular momentum and entropy production.

To begin with, an emphasis shall be placed on the dissipation function

derived from the balance of energy and entropy production in the classical irreversible thermodynamics. Then the thermoelastic-plastic stress analysis involved in the coupled approach will be described.

Balance of energy and the entropy production

In reality, the plastic process is irreversible in nature and the internal dissipation function D may be conveniently employed to account for the irreversible nature by means of the internal entropy production associated with plastic deformation.

From this concept Oden [51] arrived at the following relation:

$$T\dot{S} = q_{i,i} + Q_{in} + D \tag{2.7}$$

in which $\dot{S}$ is the entropy production rate, T is the absolute temperature and Q_{in} is the energy supplied to the system from internal sources. Further, Hsu [2] derived the coupled heat conduction equation:

$$(kT_{,i})_{,i} + Q_{in} - \beta_{ij}T_o\dot{\varepsilon}^e_{ij} + D = \rho C_v\dot{T} \tag{2.8}$$

Equation (2.8) is virtually identical to the Fourier heat conduction equation except for the following two extra terms of equivalent heat source: (1) the heat source associated with the thermoelastic coupling term $\beta_{ij}T_o\dot{u}_{i,j}$ (as in Eq.(2.5)) and (2) the heat source related to the thermoplastic coupling term D which is often referred to as the internal dissipation function. Both of these extra terms are related to the mechanical stresses and strains. (That is why

Equation (2.8) is referred to as the coupled heat conduction equation.) The term D reflects the fact that part of the mechanical work done on the system is converted into heat within the system. But, the introduction of the D into Eq.(2.8) implies an assumption that the process of converting the work into heat is instantaneous. The dissipation function D constitutes an important part of nonlinear coupled thermomechanical analysis. Quantification of this function, however, is an extremely difficult task. A simple model is proposed based on the following experimental observations.

1. Heat is generated when the material undergoes deviatoric deformations [36].

2. Only part of the input plastic deformation power is spent in the change of the internal structure of the material; the other part is dissipated in the form of heat [52].

Based on these observations a simple expression for D was proposed as follows [2,3,71]:

$$D = (1 - \Lambda)\sigma_{ij}\dot{\varepsilon}^p_{ij}{}' = (1 - \Lambda)\sigma_{ij}\dot{\varepsilon}^p_{ij} \tag{2.9}$$

where $\varepsilon^p_{ij}{}'$ is the plastic deviatoric strain tensor, and the positive parameter Λ is called the dissipation factor. It varies between 0 and 1, and is a measure of the ratio of energy stored to the plastic energy expended under adiabatic conditions. It can also be regarded as the ratio of the rates of energy stored in the microstructure of the material resulting from the conversion of the

kinetic energy to the internal energy during an adiabatic plastic deformation process.

Thermoelastic-plastic stress analysis

The effect of thermal input to the stress fields in a solid is considered to contribute in the following three aspects: (1) dilatation-induced thermal stress; (2) change in material properties such as Young's modulus; and (3) change in the yield surface when the solid is loaded beyond its elastic limit. These three aspects have been demonstrated in detail in references [2,3]. The following is a brief description of such phenomena.

The constitutive equation for a solid subjected to combined thermal and mechanical loads can be expressed in a tensorial form as

$$\dot{\sigma}_{ij} = C^{ep}_{ijkl}\dot{\varepsilon}_{kl} + \gamma_{ij}\dot{T} \tag{2.10}$$

where the elasto-plasticity matrix can be expressed as:

$$C^{ep}_{ijkl} = C^{e}_{ijkl} - C^{p}_{ijkl} \tag{2.11}$$

with the elasticity matrix

$$C^{e}_{ijkl} = C^{e}_{ijkl}(T) \tag{2.12}$$

the plasticity matrix

$$C^{p}_{ijkl} = C^{p}_{ijkl}(\sigma_{ij}, T) \tag{2.13}$$

generalized thermal moduli

$$\gamma_{ij} = \gamma_{ij}(\sigma_{ij}, T, C^{e}_{ijkl}, C^{p}_{ijkl}) \tag{2.14}$$

To derive the exact forms of Eqs.(2.10-14), the following information is required:

1. A yield criterion to establish a yield surface in the stress space.

2. A flow rule to relate the plastic strain increments to the yield surface.

3. A hardening rule to describe the expanding, shrinking and shifting of the yield surfaces during the deformation process.

The Von Mises yield criterion is widely regarded as an appropriate representation of the initial yield surface due to its good correlation with test data and its mathematical simplicity. This criterion is derived from the distortion energy theory which states that plastic deformation occurs when the distortion energy of the material reaches a certain critical value. For an isotropic material, the yield surface F, defined by the Von Mises criterion, is expressed as

$$F = J_2 - \frac{1}{3}\sigma_Y^2 \tag{2.15}$$

in which

$$J_2 = \frac{1}{2}S_{ij}S_{ij} \tag{2.16}$$

is the second deviatoric stress invariant, S_{ij} is the deviatoric stress tensor, and σ_Y denotes the initial yield strength of the material from a uniaxial tension test. The function F in Eq.(2.13) represents the yield function (or plastic potential function) which describes plastic yielding at the current

stress state during plastic deformation. It is obvious that a plastic state is attained when $F = 0$, while the material is in the elastic region if $F < 0$.

The Prandtl-Reuss flow rule [2,22] assumes that the plastic strain increment is linearly related to the current stress. It predicts that the plastic strain increment is normal to the associated yield surface at the stress point. Mathematically, the plastic flow rule resulting from the Von Mises yield criterion can be expressed as

$$d\varepsilon_{ij}^{p} = \frac{\partial F}{\partial \sigma_{ij}} = S_{ij} d\lambda \tag{2.17}$$

in which $d\varepsilon_{ij}^{p}$ is the components of the plastic strain increment and $d\lambda$ is a positive proportionality factor. Most materials retain some stiffness after the initial yielding. Further plastic deformation by these materials requires additional loads.

Two types of strain-hardening schemes are commonly used in finite element analysis. These are isotropic hardening and kinematic hardening. The isotropic strain-hardening behavior for biaxial stress states can be represented by the uniform expansion of the initial yield surface in the stress space. The kinematic hardening behavior for the multiaxial loading situation can be modelled by the translation of the yield surface in the stress space.

2.3.2 Finite element formulation for triangular element

Analytical solutions of the coupled equations (2.3) and (2.8) for the interrelated temperature and displacement fields are virtually impossible even for cases involving simple geometries. The nonlinear nature of these equations makes a numerical technique the only practical method of solution. The finite element method (FEM) is considered to be a suitable choice for this purpose. Thus, by using the FEM, Hsu [2] derived the coupled finite element equations applicable for an assembly of m triangular elements,

$$\sum_m \{u\}^T([K_u]\{\dot{u}(t)\} + [M_T]\{\dot{T}(t)\} - \{\dot{L}(t)\}) = 0 \tag{2.18}$$

$$\sum_m \{T\}^T([C]\{\dot{T}(t)\} + [M_u]\{\dot{u}(t)\} + [K_T]\{T(t)\} - \{D\} - \{Q\}) = 0 \tag{2.19}$$

where $[K_u]$ is an element's mechanical stiffness matrix :

$$[K_u] = [h]^T(\int_{v_m} [G(\boldsymbol{r})]^T[C_{ep}][G(\boldsymbol{r})]dv_m)[h] \tag{2.20}$$

$[M_T]$ is an element's thermal stiffness matrix :

$$[M_T] = [h]^T(\int_{v_m} [G(\boldsymbol{r})]^T\{\gamma\}\{b(\boldsymbol{r})\}dv_m) \tag{2.21}$$

$\{\dot{L}\}$ is the mechanical load matrix :

$$\{\dot{L}\} = [h]^T(\int_{v_m} \{R(\boldsymbol{r})\}\{\dot{f}\}dv + \int_{s_m} \{R(\boldsymbol{r})\}\{\dot{p}\}ds_m) \tag{2.22}$$

$[C]$ is the heat capacity matrix :

$$[C] = \int_{v_m} \{b(\boldsymbol{r})\}(\rho C_v + \bar{\gamma})\{b(\boldsymbol{r})\}^T dv_m \tag{2.23}$$

$[K_T]$ is the conductivity matrix :

$$[K_T] = \int_{v_m} \{a(\boldsymbol{r})\}[k]\{a(\boldsymbol{r})\}^T dv_m \tag{2.24}$$

$[M_u]$ is the thermomechanical coupling matrix :

$$[M_u] = -(\int_{v_m} \{b(\boldsymbol{r})\}\{\bar{\beta}^T\}[G(\boldsymbol{r})]dv_m)[h] \tag{2.25}$$

$\{Q\}$ is the thermal load matrix :

$$\{Q\} = \int_{v_m} \{b(\boldsymbol{r})\}Q_{in}dv_m + \int_{s_m} \{b(\boldsymbol{r})\}\{q\}^T\{n\}ds_m \tag{2.26}$$

and $\{D\}$ is the dissipation matrix:

$$\{D\} = \int_{v_m} D\{b(\boldsymbol{r})\}dv_m \tag{2.27}$$

in which dv_m, ds_m, m and n denote the respective element volumes, element surfaces, the total number of elements and the total number of boundary surfaces. Also, the following definitions are used in the finite element formulation in which $\mathbf{r}$ denotes the spatial coordinates whereas t is the time variable.

Element strain components:

$$\{\varepsilon(\boldsymbol{r},t)\} = [G(\boldsymbol{r})][h]\{u(t)\} \tag{2.28}$$

Element temperature gradient:

$$\bigtriangledown T(\boldsymbol{r},t) = \{a(\boldsymbol{r})\}^T\{T(t)\} \tag{2.29}$$

where $\bigtriangledown$ is the gradient operator $\bigtriangledown = \left\{ \begin{array}{c} \frac{\partial}{\partial r} \\ \\ \frac{\partial}{\partial z} \end{array} \right\}$.

Element temperature

$$T_m(\boldsymbol{r}, t) = \{b(\boldsymbol{r})\}^T \{T(t)\} \tag{2.30}$$

In Eq.(2.18) to (2.30) the matrices $\{u(t)\}$ and $\{T(t)\}$ are the respective nodal displacements and temperatures in the discretized solid, and

$$[G(\mathbf{r})] = \begin{bmatrix} 0 & 1 & 0 & 0 & 0 & 0 \\ \\ 0 & 1 & 0 & 0 & 0 & 1 \\ \\ \frac{1}{r} & 1 & \frac{z}{r} & 0 & 0 & 0 \\ \\ 0 & 0 & 1 & 0 & 1 & 0 \end{bmatrix} \tag{2.31}$$

$$[R] = \begin{bmatrix} 1 & r & z & 0 & 0 & 0 \\ \\ 0 & 0 & 0 & 1 & r & z \end{bmatrix} \tag{2.32}$$

$$[h] = \frac{1}{r_j(z_k - z_i) + r_i(z_j - z_k) + r_k(z_i - z_j)}$$

$$\begin{bmatrix} r_j z_k - r_k z_j & 0 & r_k z_i - r_i z_k & 0 & r_i z_j - r_j z_i & 0 \\ z_j - z_k & 0 & z_k - z_i & 0 & z_i - z_j & 0 \\ r_k - r_j & 0 & r_i - r_k & 0 & r_j - r_i & 0 \\ 0 & r_j z_k - r_k z_j & 0 & r_k z_i - r_i z_k & 0 & r_i z_j - r_j z_i \\ 0 & z_j - z_k & 0 & z_k - z_i & 0 & z_i - z_j \\ 0 & r_k - r_j & 0 & r_i - r_k & 0 & r_j - r_i \end{bmatrix} \tag{2.33}$$

and

$$\{b(\mathbf{r})\} = [R][h]$$

$$\{a(\mathbf{r})\} = [\bigtriangledown R][h]$$

where r_i, r_j, r_k and z_i, z_j, z_k are the nodal coordinates of a triangular toroidal element in a global coordinate (r,z).

Because the term $\beta_{ij} T \dot{\varepsilon}^e_{ij}$ in Eq.(2.8) can be expressed in terms of the total strain rates as

$$\beta_{ij} T \dot{\varepsilon}^e_{ij} = \bar{\beta}_{ij} \dot{\varepsilon}_{ij} - \bar{\gamma}_{ij} \dot{T} \tag{2.33}$$

with

$$\bar{\beta}_{ij} = \bar{\beta}_{ij}(\sigma_{ij}, T, C^e_{ijkl}, C^p_{ijkl})$$

$$\bar{\gamma}_{ij} = \bar{\gamma}_{ij}(\sigma_{ij}, T, C^e_{ijkl}, C^p_{ijkl})$$

the exact forms of the $\{\gamma\}, \{\beta\}$ matrices in the above equations can be formulated for a solid undergoing a thermoelastic-plastic deformation. As a result, when using an isotropic hardening scheme, Hsu obtained [2]:

$$\{\gamma\} = -[C_{ep}](\{\alpha\} + \frac{\partial [C_e]^{-1}}{\partial T}\{\sigma\}) - \frac{[C_e]\{\sigma\prime\}}{S}\frac{\partial F}{\partial T} \tag{2.34}$$

$$\{\bar{\beta}\}^T = \{\beta\}^T T(t)[C_e]^{-1}[C_{ep}] \tag{2.35}$$

where

$$[C_{ep}] = [C_e] - [C_p]$$

$$S = \frac{4}{9}(3G + H\prime)\bar{\sigma}^2$$

$$[C_p] = \frac{[C_e]\{\sigma\prime\}\{\sigma\prime\}^T[C_e]}{S}$$

and also

$$\{\beta\} = \{\gamma\}$$

$$\bar{\gamma} = \{\beta\}^T T(-[C_e]^{-1}[C_p](\{\alpha\} + \frac{\partial[C_e]^{-1}}{\partial T}\{\sigma\}) - \{\sigma\prime\}\frac{1}{S}\frac{\partial F}{\partial T}) \tag{2.36}$$

where $\{\sigma\prime\}$ and $\bar{\sigma}$ are the respective deviatoric stress components and the effective stress in the element. In Eqs.(2.34) to (2.36), the matrix $\{\alpha\}$ is the thermal expansion coefficient matrix. The function F is the plastic potential function expressed as [2] :

$$F = F(\{\sigma\}, K, T, \dot{\bar{\varepsilon}})$$

in which K is the work-hardening parameter of the material which is related to the effective strain rate. The internal dissipation rate D in Eq.(2.29) has already been expressed in Eq.(2.9). The finite element formulation for the entire solid can thus be achieved by expressing Eqs.(2.18) and (2.19) on a global scale to give

$$[K_u]\{\dot{u}(t)\} + [M_T]\{\dot{T}(t)\} = \{\dot{L}(t)\} \tag{2.37}$$

$$[M_u]\{\dot{u}(t)\} + [C]\{\dot{T}(t)\} = [K_T]\{T(t)\} + \{Q(t)\} + \{D\} \tag{2.38}$$

These nonlinear ordinary differential equations describe the coupled quasi-static thermoelastic-plastic behavior of a solid. The time t in the displacement functions in the above equations should be treated as a parameter such

as in cases of elastoplastic stress analysis based on incremental approaches. It is apparent from these sets of equations that the two unknown quantities, i.e., the time rate of change of the displacement vector $\dot{u}$ and the rate of temperature $\dot{T}$ must be solved simultaneously.

There are several approaches that can be used to solve the system of nonlinear first-order ordinary differential equations. However, incremental procedures, utilizing recurrence relations, are adopted by most research workers such as Bathe and Wilson [56], Owen and Hinton [57], and Snyder and Bathe [58]. Solutions are obtained by advancing through time in finite steps. In references [2, 3] a two-level finite-difference scheme was used in the time domain, and some numerical illustrations were reported.

Chapter 3

COUPLED THERMOFRACTURE STRESS ANALYSIS

Experimental results published in recent years [5-11,14-18,31] have shown very significant rises in temperature within fractured solids resulting from mechanical driving forces. Obviously, these temperature rises are due to the thermomechanical coupling effect. As these significant temperature rises were all observed in the fracturing of solids, it appears that coupled thermofracture analysis can be considered as a logical application of the coupled thermoelastic or thermoelastic-plastic analysis in engineering problems.

To establish a common basis of understanding of the phenomenon that will be studied in this thesis, a brief review of the basic concepts of fracture mechanics will be done first.

3.1 Review of Fracture Mechanics Concepts

3.1.1 Introduction

Structural failures under loading conditions well below the yield strength of the structural material can often be attributed to cracks or cracklike flaws in the structure. Such failures show that the conventional strength analysis of structures alone, no matter how accurately conducted, is not sufficient to guarantee the structural integrity under operational conditions.

The analysis of stresses in a cracked structure, the study of the initiation of crack growth and the criterion of material failure due to the existence of cracks can be generally categorized as fracture mechanics. In particular, in the absence of large plastically yielded regions surrounding cracks or cracklike flaws, such a study is referred to as linear fracture mechanics. Also, linear elastic fracture mechanics (LEFM) is concerned with cases where plastic deformation preceding fracture is sufficiently small to use the assumption of linear elastic material behavior as a basis for fracture control. Otherwise, the so-called post-yield or elastic-plastic fracture mechanics should be applied.

3.1.2 Basic principles of LEFM

The linear elastic fracture mechanics approach to evaluating stresses and displacements associated with each fracture mode is constructed on the Griffith-Irwin theory. In this approach, the general stress field near a crack tip can be expressed as the superposition of stress fields due to the three basic modes

of fracture, each mode is associated with a kinematic movement of two crack surfaces relative to each other. There are three distinct possible modes of crack extension under external load: opening mode (Mode I), edge sliding mode (Mode II) and tearing mode (Mode III). In mechanical engineering practice the importance of the opening mode I far exceeds that of the other modes [29]. Hence, further discussion throughout the thesis will be limited to mode I unless specifically stated otherwise.

Energy considerations

A crack extension requires energy, which may be supplied from the work done by the applied external load and from the strain energy stored in the structure. The latter supply of energy will increase with the crack extension, because the resulting increase in compliance (compliance = deformation/unit load) will reduce the structure's strain energy storage capacity.

A critical condition arises if the decrease in energy storage capacity per unit increase of crack area becomes at least equal to the energy absorbed per unit increase of crack area. Crack propagation can then take place without the need for additional work to be done by the external load. Denoting the instantaneous value of the rate of energy supply per unit of crack area extension by G, then the critical condition may be defined by $G = G_c$.

The elastic crack tip stress field

It was demonstrated [29] that the elastic stress and displacement fields near the tip of a crack in an infinite sheet could be described for mode I (similar expressions were subsequently derived for mode II and III) by:

$$\sigma_{ij} = \frac{K}{\sqrt{r}} f_{ij}(\theta) + \cdots \tag{3.1}$$

$$u_i = K\sqrt{r} g_i(\theta) + \cdots \tag{3.2}$$

where (r, θ) is a polar coordinate system in the material with the origin situated at the crack tip and the plane of $\theta = 0$ coincides with the crack surface. The parameter K depends on: crack size, component dimensions and applied stress. It is said to be the controlling parameter of a crack tip field, and it does not depend on the material. This is so because stresses and displacements are proportional to this factor,K. Also, the truncated terms of (3.1) and (3.2) are the terms with higher order in r, and for a small radius of r (i. e. very close to the crack tip), only the first term is significant. Accordingly, K is called stress intensity factor,and fracture is expected to occur when K reaches a critical value, K_c.

One may readily observe from Eq.(3.1) that stresses in the fractured solid reach numerical values of infinity at the crack tip ($r \rightarrow 0$). These stress singularities were the result of the linear elastic stress analysis.Such singularities have also been documented for elasto-plastic materials with nominal work hardening, both for stationary and steadily growing cracks. It is there-

fore necessary to derive alternative solutions to assess the stress field near the crack tip without having to deal with this issue in the analysis. The popular J-integral was developed as one such solution. It will be described in the latter part of this chapter. These stress intensity factors and the J-integral have been applied widely to engineering fracture problems. The concept of stress singularities were necessary to derive a nonzero stress intensity factor or J-integral which evaluates the stress field near the crack tip. As a result,this concept becomes a very useful tool in fracture mechanics,and will thus be implemented in this thesis.

There exists a unique relationship between K and G as follows:

$$G = \begin{cases} \frac{K^2}{E} & \text{(plane stress)} \\ \frac{K^2}{E}(1-\nu^2) & \text{(plane strain)} \end{cases} \tag{3.3}$$

in which E is the Young's modulus and ν is the Poisson's ratio.

The discovery of stress intensity factors in the early 1960's prompted further development in the field of fracture mechanics. Thereafter,many static or quasi-static physical systems have been studied. The effect of inertia in these cases such as existing in the dynamic loading cases ,however, has been overlooked. When problems involve such dynamic loading conditions with rapid crack propagation within a structure, it is generally acknowledged that the quasi-static results have limited application to the problems. Therefore, these problems were referred to the topic of linear elastodynamic fracture mechanics.

3.1.3 Linear elastodynamic fracture mechanics

In practice, two kinds of dynamic fracture mechanics problems have received most attention: a) solids with a stationary crack that are subjected to a rapidly varying applied load, and b) solids under conditions of fixed or slowly varying loading that contain a rapidly moving crack. In both cases the crack tip is in an environment of rapidly varying fields of stress and deformation.

Impact and vibration problems fall into the first class. In the analysis of such problems it is often found that the peak dynamic stress near a flaw is higher than the stresses computed from the corresponding static equilibrium. This stress amplification is especially pronounced in the presence of cracks.

The second class of problems is equally important, because there are several kinds of large engineering structures in which rapid crack growth is a definite possibility. The literature in this area can be divided into two categories: steady state problems and transient problems.

Because of the great success which LEFM analysis has enjoyed in the past, there is adequate justification for extending the above basic concepts to the analysis of elastodynamic problems. For example, within the framework of linear fracture mechanics, the near-tip stress and the displacement fields for elastodynamic problems are often measured by introducing the concept of the stress intensity factor. Indeed, adopting the same nomenclature from LEFM, the stress intensity factor can be defined in the same manner as the static case except that it is time-dependent. Also, this definition means

that the stresses at a crack tip all exhibit a mathematical singularity. The nature of singularity does not change. Thirdly, the equivalence between the stress intensity factor and the strain energy release rate can be extended to the dynamic situation as well. It was concluded that the dynamic stress intensity factor at its peak is 1. 2 to 1. 6 times larger than the corresponding static value. [59,60]

3.1.4 Elastic-plastic fracture mechanics

Due to the singular nature of Eq.(3.1), a plastic zone is always formed at the crack tip where the stress field exceeds the yield strength of the material. If yielding is limited to a zone in the immediate vicinity of the crack which is notionally of a vanishingly small extent, it is still the LEFM problem. However, if plastic yielding is extensive, but is small in comparison with both the crack length and thickness and other dimensions of the cracked structure, it is considered beyond the range to which LEFM is applicable. Then elastic-plastic fracture mechanics should be applied. As noted, elastic-plastic fracture mechanics also forms a logical extension of LEFM and is perhaps the condition in which many machine components with cracks and flaws are likely to operate under normal loading. Currently, much effort is being devoted to the development of an elastic-plastic fracture mechanics analysis. As a result, a number of new concepts and techniques have been developed and the following ones are the most popular: (1) plastic zone corrections; (2) crack opening displacement; (3) J integral; (4) crack growth

resistance, the R curve.

plastic zone corrections

The first attempt at extending fracture mechanics beyond the LEFM limits involved a correction to the crack length to account for the effect of the plastic zone while continuing to use the LEFM approach. This procedure concerned extending the crack by a distance r_y. The result of this adjustment is a notational crack with length $2(c + r_y)$ for a panel with a center crack of length 2c.Thus, a plasticity-modified stress intensity factor for this case becomes

$$K = \sigma\sqrt{\pi(c + r_y)} \tag{3.4}$$

Again the other concepts of LEFM outlined above are applicable.

It should be emphasized that the adjustments are approximations lacking a firm theoretical basis and they exclude such effects as work hardening and large strains at the vicinity of the crack tip.

Crack opening displacement

This method is based on the assumption that, where significant plasticity occurs, the fracture process will be controlled primarily by the intense deformations adjacent to the crack tip. The separation of the crack faces, or crack opening displacement (COD), will then be a measure of the intense deformation. Crack extension will begin at some critical value of this COD.

Because COD measurement can be made when there is considerable plastic flow around the crack tip, this technique gives useful information for elastic-plastic fracture analysis.

Burdekin and Stone [61] first showed that the COD can be determined by the following simple expression:

$$\delta = \frac{K^2}{E\sigma_y} \tag{3.5}$$

where δ is the COD value and σ_y is the yield stress. Further, the energy required to extend the crack becomes $G = \sigma_y \delta$. They also demonstrated the plausibility of the notion that fracture could be governed by critical δ values determined by experimental results. Where K reaches a critical K_c, the COD value reaches a critical value δ_c. Under plane strain conditions, unstable fracture will occur when $\delta \rightarrow \delta_c$.

J integral

Rice [62] proposed a path-independent contour integral, the J integral, for a two-dimensional deformation field, evaluated over the contour Γ in a counter clockwise direction. (See Figure 3.1.) The J is given by

$$J = \int_\Gamma (w dy - t_i \frac{\partial u_i}{\partial x} ds) \tag{3.6}$$

where w is the strain energy density function,t_i is the surface traction vector, u_i is the displacement vector, and ds is an arc length along Γ.

The J integral, derived under the assumption of nonlinear elastic material behavior, is defined as the elastic energy release rate (per unit crack extension) to the crack tip. Rice [62] proved J to be path independent (under an isothermal condition) so that one may evaluate J remote from the crack tip, and use this value of J to represent the energy release rate to the crack tip, since paths adjacent to or remote from the crack tip produce the same result. This scheme is suitable in the case of small scale yielding, for which the concept of path independence of energy release rate to the crack tip is assumed to remain valid.

Just as K was found to describe the elastic crack tip stress field in the LEFM approach, Hutchinson [63] and Rice and Rosengren [64] have proved that the stress-strain field at the crack tip may be expressed as

$$\sigma_{ij} = \left(\frac{J}{r}\right)^{\frac{1}{(n+1)}} f_{ij}(\theta, n) + \cdots$$
$$\varepsilon_{ij} = \left(\frac{J}{r}\right)^{\frac{n}{(n+1)}} g_{ij}(\theta, n) + \cdots \tag{3.7}$$

where r and θ are cylindrical polar coordinates with origin at the crack tip and n is the power hardening coefficient in the assumed uniaxial stress-strain law, which is of the form $\varepsilon \propto \sigma^n$. This is the well-known HRR theory in fracture mechanics.

Specifically, for plane strain conditions in the opening mode (Mode I),

it has been shown that

$$G = J = \frac{1-\nu^2}{E} K^2 = \delta\sigma_y \tag{3.8}$$

The standard J-integral as presented in Eq.(3.6) was formulated under the following main conditions: (1) There is no thermal strain, (b) body forces and inertia effect are neglected, (c) the solid is subjeted to monotonic and proportional loading , and (d) the solid is made of homogeneous material. Hsu and several other researchers as quoted in reference [2] developed a modified J-integral to accommodate thermal gradients for the fractured solids. This modified integral consists of an additional term of area integral for the thermal gradient effect. Their formulation however does not include the thermomechanical coupling effect. This modified J-integral was successfully used to assess the fracture behavior of leaking pipelines by the author [105].

An attempt was made in 1990 by Sheppard and her student [106] in the development of a path independent integral to account for both the thermal gradients and thermomechanical coupling effects. This integral, under the name of S-integral, was formulated under the conditions of quasi-static loading and a thermomechanical coupling with 100% plastic energy dissipation for stationary cracks. This new development can be extended to accommodate the present situation with dynamic loading conditions. It may also serve as a basis for further extension for the solution of problems involving dynamic crack propagation. These extensions will require substantially more research effort, but are highly recommended as future research endeavor.

Crack growth resistance R curve

The COD and J integral methods described previously relate their values at crack initiation to K_{Ic} under plane strain conditions. These values may not be applied when determining the fracture toughness under plane stress conditions.

The concept of the crack growth resistance R curve is based on the observation that, during the fracture process of most sheet materials, the unstable fracture is always preceded by a certain amount of stable crack growth under a monotonically rising load.

It is well known that the fracture process of a cracked thin metal sheet is not usually comprised of a single sudden explosive-type change from initial crack length to total failure. With the load increasing, considerable slow stable crack growth takes place prior to catastrophic failure. Krafft et al [65] postulated in their paper published in 1961 that, for a given material and thickness, there is a unique relationship between the amount a crack growth and the applied stress intensity factor. They illustrated this relationship in what they called a crack growth resistance curve (R-curve).

The foundational concepts of the R-curve and their use in predicting critical loads for unstable crack propagation in sheet metals of various geometries have been described in a special volume of ASTM STP No. 527 [38]. Turner [37] stated that over a modest range of geometric variables the resulting R-curve was independent of the initial crack length and size.

Wang and McCabe [66] presented some experimental data showing consistent R-curves for a Center-cracked Tension (CCT) specimen and a Cracked-line Wedge-loaded (CLWL) specimen.

As postulated by many workers [37,38,66-70], the crack growth resistance during subcritical crack extension seems to be merely a function of the crack extension,Δc. Therefore, it should be possible to obtain an expression for the R-curve by using a relationship $R = f(c_0, \Delta c)$, in which R is called the specific work per unit area of cracked surfaces or the crack growth resistance and c_0 is the initial crack length. Broek [67,68,69] has proposed the simple power law,

$$R = A(\Delta c)^p \tag{3.9}$$

in which A and p are the constants and $A = 5.0, p = 0.25$ for 7075-T6 aluminum alloy sheet. The Δc is expressed in mm and R in kg/mm. Further, a second order polynomial of the form,

$$R = R_0 + a_1 \Delta c + a_2 (\Delta c)^2 \tag{3.10}$$

to relate R and Δc have been suggested by Wang and McCabe [66]. Furthermore, Mai, Atkins and Caddell [70] determined the following relationships for a few ductile and tough materials such as 7075-T3 and 1100-0 aluminum alloys and a low carbon steel:

$$R = R_0 + F(\Delta c)^p \tag{3.11}$$

where R_0, F and p are the constants. The authors published their values for

several materials, for example $R_0 = 90(kJ/m^2), F = 50(kJ/m^2), p = 0.25$ for low carbon steel, (See Figure 3.2).

3.1.5 Thermoelastic-plastic fracture stress analysis

There are three typical environmental effects on the fracture behavior of solids: excessive hydrogen diffusion (hydrogen embrittlement), corrosion and thermal factors. Of these three effects, the thermal factor, i. e. temperature, is one of the prime concerns to engineers. Elaborate discussion of its effect on the material's behavior has been well documented, e. g. in Rolfe and Barsom [70]. The thermoelastic-plastic analysis theory accounts for the effects of temperature on the constitutive equations only, based on which the thermoelastic-plastic fracture analysis have been performed. Hsu presented this analysis in detail in reference [2], including the formula of J integral with thermal effect for application in the uncoupled elastic-plastic fracture analyses.

3.2 Coupled Thermofracture Analysis

With the coupled concept and the fracture concept mentioned in the earlier sections , a new area of investigation can be opened dealing with coupled thermofracture analysis. First, it has been found that the coupled thermofracture analysis is deemed to be a logical extension of the present coupled concept. Second, diverse experimental observations regarding the considerable

rise in temperature in cracked solids have suggested that the extensive coupling effect does occur in reality. Therefore, the peculiarities of the coupled thermofracture analysis are the main concern of this study. The following discussion will be restricted to the Mode I (in-plane tensile mode) fracture problem which is defined as a coupled analysis of a two-dimensional solid with a stationary crack subjected to dynamic (impact) loads.

3.2.1 Coupled thermomechanics theory and fracture mechanics

As mentioned above, the thermoelastic and thermoplastic coupling effects represent the primary ingredients of the present coupled thermomechanics theory. This theory has not been used before for conducting the intended analysis. This logical extension of the coupled theory thus bears special importance for the following two reasons.

The first reason is due to the singularity of the stress fields at the crack tip in fracture problems. The HRR theory indicated that the variation of stress or strain near the crack tip of an elastic or elastic-plastic solid follows an inverse power law near the crack tip. In terms of linear theory of fracture mechanics, in the stress and strain fields there is a singularity at the crack tip as shown by Eq.(3.7). Also, it has be shown that the plastic dissipation term D in the coupled heat conduction equation, Eq.(2.9), was taken as $(1-\Lambda)\sigma_{ij}\dot{\varepsilon}^p_{ij}$. (See Chapter 2). Therefore, the term, D, should also have a similar singularity at the crack tip because of its association with the stress

field. By comparing Eq.(2.8) with the Fourier's heat conduction equation, Eq.(2.2), it can be seen that the term D is the source of which has a significant effect on the temperature field. Accordingly, it is reasonable to expect that the dissipation term D with a singularity should play an important role in the temperature distribution.

The second reason is due to the extensibility of the crack. Crack extension occurs when the applied load exceeds a certain value. It is generally accepted that work must be done to the fractured solid because energy is necessary to create new crack surfaces in the solid. This work is a major deterrent to crack propagation and plays a vital part in the fracture resistance of brittle materials.

The crack does not automatically return to its initial length after fracturing happened. Thermodynamics indicates that most of this work could dissipate to generate heat at the crack tip as the growth of a crack is an irreversible process against healing.

Based on the two aforementioned reasons,one can expect that deformation fields can result in a significant and localized temperature rise near the crack tip. Particularly, when involving dynamic fracture, one should expect a more powerful coupling effect because of a larger stress intensity factor and thus a higher plastic dissipation rate. Experiments supported this expectation, as will be described in the next section.

Because temperature at the crack tip plays a vital role in the fracture be-

havior, a reliable analytical model that enables researchers and engineers to predict such significant temperature rises is thus highly desirable. This phenomenon will be referred to as the Thermofracture Coupling Effect (TFCE for short) in order to distinguish it from the conventional thermo-elastic or thermo-elasto-plastic coupling effect.

3.2.2 Review of some experimental results

> "Hence, rupture should be accompanied by phenomena such as a large rise in temperature indicative of the dissipation of an amount of energy ..." (*A.A.Griffith, 1920*)

As a familiar example, recall that in a standard tensile test the metallic sample at the moment of rupture may even be too hot to be touched. In recent years the phenomena of localized marked temperature rise of fractured solids were observed and accorded more attention. Several researchers reported their observations and measurements of these phenomena ; Weichert et al (1974, 1978) [5,6], Schonert and Weichert (1969) [7], Kobayashi et al (1981) [8] , Fox and Soria-Ruitz (1970) [14], Fuller et al (1975) [24], Loose et al (1983) [9] , and Bryant et al(1986) [31] reported on a considerable temperature rise near the tip of moving cracks during fracture in either ductile or brittle materials. All these authors found the localized temperature rises to be of the order of 10 to $100°C$, or more than $1000°C$ for some brittle materials. In one case a temperature rise as high as the melting point was observed

in titanium alloys. (See Table 3.1).

The first group of these experiments was involved with brittle materials. Schonert and Weichert (1974, 1978) [5,6] performed dynamic fracture tests in glass by applying impact loads on a glass target. The measured temperature rises were between 2500 and $3000^{o}K$ during the fracture of the glass target. The measurements of these high temperatures were carried out by observing discrete wavelengths of thermal radiation emitted from the specimen.

Fox and Soria-Ruiz (1970) [14] carried out experimental research on the thermal decomposition produced by the release of elastic strain energy when a fast cleavage crack runs through a brittle crystalline solid such as calcite. By relating the amount of decomposition to the fracture velocity and the kinetics of thermal decomposition, a profile of the crack tip temperature was deduced. For calcite,this value of temperature rise was $1250^{o}K$ for a crack propagation velocity of 3600 m/sec. These two experiments showed that a large increase in temperature during fracture is observed even for brittle materials.

The second group of experiments was involved with plastics at room temperature. Fuller, Fox and Field (1974) [24] had determined the temperature rise at the tip of fast-moving cracks in polymethylmethacrylate (PMMA) by using thermocouple and temperature sensitive liquid crystal film (TSLCF). The measured values show a continuous temperature increase with increasing crack speed. In the speed range of 200 - 600 m/sec, a temperature rise of

Table 3.1: Summary of measured temperature rises due to the coupling effect in cracked solids

Author (year)	Material	Measuring technique	Temperature rise (^oC)
Schonert et al. (1969)[7]	high purity iron	thermocouple	130.
Hahn et al. (1974) [104]	SAE 4340 steel	tempilsticks	45. - 73.
Fuller et al. (1975) [24]	PMMA[a]	thermocouple and TSLC[b]	500.
Norris (1976) [15]	18Cr8Ni steel	N/A[c]	80.
Hsieh (1977) [11]	2024-T3 aluminum	N/A	1.
Weichert (1978) [6]	Glass	infra-red	$\sim$ 3000.
Kobayashi et al. (1981) [8]	Carbon-fiber composite	thermocouple and TSLC	30.
Loose et al. (1983) [9]	AISI 4135 steel	thermovision	3.
Bryant et al. (1986) [31]	Ti-8 Mn titanium	SEM stereophotogrammetry	$\sim$ 1600.[d]

a PMMA=polymethyl methacrylate
b TSLC=temperature sensitive liquid crystal
c N/A=not available
d melting point of Titanium

approximately $500°K$ was observed.

Kobayashi and Suemasu (1981) [8] investigated the generation and subsequent conduction of heat during dynamic crack propagation in carbon-fiber composites. A TSLCF (temperature sensitive liquid crystal) and a thermocouple were employed to measure the total heat and temperature change at points along the crack passage. The experiment was carried out under the Mode I crack propagation at room temperature. They reported that a maximum temperature change of about $30°C$ at the thermal boundary front was measured during the dynamic crack propagation.

The third group of experiments was related to metals. Schonert and Weichert (1969) [7] reported a measured temperature rise of $130°C$ at a distance of 30 μm from a crack tip in steel, using a minute thermocouple. Norris (1976) [15] examined crack-tip heating during fatigue fracture in carbon steel. He observed temperature rise of up to $80°C$ at the tips of fatigue cracks. Bryant, Makel and Wilsdorf (1986) [31] observed the effect of temperature rise at fracture in two titanium alloys. From metallurgical experimental evidence they reported that a very small volume at the crack tip was heated to the melting point (approximate $1600°C$ for these titanium alloys) at the moment of final separation. In the mean time, Attermo and Ostberg (1971) [10] , Loose and Brotzen (1983)[9], and Hsieh (1977)[11] measured temperature rises under the conditions of cyclic loading on metal specimens.

Attermo and Ostberg observed a temperature rise of $14°C$ at a crack

tip by applying cyclic loadings at a frequency of 100 Hz to a steel specimen. Hsieh reported that temperature rises of about 0.2 to 1.0°C near a crack tip in aluminum alloy specimen was observed when a cyclic loading frequency of 10 Hz was used. He did not publish either his measurement technique for temperature nor the details about the measured temperature data. To the author's knowledge, this temperature rise was so small that it could easily to be confused with the noise inherented in the measuring system, or by foreign disturbances. The reason why the temperature rise was so small may be due to the low loading rate of specimen and the high heat conduction of the aluminum alloy material.

Loose and Brotzen reported an experimental verification of temperature rises. Crack tip temperatures were measured in AISI 4135 steel specimen subjected to a cyclic loading at 20 Hz by means of a scanning infrared camera system. On average, the measured temperature rise was about 2.5°C. This value has fallen into a common region of measuring error. Because the authors did not published the details such as the loading rate and the resolution of the infrared camera system, it is hard to make a judgement about the credibility of the measured temperature rise data. Therefore, the following discussion will temporarily exclude the data of temperature rises for Hsieh, Loose and Brotzen.

3.2.3 Discussion on the experimental results

The above mentioned results indicate the following points.

1. A temperature rise in the vicinity of a crack tip is much higher than that of common, plastically deformed solids without a crack. A temperature rise as high as the melting point of the material is reached in the case of titanium alloy.

2. Either a brittle or a ductile material can produce a considerable temperature rise at the vicinity of a crack tip.

3. The zone of significant temperature rise is highly localized in the crack tip.

4. The temperature of the specimen must be considered to be less than the temperature at the crack tip.

5. In some reports a small temperature rise was observed.

Points 1 - 4 reveal that the process resulting in a significant temperature rise at a crack tip should be regarded as a very different phenomenon from a common plastic dissipation. In other words, the present thermoelastic or thermoplastic coupling effects have not included these factors. Therefore, this fact does suggest a new kind of coupled thermo-mechanical phenomenon during fracture. This phenomenon will be referred to as the Thermo-fracture Coupling Effect (TFCE) in order to distinguish it from the existing thermo-elastic or thermo-elastic- plastic coupling effect.

3.2.4 Review of some reported theoretical works

All published theoretical analyses were carried out without using proper thermomechanical coupling formulations. Several researchers have attempted some theoretical formulation on the phenomenon of temperature rise in the vicinity of a crack tip from an uncoupled approach. Among them are Rice and Levy (1969) [19], Schonert (1974) [5], Loose and Brotzen (1983) [9], Kuang and Atluri (1985) [16], Atluri and Nakagaki et al (1986) [17].

Theoretical formulations concerning the temperature field induced by the deformation fields in the vicinity of a crack tip were approximated by two types of analytical models. The first model, used by Loose et al [9] and Armstrong et al [18], was based on the formula by Rice [19]

$$T(x,y,t) = \int_0^t \{ \iint_{A(t)} \frac{f(\xi,\eta,\tau)}{\rho c_v} exp[-\frac{(x-\xi)^2+(y-\eta)^2}{4a^2(t-\tau)}] \, d\xi \, d\eta \} \frac{d\tau}{4\pi a^2(t-\tau)} \tag{3.12}$$

where $A(t)$ is the plastically deforming region at time t, $f(\xi,\eta,\tau)$ denotes the plastic work, ρ is the mass density, c is the specific heat, and a is the thermal diffusivity. In his model, Rice made the following assumptions.

- A temperature rise in the vicinity of a crack tip is produced by plastic dissipation work.
- The dissipation work is calculated by using the nonhardening plastic model and directly integrating the rate of plastic work over the plastic zone near the crack tip.

- A thermal stress induced by the rise of temperature was not considered.

Because, however, no closed-form solution of Eq. (3.12) is available for this model, their attention was focused on an estimation based upon Eq. (3.12).

The second model involved solving the Fourier's heat conduction equation with a moving heat source at a known constant speed and energy-rate density by using an approximate or numerical technique. Moreover,the speed of the moving heat source is equal to the speed of crack propagation, and the shape and size of the source were assumed to be those of the plastic zone near the crack tip (Weichert and Schonert [5], Kuang and Atluri [16]). The intensity of the source, however, was estimated according to an assumed fraction of the so-called crack resistance (Weichert and Schonert) [5], or strain energy release rate (Doll) [13], or plastic work rate (Kuang and Atluri) [16]. The above models may lead to the following observations.

- All models are built on an assumption that the mechanical analysis is independent of the thermal analysis. Thus, all these analyses are, in fact, uncoupled.

- Energy dissipation caused by the creation of new crack surfaces or crack growth was not considered.

Therefore, it is necessary to put a coupled approach into a fracture problem involving the TFCE. The derivation of a modified coupled heat conduction equation involving the TFCE could be taken as the first step to the coupled

method. This will lead to an accurate assessment of the localized temperature distribution in the vicinity of an advancing crack tip during fracture. The assessment of temperature rise and its influence on fracture processes is of particular value in fracture mechanics, as this will lead to a better understanding of fracture mechanics behavior of fractured solids.

The next section will present a description of preliminary theoretical results obtained by using the coupled approach.

3.2.5 Derivation of the coupled heat conduction equation

To develop a coupled approach to the TFCE, the present coupled heat conduction equation has to be modified first. A general three dimensional formulation is beyond the scope of this thesis. Right here and now, at the early stage of research on TFCE, the research of this thesis was only able to be defined as a simpler problem of coupled thermofracture analysis, i.e. a two-dimensional fracture problem with a stationary crack subjected to an impact load.

Rice [20] pointed out in 1978 that the conventional, irreversible thermodynamics theories are applicable when the actual, time-dependent non-elastic process can be modelled suitably as sequences of constrained equilibrium states. Specifically, he proposed the following equation to calculate the entropy production rate for a cracked solid induced by the quasi-static growth

of a Griffith crack:[1]

$$\Delta = \frac{1}{T}\int_{c.f.}(G - 2\gamma)\dot{c}dl \tag{3.13}$$

where Δ is the entropy production rate, T is the absolute temperature, c is the crack length and $\dot{c}$ denotes the local crack speed which is small in comparison to the stress wave velocities in the solid. The notation 'c.f.' denotes 'crack front' and the integral with respect to arc length l is carried out over all extending portions of a crack front in the solid under consideration. The quantity G is the Irwin strain energy release rate and 2γ is the work required for reversible separation of the fracture surfaces. In the above formulation, a crack length is regarded as an internal state variable.

Now, consider the derivation of a modified coupled heat conduction equation involving TFCE, based on Eq. (3.13). As shown in Figure 3.3, a cracked plate with unit thickness can be regarded as a thermodynamic system. For the system it is assumed that: (a) The crack length c, the elastic strains ε_{ij}^{e}, the dislocation density ω and the absolute temperature T are regarded as internal state variables. (b) In the interior of this plate a two-dimensional problem and stable crack growth exists under dynamic loadings.

Hence, the Helmholtz free energy may be expressed as:

$$F = F(\varepsilon_{ij}^{e}, T, c, \omega) = u - Ts \tag{3.14}$$

[1]A 'Griffith crack' is understood to be a crack which moves in an ideally-elastic lattice without the generation or motion of dislocation, twins, etc.. 'Quasi-static' growth means that the body, during crack motion, can be regarded as traversing a sequence of contained equilibrium states corresponding to the sequence of instantaneous crack lengths. (Rice [20])

where $u = u(\varepsilon_{ij}^e, T, c, \omega)$ and $s = s(\varepsilon_{ij}^e, T, c, \omega)$ are the internal energy and entropy respectively. According to the first law of thermodynamics for a local unit volume of a continuum, the following equation can be derived (Nowinski, 1978 [21] or Fung, 1965 [22]):

$$\rho \dot{u} = \sigma_{ij} \dot{\varepsilon}_{ij} - q_{i,i} \tag{3.15}$$

in which ρ is the mass density, q is the heat flux, ε_{ij} is the strain components, σ_{ij} is the stress components, u is the internal energy per unit mass. It is noticeable that the derivation of Eq.(3.15) did not involve any limitations imposed on the speed of thermodynamic process and proceeded without considering the reversibility or irreversibility of the process. Its validity is, therefore, universal and can be extended, in particular, to dynamic as well as to quasi-static processes.

Classical thermodynamics deals with equilibrium conditions of a uniform system. However, problems involving heat conduction, plasticity and fracture are beyond the scope of classical thermodynamics and belong to the realm of irreversible thermodynamics. To describe these problems in precise terms , three new hypotheses must be introduced. The first assumption is that the entropy is a function of state in irreversible as well as in reversible processes. The second assumption is that entropy is an extensive quantity, so that it must be subjected to a conservation law. The third assumption consists of an extension of the second law of thermodynamics locally to every portion of a continuum, where the continuum is uniform or nonuniform. Based on these

basic assumptions of irreversible thermodynamics, the following expression for computing the entropy production in a system can be derived: (Fung, [22] or Nowinski, [21])

$$\rho \dot{s} = -(\frac{q_i}{T})_{,i} + \rho \dot{s}_{in} \tag{3.16}$$

where $\dot{s}_{in}$ is the entropy production rate per unit mass within the domain A in Figure 3.3. Because in the domain there are three irreversible processes of heat conduction, plastic dissipation and crack growth, the $\dot{s}_{in}$ should include the contributions to entropy production rate due to these processes. Eqs. (2.7) and (2.9) expressed the contribution due to the plastic dissipation. From Eq. (3.13) the contribution due to crack growth can be computed. Thus we have

$$\rho T \dot{s}_{in} = -\frac{q_i}{T} T_{,i} + (G - 2\gamma)\dot{c}\delta(\vec{r} - \vec{r}_o) + (1 - \Lambda)\sigma_{ij}\dot{\epsilon}^p_{ij} \tag{3.17}$$

where $-\frac{q_i}{T}T_{,i}$ denotes the entropy production rate due to the heat conduction, the Dirac-delta function $\delta(\vec{r} - \vec{r_o}) = \delta(x - x_o)\delta(y - y_o)$ is used to simulate dissipation owing to an infinitesimal crack growth at the crack tip. The variables with subscript zero denote the current coordinates of the crack tip.

By substituting Eq. (3.17) into Eq. (3.16), one may get:

$$\rho T \dot{s} = -q_{i,i} + (G - 2\gamma)\dot{c}\delta(\vec{r} - \vec{r}_o) + (1 - \Lambda)\sigma_{ij}\dot{\epsilon}^p_{ij} \tag{3.18}$$

By differentiating Eq.(3.14) with respect to time t, one may get:

$$\dot{F} = \dot{u} - T\dot{s} - \dot{T}s \tag{3.19}$$

By substituting $\dot{u}$ in Eq.(3.15) into the above expression, the following relationship is obtained:

$$\rho\dot{F} = (\sigma_{ij}\dot{\varepsilon}_{ij} - q_{i,i}) - \rho T\dot{s} - \rho\dot{T}s \tag{3.20}$$

Replacing the term, $\rho T\dot{s}$, of Eq. (3.20) with Eq. (3.18) will lead to:

$$\rho\dot{F} = \sigma_{ij}\dot{\varepsilon}_{ij} - \rho\dot{T}s - (G - 2\gamma)\dot{c}\delta(\vec{r} - \vec{r}_o) - (1 - \Lambda)\sigma_{ij}\dot{\varepsilon}^p_{ij} \tag{3.21}$$

According to the definition of the plastic dissipation parameter Λ, the latent energy, $\dot{W}_s$, stored in terms of developing dislocation systems should be equal to the difference between the plastic work rate and the plastic dissipation. Therefore, the latent energy $\dot{W}_s = \Lambda\sigma_{ij}\dot{\varepsilon}^p_{ij}$, and Λ can also be regarded as the ratio of the rates of energy stored in the microstructure of the material resulting from the conversion of the kinetic energy to the internal energy during an adiabatic plastic deformation process. In Appendix A it is proved that the dissipation factor of a metal can be calculated according to the following equation:

$$\Lambda = (1 + \nu)\xi E\prime/(E - E\prime) \tag{3.22}$$

where $E\prime$ is the slope of the stress-strain curve of the metal in the plastic range, E the Young's modulus and ξ is a constant that depends upon material. (In references there were many experimental values of ξ (See Appendix A). For example, ξ of polycrystalline OFHC (Oxygen Free High Conductance) copper is equal to 1.925 [53]. Several theoretically estimated values of ξ are listed in Appendix A.)

Further, it has been stated [71] that the $\dot{W}_s$ can be written as $\dot{W}_s = \Lambda\chi\dot{\omega}$ in which χ is the dislocation energy per unit length of a dislocation line. As a result,

$$\Lambda\chi\dot{\omega} = \sigma_{ij}\dot{\varepsilon}^p_{ij} - (1-\Lambda)\sigma_{ij}\dot{\varepsilon}^p_{ij} \tag{3.23}$$

By substituting the above expression into Eq. (3.21), the following relationship is obtained:

$$\rho\dot{F} = \sigma_{ij}\dot{\varepsilon}^e_{ij} - \rho\dot{T}s - (G-2\gamma)\dot{c}\delta(\vec{r}-\vec{r}_o) - \Lambda\chi\dot{\omega} \tag{3.24}$$

Because

$$\dot{F} = \frac{d}{dt}(F(\varepsilon^e_{ij}, T, c, \omega)) = \frac{\partial F}{\partial \varepsilon^e_{ij}}\dot{\varepsilon}^e_{ij} + \frac{\partial F}{\partial T}\dot{T} + \frac{\partial F}{\partial c}\dot{c} + \frac{\partial F}{\partial \omega}\dot{\omega} \tag{3.25}$$

the following relationship can be derived by comparing Eqs. (3.21) and (3.25):

$$\begin{aligned}
\frac{\partial F}{\partial \varepsilon^e_{ij}} &= \frac{1}{\rho}\sigma_{ij} \\
\frac{\partial F}{\partial T} &= -s \\
\frac{\partial F}{\partial c}\dot{c} &= -\frac{1}{\rho}(G-2\gamma)\dot{c}\delta(\vec{r}-\vec{r}_o) \\
\frac{\partial F}{\partial \omega}\dot{\omega} &= \frac{\Lambda}{\rho}\chi
\end{aligned} \tag{3.26}$$

By differentiating $s(\varepsilon^e_{ij}, T, c, \omega)$ with respect to time t, we have

$$\dot{s} = \frac{\partial s}{\partial \varepsilon^e_{ij}}\dot{\varepsilon}^e_{ij} + \frac{\partial s}{\partial T}\dot{T} + \frac{\partial s}{\partial c}\dot{c} + \frac{\partial s}{\partial \omega}\dot{\omega} \tag{3.27}$$

When Eq. (3.22) is substituted into Eq. (3.27), the entropy change in terms of the free energy F is obtained as

$$\rho\dot{s} = -\frac{\partial^2 F}{\partial \varepsilon^e_{ij}\partial T}\dot{\varepsilon}^e_{ij} - \frac{\partial^2 F}{\partial T^2}\dot{T} - \frac{\partial^2 F}{\partial c \partial T}\dot{c} - \frac{\partial^2 F}{\partial \omega \partial T}\dot{\omega} \tag{3.28}$$

By the definition of specific heat at constant volume of a solid:

$$C_v = -T\frac{\partial^2 F}{\partial T^2} \tag{3.29}$$

Also, from Eq. (3.26), it is seen that

$$\rho\frac{\partial^2 F}{\partial \varepsilon^e_{ij}\partial T} = \rho\frac{\partial^2 F}{\partial T\partial \varepsilon^e_{ij}} = \frac{\partial \sigma_{ij}}{\partial T} = \beta_{ij} \tag{3.30}$$

where β_{ij} is referred to as the thermal moduli tensor, and

$$\rho\frac{\partial^2 F}{\partial c\partial T} = \rho\frac{\partial^2 F}{\partial T\partial c} = \frac{\partial}{\partial T}((G-2\gamma)\dot{c}\delta(\vec{r}-\vec{r}_o)) = 0 \tag{3.31}$$

and

$$\rho\frac{\partial^2 F}{\partial \omega\partial T} = \frac{\partial^2 F}{\partial T\partial \omega} = \frac{\partial}{\partial T}(\frac{\Lambda}{\rho}\chi) = 0 \tag{3.32}$$

Equation (3.28) therefore takes the form:

$$\rho\dot{s} = -\beta_{ij}\dot{\varepsilon}^e_{ij} - \frac{\rho}{T}C_v\dot{T} \tag{3.33}$$

Finally, by substituting Eq. (3.18) into (3.33), one obtains:

$$\rho C_v\dot{T} = (kT_{,i})_{,i} + \beta_{ij}T\dot{\varepsilon}^e_{ij} + (G-2\gamma)\dot{c}\delta(\vec{r}-\vec{r}_o) + (1-\Lambda)\sigma_{ij}\dot{\varepsilon}^p_{ij} \tag{3.34}$$

Generally, it is assumed that the increment of temperature θ, as compared with the reference temperature T_o, is small, i. e.

$$\frac{\mid T - T_o \mid}{T_o} = \frac{\mid \theta \mid}{T_o} << 1 \tag{3.35}$$

Then, Eq.(3.34) becomes:

$$\rho C_v\dot{T} = (kT_{,i})_{,i} + \beta_{ij}T_o\dot{\varepsilon}^e_{ij} + (G-2\gamma)\dot{c}\delta(\vec{r}-\vec{r}_o) + (1-\Lambda)\sigma_{ij}\dot{\varepsilon}^p_{ij} \tag{3.36}$$

In the finite element method each time step is always chosen to be so small that Eq. (3.35) holds. Consequently, Eq. (3.36) can be used in the finite element analysis.

It is useful to recall the coupled heat conduction equation, Eq. (2.5), which involves the thermoelastic coupling effect. By comparing Eqs. (3.36) and (2.5), the presence of the last two terms in Eq.(3.36) is recognized as evidence of introducing the TFCE.

Obviously, Eq.(3.34) or (3.36) must be coupled with the following equation of motion of a deforming solid

$$\rho \ddot{u}_i - \sigma_{ij,j} - b_i = 0 \tag{3.37}$$

for a dynamic problem,or

$$\sigma_{ij,j} + b_i = 0 \tag{3.38}$$

for a quasi-static problem where b_i is the body force per unit volume. Also, to carry out a thermoelastic-plastic analysis, it is necessary to know the constitutive equation, Eq. (2.11). Further, to perform a coupled thermofracture analysis of a growing crack (i.e. $\dot{c} > 0$), the relationship between the crack growth and the fracture parameters such as G, K , R , J or COD value must be known. The relationship can be established by experimental observations. In fact, Eq.(3.10) is a relationship which has been published. Landes and Begley (1979) [36], Turner (1980) [37], Marandet and Sanz (1980) [38], Dally, Fourney and Irwin, 1985 [35], and Kanninen, (1985) [29], etc. have established the relationship for various cases.

Eqs. (3.34) to (3.38) form a set of independent equations which must be solved simultaneously. For the coupled analysis, the finite element method appears to be the only practical numerical approach. Therefore, the finite element method for this coupled analysis will be discussed in the next section.

Chapter 4

FINITE ELEMENT MODEL FOR COUPLED THERMOFRACTURE ANALYSIS

4.1 Introduction

The set of simultaneous differential equations (3.36) and (3.37) in Chapter 3 must be solved by using the finite element formulation which includes the following three characteristics:

1. All nodal points possess three degrees of freedom.

2. Singular elements are used.

3. Time integration is performed using optimal collocation methods.

4.1.1 Node with three degrees of freedom

In recent years, much attention has been given to the numerical solution of boundary value problems using the finite element method. In particular, the displacement-based finite element method has been used successfully for the solutions of structural mechanics problems. The temperature-based finite element method has also been widely used for the solution of heat conduction problems. This chapter presents a finite element model for two-dimensional coupled thermofracture analysis.

When using a finite element method for a coupled thermomechanical analysis, the primary unknown variables denote either a displacement or temperature at a nodal point of the finite element model. Therefore, a symbol-unified primary variable-based finite element method is required. In this method , the primary unknown variables are considered to be a generalized "displacement" with three components involving two displacement components and one temperature. In other words, a nodal point in the two-dimensional finite element model for the coupled analysis involves three degrees of freedom.

4.1.2 Singular elements

When using a finite element method for fracture analysis, the theoretical singularity of the strain field at crack tip is simulated. The inclusion of such a singularity in the formulation is a necessary condition to achieve maximal

accuracy. Generally, it can be done through special elements with singular properties in the finite element model. Early in the 1970's, a number of special crack tip finite elements were developed to satisfy this condition. These special crack tip elements contain a singularity of the strain field at the crack tip, equal to the theoretical singularity. But, these special elements also result in unsatisfactory convergence in the solution for lack of the constant strain (first order terms) and rigid body motion (constant terms) modes in their shape functions for the displacements. In late 1970's, this problem was solved by using eight-node isoparametric singular elements for two-dimensional analyses and 20-node isoparametric elements for three-dimensional analyses (called "singular elements" for short in the following). Besides, the method of using these singular elements have an other merit. They are simple for program design, because the geometrical continuity and the continuity of shape functions between the singular elements and the neighboring normal elements are automatically satisfied. Therefore, singular elements will be adopted in the present coupled thermofracture analysis.

4.1.3 Time integration schemes

By using the weighted residual methods [55], a set of semidiscrete equations for the generalized displacement field can be obtained from the set of simultaneous differential equations, (3.35) and (3.36). This set of semidiscrete equations represents a set of second order differential equations which require

an appropriate time integration scheme for solution. One commonly used algorithm in structural dynamics is a collocation scheme which generalizes and combines aspects of the Newmark method and Wilson-θ method. Also, the best-behaved collocation schemes were determined and are referred to as optimal collocation methods. (Chapter 9 of [72]). Therefore, the subfamily of collocation methods is used to perform time integration in this finite element model.

The present finite element method will be based on the above outlined characteristics. To realize these characteristics, this method adopts isoparametric elements which offer a very convenient way of implementing these characteristics.

4.2 Discrete Method:Weighted Residual Approach

Posing the problem to be solved in the most general terms, it is necessary that we seek an unknown function y such that it satisfies a certain differential equation set

$$\boldsymbol{A}(\boldsymbol{y}) = \left\{ \begin{array}{c} A_1(\boldsymbol{y}) \\ A_2(\boldsymbol{y}) \\ \vdots \end{array} \right\} = 0 \tag{4.1}$$

in a domain Ω together with certain boundary conditions

$$\boldsymbol{B}(\boldsymbol{y}) = \left\{ \begin{array}{c} B_1(\boldsymbol{y}) \\ B_2(\boldsymbol{y}) \\ \vdots \end{array} \right\} = 0 \tag{4.2}$$

on the boundaries Γ of the domain. In Eq.(4.1) and (4.2) $A_1(\boldsymbol{y}), B_1(\boldsymbol{y})$, etc., are the operators defining govering differential equations and boundary conditions. The integral or weak statement that

$$\int_\Omega \mathbf{z}^{\mathrm{T}} \mathbf{A}(\mathbf{y}) d\Omega + \int_\Gamma \bar{\mathbf{z}}^{\mathrm{T}} \mathbf{B}(\mathbf{y}) d\Gamma = 0 \tag{4.3}$$

is satisfied for arbitrary functions $\mathbf{z}$ and $\bar{\mathbf{z}}$ (the superscript denotes the prescribed values on the boundaries) is equivalent to the satisfaction of the differential equations (4.1) and their boundary conditions (4.2). The Weighted Residul Method involves choices of $\mathbf{z_j} = \mathbf{w_j}$ and $\mathbf{y} = \mathbf{N_i a_i}$ where $\mathbf{w_j}$ are a finite set of prescribed functions and $\mathbf{N_i}$ are the shape functions. Then Eq.(4.3) is approximated by the expansion (4.4), i. e. ,

$$\int_\Omega \mathbf{w}_\mathbf{j}^{\mathrm{T}} \mathbf{A}(\mathbf{N_i a_i}) d\Omega + \int_\Gamma \bar{\mathbf{w}}_\mathbf{j}^{\mathrm{T}} \mathbf{B}(\mathbf{N_i a_i}) d\Gamma = 0 \quad (i, j = 1, 2, \cdots, n) \tag{4.4}$$

in which n is the number of unknown parameters $\mathbf{a_i}$ entering the problem. Almost any set of independent functions $\mathbf{w_j}$ could be used for the purpose of weighting. The common choice is $\mathbf{w_j} = \mathbf{N_j}$, i.e. the original shape functions are used as the weighting function (the Galerkin method). Equations (4.4) thus yield a set of simultaneous ordinary differential equations from which parameters $\mathbf{a_i}$ can be determined. This is a standard discrete approach in a space domain in the finite element method.

4.3 Shape Functions

The fundamental concept of the finite element method is to construct a discrete model composed of a set of piece-wise continuous functions defined over a finite number of closed sub- regions. The sub-regions, "finite elements", are connected to each other at their common nodes, and collectively approximate the shape of the domain. The generalized displacement components of these nodes are the basic unknowns.

An isoparametric quadrilateral element was used in the present finite element model. The shape function formulation of this element has been well documented. The basic idea is to map the plane isoparametric element in global coordinates (x,y) into the normalized square in local coordinates (r, s) through the following transformations:

$$x = \sum_{i=1}^{n} N_i(r,s)x_i = \boldsymbol{N}\boldsymbol{x}$$
$$y = \sum_{i=1}^{n} N_i(r,s)y_i = \boldsymbol{N}\boldsymbol{y} \qquad (4.5)$$

where $N_i(r, s)$ are the shape functions corresponding to node i, and $\mathbf{N} = \{N_1 N_2 N_3 \cdots N_n\}$, and for a 2-D element n is the number of nodal points of an element and n can vary from 4 to 9. An element with n=4 (or 8) is called a four-node (or eight-node) isoparametric element which is commonly used in finite element models. The shape functions corresponding until nine node

isoparametric elements can be listed as follows.

$$
\begin{aligned}
N_1 &= -\frac{1}{4}(1+r)(1+s)(1-r-s) \\
N_2 &= -\frac{1}{4}(1-r)(1+s)(1+r-s) \\
N_3 &= -\frac{1}{4}(1+r)(1+s)(1-r-s) \\
N_4 &= -\frac{1}{4}(1-r)(1+s)(1+r-s) \\
N_5 &= \frac{1}{2}(1+s)(1-r^2) \\
N_6 &= \frac{1}{2}(1-r)(1-s^2) \\
N_7 &= \frac{1}{2}(1-s)(1-r^2) \\
N_8 &= \frac{1}{2}(1+r)(1-s^2) \\
N_9 &= (1-r^2)(1-s^2)
\end{aligned}
\tag{4.6}
$$

These shape functions were incorporated in the finite element program DCT-EPSA (Dynamic Coupled Thermo-Elatic-Plastic Stress Analysis), developed for this research project.

Now, we define the column vector $\mathbf{d^e}$ to be the generalized displacement at all the nodes of a given element; and the column vector $\mathbf{d}$, as the state of displacement at any point within the element. In this finite element formulation the generalized displacement at a nodal point consists of three components,u_i, v_i and T_i, where u_i, v_i are the respective displacement components in the x and y directions, respectively , and T_i is temperature at the nodes.

Therefore, the generalized displacement field within a given element can

be expressed in matrix form as:

$$\begin{Bmatrix} u \\ v \\ T \end{Bmatrix} = \begin{bmatrix} \boldsymbol{N}_e & 0 & 0 \\ 0 & \boldsymbol{N}_e & 0 \\ 0 & 0 & \boldsymbol{N}_e \end{bmatrix} \begin{Bmatrix} \boldsymbol{u}^e \\ \boldsymbol{v}^e \\ \boldsymbol{T}^e \end{Bmatrix} \tag{4.7}$$

or in a simplified form as

$$\boldsymbol{d} = \boldsymbol{N}\boldsymbol{d}^e \tag{4.8}$$

where the matrix $\mathbf{N}$ is the shape function which is a function of special coordinates and has to be evaluated at each of the nodal points, and

$$\boldsymbol{N}_e = \{N_1 \; N_2 \; \cdots N_n\} \tag{4.9}$$

and

$$\boldsymbol{d}^e = \begin{Bmatrix} \boldsymbol{u}^e \\ \boldsymbol{v}^e \\ \boldsymbol{T}^e \end{Bmatrix} = \begin{bmatrix} u_1 & u_2 & \cdots & u_n \\ v_1 & v_2 & \cdots & v_n \\ T_1 & T_2 & \cdots & T_n \end{bmatrix} \tag{4.10}$$

Denoting the strain tensor as $\boldsymbol{\varepsilon}$, the strain components can be expressed in terms of the displacement functions through the compatibility condition.

$$\boldsymbol{\varepsilon} = \boldsymbol{B}_u \boldsymbol{U} \tag{4.11}$$

where $\boldsymbol{\varepsilon} = (\varepsilon_{xx}, \varepsilon_{yy}, \varepsilon_{xy})$ is the strain tensor, and $\mathbf{B_u}$ is a partial differential operator matrix which can be written as:

$$\boldsymbol{B}_u = \begin{Bmatrix} \frac{\partial}{\partial x} & 0 \\ 0 & \frac{\partial}{\partial y} \\ \frac{\partial}{\partial y} & \frac{\partial}{\partial x} \end{Bmatrix} \tag{4.12}$$

and $\mathbf{U} = \{u, v\}^T$. Also, the stress tensor $\boldsymbol{\sigma}$ can be expressed in terms of the strain tensor $\boldsymbol{\varepsilon}$ by the constitutive relations.

The physical components of the temperature gradient form a 2×1 matrix which is related to temperature through the gradient operator $\mathbf{B_T}$:

$$\nabla \boldsymbol{T} = \left\{ \begin{array}{c} \frac{\partial}{\partial x} \\ \\ \frac{\partial}{\partial y} \end{array} \right\} T = \boldsymbol{B}_T T \tag{4.13}$$

Note that the shape functions, Eq. (4.6), are expressed in the terms of local coordinates in the r,s plane. To compute the equations in the x,y plane, it is necessary to evaluate the Jacobian. This can be done by the following transformation:

$$\left\{ \begin{array}{c} \frac{\partial}{\partial r} \\ \\ \frac{\partial}{\partial s} \end{array} \right\} = \boldsymbol{J} \left\{ \begin{array}{c} \frac{\partial}{\partial x} \\ \\ \frac{\partial}{\partial y} \end{array} \right\} \tag{4.14}$$

where

$$\boldsymbol{J} = \left[\begin{array}{cc} \frac{\partial x}{\partial r} & \frac{\partial y}{\partial r} \\ \\ \frac{\partial x}{\partial s} & \frac{\partial y}{\partial s} \end{array} \right] = \left[\begin{array}{cc} \sum_{i=1}^{n} \frac{\partial N_i}{\partial r} x_i & \sum_{i=1}^{n} \frac{\partial N_i}{\partial r} y_i \\ \\ \sum_{i=1}^{n} \frac{\partial N_i}{\partial s} x_i & \sum_{i=1}^{n} \frac{\partial N_i}{\partial s} y_i \end{array} \right] \quad (n \in [4,9]) \tag{4.15}$$

To solve the cartesian derivatives, we should rewrite Eq.(4.14) as:

$$\left\{ \begin{array}{c} \frac{\partial}{\partial x} \\ \\ \frac{\partial}{\partial y} \end{array} \right\} = \boldsymbol{J}^{-1} \left\{ \begin{array}{c} \frac{\partial}{\partial r} \\ \\ \frac{\partial}{\partial s} \end{array} \right\} \tag{4.16}$$

where the inverse of Jacobian operator exists and has the form [55]:

$$\boldsymbol{J}^{-1} = \frac{1}{detJ} \left[\begin{array}{cc} \frac{\partial y}{\partial s} & -\frac{\partial x}{\partial s} \\ \\ -\frac{\partial y}{\partial r} & \frac{\partial x}{\partial r} \end{array} \right] \tag{4.17}$$

Therefore, using Eqs. (4.14),(4.15) and (4.16), we have the following equation

for the strain components in the element:

$$\varepsilon = \begin{Bmatrix} \varepsilon_{xx} \\ \varepsilon_{yy} \\ \varepsilon_{xy} \end{Bmatrix} = \frac{1}{detJ} \begin{bmatrix} \frac{\partial y}{\partial s} & -\frac{\partial x}{\partial s} & 0 & 0 \\ 0 & 0 & -\frac{\partial y}{\partial r} & \frac{\partial x}{\partial r} \\ -\frac{\partial y}{\partial r} & \frac{\partial x}{\partial r} & \frac{\partial y}{\partial s} & -\frac{\partial x}{\partial s} \end{bmatrix} \begin{Bmatrix} \frac{\partial u}{\partial r} \\ \frac{\partial u}{\partial s} \\ \frac{\partial v}{\partial r} \\ \frac{\partial v}{\partial s} \end{Bmatrix} \tag{4.18}$$

4.3.1 Crack tip element - singular elements

In the conventional displacement formulation of finite elements, the displacement field is modelled as a polynomial. This approximation of the displacement field cannot model any singularity of strains at the crack tip as indicated by the classical linear fracture mechanics theory. Consequently, a conventional "element" may not be used for the analysis of strains and stresses in the neighborhood of a crack tip where a singularity in strains exits. However, Tong and Pian [73] have shown that in order to achieve a reasonable convergence rate the appropriate singularity at the crack tip must be modelled. A great deal of effort has gone into the development of special elements which incorporate the appropriate singularity in their formulation, as the survey papers on the topic indicate [74,75,78]. These fundamental ideas in the generation of special and singular elements with singularities will be explained as follows.

From Eq.(4.17) it is immediately noticed that the desired form of singularity may be introduced in $(\partial/\partial x), (\partial/\partial y)$ by letting (a) $\mathbf{J^{-1}}$, or (b)$(\partial/\partial r)$, $(\partial/\partial s)$,or (c) both (a) and (b) to be singular at the desired point,i.e. the

crack tip. Thus, three types of such singular elements are considered: (1) those involving singular geometric transformation (i.e. making $detJ = 0$); (2) those whose shape functions have been modified to reflect the known singular behavior in the function derivatives, while retaining the linearity of geometric transformation between (x,y) and (r,s); (3) those combining both the above.

According to the first approach, Henshell and Shaw [76] and Barsoum [77] developed an attractive singular element by means of a special placement of nodal points in a conventional isoparametric element. This special placement results in $detJ = 0$ or a singular geometric transformation at a given nodal point. It can be seen from Eq.(4.17) that an appropriate singularity of the strain at the given nodal point or crack tip is therefore modelled by this element. Because this type of singular elements involves only the arrangement of finite element mesh, it is easy to implement in a large number of existing finite element codes.

Quarter point isoparametric elements are the well-known example of such type of singular elements. For a eight-node quadrilateral element, a singular geometric transformation can be obtained by placing the mid-side nodes at the quarter points. As a result, the inverse square root singularity of the strain field at the crack tip can be achieved. However, Habbitt [79] and Barsoum [77] have indicated that for this quadrilateral singular quarter-point element, the strain energy is unbounded and the desired singularity is

only along the two boundary lines. They recommend the use of triangular quarter-point singular element which can be realized by collapsing one side of the quadrilateral with node 1 being the crack tip. (See Figure 4.1.) The finite element model of the present work adopted this triangular quarter-point element as crack tip element.

4.4 Finite Element Formulation

Substituting the governing equations (3.35) and (3.36) into the integral statement (4.3), and then following the standard discretization scheme of finite element method described by Bathe [54] and Zienkiewicz [55], one obtains the following coupled semidiscrete equations for m isoparametric elements:

$$\begin{aligned} \sum_m (\mathbf{M_{uu}}\ddot{\mathbf{u}} + \mathbf{K_{uu}}\mathbf{u} + \mathbf{K_{uT}}\boldsymbol{\theta} - \mathbf{L_u}) &= \mathbf{0} \\ \sum_m (\mathbf{C_{TT}}\dot{\boldsymbol{\theta}} + \mathbf{C_{Tu}}\dot{\mathbf{u}} + \mathbf{K_{TT}}\boldsymbol{\theta} - \mathbf{D} - \mathbf{Q_f} - \mathbf{Q}) &= \mathbf{0} \end{aligned} \tag{4.19}$$

where $\mathbf{M_{uu}}$ is the element mass matrix for elements with unit thickness:

$$\mathbf{M_{uu}} = \int_{-1}^{1}\int_{-1}^{1} \rho \mathbf{N}^{\mathbf{T}}\mathbf{N} det\mathbf{J} dr ds \tag{4.20}$$

$\mathbf{K_{uu}}$ is the element mechanical stiffness matrix:

$$\mathbf{K_{uu}} = \int_{-1}^{1}\int_{-1}^{1} \mathbf{B_u^T C_{ep} B_u} det\mathbf{J} dr ds \tag{4.21}$$

where C_{ep} is the elastic-plastic matrix given in reference [2].

$\mathbf{K_{uT}}$ is the element thermal coefficient matrix:

$$\mathbf{K_{uT}} = \int_{-1}^{1}\int_{-1}^{1} \mathbf{B_u^T} \gamma \mathbf{N} det\boldsymbol{J} dr ds \tag{4.22}$$

$\mathbf{L_u}$ is the mechanical load matrix:

$$\mathbf{L_u} = \int_{-1}^{1}\int_{-1}^{1} \mathbf{N^T b} det\mathbf{J} drds + \int_{-1}^{1} \mathbf{N^T p}\sqrt{(\partial x/\partial r)^2 + (\partial y/\partial r)^2}dr \quad (4.23)$$

where $\mathbf{b}$ and $\mathbf{p}$ are respective the body force and surface fraction matrices.

$\mathbf{C_{TT}}$ is the heat capacity matrix:

$$\mathbf{C_{TT}} = \int_{-1}^{1}\int_{-1}^{1} \mathbf{N^T}(\rho C_v + \bar{\gamma})\boldsymbol{N} det\boldsymbol{J} drds \quad (4.24)$$

where C_v is the specific heat at constant strain, and $\bar{\gamma}$ is already expressed by Eq.(2.38).

$\mathbf{K_{TT}}$ is the conductivity matrix:

$$\mathbf{K_{TT}} = \int_{-1}^{1}\int_{-1}^{1} \mathbf{B_T^T k B_T} det\boldsymbol{J} drds + \int_{-1}^{1} \mathbf{N^T}\bar{h}\boldsymbol{N}\sqrt{(\partial x/\partial r)^2 + (\partial y/\partial r)^2}dr \quad (4.25)$$

where $\mathbf{k}$ is the thermal conductivity matrix, and $\bar{h}$ is the heat transfer coefficient across the thermal convection boundary.

$\mathbf{K_{Tu}}$ is the thermomechanical coupling matrix:

$$\mathbf{K_{Tu}} = -\int_{-1}^{1}\int_{-1}^{1} \mathbf{B_u^T}\bar{\boldsymbol{\beta}}\mathbf{N} det\boldsymbol{J} drds \quad (4.26)$$

where $\bar{\boldsymbol{\beta}}$ is already expressed by Eq.(2.37).

$\mathbf{D}$ is the plastic dissipation matrix:

$$\mathbf{D} = \int_{-1}^{1}\int_{-1}^{1} \mathbf{N^T} D det\mathbf{J} drds \quad (4.27)$$

where D is already expressed by Eq.(2.9).

$\mathbf{Q_f}$ is the fracture dissipation matrix and

$$\mathbf{Q_f} = \int_{-1}^{1}\int_{-1}^{1} \mathbf{N^T}(G - 2\gamma_c)\dot{c}\delta(r - r_o)\delta(s - s_o) drds \quad (4.28)$$

where (r_o, s_o) is the local coordinates of the mapped point of the crack tip. $\mathbf{Q}$ is the thermal load matrix:

$$\mathbf{Q} = \int_{-1}^{1}\int_{-1}^{1} \mathbf{N}^{\mathbf{T}} Q_{in} det\mathbf{J} dr ds + \int_{-1}^{1} \mathbf{N}^{\mathbf{T}} \mathbf{q} \sqrt{(\partial x/\partial r)^2 + (\partial y/\partial r)^2} dr \quad (4.29)$$

where Q_{in} is the energy supplied to the system from internal sources, and $\mathbf{q}$ is the heat flux matrix across the heat flux boundary. In the above equations,(4.20) to (4.29), r and s denote local coordinates, and $\mathbf{J}$ is the Jacobian matrix between the global and local coordinates. Matrices, $\boldsymbol{\gamma}, \bar{\boldsymbol{\beta}}$ and the the scalars, $\bar{\gamma}, D$, have already been given in Chapter 2. Also, these equations can be computed by using Gauss quadrature formula for the two-dimensional integral, as $\int_{-1}^{1}\int_{-1}^{1} f(r,s) dr ds \approx \sum_{i=1}^{n}\sum_{j=1}^{n} H_i H_j f(r_i, s_j)$ in which $r_i(s_i)(i = 1, 2, \cdots, n)$ are Gauss sampling points, and $H_i(H_i)(i = 1, 2, \cdots, n)$ are the coefficients which are independent of the function $f(r, s)$.

The finite element formulation for the entire solid can be achieved by expressing Eqs.(4.19) on a global scale to give

$$\begin{aligned} \mathbf{M_{uu}}\ddot{\mathbf{u}} + \mathbf{K_{uu}}\mathbf{u} + \mathbf{K_{uT}}\boldsymbol{\theta} &= \boldsymbol{L} \\ \mathbf{C_{TT}}\dot{\boldsymbol{\theta}} + \mathbf{C_{Tu}}\dot{\mathbf{u}} + \mathbf{K_{TT}}\boldsymbol{\theta} &= \mathbf{D} + \mathbf{Q_f} + \mathbf{Q} \end{aligned} \quad (4.30)$$

This is a set of simultaneous second-order ordinary differential equations with two unknown quantities, i.e. the displacement vector and the temperature. In terms of the generalized displacement field mentioned above, Eq.(4.30)

can be rewritten in the following form:

$$\begin{bmatrix} \mathbf{M_{uu}} & 0 \\ 0 & 0 \end{bmatrix}\begin{Bmatrix} \ddot{\mathbf{u}} \\ \ddot{\boldsymbol{\theta}} \end{Bmatrix}+\begin{bmatrix} 0 & 0 \\ \mathbf{C_{Tu}} & \mathbf{C_{TT}} \end{bmatrix}\begin{Bmatrix} \dot{\mathbf{u}} \\ \dot{\boldsymbol{\theta}} \end{Bmatrix}+\begin{bmatrix} \mathbf{K_{uu}} & \mathbf{K_{uT}} \\ 0 & \mathbf{K_{TT}} \end{bmatrix}\begin{Bmatrix} \mathbf{u} \\ \boldsymbol{\theta} \end{Bmatrix}=\begin{Bmatrix} \mathbf{L_u} \\ \mathbf{Q_T} \end{Bmatrix} \tag{4.31}$$

or in the following standard second-order form:

$$\boldsymbol{Ma} + \boldsymbol{Cv} + \boldsymbol{Kd} = \boldsymbol{f} \tag{4.32}$$

where

$$\boldsymbol{M} = \begin{bmatrix} \boldsymbol{M_{uu}} & \mathbf{o} \\ \mathbf{o} & \mathbf{o} \end{bmatrix} \tag{4.33}$$

is the generalized mass matrix;

$$\boldsymbol{C} = \begin{bmatrix} \mathbf{o} & \mathbf{o} \\ \boldsymbol{C_{Tu}} & \boldsymbol{C_{TT}} \end{bmatrix} \tag{4.34}$$

is the generalized damping matrix;

$$\boldsymbol{K} = \begin{bmatrix} \boldsymbol{K_{uu}} & \boldsymbol{K_{uT}} \\ \mathbf{o} & \boldsymbol{K_{TT}} \end{bmatrix} \tag{4.35}$$

is the generalized stiffness matrix;

$$\mathbf{a} = \begin{Bmatrix} \ddot{\mathbf{u}} \\ \ddot{\boldsymbol{\theta}} \end{Bmatrix} \tag{4.36}$$

is the generalized acceleration vector;

$$\mathbf{v} = \begin{Bmatrix} \dot{\mathbf{u}} \\ \dot{\boldsymbol{\theta}} \end{Bmatrix} \tag{4.37}$$

is the generalized velocity vector;

$$\boldsymbol{d} = \begin{Bmatrix} \boldsymbol{u} \\ \boldsymbol{\theta} \end{Bmatrix} \tag{4.38}$$

is the generalized displacement vector;

$$f = \left\{ \begin{array}{c} \boldsymbol{L}_u \\ \boldsymbol{Q}_T \end{array} \right\} \tag{4.39}$$

is the generalized force vector, and $\mathbf{Q}_T = \mathbf{D} + \mathbf{Q}_f + \mathbf{Q}$.

4.5 Time Integration Algorithm

Mathematically, Eq.(4.32) represents a system of differential equations of the second-order and, in principle, the solution to the equations can be obtained by standard procedures for the solution of differential equations. In practical finite element analysis, a few effective methods can be considered.

The optimal collocation scheme for performing time integration of Eq. (4.32) was adopted, because the scheme is unconditionally stable, second-order accurate and best behaved. (Hughes, 1987 [72].). In the sense of a linear multistep method for second- order systems, the collocation method is a two-step method which generalizes and combines aspects of the Newmark method and Wilson-θ method. The collocation schemes are defined by:

$$\boldsymbol{M}\boldsymbol{a}_{n+\vartheta} + \boldsymbol{C}\boldsymbol{v}_{n+\vartheta} + \boldsymbol{K}\boldsymbol{d}_{n+\vartheta} = \boldsymbol{f}_{n+\vartheta} \tag{4.40}$$

$$\boldsymbol{a}_{n+\vartheta} = (1-\vartheta)\boldsymbol{a}_n + \vartheta\boldsymbol{a}_{n+1} \tag{4.41}$$

$$\boldsymbol{f}_{n+\vartheta} = (1-\vartheta)\boldsymbol{f}_n + \vartheta\boldsymbol{f}_{n+1} \tag{4.42}$$

$$\boldsymbol{d}_{n+\vartheta} = \boldsymbol{d}_n + \vartheta\triangle t\boldsymbol{v}_n + \frac{1}{2}(\vartheta\triangle t)^2\{(1-2\alpha)\boldsymbol{a}_n + 2\alpha\boldsymbol{a}_{n+\vartheta}\} \tag{4.43}$$

$$\boldsymbol{v}_{n+\vartheta} = \boldsymbol{v}_n + \vartheta\triangle t\{(1-\delta)\boldsymbol{a}_n + \delta\boldsymbol{a}_{n+\vartheta}\} \tag{4.44}$$

Table 4.1: Smallest collocation parameter, ϑ^*.

α	ϑ^*
0.25	1
0.24	1.021712
0.23	1.047364
0.22	1.077933
0.21	1.114763
0.20	1.159772
0.19	1.215798
0.18	1.287301
0.17	1.381914
$\frac{1}{6}$	1.420815
0.16	1.514951

where ϑ is called the collocation parameter. If $\vartheta = 1$, the scheme reverts to the Newmark's method. If $\alpha = 1/6$ and $\delta = 1/2$, the Wilson-θ method is obtained. A necessary and sufficient condition for second-order accuracy is that $\delta = 1/2$. Unconditionally stable, second- order accurate schemes are defined in [72] to correspond to

$$\delta = \frac{1}{2} \qquad \vartheta \geq 1 \qquad\qquad \frac{\vartheta}{2(\vartheta+1)} \geq \delta \geq \frac{2\vartheta^2 - 1}{4(2\vartheta^3 - 1)}$$

The best-behaved collocation schemes have been determined. This amounts to a one-parameter subfamily of methods with $\delta = 0.5$ and $\vartheta = \vartheta^*(\delta)$ defined by Table 4.1 [72]. These methods are referred to as optimal collocation methods and they are the only ones considered henceforth. Based on Eq.(4.42), it is known that these methods are implicit, unconditionally stable and second-order accurate.

For convenience, $\delta = 0.5, \alpha = 0.25$ and thus $\vartheta^* = 1$ will be selected in the following. Indeed, the optimal collocation method defined by these values is equivalent to the Newmark method.

Substituting $\delta = 0.5, \alpha = 0.25$ and thus $\vartheta^* = 1$ into Eqs.(4.37) to (4.42), one finds that:

$$\boldsymbol{M}\boldsymbol{a}_{n+1} + \boldsymbol{C}\boldsymbol{v}_{n+1} + \boldsymbol{K}\boldsymbol{d}_{n+1} = \boldsymbol{f}_{n+1} \tag{4.45}$$

$$\begin{aligned}
\boldsymbol{d}_{n+1} &= \boldsymbol{d}_n + \triangle t \mathbf{v}_n + \frac{1}{4}\triangle t^2(\boldsymbol{a}_n + \boldsymbol{a}_{n+1}) \\
\boldsymbol{v}_{n+1} &= \boldsymbol{v}_n + \frac{1}{2}\triangle t(\boldsymbol{a}_n + \boldsymbol{a}_{n+1}) \\
\mathbf{a}_{n+1} &= \alpha_c(\mathbf{d}_{n+1} - \mathbf{d}_n) - \alpha_2 \mathbf{v}_n - \alpha_3 \mathbf{a}_n \\
\boldsymbol{v}_{n+1} &= \boldsymbol{v}_n + \alpha_6 \mathbf{a}_n + \alpha_7 \mathbf{a}_{n+1}
\end{aligned} \tag{4.46}$$

Substituting Eqs.(4.44) into Eq.(4.43), we get

$$\hat{\mathbf{K}}\mathbf{d}_{n+1} = \hat{\mathbf{f}}_{n+1} \tag{4.47}$$

where

$$\begin{aligned}
\hat{\mathbf{K}} &= \mathbf{K} + \alpha_o \mathbf{M} + \alpha_1 \mathbf{C} \\
\hat{\mathbf{f}}_{n+1} &= \mathbf{f}_{n+1} + \mathbf{M}(\alpha_o \mathbf{d}_n + \alpha_2 \mathbf{v}_n + \alpha_3 \mathbf{a}_n) + \\
&\quad \mathbf{C}(\alpha_1 \mathbf{d}_n + \alpha_4 \mathbf{v}_n + \alpha_5 \mathbf{a}_n)
\end{aligned} \tag{4.48}$$

Because the analysis involves thermal stress, plastic deformation, a nonlinear coupling effect and a crack, it is more convenient to express Eq.(4.45) in an incremental form as:

$$\hat{\mathbf{K}} \triangle \mathbf{d}_{n+1} = \triangle \hat{\mathbf{f}}_{n+1} \tag{4.49}$$

where

$$\begin{aligned}
\triangle\hat{\mathbf{f}}_{\mathbf{n+1}} &= \triangle\mathbf{f}_{\mathbf{n+1}} + \mathbf{M}(\alpha_2\mathbf{v_n} + \alpha_8\mathbf{a_n}) + \mathbf{C}(\alpha_9\mathbf{v_n} + \alpha_{10}\mathbf{a_n}) \\
\triangle\mathbf{d_n} &= \mathbf{d_{n+1}} - \mathbf{d_n} \\
\triangle\mathbf{v_n} &= \triangle t\mathbf{a_n} + \delta\triangle t(\frac{\mathbf{1}}{\alpha_o}\triangle\mathbf{d_n} - \frac{\alpha_1}{\delta}\mathbf{v_n} - \frac{\mathbf{1}}{\mathbf{2}\alpha}\mathbf{a_n}) \\
\triangle\mathbf{a_n} &= \frac{\mathbf{1}}{\alpha}(\frac{\mathbf{1}}{\triangle\mathbf{t^2}}\triangle\mathbf{d_n} - \frac{\mathbf{1}}{\triangle\mathbf{t}}\mathbf{v_n} - \frac{\mathbf{1}}{\mathbf{2}}\mathbf{a_n})
\end{aligned} \tag{4.50}$$

In equations (4.46), (4.48) and (4.50), we define

$$\begin{array}{lll}
\alpha_o = \frac{1}{\alpha\triangle t^2} & \alpha_1 = \frac{\delta}{\alpha\triangle t} & \alpha_2 = \frac{1}{\alpha\triangle t} \\
\alpha_3 = \frac{1}{2\alpha} - 1 & \alpha_4 = \frac{\delta}{\alpha} - 1 & \alpha_5 = \frac{\triangle t}{2}(\frac{\delta}{\alpha} - 2) \\
\alpha_6 = \triangle t(1-\delta) & \alpha_7 = \delta\triangle t & \alpha_8 = \frac{1}{2\alpha} \\
\alpha_9 = \frac{\delta}{\alpha} & \alpha_{10} = \triangle t(\frac{\delta}{2\alpha} - 1) &
\end{array} \tag{4.51}$$

4.6 Numerical Integrals over the Singular Elements

It is well known [55] that, for a linear quadrilateral or triangular element, a single Gauss sampling point integration is adequate. For a parabolic quadrilateral (or brick) element 2×2 (or $2 \times 2 \times 2$) Gauss point integration is adequate and, for a parabolic triangle (or tetrahedra) element, three-point (and four-point) formulae are needed ([55] p.203). In most cases, Gauss' quadrature rules with two or three sampling points are used to calculate integrals such as Eqs. (4.20) to (4.29). Of these equations, however, Eq.(4.27) represents the integration of the dissipation matrix, $\mathbf{D}$, over elements around

the crack tip. The integrand, D, in Eq.(4.27), involves the singularity at a crack tip which may lead to a numerical integration that is difficult to calculate exactly.

4.6.1 Numerical integration of singular functions

It has been shown after many years of experimentation that Gauss' and other quadrature formulas of the highest algebraic degree give excellent precision in comparison with other types of numerical integration formulas. However, these quadrature formulas are not universal, and in some practical cases they are known to give worse results. This usually happens when the integrand has a low order of differentiability or is an analytical function with singular points close to the segment of integration. Therefore, there is speculation that a rough approximate numerical integration of Eq.(4.27) may be acquired by using Gauss' or other quadratures of the highest algebraic degree of precision with two or three sampling points.

For example, $I = \int_0^1 \frac{dx}{\sqrt{x}} = 2\sqrt{x}|_0^1 = 2.0$. But, using the Gaussian quadrature formula with:

1. two sampling points (i.e. n=2), $I \approx 1.65068$, and the error = 17.47 %;
2. three sampling points (i.e. n=3), $I \approx 1.75086$, and the error = 12.46 %;
3. four sampling points (i.e. n=4), $I \approx 1.80634$, and the error = 9.68 %;

4. ten sampling points (i.e. n=10), $I \approx 1.91706$, and the error = 4.27 %;

5. thirty two sampling points (i.e. n=32), $I \approx 1.97321$, and the error = 1.34 % .

This is so because the integrand, $1/\sqrt{x}$, has the singular point at $x = 0$.

Equally importantly, in passing from one dimension to two or more dimensions, the diversity of integrals and the difficulty in handling them is usually increased [80, 81]. Accordingly, when singular elements were introduced into 2-D or 3-D finite element analyses, it becomes a more important and difficult task to determine how to improve the precision of evaluating a singular integral which is essentially obtained by using the Gaussian quadrature formula with 2×2 (or $2 \times 2 \times 2$) or 3×3 (or $3 \times 3 \times 3$) sampling points. As a general rule, it is impossible to obtain as much accuracy with a multi-dimensional integral as it is with a one-dimensional integral for reasonable computing times. Fortunately, in the range of integral having a dimension 2 to about 5 or 6, the dimensional effect is not yet sufficient to rule out the use of common numerical quadrature rules [81]. Therefore, one-dimensional quadrature still is the basis of the following discussion.

4.6.2 Increasing the precision of Gauss' quadrature formulas

To increase the precision of a singular integral, a number of methods have been developed for the numerical integration of functions with *integrable*

singularities [80-83]. They are illustrated as follows.

The first of these methods is called the series expansions method.This method converts all or part of the integrand into a series. Numerical quadrature is then applied to each term of the series. This method can provide adequately fast convergence.

The second method is called the singularity substruction method. It amounts to splitting the integral into a singular part which can be handled by classical methods and a nonsingular part to which approximate integration formulae such as Gauss quadrature rule may be applied without anxiety.

The third method is called the changing argument method. This is one of the most powerful techniques for numerical analysis. This method can be used to exchange a difficult singularity for a more cooperative one, or even to remove the singularity completely.

The fourth method is called the differentiation method relative to a parameter. It involves imbedding the given integrals in a family of integrals and then exposing some basic property of the family by differentiation.

The fifth method is called the estimating remainder method. This method calculates a principal part of the remainder. Then the correction provided by this new term can improve the accuracy.

The last one is called the ignoring singularity method. It uses a sufficiently large number of sampling points which is estimated from the convergence rate of a series of the quadrature values. This method avoids singular-

ities in the integrands.

The singularity and integrability

The present task is to look for an appropriate way from the above methods, and then to apply it to the calculation of Eq.(4.27). For this purpose, it is necessary to show, firstly, that Eq.(4.27) indeed does represent the integration of the function with the integrable singularity. It is generally accepted that when strain hardening occurs in the material and such behavior is characterized by a power law, then the dominant singularity governing the plastic behavior at the tip of a line crack can be referred to as the HRR singularity, i.e.

$$\begin{aligned} \sigma_{ij}(r,\theta) &= (\frac{J}{r})^{\frac{1}{(n+1)}} f_{ij}(\theta,n) + \cdots \\ \varepsilon_{ij}(r,\theta) &= (\frac{J}{r})^{\frac{n}{(n+1)}} g_{ij}(\theta,n) + \cdots \end{aligned} \tag{3.7}$$

where r and θ are polar coordinates centered at the crack tip, n is the power hardening coefficient in the assumed uniaxial stress-strain law, and the J integral is a path independent value. Ideally, the J integral should incorporate both the thermal gradients and themomechanical coupling effect. Having established the stress and strain distributions, one can evaluate the dissipation, D defined by Eq.(2.9).

Differentiating ε_{ij} in Eq.(3.7) with respect to time t yields:

$$\dot{\varepsilon}_{ij}(r,\theta) = \frac{n}{n+1} J^{\frac{-1}{n+1}} \dot{J}\ r^{\frac{-n}{n+1}} g_{ij}(\theta,n) + \cdots \tag{4.52}$$

The D may be evaluated as

$$\begin{aligned} D &= (1-\Lambda)\sigma_{ij}\dot{\varepsilon}^{p}_{ij} \\ &\leq \sigma_{ij}\dot{\varepsilon}_{ij} \\ &= \frac{n}{n+1}\dot{J}\frac{1}{r}f_{ij}(\theta,n)g_{ij}(\theta,n)+\cdots \end{aligned} \tag{4.53}$$

where the truncated terms are the terms with $r^q(q \geq 0)$, and, for small radius r (i.e. very close to the crack tip), only the first term is significant. Therefore, the integrand of Eq.(4.27), D, is a function which behaves as an inverse first power law in the vicinity of the crack tip, and thus has a singular point at the crack tip node.

Consequently, the dissipation matrix

$$\begin{aligned} \mathbf{D} &= \int\int_e \mathbf{N}^{\mathbf{T}} D(x,y)dxdy \\ &= \int\int_e \mathbf{N}^{\mathbf{T}} D(r,\theta)rdrd\theta \\ &\leq \int\int_e \mathbf{N}^{\mathbf{T}} \sigma_{ij}\dot{\varepsilon}_{ij}rdrd\theta \\ &= \int\int_e \mathbf{N}^{\mathbf{T}} (\frac{n}{n+1}\dot{J}\frac{1}{r}f_{ij}(\theta,n)g_{ij}(\theta,n)+\cdots)rdrd\theta \\ &= \int\int_e \mathbf{N}^{\mathbf{T}} (\frac{n}{n+1}\dot{J}f_{ij}(\theta,n)g_{ij}(\theta,n)+\cdots)drd\theta \end{aligned} \tag{4.54}$$

where the subscript e denotes the elements around a crack tip. It can be seen from the right sides of the above expression that the singularity of the integrand has been removed. As a result, this shows that the integrability of Eq.(4.27) is satisfied. Thus one of the above mentioned methods of increasing the precision of singular integral can be adopted for computing Eq.(4.27).

Improvement of Gauss' quadrature in finite element code

The fifth and the sixth method are further discussed in the following sections, because they are appropriate for the present finite element code.

Firstly, the estimating remainder method is considered. It is clear that additional terms from the remainder must be added to the Gauss' quadrature formula in order to increase precision. For Gauss' quadrature formulas, the remainder $R(f)$ is expressed in the following form given in [80]. Here the $R(f)$ is defined as the difference between the true integration and the Gauss' quadrature values. It is given by

$$\begin{aligned} R(f) &= \frac{1}{(2n+1)!}\left[\frac{2^n(n!)^2}{(2n!)}\right]^2 [f^{(2n-1)}(1) - f^{(2n-1)}(-1)] + \\ &\quad \frac{1}{(2n+2)!}\left[\frac{2^n(n!)^2}{(2n!)}\right]^2 \left[\frac{-n(4n^2+5n-2)}{3(2n-1)(2n+3)}\right] \\ &\quad [f^{(2n+1)}(1) - f^{(2n+1)}(-1)] + \cdots \end{aligned} \tag{4.55}$$

where f is the integrand. To apply the above formula it is necessary to find the values of the derivative of the integrand at the ends of the segment [-1, 1]. In many cases this may be difficult to do. However,in numerical analysis the derivatives can be replaced by finite differences of the f, and thus the additional terms can be calculated. As a result, accuracy can be improved by the addition of the quantities to the Gauss' quadrature sum.

Next, consider ignoring the singularity method. From the foregoing example of the singular integral, $I = \int_0^1 \frac{dx}{\sqrt{x}}$, one may conclude that Gauss' quadrature formulas can be adopted successfully when many sampling points

are used. Indeed, Gauss' quadrature formula can estimate an integral to any degree of precision with a sufficiently large number of sampling points. To decide on the number of sampling points to be adopted in the calculation, the convergence rate derived from the previous quadrature values must be taken into account. In principle, the convergence rate can be determined by a relative difference between two quadrature values calculated from two consecutive sampling points. If the desired convergence rate is not achieved, then another sampling point is tested and the calculation process is repeated. In order to obtain the desired accuracy at a reasonable computer cost, it is necessary to decide on an appropriate convergence rate for the integral. This rate can be estimated from numerical experiments. Some numerical tests have indicated that a convergence rate of 2 % may be an appropriate value. The selection of a suitable convergence rate is, however, largely a matter of experience.

From the point of view of matching the finite element code, the second method seems to be easier than the first one. Therefore, the present DCTEPSA code includes the second method as an improvement of numerical integration of Eq.(4.27).

4.7 Limits on Time Step

In Section 4.5 consideration is given to the optimal collocation methods of time stepping schemes which are unconditionally stable with a second-order

accuracy. Owing to the non-linear nature of the analysis, however, the time step size is still restricted in the handling of plastic deformation, inertia terms from the dynamic loading, and coupled terms from the stable crack extension in the case involving a non-stationary crack. It follows that the selection of an appropriate time step is of great importance. On one hand, the time step must be small enough to obtain accuracy in the solution; and on the other hand, the time step must not be smaller than necessary, because this would mean that the solution is more costly than actually required. The aim in this section is to discuss the problem of placing limits on selecting an appropriate time step for direct integration.

4.7.1 The limit of incremental algorithm for plastic analysis

The incremental deformation theory is adopted for the dynamic plastic analysis. Also, the adoption of the Hsu-Bertel's polynomial constitutive relation for the material given in the following equation, (4.56), makes the incremental approach unique by the fact that the thermoelastic-plastic constitutive equations are valid for the entire range of the flow curve.

$$\bar{\sigma} = \bar{E}\bar{\varepsilon} \Big/ \left\{ 1 + \left[\frac{\bar{E}\bar{\varepsilon}}{(1 - \bar{E}\prime/\bar{E})\sigma_k + \bar{E}\prime\bar{\varepsilon}} \right]^n \right\}^{1/n} \tag{4.56}$$

where $E\prime$ = the slope for plastic range of the flow curve,σ_k= stress level at the intersection (kink) of the elastic-plastic curve, n = stress power or shape parameter, $\bar{E} = 3G$, and $\bar{E}\prime = 3E\prime \Big/ \left[3 - \frac{(1-2\nu)E\prime}{E} \right]$. (See Figure 4.2 and

4.3.) The main advantage of this adoption is that no iterative procedure is necessary as in the case of the initial stress approach. A disadvantage of the incremental approach is the necessity of using very small load increments in order to insure the convergence of the solution, which means that a very small time step size is needed for a dynamic plastic analysis. Let Δt_1 denote the time step size limited by plastic analysis. Obviously, Δt_1 depends on the loading rate and on the material properties.

4.7.2 The limit of dynamic fracture analysis

For an ordinary elasto-dynamic analysis using a step-by-step integration scheme, accuracy can best be achieved when

$$l_e = c_w \Delta t_2 \tag{4.57}$$

i.e. the element size l_e should roughly equal the distance traveled at a wavespeed, c_w, by a disturbance during the time step Δt_2. Therefore, Δt_2 denotes the second time step size limited by common dynamic analysis.

In fracture mechanics this is a rather undesirable condition because more elements are usually required around the crack tip to approximate the singularity. For such a case ,l_e can be significantly less than $c_w \Delta t_2$. However, Bazant, Glazik and Achenbach [84] show that when

$$\Delta t_2 \approx 0.1 \frac{l_e}{c_w} \tag{4.58}$$

it is possible to obtain accurate results even with a grid containing varying element sizes. The conditions described in equations (4.57) and (4.58)

will be inevitable to some extent in planar motion (Mode I) because there are two significantly different wavespeeds, namely, the longitudinal and the shear wavespeeds. Eq.(4.57) or Eq.(4.58) cannot satisfy both of them at the same time.The numerical experiments by Chan [8] have concluded that, for a dynamic fracture analysis, the optimal time step should be

$$\Delta t_3 \leq 0.1 \frac{l_e}{c_c} \tag{4.59}$$

where the c_c is the longitudinal wavespeed.

In brief, Δt_1 reflects a requirement for a non-linear strain-stress law, and Δt_3 reflects a requirement for the geometry of the finite element mesh. Therefore, the time increment for this finite element analysis should be selected by the minimum of the above two restrictions, i.e.

$$\Delta t = Min(\Delta t_1, \Delta t_3) \tag{4.60}$$

Accordingly, the present finite element code includes a function of automatic time step control based on the above two considerations. It has been shown from the present numerical analysis that $\Delta t_1 \approx (0.1 \sim 0.05)\Delta t_3$ was used.

4.7.3 The limit of handling the coupled term from a stable crack extension

In the preceding text (Section 3.1.4 and 3.3), mention was made of the phenomenon of stable crack growth. Stable growth is said to occur if an infinitesimally small increase in load causes a correspondingly small increase

in crack length. In plane stress situations the crack growth resistance, R, with crack extension was expressed as a rising curve or a simple equation such as shown in Eq.(3.9). Besides that, it is generally accepted [37] that stable crack growth occurs in at least partly plane strain situations. Hence, the coupled thermofracture analysis needs the appropriate handling of stable crack extension.

The coupled heat conduction equation, Eq.(3.35), involves the coupling effect term due to stable crack extension, $(G - 2\gamma)\dot{c}\delta(\vec{r} - \vec{r_o})$,(See Section 3.3). It is known [47,70] that in either of the plane stress and plane strain cases there are the relationships known as resistance curves, between the resistance of the material and the crack extension, and it is the necessary condition for and during stable crack extension that the resistance equals the driving force. The curves for some materials such as low carbon steel have been published. (See Section 3.1.4.) Given this curve, at each step the G and $\dot{c}$ of this term can be calculated by the following procedure.

1. Set time step.

2. Solve for the displacement increments by using standard procedure.

3. Compute the strain increment in each element.

4. Compute the stress increment in each element according to the thermo-elastoplastic constitutive equation.

5. Compute the total element strains and stresses.

6. Compute the J_T integral based on the strain, stress and the induced temperature fields.

7. Check the criteria of stable crack extension by comparing the J_T with the critical value, J_c.

8. Compute the subcritical crack extension along the original crack axis, Δc, from the crack growth resistance curve of J_T versus Δc or R versus Δc or equations such as Eq.(3.11).

9. Check if $\Delta c/W \leq 0.005$ [86] in order to assure the selection of an adequate time step, where W is the length along crack line. Otherwise a smaller time step size is selected.

10. Compute the crack extension speed based on Δc and the time step.

11. Compute the coupling term from Eq.(4.28), based on the crack extension speed.

12. Readjust the nodal pattern immediately surrounding the crack tip by moving singular elements [85] which specify the current location of the crack tip due to the crack growth during this time interval.[1]

13. Repeat the above steps until the end criteria (e.g. the total number of time steps or the end time for the analysis) are met.

[1]The moving singular element algorithm is not implemented thoroughly in the present version of the code DCTEPSA, and remains to be done in the next stage of research.

4.8 Computer Code

A finite element computer code, CTEPSA [2,3], has been employed as the basic code of this investigation for the numerical modeling of dynamic coupled thermofracture analysis. The CTEPSA code was originally developed by Hsu and his associates to analyze quasi- static, coupled thermoelastic plastic stress problems for two-dimensional and three-dimensional axisymmetric structures. Then, equations (4.19) to (4.49) have been incorporated into the computer code. With these modifications, the CTEPSA code now becomes the code DCTEPSA (Dynamic Coupled Thermo-Elastic-Plastic Stress Analysis). In the following, a test problem is presented for the code.

4.9 Test Problem: Sternberg-Charkravoty Problem

A few analytical solutions of the initial-boundary-value problem of linear dynamic coupled thermoelasticity have been obtained. Sternberg and Chakravorty [48] determined one of the solutions for a half space subjected to a ramp-type heating of the bounding plane, including both displacement and stress solutions. In the present work, the Sternberg-Charkravoty's problem is selected as the test problem of the finite element code, and its solution is used to demonstrate the validity and accuracy of the code. By the way, other test problems for the code which involve quasi-static coupled thermoelastic analyses have been presented in references [2,3].

The problem geometry is depicted in Figure 4.4(a). A half space ($x > 0$) is subjected to surface heating on its traction-free boundary $x = 0$, by sudden exposure to a linear temperature rise during a finite time interval, after which the temperature is held constant. The finite element mesh is shown in Figure 4.4(b).

As a special form of Eqs.(3.36) and (3.37), the coupled thermoelastic differential equations for this problem can be taken to be

$$(\lambda + 2\mu)\frac{\partial^2 u_x}{\partial x^2} = \rho\frac{\partial^2 u_x}{\partial t^2} + \alpha(3\lambda + 2\mu)\frac{\partial(T - T_o)}{\partial x}$$
$$k\frac{\partial^2 T}{\partial x^2} = \rho c_v\frac{\partial T}{\partial t} + \alpha(3\lambda + 2\mu)T_o\frac{\partial^2 u_x}{\partial x \partial t} \tag{4.61}$$

where λ, μ are the isothermal Lamé constants,α is the linear coefficient of thermal expansion, T_o is the reference temperature, k is the thermal conductivity, and c_v is the specific heat at constant volume. The initial conditions are taken to be

$$u_x(x, 0) = \frac{\partial u_x(x, 0)}{\partial t} = 0$$
$$T(x, 0) = T_o \tag{4.62}$$

The boundary condition for the normal stress is $\sigma_{xx}(0, t) = 0$ and that for the temperature is

$$T(0, t) = \begin{cases} (T_1 - T_o)t/t_o + T_o & \text{if } 0 \leq t \leq t_o \\ T_1 & \text{if } t \geq t_o \end{cases}$$

for ramp surface heating. In these equations, t_o is the boundary temperature rise time, and T_1 is the final surface temperature. These boundary conditions

are to be supplemented by regularity conditions at infinity, i.e.

$$\lim_{x\to\infty} T(x,t) = T_o, \qquad t > 0$$

$$\lim_{x\to\infty} \frac{\partial T(x,t)}{\partial x} = 0, \qquad t > 0$$

$$\lim_{x\to\infty} u_x(x,t) = 0, \qquad t > 0$$

$$\lim_{x\to\infty} \frac{\partial u_x(x,t)}{\partial x} = 0, \qquad t > 0$$

Introducing the dimensionless variables

$$\begin{aligned} \xi &= ax/\kappa \\ \tau &= a^2 t/\kappa \\ \sigma &= \sigma_{xx}/(\beta T_o) \\ \theta &= (T - T_o)/T_o \\ u &= a(\lambda + 2\mu)u_x/(\kappa\beta T_o) \end{aligned} \tag{4.63}$$

where $\kappa = k/\rho c_v$; $a^2 = (\lambda + 2\mu)/\rho$; $\beta = \alpha(3\lambda + 2\mu)$, equations (4.61) can be written as:

$$\begin{aligned} \frac{\partial^2 u}{\partial \xi^2} &= \frac{\partial^2 u}{\partial \tau^2} + \frac{\partial \theta}{\partial \xi} \\ \frac{\partial^2 \theta}{\partial \xi^2} &= \delta \frac{\partial^2 u}{\partial \xi \partial \tau} + \frac{\partial \theta}{\partial \tau} \end{aligned} \tag{4.64}$$

The thermomechanical coupling parameter δ is defined by the relationship $\delta = \beta^2 T_o/\rho c_v(\lambda + 2\mu)$. The initial conditions become $u(\xi, 0) = \frac{\partial u}{\partial \tau}(\xi, 0) = \theta(\xi, 0) = 0$, and the boundary conditions are $\sigma(0, \tau) = 0$, for all τ, and

$$\theta(0,\tau) = \begin{cases} \tau/\tau_o & \text{if } 0 \le \tau \le \tau_o \\ 1 & \text{if } \tau_O \le \tau \end{cases}$$

where $\tau_o = a^2 t_o/\kappa$ The governing equations (4.61) can be solved formally through the use of the Laplace transform. The "exact" solutions can be found in [48,49]. The results obtained through the use of the finite element code, DCTEPSA, and the "exact" solutions of the Sternberg- Chakravorty problem for $\tau_o = 0.25$ are shown in Figures 4.5 to 4.7. In these figures, the solid lines represent the "exact" solution. These values of the coupling parameter were used : $\delta = 0$ (corresponding to the uncoupled theory), $\delta = 0.36$, and $\delta = 1.0$. The value of $\tau_o = 0.25$ was used in the study case. In the numerical examples treated here, a limited region of the half space from $\xi = 0$ to $\xi = 30$ was divided into 40 eight-isoparametric elements (203 nodal points). The size of the elements were 0.2 between $\xi = 0$ and $\xi = 3$, then increased uniformly in size between $\xi = 3$ and $\xi = 6$, to the maximum size of 0.6. Between $\xi = 6$ and $\xi = 30$, the mesh size was held constant at 0.6. The time increment used varied from $\Delta\tau = 0.005$ to $\Delta\tau = 0.01$. It is seen, from Figures 4.5 to 4.7, that the finite element solutions compare favorably with exact solutions. This indicates that the finite element code can yield accurate results in a dynamic coupled analysis without crack growth.

Chapter 5

EXPERIMENTAL INVESTIGATION

5.1 Introduction

The purpose of this experimental investigation was to demonstrate the coupling effect of a specimen with a line crack by measuring its temperature change when it was subjected to an impulsive force that opened the crack surfaces. In addition, this investigation measured the temperature change histories induced by this impulsive force in order to assess the validity of the finite element model mentioned in Chapter 4. An experiment was conducted to demonstrate this measurement. It was shown from the experimental study that the coupling effect was significant if the temperature change induced by loading is regarded as an indication. Further, the measured force history applied to the specimen could be used as the input data to the finite element model developed by this research work. Results of the finite element analysis will be described in Chapter 6.

5.2 Experimental Arrangement

The requirements for the test facilities may be briefly stated as follows.

1. Because the dynamic coupling effect of a fractured solid with stable crack is involved in the present study, a device which generates controllable loading pulses and also a specimen with a highly stable crack are required.

2. Because the dynamic coupling effect is an instantaneous phenomenon of transformation from mechanical energy to heat, the temperature changes induced by this effect take place over a short duration. Sensors and data acquisition systems with fast response are required.

3. Because the induced temperature change and the deformation are both of a small magnitude, high sensitivity and accuracy for measuring the temperature and the deformation are thus required.

The establishment of the experimental set-up takes account of both the aforementioned requirements and the limitation of the laboratory conditions.

5.2.1 General layout

A block diagram of the experimental arrangement is illustrated in Figure 5.1. It can be seen from this sketch that the system involved three parts. One part was the Split Hopkinson's Bar (SHB) system. The second was the wedge-loaded Double Cantilever Beam (DCB) test specimen onto which the thin-

foil thermocouples were spotwelded and the strain gages for measuring the driving force were mounted.The third was the data sensing and acquisition system as well as the data processing system. A photograph of the system is given in Figure 5.2.

The experiment operated as follows.The SHB is used to generate a loading pulse which applies an impact force to the DCB specimen. During the impact loading, the thin-foil thermocouple mounted on the specimen produces a signal of electromotive force. Meanwhile, the strain gage fixed on the DCB specimen also generates a voltage output. These signals are amplified and then digitized and recorded by the data acquisition system. The whole measuring system is triggered by a signal from the strain gages fixed on the incident bar. Later, the measured data is processed by means of the Hewlett-Packard (HP) computer in the data processing system. Finally, a hard copy of temperature or force versus time curves was provided by the computer.

5.2.2 The Split Hopkinson's Bar System

For the purpose of generating a dynamic loading , the existing SHB system was employed to generate a controllable impulsive force on the DCB specimen. The SHB system is composed of three bars, a striker bar, an incident bar and a transmitter bar. In the present experiment, only the striker and incident bars are used. All bars have a diameter of 38 mm (1-1/2 inch) and are made of steel. The striker bar is accelerated by a pneumatic gun. The

desired impact velocity can be reached by controlling the launching pressure of the gun. As a result, a loading pulse of appropriate strength is initiated by the impact of the striker bar against the incident bar.The stress wave induced by the impact force travels through the incident bar. While traveling through the strain gages mounted on the incident bar, the stress wave induces a signal which triggers the data acquisition system. Very shortly thereafter, the stress wave applies an impulsive force through the wedge and pins to the DCB specimen with a crack. (See Figure 5.1.)

5.2.3 DCB specimen

As mentioned in Chapter 4, the research effort was restricted to a fractured solid with a stable crack under dynamic loading. The wedge-loaded, double cantilever beam (DCB) test specimen is a laboratory test specimen used effectively by many investigators [39]. Figure 5.3 shows the wedge-loaded DCB specimen made of the low carbon steel , AISI 1018. Its configuration offers a number of significant advantages over tests conducted using other specimen types.

1. The cost of machining a DCB specimen is low because of its simple geometry.

2. The beam-like character of the DCB specimen was effectively exploited to produce one-dimensional (spatial) analysis models [39]. These simpler analysis models are always useful.

3. The crack propagation is controllable by the degree of crack tip blunting. As the blunted initial crack tip is commonly used in this type of experiment, the stress intensity factor at the onset of crack growth, K_Q, can be made greater than K_{Ic}. Consequently, even though it is under the condition of an impact, either a stable or a propagating crack within the DCB specimen is achievable.

4. Because the wedge for loading also induced a compressive load parallel to the direction of crack propagation and because the two free surfaces of the specimen are parallel to the crack plane, the need for side grooves to promote a straight-line crack path was eliminated. Hence, the arrangement of thermocouples and strain gages, and the measurement of crack speed could be readily accommodated.

5. Because the crack run event proceeds under essentially fixed grip conditions, the arrest of a fast moving crack within a DCB specimen was possible. This is very useful feature in research on dynamic fracture with running cracks.

5.2.4 Thin-foil thermocouple

A thermal sensor with a rapid response was required by this experiment. In order to meet the requirement, two kinds of sensor techniques for temperature measurement are considered to be feasible. One technique is the use of a special thermocouple with fast response, and the other is based on the

measurements of the emission of infrared radiation from the solid surface. The latter technique is much more expensive than the former technique and is not suitable for the present case. The thermocouple technique is of low cost, reliable and is suitable for many engineering application. Besides, a new kind of special thin-foil superfast thermocouple, which has been made available in recent years, improves the response time even further. The response time for this kind of thermocouple is in the range of less than 1 ms. Consequently, this kind of thermocouple provide a means for measuring the fast temperature change history. Indeed, many attempts have been made to measure such temperature histories of shock-loaded solids. (See, e.g., [87].) In brief, the superfast thin-foil thermocouples supplied by RdF Corporation are considered as a suitable thermal sensor for measuring the temperature response of an impacted cracked solid.

The thin-foil thermocouple is 5 μm thick,and is fabricated from a butt welded foil which is rolled and then cut to shape by a photo- etching process. It has been shown that the conditions at the junction interface between the two metals are critical to achieving superfast behavior of the thermocouple. Accordingly, the junction was carefully examined with the aid of a scanning electron microscope by the manufacturer. The shape and the dimensions of the thin-foil thermocouples used in the present experiments are illustrated in Fig. 5.6(a).

The thin-foil thermocouples are made of either chromel and alumel (type

K) or copper and constantan (type T). The K-type thin-thermocouple was adopted for this experiment because of its high sensitivity and stability of emf (electromotive force) as well as its superb resistance to oxidation.

One technical problem to be overcome is rapid heat transfer or thermal equilibration from the host material to the thermocouple.This requirement of rapid equilibration puts constraints on the conditions of the interface between the thermocouple and the host material. One common technique for improving the condition is simply to drill a clearance hole and then cement or bury a thermocouple into the hole. But the hole considerably changes the distribution of stress and temperature near the hole. In our case this is a very severe disadvantage. Hence, a spot welding technique for mounting the thermocouple was adopted in the present experiment. By following this technique, two thin-foil thermocouples were spotwelded onto the DCB specimen surface. One was close to and the other was far from the crack tip (See Fg. 5.1). The condition of the interface between the thermocouple and the specimen was checked by measuring the contact electric resistance due to the interface. Based on the author's previous experience, a contact electric resistance less than 1 ohm of the interface was considered to be satisfactory.

5.2.5 Data acquisition system

A data acquisition system was used to feed the measured data to the computer. The data acquisition system consisted of a Model 204-A digital memory oscilloscope and a Model 2310 amplifier which can precisely control the

gain. The output signals generated by sensors such as thermocouples are amplified first to increase the accuracy and resolution of the temperature measurement [88]. Thereafter, the signals were sampled and converted into a digital form acceptable to the computer. Because real time processing is unnecessary in this experiment, the signals in the digital form are stored in the memory of the oscilloscope or on a minidisk before the next processing.

Some main performance indexes of the oscilloscope are listed as follows.

- Maximum digitizing rate, MHz : 20
- Resolution, percent : 0.4
- Accuracy, percent of full scale : 0.5
- Maximum sensitivity, full scale range, mv : ± 100
- Maximum voltage range, volts : ± 40
- Sample time uncertainty, nsec : 3
- Maximum speed, time per point, μsec: 0.05
- Trigger sensitivity, percent of full scale range : 3
- Noise : 100 μv r.m.s. max. (0.1 to 100 Hz)
  0.1 % full scale ($>$ 100 Hz)

The amplifier used in this system can provide gains of 10, 100 and 1000, and outputs of low noise level which is equal to 5μ v r.m.s. max. from 0.5 Hz to 50 kHz.

The Nyquist Theorem or Sampling Theorem states that "the original signal can be recovered without distortion if it is sampled at a rate of at least twice its frequency." According to this theorem, this data acquisition system can be successfully adapted to sample a signal with a frequency as high as 10 MHz. It thus meets the requirement for the present experimental investigation.

5.2.6 Data processing system

The Hewlett-Packard System 45B computer is connected with the foregoing digital oscilloscope in order to process the measured data during the experiment. The special program developed by our group was used to collect the data from a minidisk which stored the measured data,and then to compute the time curve from the measured data such as a curve of time versus temperature. In addition, this program can plot this curve on the CRT display with high resolution. Finally, this program can provide a hard copy output of this curve by controlling the internal printer of the computer.

During this experimental study, temperature and loading versus time curves were obtained as described in the previous paragraph.

5.3 Calibration

The errors which arise in an experiment are usually categorized according to: mistakes or blunders, systematic or fixed errors and accidental or random errors. It is generally a recognized fact that of these errors, the systematic errors can be eliminated by calibrating the instruments. Therefore, the calibration of the instruments for temperature and force measurement were carried out.

5.3.1 Calibration of the temperature measurement circuit

The thin-foil thermocouple, the digital memory oscilloscope and the operational amplifier together form the temperature measuring circuit in the present experimental study. The calibration of the circuit involved the determination of the response time and transfer function [1] of the response time of the whole circuit and the relationship between the voltage output of the oscilloscope and the temperature of the measuring junction of the thin-foil thermocouple.

[1]The 'transfer function' is the ratio of the Laplace trasform of the output of a time-varying physical linear system (e.g. temperature measurement circuit) to the Laplace transform of its input.

Determination of the response time and transfer function

It is a well known fact that a thermocouple of finite size cannot have an infinitely fast response because of the thermal inertia of the measuring junction. Thus, it is necessary to determine the response time and transfer function of the thin-foil thermocouple or, at best, for the whole temperature measurement circuit. For this particular test the response time and transfer function of the whole circuit was estimated.

By using the ruby laser device (the Holobeam Series 810 model) , the response time and transfer function of the temperature measurement circuit were determined. Figure 5.4 shows the arrangement for determining the response time and the transfer function. Such response time and the transfer function were determined by following this procedure. Firstly, connect the thermocouple from the DCB specimen to the temperature measurement circuit and by using the aiming device insure that the laser beam hits the thin-foil thermocouple mounting on the DCB specimen. The firing of the ruby laser began with the turning on of the switch for the cooling water circulation pump for the laser head. Set a power level of the laser device at 0.85 kv which is equivalent an energy output of 30 Joules. Fire the laser beam and record both the output of the temperature measurement circuit and the pulse signal which was used to trigger the laser head. These signals were recorded by an oscilloscope. The recorded pulse for triggering marked the starting point of the temperature rise and the output of the circuit had the

time delay due to the thermal inertia of the thermocouple. A typical output curve is shown in Figure 5.6(b). It was estimated from Figure 5.6 that the response time [1] was approximately 0.6 ms. More importantly, this output curve was used to calculate the transfer function of the circuit which can be served to convert "observed" readings of temperature into "true" readings of temperature. (See Section 6.5.2 and Appendix B).

Calibration curve

The output recorded by the circuit for temperature measurement was a voltage signal. The task of the calibration was to establish the relationship of output voltage versus temperature. The principal layout for this calibration is shown in Figure 5.7. When the DCB specimen shown in Figure 5.7 was heated by an infrared light which was used as a controllable heat source, the temperature reading in region A of the specimen was observed by using a thermocouple digital thermometer (Model 115 KC by Omega Co.) with two thermocouples of standard K-type. On the condition that the temperature reading of the digital thermometer was stable, the temperature of the measuring junction of the thin- foil thermocouple was considered to be the same as the reading of the digital thermometer. Meanwhile, the output voltage of the circuit was recorded synchronously. As a result, the temperature reading of the digital thermometer and the output voltage of the temperature mea-

[1] Response time is defined as the time required for the sensor output to reach 63.3 per cent of the total change following a step change in monitored temperature.

surement circuit formed a point on the calibration curve, and the calibration curve was thus drawn up.The calibration curve is indicated in Figure 5.8.

5.3.2 Calibration of the circuit for measuring impact force

This calibration was carried out by means of the same arrangement as the actual experiment. The circuit for measuring impact consisted of the strain gage bridge, the amplifier and the digital oscilloscope. Also, the strain gage fixed on the surface of the DCB specimen formed an arm of the above bridge of this circuit. When loading was applied to the DCB specimen during either the actual experiment or the calibration, the signals from the bridge were amplified and recorded in the same way.Therefore,the calibration procedure for the circuit is described as follows.

- Connect a standard load cell direct with the DCB specimen.
- Gradually apply a static force on the system by using a hydraulic loading device.
- Record both the output voltage of the circuit and the force reading of the loading cell,every 250 kgf (2.45 kN) until 5000 kgf (49 kN).

Consequently, the calibration curve of the impact versus the output voltage of the strain gage circuit was plotted. The calibration curve is displayed in Figure 5.9.

5.4 Experimental Procedure, Results and Errors

5.4.1 Experimental procedure

Alignment of the split Hopkinson bars and wedge

It is necessary to align the axis of the striker and incident bars of the SHB system as well as the wedge by means of a horizon and a clearance gauge. The alignment was carried out as follows:

1. Insure that the pneumatic gun is on a horizontal plane by using a horizon gauge. At this point the axis of the striker bar within the gun should be on the same horizontal plane because the striker bar was co-axial with the axis of the gun.

2. Make the striker bar contact the incident bar, and then measure the clearances between both the end surfaces on the top and the bottom positions of the circumference.

3. Turn the incident bar about 180 degree and repeat the measurement for clearances at the second step.

4. Move the axis of the incident bar by means of the adjusting screws on the bearings in order to decrease the differences between both groups of the measured clearances at Step 2 and 3.

5. Repeat the above steps until an acceptable difference of clearances ($\approx 0.20mm$) is obtained. The alignment of the striker and incident bars can then be considered acceptable.

6. Align the wedge in a similar manner.

Grounding and shielding of conductors

It should be noted that the reliable grounding and shielding of wires are very important measures for decreasing noise level. Therefore, only shielded ground wires were selected,and the grounding was checked by using a digital multimeter before the firing of the striker bar.

Test procedure

The sequence of the actual performance of the shock test on the DCB specimen was: set the required time scale and the triggering level of the digital oscilloscope; set the gain of the amplifier; turn on the computer system; fire the striker bar; store the signals shown on the screen in a minidisk; and finally get a hard copy of the output from the computer . To check the triggering level,the firing pressure of the pneumatic gun was first set at $\approx 6psig(41.4kPa)$ and then an appropriate triggering level of the data acquisition and record system can be assessed. The firing pressure was then adjusted before the desirable pressure was switched on. After setting this pressure, the vacuum pump was turned on and the striker bar was "sucked"

back to a firing position. The actual firing pressure level was set at 15 psig (103.4 kPa).

5.4.2 Typical results

Typical experimental records of the impact force and corresponding temperature rise are shown separately in Figure 5.10 to 5.12. The curve shown in Figure 5.10 represents the dynamic force history at the location of the strain gage. The high frequency components reflects the pattern of stress waves passing through that point. From these figures it can be seen that the maximum impulsive force is approximately 43 kN;the duration of the impact is 2.67 ms; and the maximum temperature rise is $12.2^{o}C$. The error ranges in the impact force measurement and the temperature measurement were estimated at $\pm 1.5kN$ and $\pm 2.5^{o}C$, respectively.

5.4.3 Discussion of errors

When making surface temperature measurements with thermocouples attached externally, the physical situation permits at least two interesting statements. (a) The thermocouple junction may not be at the same temperature as the solid at the location of the thermocouple junction. (b) The temperature of the solid, at the location of the junction, may be affected by the presence of the thermocouple. Therefore, it is necessary to discuss and estimate the approximate analysis of and correction for the errors in the experiment.

The errors in the temperature measurements result from the presence of the thermocouple for the reasons stated above. There are several other causes for errors but the more significant ones during this temperature measurement are:

- Thermal inertia of the thermocouple,
- heat loss from the extension lead wires of the thermocouple to the surroundings,
- imperfect contact between the thermocouple and the surface of the specimen,
- thermal constriction in the specimen to which the thermocouple is attached.

A number of methods and simplifying assumptions have been utilized in accounting for these errors. Singh and Dybbs [89] described an analysis of the error caused by conduction when there is an arbitrary temperature distribution in the solid along the sensor which is modeled as a cylindrical fin. Keltner and Beck [90] developed the mathematical models for the response of surface mounted thermocouples on a thick wall. These models account for the significant causes of errors in both transient and steady-state responses to changes in the wall temperature. In principle, using these models can help to develop an appreciation for the errors in the temperature measurements.

However, the interactions between the thermocouple, the specimen and the ambient air are so complex that it is, for all practical purposes, impossible to calculate the exact error. At best, the error could be estimated to an order of magnitude or a range by employing assumptions. The ASTM Specification E230-77 suggests the standard limits of error for K-type thermocouples as $\pm 2.2^{o}C$ or $\pm 0.75\%$ or the special tolerances of $\pm 1.1^{o}C$ or $\pm 0.4\%$, whichever is greater, for the temperature range of 0 to $1250^{o}C$. As described previously and in [88], the use of an operational amplifier in the data acquisition system considerably improved the accuracy and the resolution of the present temperature measurements with the thermocouple, which thus resulted in the maximum deviation of $0.3^{o}C$. In conclusion, the error range in the present temperature measurements may be estimated from $\pm 1.4^{o}C$ to $\pm 2.5^{o}C$.

When making the impact force measurements with the method mentioned in Section 5.3.2, the errors in the measurements result from the following causes for errors. (a) The output voltage of the measurement circuit may contain a noise component. The accuracy of the data acquisition system is estimated as 0.5 percent of full scale. (b) The force reading of the loading cell during the calibration may include an error of approximate 0.5 percent of full scale. (c) It can be seen from the calibration curve (Figure 5.9) that there exists a stationary drift of the approximate 12 mv or 30 kgf. Therefore, the resultant error range in the present force measurements may be estimated from $\pm 0.3kN$ to $\pm 0.7kN$.

Chapter 6

NUMERICAL ILLUSTRATION OF THE EXPERIMENTAL CASE

6.1 Introduction

Temperature rises in cracked plates due to the coupling effect have been measured as described in Chapter 5. The finite element computer code DCTEPSA with the numerical modeling technique presented in Chapter 4 will be employed in the analysis of the foregoing experimental case. This chapter will discuss these analytical results. The main concern of this study was the role of the instantaneous coupling effect on a fractured solid, the DCB specimen, under dynamic loading. Therefore, the force history applied to the DCB specimen which has been measured in the experimental case was used as the input force data of the finite element analyses. Two cases, with coupled and uncoupled considerations, were analyzed by using

the DCTEPSA code. The influence of the coupling effect on the histories of the displacements, velocities, accelerations and temperatures at the three positions along the crack extension line, and on the stress and strain distribution ahead of the crack tip will be discussed by comparing both the results in the uncoupled and coupled considerations.

6.2 Description of the Problem

The dimensions of DCB specimen is defined in Figure 5.3. The geometry of the DCB specimen is a two-dimensional thin plate, because the ratio of the thickness over a characteristic dimension is less than 1/10. Also, the DCB specimen was subjected to an applied impulsive force, $\mathbf{L}(t)$, which was measured, and this load pulse may be considered to be uniform along the thickness of the DCB specimen. Consequently, this specimen was assumed to be in a plane stress condition.

Further, due to this plane stress condition, the plastic zone ahead of the crack tip and, thus, the plastic dissipation can be considered to be uniform along the thickness of the DCB specimen. In other words, the distribution of the dissipation or the coupling term in the coupled heat conduction equation, Eq.(3.34), is independent of the thickness coordinate. Furthermore, the heat transfer boundary condition in this case may be considered to be in a plane heat conduction condition. This is due to the facts that the out-plane heat transfer of the DCB specimen is mainly caused by free convection heat trans-

fer at room temperature with a very small heat transfer coefficient, and that the duration of the whole loading process is of the order of three milliseconds and thus this out-surface heat loss is negligible. Therefore, the temperature distribution within the DCB specimen is a two-dimensional field.

At this point, one more question which must be answered is the choice of either a static or a dynamic analysis (i.e., of including or neglecting acceleration-dependent inertia forces in the analysis) to be used in the present case. Generally speaking, such choices are usually made by engineering judgment. However, it should be noted that the assumption of static analysis in some cases may result in meaningless solutions. For example, in nonlinear analyses the effect of neglecting the inertia forces may be so severe that a meaningful solution may be difficult or impossible to obtain [54, pp.499]. The nonlinear nature of the present case, therefore, was the prime reason for selecting a dynamic analysis.

Moreover, this choice of dynamic analysis in the present case is supported by the significant difference between the maximun stresses obtained from both static and dynamic analyses. This difference can be estimated by using an example of a simple one-dimensional model. In this model the magnification factors which are defined as the ratio of the maximum dynamic stress to that of the static one can be expressed as a function of the value of the ratio,t_d/τ_1, where the t_d is the time duration of the applied impulsive force and the τ_1 is the fundamental or the first natural period (i.e. the recip-

rocal of the first natural frequency) of the model [94]. The ratio t_d/τ_1 in this case can be calculated as follows. From Figure 6.2, t_d is equal to $2.57ms$. To calculate τ_1, we may assume that the DCB specimen can be simplified as a model of a cantilever beam with constant cross section acted on by a lateral force. Then the fundamental period of the model can be estimated from the classical beam theory [93], i.e.

$$\tau_1 \approx \frac{2\pi}{1.875^2}\sqrt{\frac{ml^4}{EI}} = \frac{2\pi}{1.875^2}\sqrt{\frac{0.05403 \times 9^4}{2.06 \times 10^6 \times 100 \times 9.80 \times 11.39}} = 0.22ms \tag{6.1}$$

As a result, the ratio t_d/τ_1 is equal to 11.6. The magnification factors versus the ratios t_d/τ_1 have been depicted in Fig. 2-5 of reference [94].Consequently,the magnification factor of 1.9 was obtained from that figure by using $t_d/\tau_1 = 11.6$. This indicates that in the present case the maximum stress given by a dynamic analysis may be 1.9 times that given by a static analysis. Therefore, a dynamic analysis is necessary for the present case.

On the whole, the problem can be defined in terms of coupled dynamic stress analysis of a two-dimensional fractured solid body.

6.3 Material Properties

The DCB specimen was made of low carbon steel, AISI 1018. The uniaxial tension, stress-strain curve of this material at room temperature, which was tested at the metallurgical laboratory in University of Manitoba, is shown in Figure 6.3. This curve may be approximately described by the Hsu-Bertel's

Table 6.1: Elastic-plastic Properties of AISI 1018 Steel

Property	Symbol	Data	Unit
Young's modulus	E	206,000	MPa
Plastic tangent modulus	$E\prime$	5,220	MPa
Yield strength	σ_Y	234	MPa
Curve shape parameter	n	10.0	

polynomial constitutive relation, Eq. (4.56). The corresponding elastic- plastic properties taken from this figure are given in Table 6.1. Also, the Poisson's ratio was read as 0.25 from a source book [92]. The thermal properties were determined from the same book [92]. Table 6.2 summarizes the thermal properties used in the analysis. Also, the temperature dependence of the mechanical properties for this AISI 1018 steel [92] is listed in Table 6.3. The relationship between crack growth resistance and crack extension for low carbon steel has been given in Section 3.1. (See Eq.(3.11)).

The plastic dissipation factor, Λ in Eq.(3.34), of AISI 1018 steel can be estimated from Eq.(3.22) by substituting the material properties and ξ which is equal to $\frac{\ln R/r_o}{\pi(1-\nu)} = 3.60$. (See Appendix A). Therefore, $\Lambda = \frac{(1+\nu)\xi E\prime}{(E-E\prime)} = \frac{(1+0.25)\times 3.60\times 5220}{(206000-5220)} = 0.116 \approx 0.12$.

Table 6.2: Thermal Properties of AISI 1018 Steel

Property	Symbol	Temperature (^oC)	Data	Unit
Thermal conductivity	k	20	65.2	W/m*K
		100	60.2	W/m*K
		200	55.0	W/m*K
Specific heat	C_v	20	0.450	kJ/kg*K
		100	0.452	kJ/kg*K
		200	0.455	kJ/kg*K
Thermal diffusivity	a	20	1.850×10^{-5}	m^2/sec
		100	1.700×10^{-5}	m^2/sec
		200	1.543×10^{-5}	m^2/sec
Thermal expansion	α	20	11.9×10^{-6}	$1/^oC$
		100	12.5×10^{-6}	$1/^oC$
		200	13.8×10^{-6}	$1/^oC$

Table 6.3: Temperature Dependence of Mechanical Properties

Property	Symbol	Temp. (^oC)	Data	Unit
Young's modulus	E	20	206,000	MPa
		100	202,800	MPa
		200	201,200	MPa
Plastic tangent modulus	$E\prime$	20	5,220	MPa
		100	5,200	MPa
		200	5,140	MPa
Yield strength	σ_Y	20	234	MPa
		100	208	MPa
		200	156	MPa

6.4 Finite Element Model

6.4.1 The mesh

A finite element model of the specimen is shown in Figure 6.1(a), with the details of the refined mesh surrounding the crack tip given in Figure 6.1(b). Due to symmetry in the geometry and boundary conditions with respect to the crack plane, only one half of the plate needed be considered. A total of 124 eight-node isoparametric elements were used together with 476 nodes. In order to minimize the possible discretization effects, singular elements were adopted in the vicinity of the crack tip. (See Fig.6.1(b)).

6.4.2 The boundary and initial conditions

The force boundary condition is:

$$\begin{aligned} \mathbf{L}_x &= f(t)sin\vartheta \qquad \text{at the point p} \\ \mathbf{L}_y &= f(t)cos\vartheta \qquad \text{at the point p} \end{aligned} \tag{6.2}$$

where the f(t) is the given force history shown in Figure 6.2 and is applied at the point p (its coordinates are $x = 0.016m, y = 0.020m.$) with the inclination ($\vartheta = 12.5°$) from the y axis. (See Figure 6.1(a)). The curve f(t) shown in Figure 6.2 was the time average of the measured force history depicted in Figure 5.10. Since the input force history is close to an impulse wave with no wave reflections, a time-averaging scheme of Figure 5.10 was thus considered to be a reasonable approximation to the input driving force

history for the finite element analysis.

In the following, the x- or y-components of the initial displacement, velocity and acceleration vectors, and the initial temperature are denoted by $\mathbf{u_o}, \mathbf{v_o}$, $\dot{\mathbf{u}}_\mathbf{o}$, $\dot{\mathbf{v}}_\mathbf{o}$, $\ddot{\mathbf{u}}_\mathbf{o}$, $\ddot{\mathbf{v}}_\mathbf{o}$,and $\mathbf{T_o}$, respectively. The initial conditions in this numerical case are:

$$\begin{aligned}
\mathbf{u_o} &= 0 \\
\mathbf{v_o} &= 0 \\
\dot{\mathbf{u}}_\mathbf{o} &= 0 \\
\dot{\mathbf{v}}_\mathbf{o} &= 0 \\
\ddot{\mathbf{u}}_\mathbf{o} &= \begin{cases} a_{xp} & \text{if at the point p} \\ 0 & \text{otherwise} \end{cases} \\
\ddot{\mathbf{v}}_\mathbf{o} &= \begin{cases} a_{yp} & \text{if at the point p} \\ 0 & \text{otherwise} \end{cases} \\
\mathbf{T_o} &= 20^\circ C
\end{aligned} \tag{6.3}$$

where a_{xp} and a_{yp} are the respective x- and y-components of the acceleration vector at point p. These quantities can be solved from the equilibrium equations, Eq.(4.32), at time $t = 0$ and the given load applied at the point p.

The thermal boundary condition is:

$$\mathbf{q} \cdot \mathbf{n} = 0 \tag{6.4}$$

on the entire surface , in which $\mathbf{n}$ is the outward normal vector. In fact, this is an adiabatic boundary condition.

Finally, the specimen material was assumed to be in a virgin state.

6.4.3 Integration time step

Mathematically speaking, the collocation method, one of the implicit direct integration schemes, is unconditionally stable with increasing accuracy as the integration time step decreases. On one hand, large integration time steps tend to introduce numerical errors and, in the limit, the dynamic analysis with an infinitely large time step degenerates into a static analysis. But, on the other hand, small integration time steps mean more computation and higher truncation and round-off errors. Therefore,the time steps in real computer analysis must not be too small. In brief, an appropriate time step should be the size that is necessary to obtain acceptable results. The following applicable conditions were taken account in the time-step selection.

1. Resolve the Input Force Curve - The integration time step (ITS) must be small enough to characterize the input force curve. The smaller the ITS, the more closely the input curve will be followed. If an input curve is to be reasonably followed, it is recommended that at least 7 integration points occur along the shortest "length" side [91]. In the present case, 0.3 ms resulted from this guide. (See Figure 6.2)

2. Wave Propagation - In Section 4.7.2 the limit of ITS from this consideration has been discussed in detail. The longitudinal elastic wave speed in the present case is given by $c_c = \sqrt{E/\rho} = 5139.1 mm/ms$.

The minimum element size in the mesh is 0.2 mm. From Eq. (4.59), the ITS should be approximately 0.4 μs. As a result, a disturbance traveling at the wavespeed during a time step of $0.4\mu s$ does not extend over the region of an element.

3. Ensure an accurate integration of the response in the fundamental period - The definition of the fundamental period and the value of $0.22ms$ in the present case have been described in detail in Section 6.2. Generally speaking, the ITS can be taken as one fiftieth or hundredth of the period [72], i.e. $2 \sim 4\mu s$.

4. Ensure an accurate loading increment for the plastic analysis. The limit of ITS from this consideration has been discussed in Section 4.7.1. In the present program, the ITS can be automatically varied as needed by the plastic or elastic analysis. Numerical experiments have indicated that the plastic analysis imposed the strictest restriction on the ITS at the peak period of loading. The corresponding ITS decreased to $0.02\mu s$ due to yielding in the vicinity of the crack tip.

Obviously, the minimum of the above requirements i.e. $0.02\mu s$ for the ITS should be used in the present finite element analysis. However, this very small time step resulted in an integration of about 20,000 steps which need a CPU time of approximately 25 hours on the main frame computer at the University of Manitoba. The Computer Center at the University discourages

any job more than 10 minutes of CPU time. In order to overcome this difficulty, the DCTEPSA code provided the function of a "computing pause and restart" scheme. Accordingly, the entire analysis can be completed by approximately 150 job submissions.

6.5 Numerical Results

This numerical study is presented to illustrate the significance of the thermomechanical coupling on a fractured solid subjected to dynamic loading. In this study two approaches were used to analyze this experimental case as described above. One is the uncoupled approach by which the coupling effect was neglected, and the degree of freedom at a node in the finite element mesh was taken as two, i.e. the x- and y-components of the displacement. The other is the coupled approach by which the coupling effect was taken account and a degree of freedom of three was assigned for each node, i.e. the two displacement components and the temperature.

Results obtained from both the approaches are compared graphically as follows.

6.5.1 Crack driving force

The crack driving force is generally referred to as the strain energy release rate [39]. For dynamic loading conditions, the crack driving force, G, is

defined as

$$G = \lim_{\Delta c \to 0} \frac{\Delta W - \Delta U - \Delta T}{\Delta c} \tag{6.5}$$

where the Δc is a crack extension, W and U denote the external work done on the solid body and its elastic energy, per unit thickness, respectively, while T denotes the kinetic energy in the solid body per unit thickness.

Exploiting the beam-like character of this DCB specimen, Kanninen and Popelar [39] derived the following equation for establishing the crack driving force:

$$G = 2E(w^2/h)_{x=c} \tag{6.6}$$

where w is the vertical displacement of the geometric centerline of the arm of the DCB specimen during dynamic loading, h is the height of this arm ($h = 50mm$ in the present case) and c is the crack length. Also, Kanninen and Popelar stated that the predictions of this equation are in excellent agreement with more exact approaches [39, pp.243]. Eq.(6.6) was used in this study, because it is simple and accurate and, thus, decreased the CPU time for the present analysis.

The numerical results of the crack driving force in the two cases by using the uncoupled and coupled approaches are shown in Figure 6.4. Based on this Figure, the following points can be made.

- The maxima in the two cases all are less than the critical value,$90kJ/m^2$ [66]. Therefore, the crack does not grow, i.e. there was no crack extension during the dynamic loading.

- The difference of the maxima between the two cases is small,and the three main peaks of the crack driving force history obtained by using the coupled approach are always slightly higher than that obtained by using the uncoupled approach.

- The modes of the crack driving forces in the two cases are almost the same during this whole process.

6.5.2 Temperature change

At the crack tip

The results of the temperature change at the crack tip are shown in Figure 6.5(a). No temperature change can be obtained by using the uncoupled approach. This figure revealed a very obvious effect of the thermomechanical coupling. Also, the maximum temperature rise at the crack tip was approximately $16°C$, i.e. the temperature at the crack tip was $16°C$ higher than the bulk temperature of the plate.

Along the crack-line

The temperature distribution along the crack-line ahead of the crack tip is shown in Figure 6.5(b). It can be seen from this figure that the temperature rise due to the coupling effect was a local phenomenon, as expected. Physically, it suggested that the coupling effect mainly occurred in the vicinity of the crack tip.

A comment on the temperature rise

The above temperature rise seems to be small. However, whether this local temperature increase is considered "small" or "large" depends on its effect on the fracture behavior. Accordingly, for the moment,consider an example in which a special situation may result in great significance for fracture behavior. Assume that the bulk temperature of a structure, e.g. the hull of an icebreaker, made of A517-F steel is exposed to a cold environment at $-40°C$ which just falls into the brittle-ductile transition temperature range of this steel. Further,its dynamic critical stress-intensity factor is in the neighborhood of 75 $MN \cdot m^{-3/2}$ from the curve of dynamic K_{Ic} versus temperature established in [33] which was obtained by shifting the actual slow-bend K_{Ic} curve to an appropriate higher temperature region. (See Figure 6.39). Now, if a temperature rise of $16°C$ at the crack tip due to the coupling effect, such as computed from the foregoing case, would be taken into account, a significantly higher dynamic critical stress-intensity factor of 110 $MN \cdot m^{-3/2}$ was read from the preceding curve of dynamic K_{Ic} versus temperature shown in Figure 6.39. Such a rise in the dynamic K_{Ic} value would certainly affect the fracture characteristics of that structure. This problem will be further discussed in Section 6.6.

Comparison with measurement

It is a well-known fact that a thermocouple of finite size cannot have an infinitely fast response, because of the thermal inertia of the measuring junction. Thus the "observed" readings must be converted into "true" readings. To the best of the author's knowledge, this conversion is a difficult task, and only a few references [96,102,103] deal with this issue. The authors of these papers all adopted the Laplace transform technique. The transfer function of a thermocouple circuit is defined in a transformed variable as $G_T(s) = \frac{T_B(s)}{T_P(s)}$. It is shown analytically in [96] that

$$G_T(s) = \frac{a_T}{s + c_T} \tag{6.7}$$

where a_T and c_T are constants, the values of which depend on the particular thermocouple installation. This simplified transfer function for the thermocouple permits the calculation of the actual surface temperatures from the thermocouple readings. Because, however, the values of a_T and c_T are different for each thermocouple circuit, it is necessary to experimentally measure these values in each case. This is done by the following procedure which requires a special device and technique [96]. Firstly, an electric current with a step change generated by a special device is applied through a test section on which the thermocouple is installed. Secondly, the resulting response of the tested thermocouple is recorded. Thirdly, a developed technique is used to calculate the theoretical ramp change in temperature produced by the step change in the current through the test section under an adiabatic condition.

Fourthly, the theoretical ramp change in temperature and the measured thermocouple change in temperature are together depicted in the same figure. Then from the figure, the graphical determination is performed to evaluate the constants of the thermocouple. Finally, the obtained value of $G_T(s)$ can be used to calculate the true surface temperature from any measured thermocouple readings by an inversed Laplace transform, i.e. $\mathcal{L}^{-1}\frac{T_B(s)}{G_T(s)}$.

In the present experimental conditions the above method for producing a ramp temperature change has been modified. The theoretical ramp change in temperature was approximately produced by an existing ruby laser device. Appendix B gives the details of the calculation by which the "observed" temperature readings were converted into "true" temperature history at the measured point. Generally,the measuring junction of a thermocouple is regarded as a point. The output of this thermocouple is considered to describe the temperature in a position of this measuring junction. The temperature obtained from the output is probably an average over the area covered by this measuring junction. The foil-thermocouple used in the present study has a measuring junction of $0.37 \times 0.5mm^2$. (See Figure 5.6(a)). This junction was welded on the surface of DCB specimen,and it approximately covered the nine nodal points in the finite element mesh. (See Figure 6.6). It is a well known fact that the Peltier emf (electromotive effect) produced by the welded seam of thermocouple junction is the main contribution of thermocouple output emf. Therefore, temperatures at points in the vicinity of the

welded seam of the junction would be close to the temperature measured by the thermocouple. Based on this judgement, the results of finite element analysis at the four nodal points (i.e. points a,b,c and d shown in Figure 6.6) were compared with the "true" temperature history measured by the foil-thermocouple. Figure 6.6 shows this comparison. It can be seen from Figure 6.6 that

- The patterns of these curves are similar: they show a decrease of temperature in the initial stage, and then pass through points of inflection to be followed by a rapid temperature rise until reaching maxima, and then gradually slope downwards.

- These curves come for a duration up to 1.6 ms, and then diverge. The maxima of these curves, however, are of the same order.

- The analytical curves rise more steeply than the measured curve. Therefore,it may imply that the response of the foil-thermocouple is still not fast enough. But it may also imply that the conversion of mechanical energy into heat needs time which was not taken account of by the coupled thermomechanical analysis. This is a worthwhile future investigation.

6.5.3 Displacement, velocity and acceleration

Figures 6.7 to 6.15 depict the histories of the displacement, velocity and acceleration at the crack tip, Node #93 ($0.4c_o$ apart from the crack tip,

where the c_o denotes the crack length) and #185 ($1.5c_o$ apart from the crack tip) for the uncoupled and coupled cases, separately. Basically, the small differences in the displacements and velocities of the uncoupled and coupled cases were revealed from these figures. However, there were major differences in the accelerations at the crack tip between both cases. From Figure 6.9 it can be seen that the difference of acceleration between the uncoupled and coupled cases after 1.5 ms is very large. The results by using the coupled approach represent considerable dissipation of energy, and the results by using the uncoupled approach represent no dissipation of energy. This fact is reasonable, because the coupling terms are equivalent to energy dissipation terms and play a damping role, and just at the crack tip the coupling terms reached a maximum.

6.5.4 Effective strains and stresses

There were the four singular elements around the crack tip. (See Figure 6.1(b)). The DCTEPSA code printed out the strains and stresses at all the sampling points in all elements. The coordinates at some Gauss' quadrature sampling points shown in Figures 6.16 to 6.35 are listed in Table 6.4. Note that the coordinates at the crack tip are $x = 90.00mm, y = 0.00$. Figures 6.16 to 6.31 illustrate the histories of the effective stresses and strains at the sampling points No. 3 and 4 in the four singular elements, separately. It can be seen from these figures that, after 1.5 ms, the effective strains and stresses in the coupled case are usually greater than that in the uncoupled case.

Table 6.4: The coordinates at the eight sampling points

Element No.	Sampling Point No.	x (mm)	y (mm)
1	3	90.04	0.03
1	4	90.04	0.008
2	3	90.01	0.04
2	4	90.03	0.04
3	3	89.89	0.04
3	4	89.99	0.04
4	3	89.96	0.008
4	4	89.96	0.03
13	3	93.42	2.70
13	4	93.42	0.72

Compared with the temperature history at the crack tip shown in Figure 6.5, both of the variations coordinated in time. Obviously, the temperature rises in the vicinity of the crack tip due to the coupling effect exerted a marked influence on the strains and stresses. Also, the above figures show that this influence in the elements No. 1 and 2 ahead of the crack tip is rather larger than that in the elements No. 3 and 4 on the crack surface, as expected. Furthermore, the output data in the neighboring elements revealed that these differences between the uncoupled and coupled cases declined considerably beyond the scope of a distance 5 millimeter from the crack tip, as shown in Figures 6.32 to 6.35. In other words, the coupling effect is definitely a local phenomenon.

6.6 Discussion and Summary

The motivation for this thesis is to illustrate that the coupling effect might be strong enough to influence the fracture characteristics of structures, particularly when they are subjected to high loading rates. In conventional cases, the crack toughness of structural materials, particularly steels, increases with increasing bulk temperature and decreasing loading rate [33]. These two general types of behavior are shown schematically in Figures 6.36 and 6.37. Figure 6.36 shows that K_{Ic} increases with increasing bulk temperature of the specimen. Figure 6.37 shows that, at a constant bulk temperature, higher loading rates generally result in lower values of the fracture toughness of materials. Also, the trend revealed by Figure 6.37 is that fracture toughness shows a monotonic reduction with loading rate. An explanation for this phenomenon lies with the elevation of flow stress curve with strain rate.

However, Klepaczko (1982) [95] observed a minimum in the fracture toughness spectrum of carbon steel (0.45 % carbon) when employing a loading rate scale of parameter $\dot{K}_I$, which is frequently used to characterize how fast the crack tip region is loaded. (See Figure 6.38). It is, therefore, logical to consider the thermofracture coupling effect as a possible factor in explaining the above experimental results presented by Klepaczko, because the coupled effect involves both temperature and loading rate effects.

As described in the preceding section, the measured temperature rise of $16°C$ at the tip of a stationary crack under the conditions of dynamic

loading in the present study may be considered to have a significant influence on the fracture toughness of the material. Therefore, the coupling effect would become a very important factor in the case of evaluating the fracture toughness spectrum of material such as shown in Figure 6.38.

For the moment, let us assume, firstly, that a local heating at the crack tip to a temperature T_d will result in a behavior similar to that of a specimen at a uniform bulk temperature T_d. On the one hand, it is generally observed that increasing the temperature of a notched specimen increases the fracture toughness for a given loading rate. (See Section 6.5). On the other hand, as the loading rate is increased, the toughness usually decreases for a given temperature.

From the coupled heat conduction equation (3.34), it shows that:

- The plastic dissipation term, $(1 - \Lambda)\sigma_{ij}\dot{\varepsilon}^p_{ij}$, increases with increasing strain rate.

- The strain rate increases with increasing crack speed, $\dot{c}$, so that the other coupling term, $(G - 2\gamma)\dot{c}\delta(\mathbf{r} - \mathbf{r_o})$, also increases.

- The rise in temperature of the crack tip thus becomes more significant when the above two coupling terms increase because these two terms are equivalent to internal heat sources involved in the heat conduction equation.

- The fracture toughness, therefore, increases with increasing tempera-

ture of the crack tip.

Accordingly, the curve published by Klepaczko [95] can be explained from the coupled theory in the following way. In a region of lower loading rate, the increment of toughness due to the temperature rise may be less than the decrement due to the loading rate, and thus the curve would firstly slope downward as shown in Figure 6.38. When both effects become equal in a certain region at certain instants, the curve reached the minimum point of the curve. Further increasing the loading rate would result in an upward sloping segment of the curve. In brief, this shapes the curve form measured by Klepaczko. Moreover, it is expected that Klepaczko's curve finally slopes downward, following the above upward sloping segment, because the temperature rise at the tip of the crack in the specimen is close to or has attained the melting point of the material, as presented in the example of titanium alloy experiment described in Chapter 3.

In conclusion, if one considers the influence of loading rate and the temperature rise due to the coupling effect at the crack tip,which increases with loading rate, there will be a pair of opposing effects acting simultaneously on the fracture toughness. It would be possible to explain a pattern in the measured curve of fracture toughness versus loading rate as demonstrated by Klepaczko [95]. This pattern was difficult to explain by conventional analyses.

Chapter 7

CONCLUSIONS AND RECOMMENDATIONS

7.1 Summary and Conclusions

An experimental procedure and corresponding uncoupled and coupled finite element analyses have been presented. The experimental investigation includes the following major activities: the preparation of DCB specimens, the alignment of the experimental set-up, the calibrations of circuits for temperature and force measurements, the determination of response time and transfer function of the circuit for temperature measurements, the experimental observation of transient changes in temperature and impulsive forces and the conversion of the observed temperature readings into "true" readings. All these activities were necessary for the measurement of the coupling effect on a fractured specimen subjected to impulsive force. Also, this measurement of impulsive force provided the input data for the subsequent uncoupled and coupled finite element analyses which were carried out by using

the DCTEPSA program. This code contains the following major elements: algorithms to account for three degrees of freedom at nodes; the singular elements for crack tip deformation fields; the constitutive equation for thermal elastic-plastic deformation of solids under dynamic loading; the coupled heat conduction; the optimal collocation methods for performing time integration; the temperature dependent properties of materials; the pause and restart function of the analysis; the automatic control of time step size and, finally, the mixed coupled-uncoupled algorithm for saving computational effort which can be performed by assigning the three degrees of freedom to the nodes in the regions of desired coupled analysis (e.g. in the crack zone), and assigning the two degrees of freedom (i.e. keeping x- and y-component of displacement only) to those nodes in the regions of uncoupled analysis (e.g. away from the crack zone). This program leads to the following features.

- The program has the capacities of performing 2-D (or 3-D axisymmetric) quasi-static or dynamic coupled thermoelastic-plastic stress analyses for fractured solids.

- The program includes a transient heat conduction analysis.

- The program can conduct analyses of static or dynamic uncoupled thermoelastic-plastic stress for fractured solids.

- The program can perform a mixed coupled-uncoupled algorithm ,resulting in high computational efficiency.

- The program can thus predict the coupling effect on 2-D fractured solids with a stable crack under dynamic loading conditions.

Significant observations were made on the temperature rise and damping of acceleration change in the vicinity of crack tip through experimental and analytical case studies performed on a DCB specimen subjected to an impulsive force. A number of these observations have never been reported before in the published literature. The role of the coupling effect on fractured solid was also investigated. The major conclusions which can be drawn from the present research are as follows.

1. The coupling effect on a fractured solid subjected to an impulsive force is considerable in comparison to the same effect on unfractured solids.

2. The inherent coupling effect increases the temperature in the vicinity of a crack tip. This rise in temperature is significant enough to influence the fracture toughness, especially when the temperature of the fractured solid is close to the brittle-ductile transition temperature.

3. Neglecting the coupling effect in some dynamic fracture analyses may lead to under estimations of the crack driving force, the effective stresses and strains in the vicinity of the crack tip, and over-estimations of the velocity and acceleration fields in the vicinity of the crack tip.

4. There were no significant differences between entire stress and strain fields obtained from the coupled and uncoupled analyses under the

loading and geometric conditions in the present studies.

5. The coupling, in combination with the loading rate effect on the fracture toughness of material, can be used to explain the specific pattern of fracture toughness versus loading rate measured by Klepaczko [95].

6. The dynamic coupled, thermofracture analysis by the finite element code is a feasible approach.

Major contributions were made in this thesis research as can be summarized as follows:

- The extension of thermomechanical coupling theory for fractured solids.
- The derivation of a new coupled heat conduction equation to account for the Thermofracture Coupling Effect (TFCE).
- The development of DCTEPSA computer code which has the following unique features

    1. It is capable of performing coupled dynamic thermoelastoplastic analysis of fractured solid.
    2. All nodes possess three degrees of freedom (two displacement components and temperature).
    3. A mixed uncoupled-coupled algorithm was developed.

- The proposition of an experimental arrangement for measuring temperature rises in fractured specimens subjected to impact load.

- The development of an effective technique for determining the transfer function of a foil thermocouple by using a ruby laser beam device.

7.2 Recommendations

The present study has extended the coupled thermomechanical approach to the analysis of fractured solids subjected to impulsive forces.Results obtained from this study have demonstrated that there is a stronger coupling effect on a fractured solid than that on an unfractured solid. This approach provides a good potential for further research in the area of dynamic fracture. With this experience in hand, the following recommendations with regard to further work in this area are in order.

- More experimental verifications are necessary for various loading rates and stable crack extensions and, if possible, for unstable crack propagation.

- The conversion techniques of "observed" temperature readings into the corresponding "true" temperature readings need furthermore improving,especially for the cases involving rapid temperature variations induced by very high loading rates.

- The present coupled approach should be used to check the analytical results of dynamic fracture or thermofracture problems which were customarily solved by the uncoupled approach. Present case studies have already indicated the inadequacy of this traditional approach for certain problems.

- Although it will be a quite complicated and expensive proposition, it is desirable to implement a moving mesh algorithm given in [23] into the present finite element code, which would permit more precise computation and general application for the problems involving unstable crack propagation.

- The energy dissipation mechanism and its time requirement in the fracture process zone is necessary to develop a more precise model. Investigations from a microscopic point of view of the dissipation mechanism will be much needed.

Bibliography

[1] G. Tammann and H. Warrentrup, "Zeitschrift fuev Matallkunde", 29(1927), p.84, quoted from "The Stored Energy of Cold Work", in "Progress in Metal Physics", 7, pp.251-252,1958.

[2] T.R. Hsu, "The Finite Element Method in Thermomechanics", George Allen and Unwin Ltd., London, 1986.

[3] A. Banas, T.R. Hsu and N.S. Sun, "Coupled Thermoelastic-plastic Stress Analysis of Solids by Finite Element Method", Journal of Thermal Stresses, Vol.10, pp.319-344, 1987

[4] D.H. Allen and W.E. Haisler, "A Theory for Analysis of Thermoplastic Materials", Computers and Structures, Vol.13, 129-135, 1981.

[5] R. Weichert and K. Schonert, "On the Temperature Rise at the Tip of a Fast Running Crack", J. Mech. Phys. Solids, Vol.22, pp.127-133, 1974.

[6] R. Weichert and K. Schonert, "Heat Generation at the Tip of a Moving Crack", J. Mech. Phys. Solids, Vol.26, pp.151-161, 1978.

[7] K. Schonert and R. Weichert, Chem. Ing. Technik, Vol.41, pp.295, 1969.

[8] A. Kobayashi and H. Suemasu, "Generation and Conduction of Heat during Fracture in Carbon-Fiber Composites", in "Composite Materials", ed. by K. Kawata and T. Akasaka, Proc. Japan-U.S. Conference, Tokyo, 1981.

[9] Peter J. Loose and F.R. Brotzen, "Localized Heat Generation during Fracture of Cyclically Loaded Steel", Metall. Trans. A, Vol.14A, pp.1409-1419, 1983.

[10] R. Attermo and G. Ostberg, "Measurements of the Temperature Rise Ahead of a Fatigue Crack", Int'l J. Frac. Mech., Vol.7, pp.122, 1971

[11] J.C. Hsieh, Ph.D. Dissertation, Virginia Polytechnic Inst., Dept. of Mech. Engr., Schenectady, N.Y., 1977.

[12] S.Y. Chen and T.R. Hsu, "Finite Element Elasto-Plastic Stress Analysis of Solids by Finite Strain Theory, Thermomechanics Lab. report No.7710-48, University of Manitoba, Winnipeg, Canada, October 1977.

[13] W. Doll, "Application of an Energy Balance and an Energy Method to Dynamic Crack Propagation", Int. J. of Frac., Vol.12, No.4, pp.595-605, Aug., 1976.

[14] P.G. Fox and J. Soria-Ruiz, "Fracture-induced Thermal Decomposition in Brittle Crystalline Solids", Proc. Roy. Soc. London, A.317, pp.79-90, 1970.

[15] J.T. Norris, Undergraduate Honors Thesis, Union College, Dept. of Mechanical Engineering, Schenectady, N.Y., 1976.

[16] Z.B. Kuang and S.N. Atluri, "Temperature Field due to a Moving Heat Source: A Moving Mesh Finite Element Analysis", J. App. Mech., Vol.52, pp.274-280, June 1985.

[17] S.N. Atluri, M. Nakagaki et al, "Crack-tip Parameters and Temperature Rise", in "Dynamic Crack Propagation", Engr. Frac. Mech., Vol.23, No.1, pp.167-182, 1986.

[18] R.W. Armstrong, C.S. Coffey and W.L. Elban, "Adiabatic Heating at a Dislocation Pile-up Avalanche", Acta Metall., Vol.30, pp.2111-2116, 1986.

[19] J.R. Rice and N. Levy, "The Physics of Strength and Plasticity", A.S. Argon ed., MIT Press, Cambridge, MA, pp.277,1969.

[20] J.R. Rice, "Thermodynamics of the Quasi-static Growth of Griffith Cracks", J. Mech. Phys. Solids, Vol.26, pp.61-78, 1978.

[21] J.L. Nowinski, "Theory of Thermoelasticity with Appreciation, European Printing Cooperation", Ireland, 1978.

[22] Y.C. Fung, "Foundations of Solid Mechanics", Prentice-Hall, Inc., Englewood Cliffs, 1965.

[23] S.N. Atluri and T. Nishioka, "Numerical Studies in Dynamic Fracture Mechanics", Int. J. of Frac., Vol.27, No.3-4, pp.245-262, 1985.

[24] K.N.G. Fuller, P.G. Fox, and J.E. Field, " The Temperature Rise at the Tip of Fast-moving Cracks in Glassy Polymers", Proc. R. Soc. London, A.341, pp.537-557, 1975.

[25] K.B. Broberg, "On Effects of Plastic Flow at Fast Crack Growth", in "Fast Fracture and Crack Arrest", ASTM STP 627, G.T. Hakn and M.F. Kanninen, eds., pp.243-256, 1977.

[26] A.S.Kobayashi,M.Ramulu,M.S.Dadkhah,K.H.Yang and B.S.J.Kang, "Dynamic Fracture Toughness", Int. J. Frac., Vol.30, pp.275-285, 1986.

[27] L.R.F. Rose, "Recent Theoretical and Experimental Results on Fast Brittle Fracture", Int. J. Frac., Vol.12, pp.799-813, 1976.

[28] W.G. Knauss and K. Ravi-chandar, "Some Basic Problems in Stress Wave Dominated Fracture", Int. J. Frac., Vol.27, pp.127-143, 1985.

[29] M.F. Kanninen, "Applications of Dynamic Fracture Mechanics for the Prediction of Crack Arrest in Engineering Structures", Int. J. Frac., Vol.27, pp.299-312, 1985.

[30] A.S. Kobayashi, "Experimental Mechanics 23", No.3, pp.338-347, 1983.

[31] J.D. Bryant, D.D. Makel and H.G.F. Wilsdorf, "Observations on the Effect of Temperature Rise at Fracture in Two Titanium Alloys", Materials Science and Engineering, 77, pp.85-93, 1986.

[32] A.J. Rosakis, J. Duffy, and L.B. Freund, "The Determination of Dynamic Fracture Toughness of AISI 4340 Steel by the Shadow Spot Method", J. Mech. Phys. Solids, Vol.32, No.4, pp.443-460, 1984.

[33] J.M. Barsom and S.T. Rolfe, "Correlations between K_{Ic} and Charpy V-Notch Test Results in the Transition-Temperature Range", in Impact Testing of Metals, ASTM STP 466, ASTM, pp.281-302, 1970.

[34] T. Kanazawa, S. Machida, T. Teramoto and H. Yoshinari, "Study on Fast Fracture and Crack Arrest", Experimental Mechanics, Vol.21, pp.78-88, 1981.

[35] J.W. Dally, W.L. Fourney and G.R. Irwin, "On the Uniqueness of the Stress Intensity Factor - Crack Velocity Relationship", Int. J. Frac., Vol.27, pp.159-168, 1985.

[36] J.O.W. Dillon, "Coupled Thermoplasticity", J. Mech. Phys. Solids, Vol. 11, pp.21-33, 1963.

[37] C.E. Turner, "Methods for Post-yield Fracture Safety Assessment, in Post-yield Fracture Mechanics", Ed. by D.G.H. Latzko, Applied Science Publishers LTD., London, pp.23-210, 1979.

[38] R.H. Heyer, "Crack Growth Resistance Curves (R-Curves) - Literature Review," Fracture Toughness Evaluation by R-Curve Methods, ASTM STP 527, American Society for Testing and Materials, pp.3-16, 1973.

[39] M.F. Kanninen, and C.H. Popelar, "Advanced Fracture Mechanics", Oxford University Press, New York, 1985

[40] J.D. Lndes and J.A. Begley, "Test Results from J-Integral Studies: An Attempt to Establish a J_{Ic} Testing Procedure", in "Fracture Analysis", ASTM STP 560, American Society for Testing and Materials, pp.170-186, 1974.

[41] J.D. Landes and J.A. Begley, "Experimental Methods for Elastic-Plastic and Post-yield Fracture Toughness Measurements", in "Post-yield Fracture Mechanics", Ed. by D.G.H. Latzko, Applied Science Publishers LTD., London, pp.211-253, 1979.

[42] E.F. Boyle, "Calculation of Elastic and Plastic Crack Extension Forces", Ph.D. Thesis, The Qeen's University, Belfast. 1972.

[43] H. Andersson, "Finite Element Treatment of a Uniformly Moving Elastic-plastic Crack Tip", J. Mech. Phys. Solids, v.22, pp. 285-308, 1974.

[44] A.S. Kobayashi,S.T. Chiu and R. Beeuwkes, "A Numerical and Experimental Investigation on the Use of the J-integral", Engng. Fract. Mech., vol.5, pp.293-305, 1973.

[45] M.F. Light and A.R.Luxmoore, "Some Further Results on Slow Crack Growth Predictions by a Finite Element Method", Int. J. Fract., vol.12, pp.503-504, 1976.

[46] I.S. Raju, "Calculation of Strain-energy Release Rates with Higher Order and Singular Finite Elements", Engng. Fract. Mech., vol.28, pp.251-274, 1987.

[47] J.P. Gudas and O.R. Anderson ,"J_I -R Curve Characteristics of Piping Material and Welds, U.S.N.R.C. 9th Water Reactor Safety Research Information Meeting, Washington D.C. , Oct. 1981.

[48] E. Sternberg and J.G. Chakravorty, "On Inertia Effect in a Transient Thermoelastic Problem", J. Appl. Mech., vol. 26, No. 4, Trans. ASME, Vol. 81, Series E, pp.503-509, 1959.

[49] R.E. Nickell and J.L. Sackman, "Approximate Solutions in Linear, Coupled Thermoelasticity", J. Appl. Mech., ASME, pp.255-266, June, 1968.

[50] Th. Lehmann, "Coupling Phenomena in Thermoplasticity", Paper L1/1, 5th Int. Conf. on Structural Mechanics in Reactor Technology, Berlin, 1979.

[51] J.T. Oden, "Finite Elements on Nonlinear Continua", McGraw-Hill, New York, 1972.

[52] F.A. McClintock and A.S. Argon, "Mechanical Behavior of Materials", pp. 179-180, Addison-Wesley, Reading, Mass., 1966.

[53] J.E. Bailey, "The Dislocation Density, Flow Stress and Stored Energy in Deformed Polycrystalline Copper", The Philosophical Magazine, vol. 8, pp. 223, 1963.

[54] K.J. Bathe, "Finite Element Procedures in Engineering Analysis", Prentice-Hall, Englewood Clifs, N. J., 1982

[55] O.C. Zienkiewicz, "The Finite Element Method", 3rd ed., McGraw-Hill, London, 1977.

[56] K.J. Bathe and E.L. Wilson, "Numerical Methods in Finite Element Analysis", Prentice-Hall, Englewood Cliffs, N.J., 1976.

[57] D.R.J. Owen and E. Hinton, "Finite Elements in Plasticity: Theory and Practice", pp. 377-462, Pineridge Press, Swansea, U.K., 1980.

[58] M.D. Snyder and K.J. Bathe, "A Solution Procedure for Thermoelastic-plastic and Creep Problems", Nucl. Eng. Des., Vol. 64, pp.49-80, 1981.

[59] G.C. Sih and J. F. Loeber, "Wave Propagation in an Elastic Solid with a Line of Discontinuity or Finite Crack", Q. App. Math., vol.27, p.193, 1969.

[60] S. A. Thau and T. H. Lu, " Transient Stress Intensity Factors for a Finite Crack in an Elastic Solid Caused by a Dilatational Wave", Int. J. Solids Struct., vol.7 ,p.731, 1971.

[61] F. M. Burdekin and D. E. W. Stone, "The Crack Opening Displacement Approach to Fracture Mechanics in Yielding Materials", J. of Strain Analysis, vol.1, p.145-153, 1966.

[62] J. R. Rice, " A Path Independent Integral and The Approximate analysis of Strain Concentration by Notches and Cracks", J. Appl. Mech. ASME Trans., **35**, p.379, 1986.

[63] J. W. Hutchinson, "Singular Behavior at the End of a Tensile Crack in a Hardening Material", J. Mech. and Phys. Solids.,vol.16, p.13-31, 1968.

[64] J. R. Rice and G. F. Rosengren, " Plane Strain Deformation near a Crack Tip in a Power-law Hardening Material", J. Mech. and Phys. Solids, vol.16, p.1-12, 1968.

[65] J. M. Krafft, A. M. Sullivan and R. W. Boyle, in Proceedings, Crack Propagation Symposium, College of Aeronautics, Cranfield, England, vol.1, p.8-26, 1961.

[66] D. Y. Wang and D. E. McCabe, "Investigation of R-curve Using Comparative Tests with CCT and CLWL Specimens", Presented at Eight National Fracture Symposium, Brown University, August, 1974.

[67] D. Broek, "Artificial Slow Crack Growth under Constant Stress. The R-curve Concept in Plane Stress", Engineering Fracture Mechanics, vol.5, p.45-53, 1975.

[68] D. Broek, "The Residual Strength of Aluminium Sheet Alloy Specimens Containing Fatigue Cracks or Saw Cuts", Tech. Rept. NRL-TRM. 2143, National Aerospace Laboratory, Amsterdam, 1965.

[69] D. Broek, "The Effect of Finite Specimen Width on the Resdual Strength of Light Alloy Sheet", Tec. Rept. NRL-TR M2152, National Aerospace Laboratory, Amsterdam, 1965.

[70] S. T. Rolfe and J. M. Barsom, "Fracture and Fatigue Control in Structures", Englewood-Cliffs, N.J.,Prentice-Hall, Ch.4,1977.

[71] H. A. Nied, " On the Thermal Feedback Reduction of Latent Energy in the Heat Conduction Equation", Mater. Sci. Eng., vol.9, p.243-245, 1972.

[72] Thomas J. R. Hughes, "The Finite Element Method", Prentice-Hall, New Jersey, Ch. 4-6, 1987.

[73] P. Tong and T. H. Pian," On the Convergence of the Finite Element Method for the Problem with Singularities", Int. J. Solids Struct., vol.9, p.313, 1973.

[74] R. H. Gallagher, "A Review of Finite Element Techniques in Fracture Mechanics", in "Numerical Methods in Fracture Mechanics", Eds. Luxmore and Owen, 1978.

[75] Y. Yamada, Y. Ezawa, I. Nishigashi and Okabe, "Reconsiderations on Singularity or Crack Tip Elements", Int. J. Num. Meth. Engng., vol.4, p.1525-44, 1979.

[76] R. D. Henshell and K. G. Shaw,"Crack Tip Elements are Unnecessary", Int. J. Num. Meth. Engng., vol.9, p.495-509, 1975.

[77] R. S. Barsoum, "On the Use of Isoparametric Finite Elements in Linear Fracture Mechanics", Int. J. Num. Meth. Engng., vol.10, p.25-37, 1976.

[78] S. N. Atluri, "Higher-order, Special and Singular Finite Elements", Ch. 4 in "Finite Element Methods", Eds. A. K. Noor and W. Pilkey, ASME, N.Y., 1983.

[79] H. D. Habbith, "Some Properties of Singular Isoparametric Elements", Int. J. Num. Meth. Engng., vol.11, p.180-184, 1977.

[80] V. I. Krylov,"Approximate Calculation of Integrals", McMillar Co.,N. Y., Ch. 7, 1962.

[81] Carl-Erik Fröberg,"Numerical Mathematics - Theory and Computer Applications", The Benjamin Inc., Ch. 5, 1985.

[82] C. F. Osgood and O. Shisha, "The Dominated Integral", J. Approx. Theory, vol. 17, p.150 - 165, 1976.

[83] P. M. Anselone and G. Opfer,"Numerical Integration of Weakly Singular Functions", Int. Series of Num. Math. (ISNM), vol. 45, p.11-43, 1979.

[84] Z. P. Bazant, J. L. Glazik and J. D. Achenback, "Finite Element Analysis of Wave Diffraction by a Crack", Mech. Div., ASCE, 102-EM3, p.479, 1976.

[85] K. W. Chan, "The Study of Dynamic Fracture Problems Using Finite Element Method", Ph. D. Dissertation, Clarkson College of Technology, Ch. 4, 1982.

[86] S. N. Atluri and T. Nishioka, " Numerical Modeling of Dynamic and Nonlinear Crack Propagation in Finite Bodies by Moving Singular Elements", in "Nonlinear and Dynamic Fracture Mechanics", Ed. by N. Perrone and S. N. Atluri, AMD-vol.35, ASME, 1979.

[87] D. D. Bloomquist and S. A. Sheffield," Thermocouple Temperature Measurements in Shock-compressed Solids", J. Appl. Phys., vol.51(10), p.5260-66, Oct. 1980.

[88] Y. A. Cengel , P. T. L. Zing and M. J. Kalinski,"The Use of Operational Amplifiers in Temperature Measurements with Thermocouples for Increased Accuracy and Resolution", The Winter Annual Meeting of the ASME, Anaheim, California, Dec. 7-12, 1986, Ed. by J. H. Kim and R. J. Moffat, p.87-91.

[89] B.S. Singh and A. Dybbs,"Error in Temperature Measurements Due to Conduction along the Sensor Leads", Transactions of the ASME, J. Heat Transfer, p.491-495, Aug. 1976.

[90] N. R. Keltner and J. V. Beck," Surface Temperature Measurement Errors", Transactions of the ASME, J. Heat Transfer, vol. 105, p.312-318, May. 1983.

[91] Swanson Analysis Systems Inc., "Nonlinear Transient Dynamic Analysis", in "ANSYS Engineering Analysis System User's Manual", vol.1, Section 2.14,p.2.14.1-6, 1987.

[92] W. H. Cubberly, B. P. Bardes, H. Baher, D. Benjamin, P. M. Unterweisei and C. W. Kirkpatrick,"Metal Handbook", 9th edition, vol. 1, ASM, 1978.

[93] W. C. Hurty and M. F. Rubinstein, " Dynamics of Structures", Prentice-Hall, Englewood Cliffs, N. J.,p.203, 1964.

[94] Fertis, "Dynamics and Vibration of Structures", Wiley- Interscience Publication, p.60-79,1973.

[95] J. R. Klepaczko,"Discussion of a New Experimental Method in Measuring Fracture Toughness Initiation at High Loading Rates by Stress Waves", J. Engng. Math. Tech., vol.104, p.29-35, Jan. 1982.

[96] S. J. Green and T. W. Hunt,"Accuracy and Response of Thermocouples for Surface and Fluid Temperature Measurements", in "Temperature: Its Measurement and Control in Science and Industry", vol.3, pt. 2, Ed. C. M. Herzfeld and A. I. Dahl, Peinhold Pub. Co., New York, p.695-722, 1962.

[97] M. B. Bever, D. L. Holt and A. L. Titchener, "The Stored Energy of Cold Work", Progress in Materials Science, vol. 17, 1973.

[98] A. Seeger and H. Kronmuller,"Stored Energy and Recovery of Deformed F.C.C. Metals", The Phil. Mag., vol.7 - eight series, p.897, 1962.

[99] D. Kuhlmann - Wilsdorf,"A New Theory of Work Hardening", Trans. Amer. Inst. Min. (Metal) Engrs. 224 ,p.1047, 1962.

[100] W. W. Duley,"Laser Processing and Analysis of Materials", Prenum Press, New York, p.85-98, 1983.

[101] P. W. Bridgeman, "Thermodynamics of Plastic Deformation and Generalized Entropy", Rev. Mod. Phys., vol. 22, p.56, 1950.

[102] T. C. Linahan,"The Dynamic Response of Industrial Thermometers in Well", Trans. Am. Soc. Mech. Engrs. 78, p.759-763,1956.

[103] E.R.Quandt and E.W.Fink,"Experimental and Theoretical Analysis of the Transient Response of Surface Bonded Thermocouples", Bettis Technical Review,WAPDBT-19 (June,1960),p.31-49 (available from the Office of Technical Services,Department of Commerce,Washington 25, D.C.).

[104] G.T.Hahn,R.G.Hoagland,A.R.Rosenfield, and R.Sejnoha, "Rapid Crack Propagation in a High Strength Steel",Metallurgical Transactions, vol.5,p.475-482, 1974.

[105] T.R. Hsu, G.G. Chen, Z.L. Gong and N.S. Sun, "On Thermofracture Behavior of Leaking Thin-wall Pipes", Int. J. Pres. Ves. and Piping vol. 24, p.269-281, 1986.

[106] David Anthony Wagner, "Fracture Characterization for Thermoinelasticity", Ph. D. thesis, Dept. of Mech. Eng., Stanford University, 1990.

Appendix A

The Estimation of Plastic Dissipation Parameter

The coupled heat conduction equation 3.34 in Chapter 3 contains a plastic dissipation factor or parameter, Λ, which was defined as the ratio of the rates of energy stored in the microstructure of the material resulting from the conversion of the kinetic energy to the internal energy during an adiabatic plastic deformation process. (See Section 3.3). It will be shown in this Appendix that this plastic dissipation factor for metals can be estimated according to the following formula:

$$\Lambda = \frac{(1+\nu)\xi E\prime}{(E - E\prime)} \tag{A.1}$$

where E is the Young's modulus and $E\prime$ is the slope of the plastic range of the stress-strain curve of the metal, and ξ is a constant to be evaluated by the dislocation theory.

The derivation of the plastic dissipation factor was based on the stored energy which can be firstly estimated by using some results of material sci-

ence. Literature on the topic of the stored energy of metals, either by experimental or theoretical works, are abundant. Bever, Holt and Titchener [98] summarized the progress of the research work on this topic up to 1973. They indicated [98] that the basic analytical methods for estimating the stored energy was to apply the dislocation theory to compute the elastic strain energy of the dislocations. There is, indeed, an abundance of experimental data about the stored energy for various metals in the published literature. The following formulae for the stored energy is given in reference [98]:

$$E_s = \xi_1 \frac{\sigma^2}{4G} \tag{A.2}$$

$$\xi_1 = \frac{\ln(R/r_o)}{4\pi(1-\nu)} \tag{A.3}$$

where G is the shear modulus, ν is Poisson's ratio, R is the dislocation cell radius and r_o is the radius of the stress field of the dislocation core which is taken as $\frac{\mathbf{b}}{2}$ with $\mathbf{b}$ being the Burgers' vector.

Seeger and Kronmuler [99] calculated the stored energy from the model of the dislocation arrangement assumed in Seeger's theory of work hardening.The formulae proposed by them have the forms:

$$E_s = \xi_2 \frac{\sigma^2}{4G} \tag{A.4}$$

$$\xi_2 = 2\pi(2-\nu)(0.776 + \frac{1}{n^2}\ln(\frac{R_o}{r_o} - 0.1159)) \tag{A.5}$$

where n is the number of dislocations in each dislocation group and R_o is half the distance between dislocation groups of opposite sign.

Bailey [53] computed the stored energy from the C-B-H (Cottrel, Basinki and Hirsch) theory of dislocation. The formulae derived by him are:

$$E_s = \xi_3 \frac{\sigma^2}{4G} \tag{A.6}$$

$$\xi_3 = \frac{4\pi}{m}(\ln(\frac{R}{r_o}) + 1 + \ln(\frac{R}{r})) \tag{A.7}$$

where R is the radius of the volume over which the stress field of a dislocation extends.

Kuhlmann - Wilsdorf [100] calculated the stored energy from their model of the dislocation. The formulae derived by them are

$$E_s = \xi_4 \frac{\sigma^2}{4G} \tag{A.8}$$

$$\xi_4 = 4\rho\pi\bar{l}^2 \tag{A.9}$$

where ρ is the dislocation density and $\bar{l}$ is the average free length of a dislocation.

Besides, some phenomenological formulae for the stored energy were obtained by experimental observations. For example, Bailey [53] stated that:

$$E_s = 7.7 \frac{\sigma^2}{4G} \tag{A.10}$$

for OFHC (oxygen-free high conductance) copper.

In brief, the stored energy can be expressed as $E_s = \xi \frac{\sigma^2}{4G}$ in which ξ can be estimated from the foregoing formulae. It is well known that one common way of describing the effect of the general stress and strain state

of a material under a combined loading situation is by way of the "effective stress", $\bar{\sigma}$ defined as follows:

$$\bar{\sigma} = (\frac{3}{2}\sigma_{ij}\prime\sigma_{ij}\prime)^{1/2} \tag{A.11}$$

Therefore, the formula can be rewritten as the following general form:

$$E_s = \frac{\xi}{4G}\bar{\sigma}^2 \tag{A.12}$$

and

$$\dot{E}_s = \frac{\xi}{2G}\bar{\sigma}\dot{\bar{\sigma}} \tag{A.13}$$

Because the plastic work rate is

$$\dot{w}^p = \bar{\sigma}\dot{\bar{\varepsilon}}^p \tag{A.14}$$

then Λ can be calculated by its definition, i.e.

$$\begin{aligned} \Lambda &= \frac{\dot{E}_s}{\dot{w}^p} \\ &= \frac{\xi}{2G}H\prime \end{aligned} \tag{A.15}$$

where $H\prime = d\bar{\sigma}/d\bar{\varepsilon}^p$, and is called the equivalent plastic modulus. It was proved in [2] that

$$H\prime = \frac{1}{\frac{1}{E\prime} - \frac{1}{E}} \tag{A.16}$$

where $E\prime$ is the slope of the stress-strain curve of a metal. Substituting Equation (A.14) into (A.13), one gets:

$$\Lambda = \frac{(1+\nu)\xi E\prime}{(E - E\prime)} \tag{A.17}$$

which is Equation 3.22 in Chapter 3. For an ideal plastic metallic material,all plastic work should be converted into heat, as Bridgeman [101] has pointed out, i.e. the plastic dissipation factor $\Lambda = 0$. This is in agreement with the result of the calculation from the above formula with $E\prime = 0$ for this material. For metals with a linear strain hardening behavior, the factor Λ becomes a constant and may be considered as a material property, with $E\prime$ being constant in this case. Within small strain regions, most polycrystalline f.c.c. (face-centered cubic) metals can be treated as this kind of material.

Appendix B

Transient Surface Temperature Measurements

A well known fact is that a thermocouple of finite size cannot have an infinitely fast response because of the thermal inertia of the measuring junction. Thus the "observed" readings should be converted into "true" readings. The present study adopted the method involving the Laplace transform technique [96]. Therefore, the main task of the method is to experimentally determine the two unknown constants, a_T and c_T, of a simplified transfer function of the foil-thermocouple which was welded on the DCB specimen.This was possible because this simplified transfer function can be expressed as:

$$G_T(s) = \frac{a_T}{s + c_T} \tag{B.1}$$

where s is the parameter of the Laplace transform. (See Section 6.5 and [96]). This was done by the following procedure.

(1) The procedure for evaluating the transfer function required a theoretical ramp temperature change.In [96] this ramp change in temperature is

Table B.1: The calibration of the ruby laser device

charged voltage (volt)	output energy (Joule)
700	3.5
750	10.4
800	20.0
850	30.0
900	40.0
950	50.5
999	61.0

produced by imposing a step change in an electric current passing through a test section under adiabatic conditions. In the present experiment ,however,a ramp temperature change was approximately produced by using the existing ruby laser device, the Holobeam Series 810 Ruby Laser System. Ruby is formed when a small amount of Cr_2O_3 is dissolved in sapphire, Al_2O_3. Thus a Laser beam of the wavelength 694.3 nm can be emitted by this device at room temperature. Also, this ruby device is a pulsed energy-emitting source with typical output energy levels of from less than 1 Joule to over 100 Joules. The calibration of output energy was carried out by the Thermomechanics Laboratory at the University of Manitoba. The related data is listed in Table B.1. In the present experiment the charged voltage was set for 850 v and no lens was used on the optical path. It was found that the laser beam emitted by the ruby device had a circular section of radius 12 mm and a duration of 3 ms. As seen from Eq.(B.2), an approximate ramp temperature change

occured when the beam hit the test region of the foregoing DCB specimen with the foil- thermocouple which was at the center of this test region. (See Figure 5.4).

(2) The resulting response of the tested thermocouple circuit was triggered by the fire trigger output of the ruby laser device and was recorded.

(3) An analytical expression for the temperature in an infinite sheet subjected to an incident circular laser beam with the a Gaussian intensity distribution was used to calculate the theoretical temperature change in this test region under adiabatic conditions. The reference [102] has given this expression in this case as follows.

$$T(z,t) = \frac{\epsilon I_o t}{\rho C L} + \frac{\epsilon I_o L}{K}[\frac{3z^2 - L^2}{6L^2} - \frac{2}{\pi}\sum_{n=1}^{\infty}\frac{(-1)^n}{n^2}exp(-\frac{n^2\pi^2\kappa t}{L^2})cos(\frac{n\pi z}{L})] \qquad \text{(B.2)}$$

where ϵ is the emissivity, I_o is the incident intensity of laser beam and $I_o = \frac{P}{\pi A^2}$ in which A is the radius of the beam and P is the output energy, L is the thickness of the sheet, ρ is the density, C is the specific heat, κ is the thermal diffusivity, K is the thermal conductivity, and z is the thick coordinate. It can be seen from Eq.(B.2) that an approximate ramp change in temperature can be produced on the surface of specimen, because the first term is the main term and it is a linear function of time, t.

(4) The theoretical ramp change in temperature and the measured thermocouple change in temperature are depicted together in Figure B.1. From

this figure the graphical determination is performed to evaluate the two transfer function constants of Eq. (B.1). This depicted theoretical temperature was based on the following data in the present case: $z = L = 0.01m$ (the thickness of the specimen), $K = 60.5\ w/m^oC$ and $\kappa = 18.5 \times 10^{-6}\ m^2/s$ (L, K, κ have been given in Section 6.3), and $I_o = 2.4 \times 10^3\ w/cm^2$ (calculated from $P = 30.0$ Joules and $A = 12mm$) and $\epsilon = 0.61$ (determined based on the wavelength 694.5 nm of the laser beam and the material of the specimen [102]). The two constants are: $a_T = 2.611/ms$ and $c_T = 4.351/ms$. The a_T/c_T ratio is approximately 0.60. It was known from reference [96] that the ratios commonly were of 0.47 to 0.65. Therefore, the transfer function is

$$G_T(s) = \frac{a_T}{s + c_T} = \frac{2.61}{s + 4.35} \tag{B.3}$$

Finally, the $G_T(s)$, Eq.(B.3), can be used to calculate the "true" surface temperature, T_t, from any measured thermocouple readings from

$$T_t = \mathcal{L}^{-1} \frac{T_B(s)}{G_T(s)} \tag{B.4}$$

where $\mathcal{L}^{-1}$ denotes the inverse Laplace transfer operator. When solving for T_t, the measured curve, T_B, can be approximated by an appropriate mathematical expression which can be obtained by using a curve-fitting technique such as polynomial regression with least square fit. In the present study the measured temperature curve shown in Figure 5.9 is described by the following equation:

$$T_B(t) = -4.4237t + 4.0808t^2 - 0.9161t^3 + 0.0865t^4 - 0.003024t^5 \tag{B.5}$$

where t is time in millisecond and $t \leq 10ms$. The Graphical representation of this function and the measured curve are shown in Figure B.2. As a result,

$$T_B(s) = -4.4237/s^2 + 8.1616/s^3 - 5.4966/s^4 + 2.0760/s^5 - 0.3629/s^6 \quad \text{(B.6)}$$

and

$$\begin{aligned} T(t) &= \mathcal{L}^{-1} \frac{T_B(s)}{G_T(s)} \\ &= -1.6807t - 4.2069t^2 + 11.3944t^3 - 8.2915t^4 \\ &\quad +3.2916t^5 - 0.5995t^6 \end{aligned} \quad \text{(B.7)}$$

This is the "true" temperature change at the measured junction of the thermocouple which was depicted in Figure 6.6.

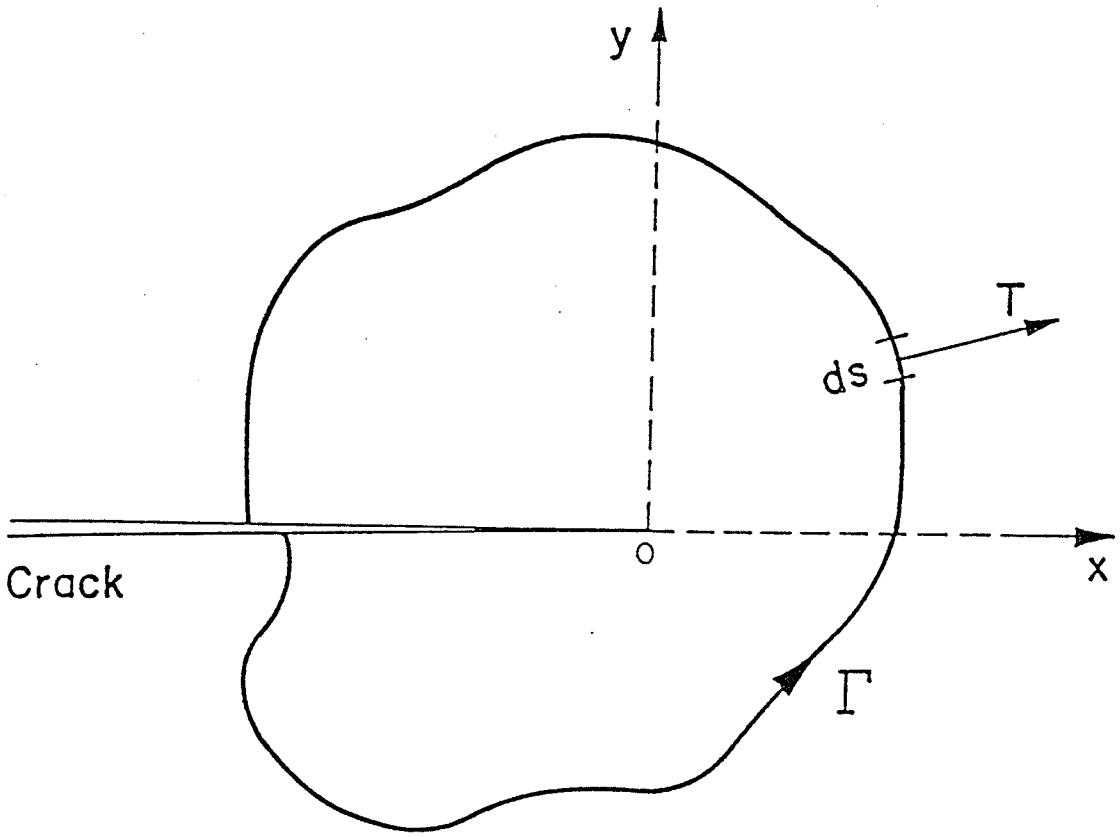

Figure 3.1 Path of integration for J-integral.

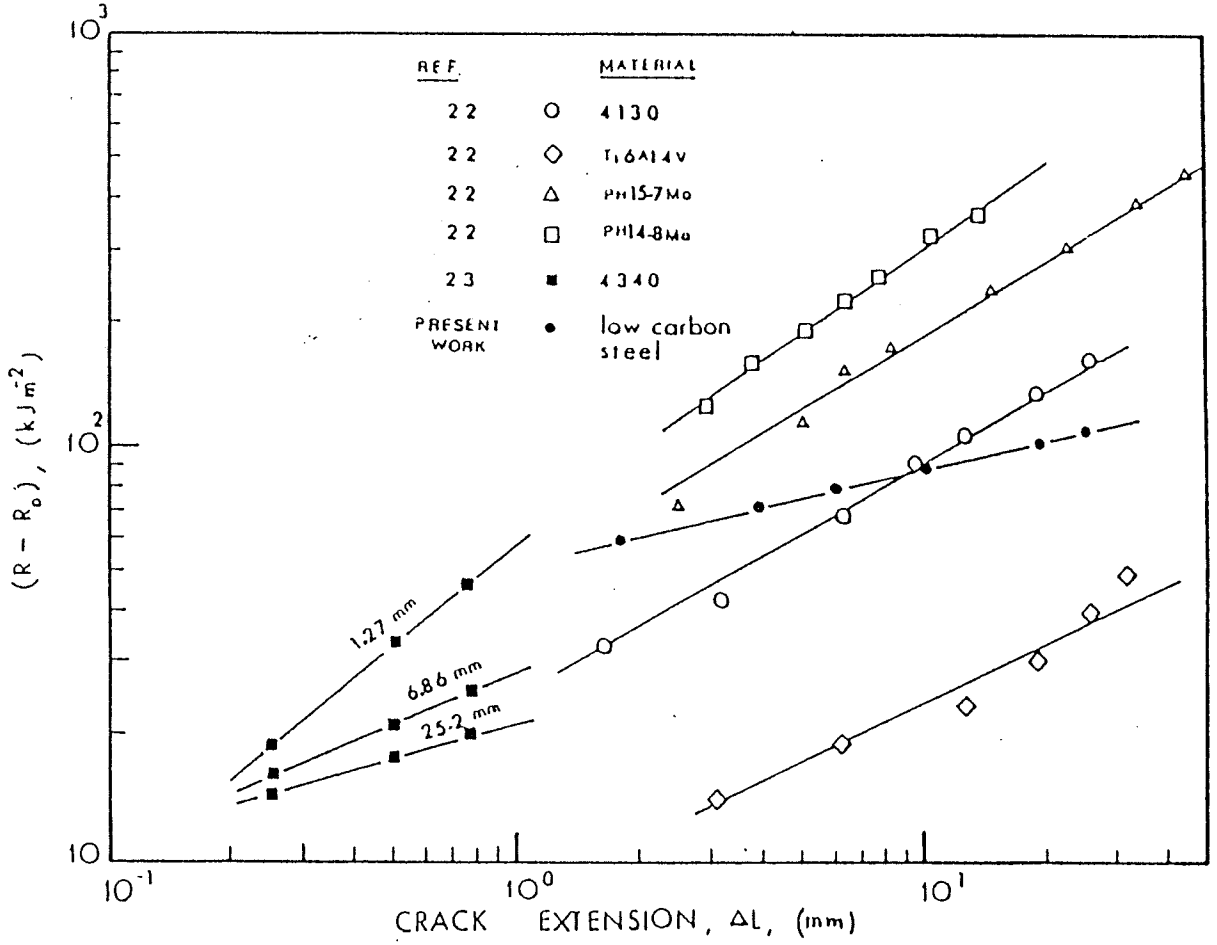

Figure 3.2 Crack growth resistance curve for steels. [70]

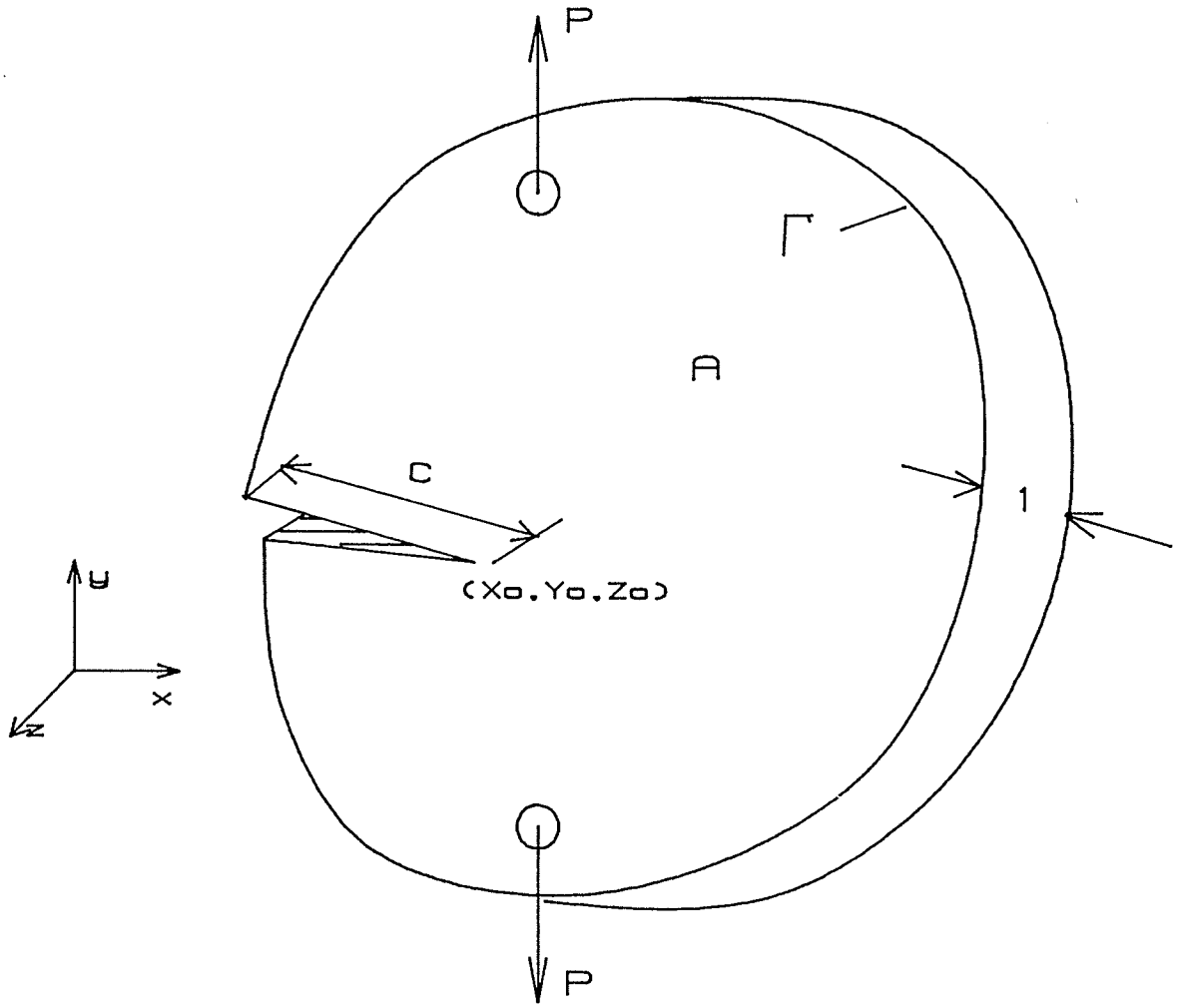

Figure 3.3 A 2-D cracked body

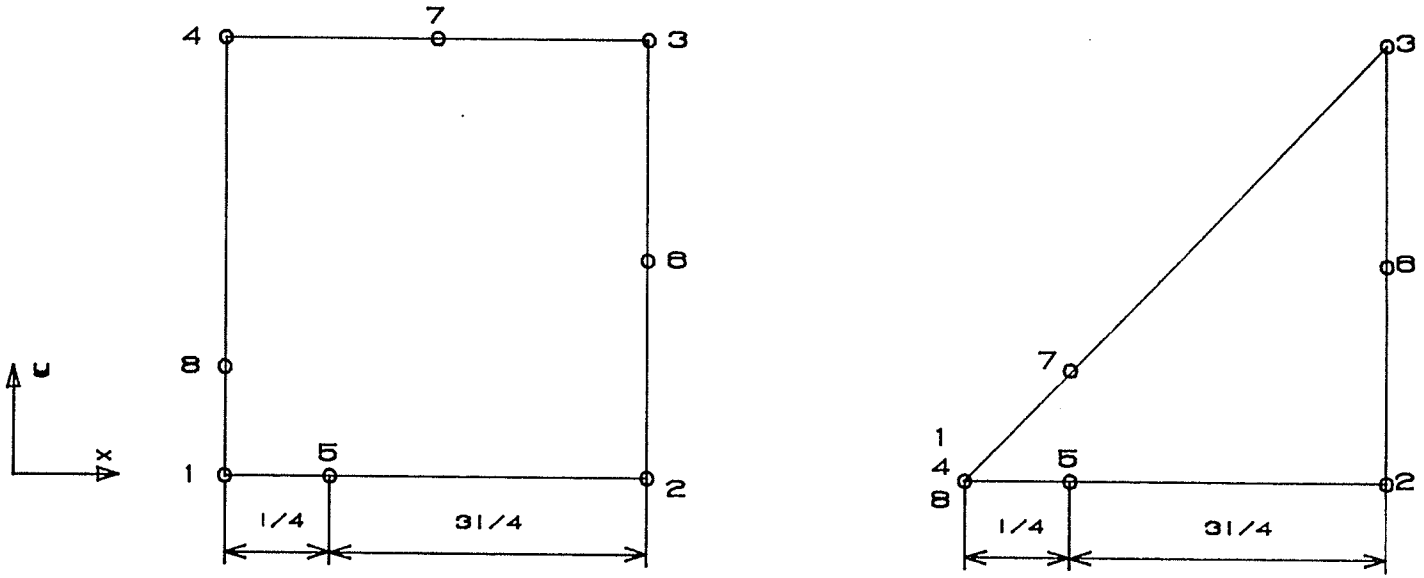

Figure 4.1 Quater Point Element Around the Crack Tip

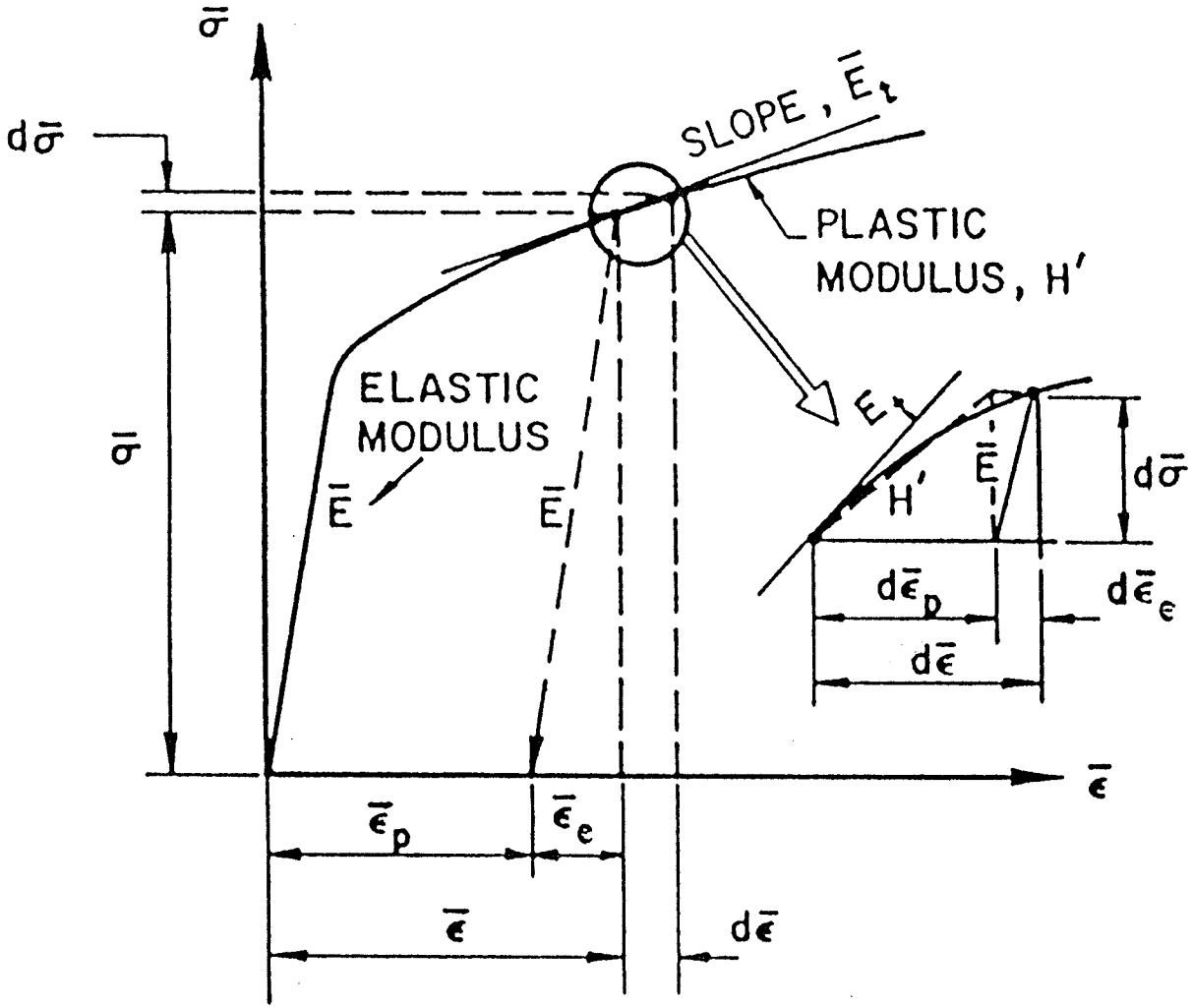

Figure 4.2 Graphic representation of material stiffness during elastic-plastic deformation.

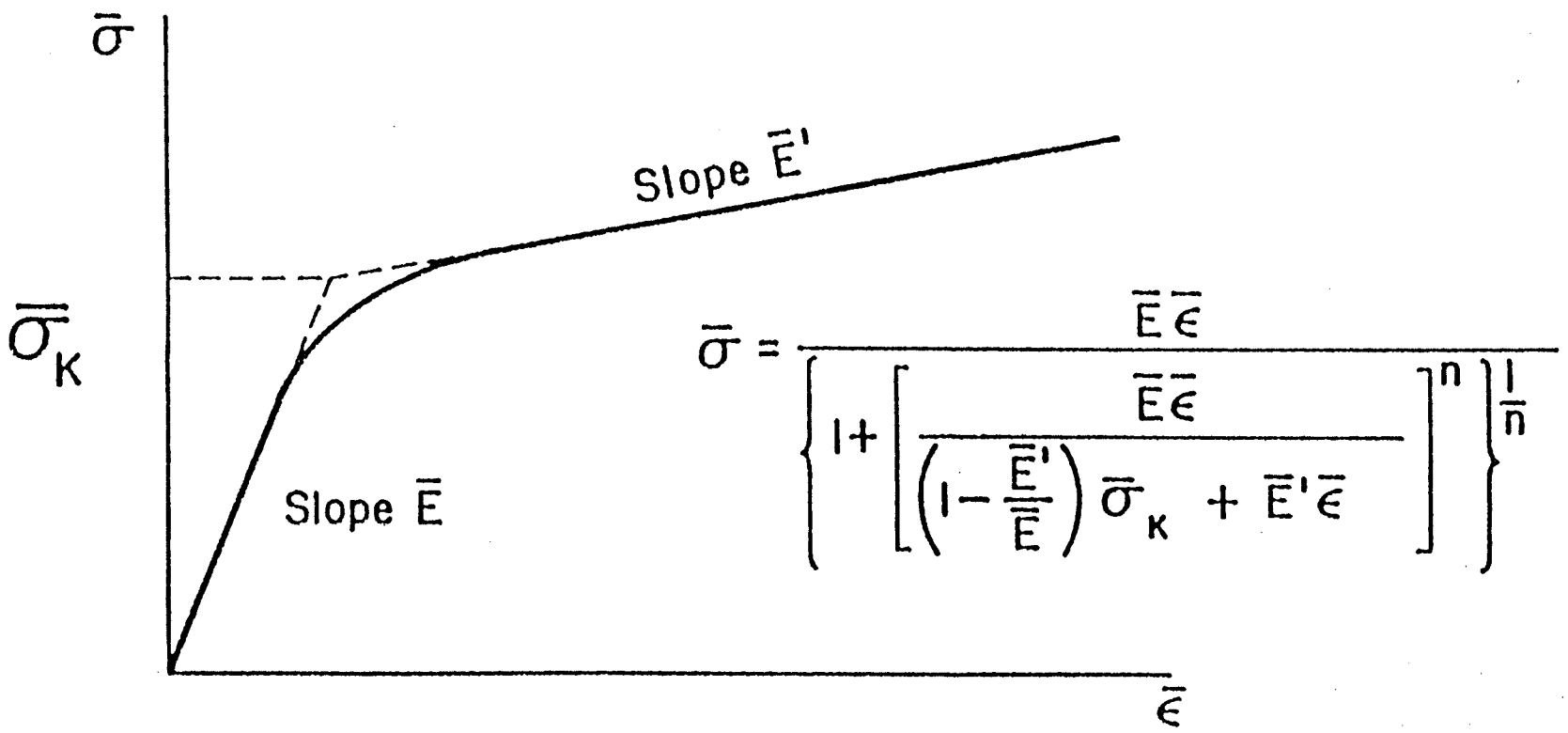

Figure 4.3 The Hsu-Bertel's polynomial approximation.

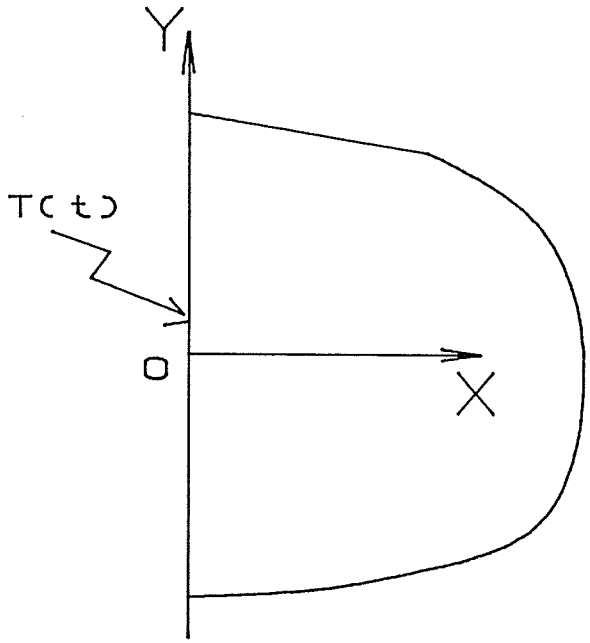

Figure 4.4(a) Problem geometry

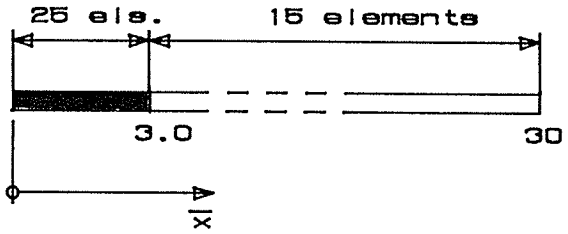

Figure 4.4(b)Finite element mesh

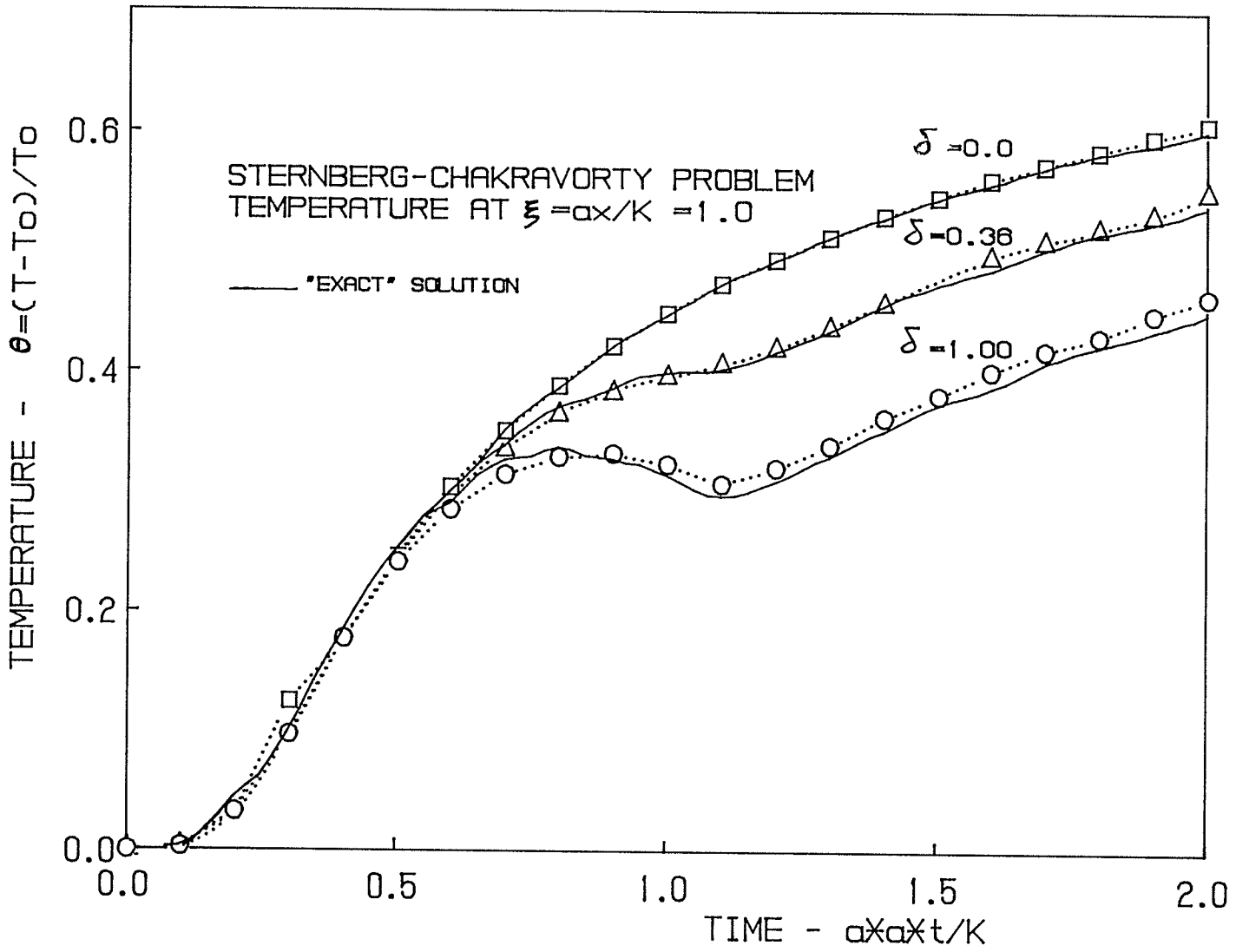

Figure 4.5 Temperature at $\xi = 1.0$ as a function of time for the Sternberg-Chakravorty problem with $\tau_o = 0.25$.

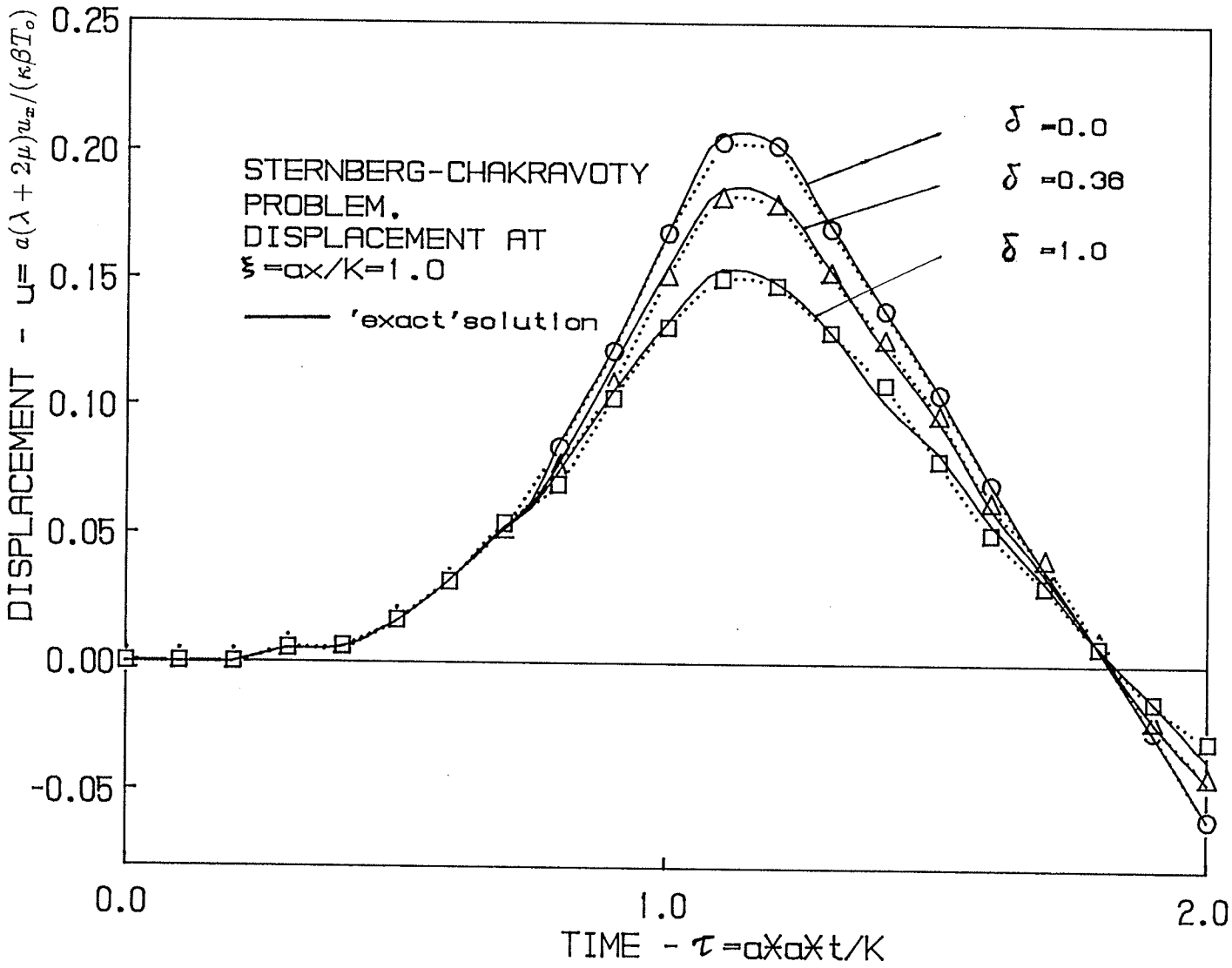

Figure 4.6 Displacement at $\xi = 1.0$ as a function of time for the Sternberg-Chakravorty problem with $\tau_o = 0.25$.

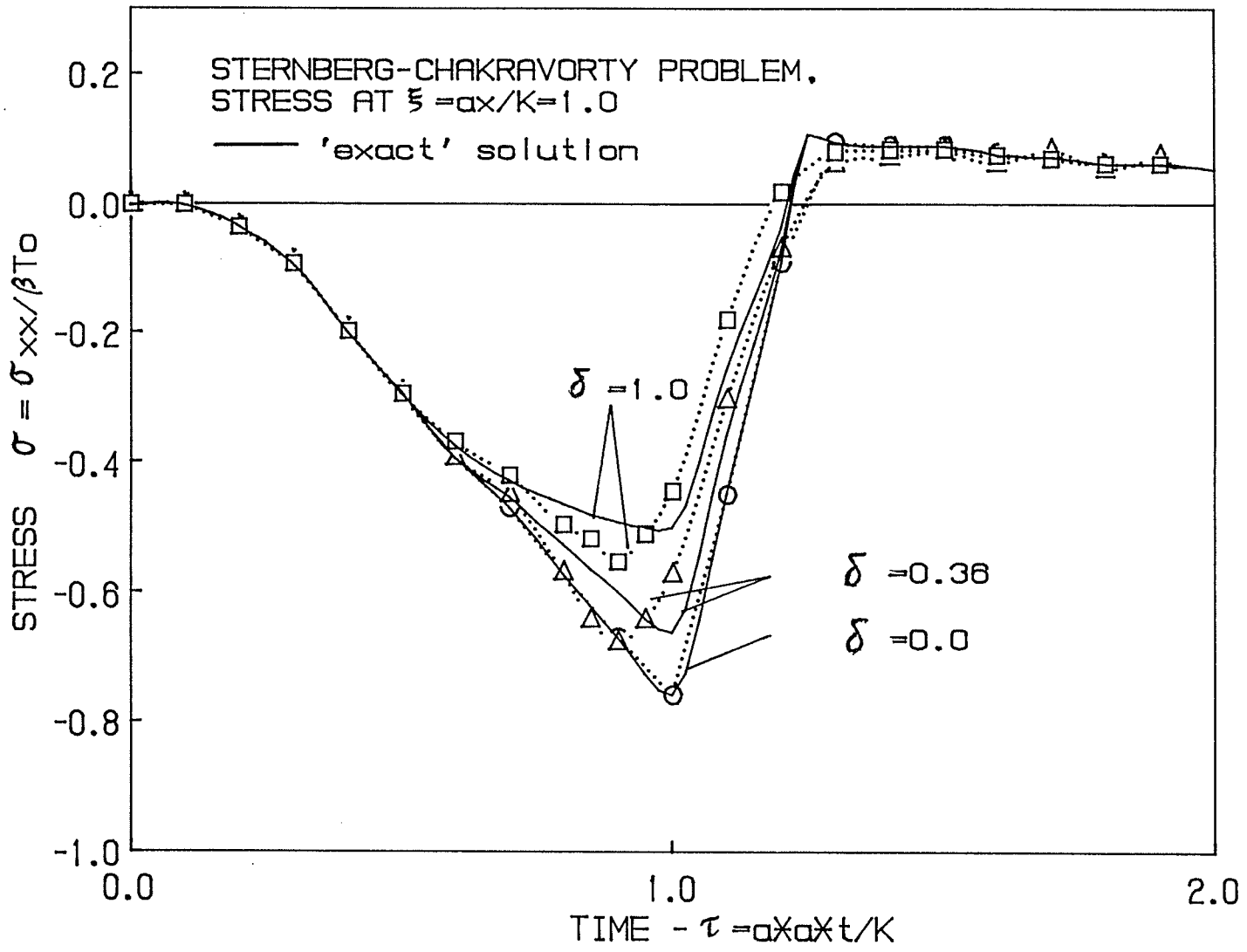

Figure 4.7 Normal stress at $\xi = 1.0$ as a function of time for the Sternberg-Chakravorty problem with $\tau_o = 0.25$.

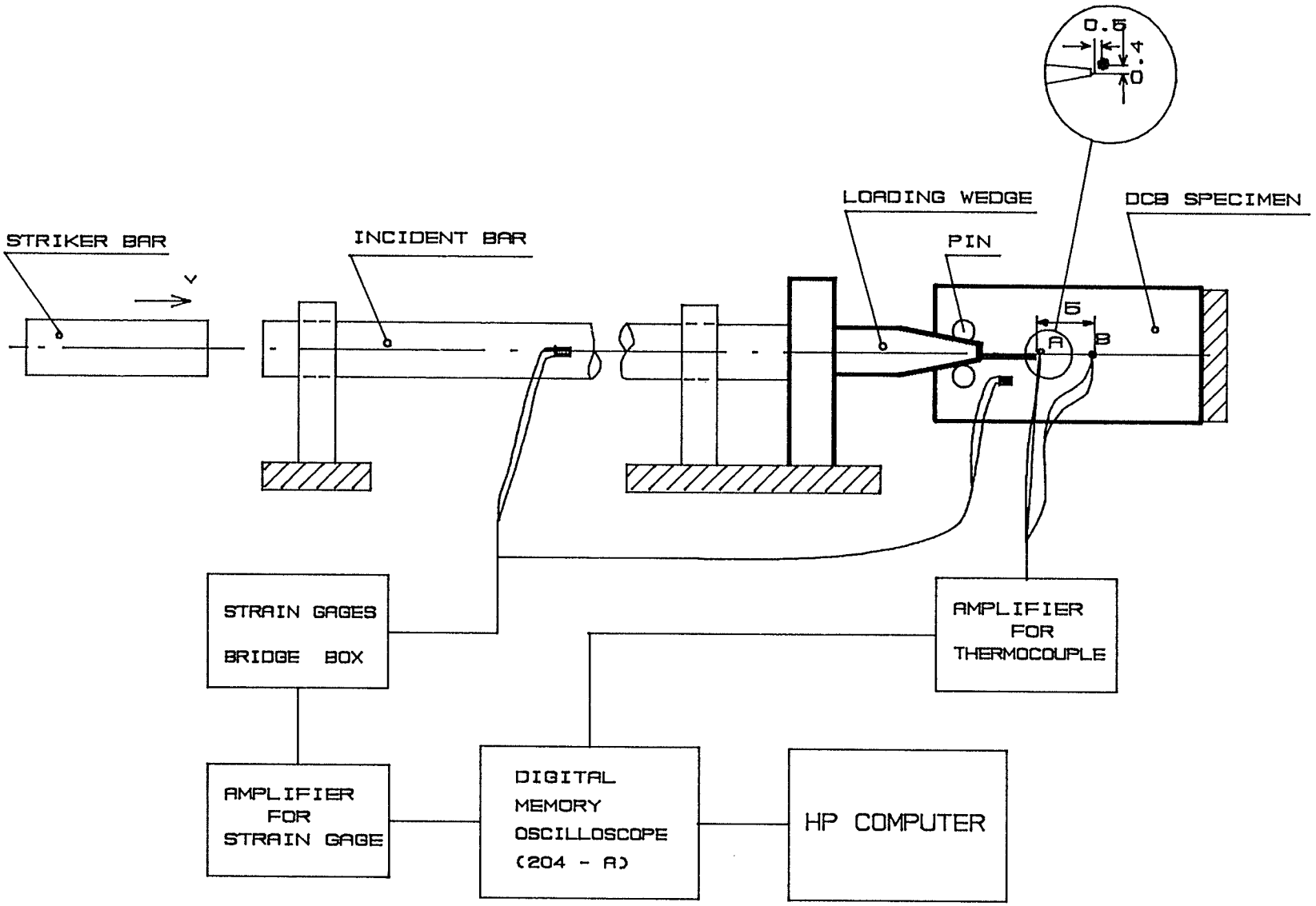

Figure 5.1 Schematic of the experimental set-up.

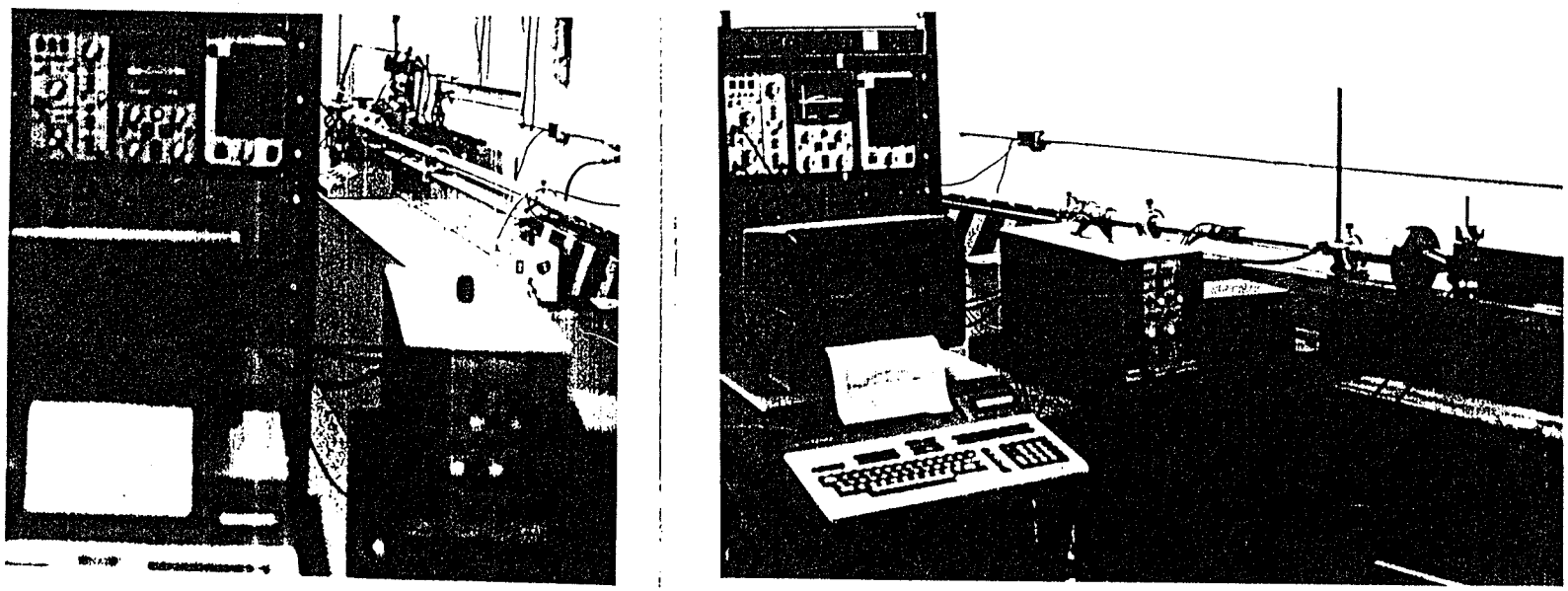

Figure 5.2 Photograph of the general test arrangement.

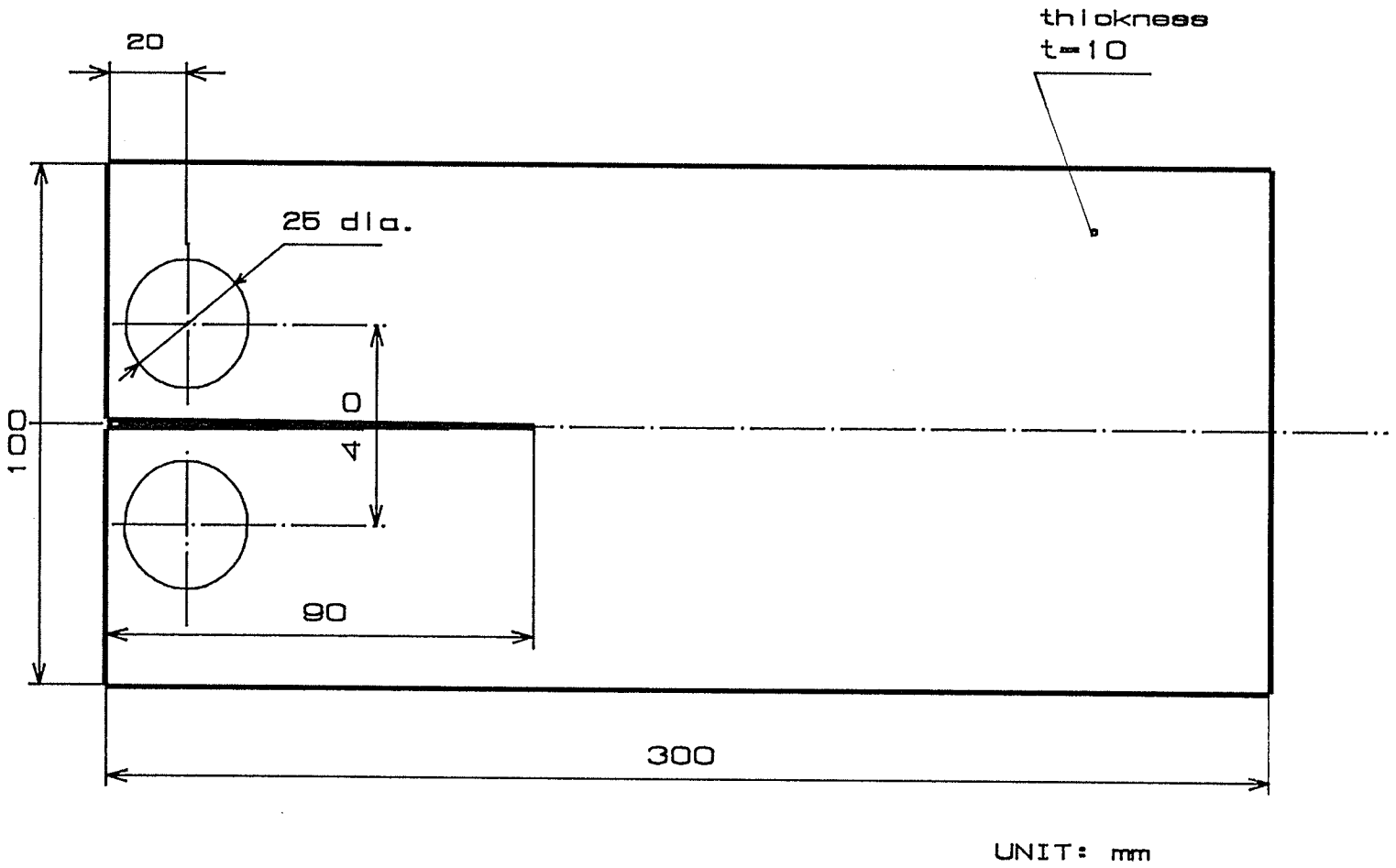

Figure 5.3 Double cantilever beam specimen.

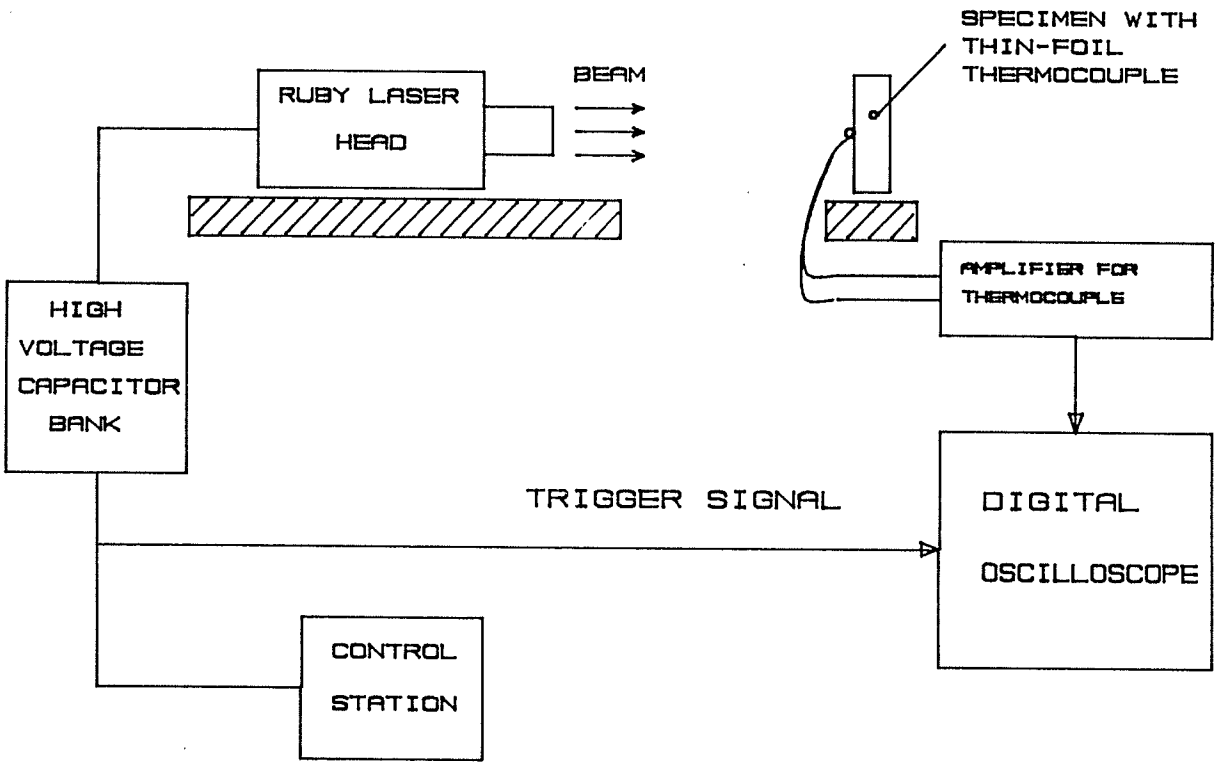

Figure 5.4 Principle layout for determining transfer function of the circuit of temperature measurement.

Figure 5.5 Photograph of the principle layout for determining transfer function of the circuit of temperature measurement.

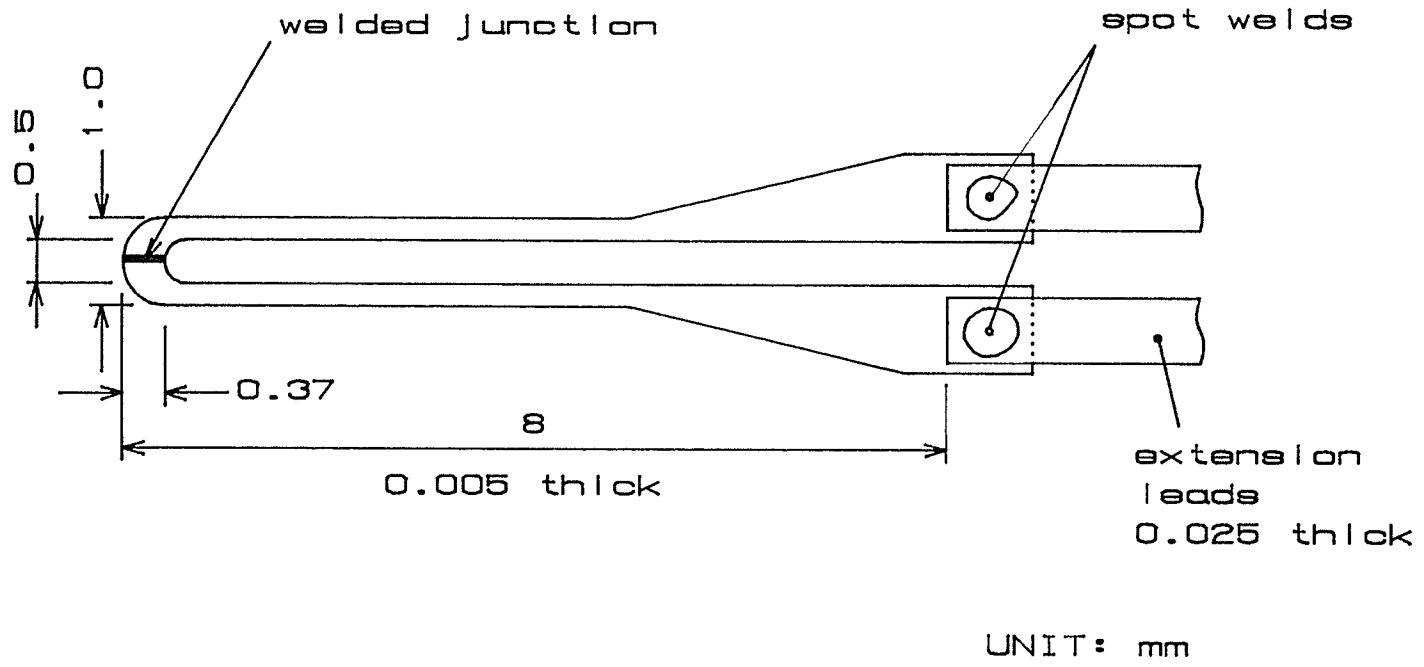

Figure 5.6(a) The size of thin-foil thermocouple.

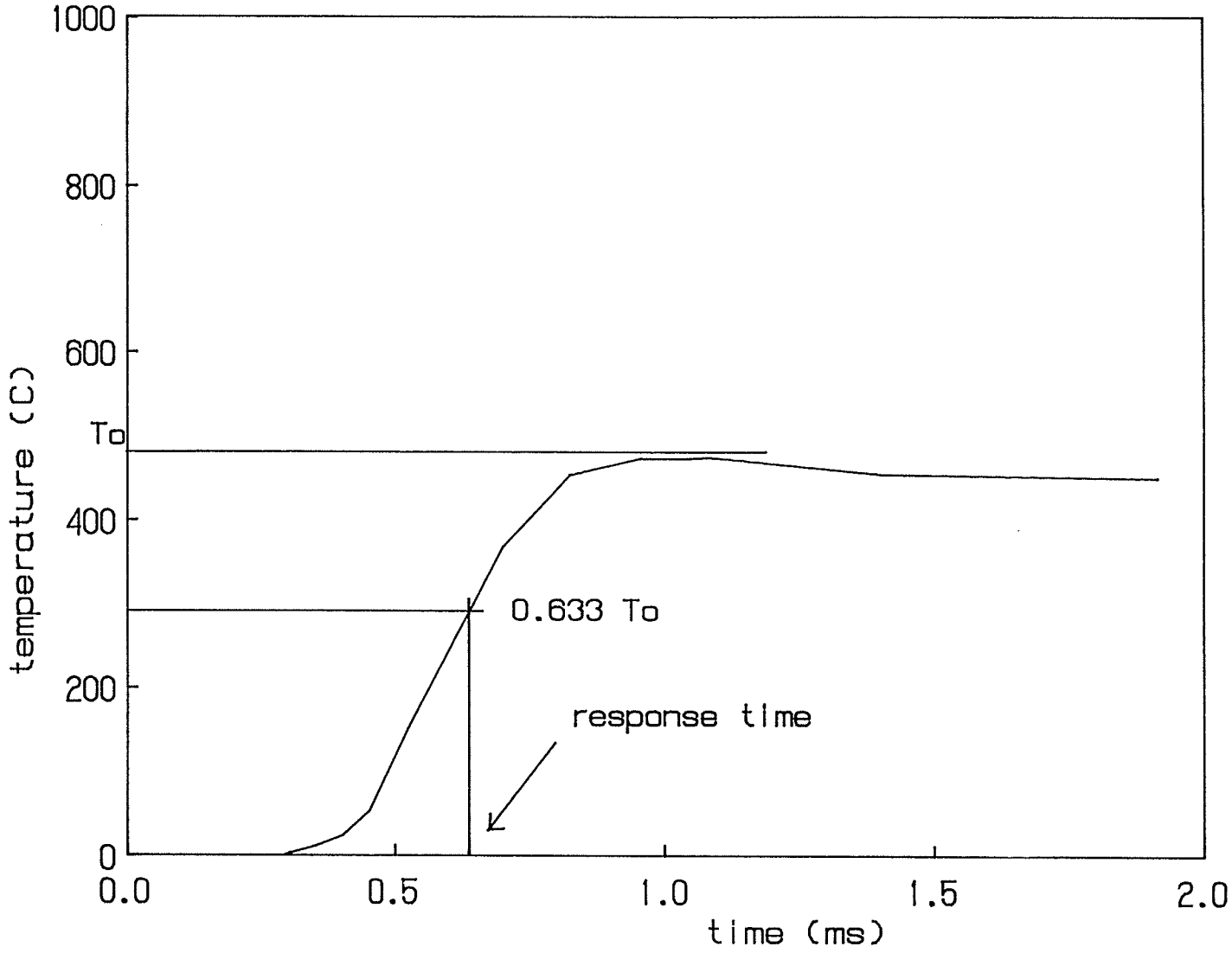

Figure 5.6(b) Typical output of the circuit of temperature measurement for determining its transfer function.

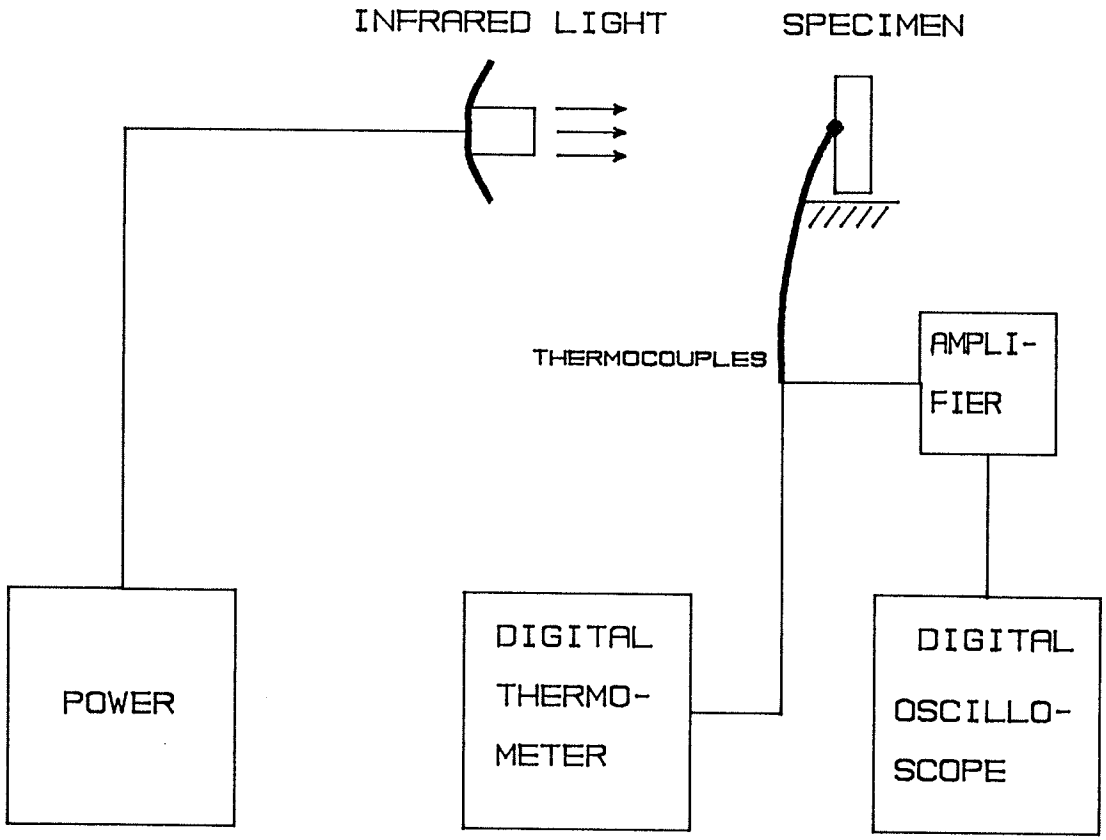

Figure 5.7 Principle layout for calibration of the circuit of temperature measurement.

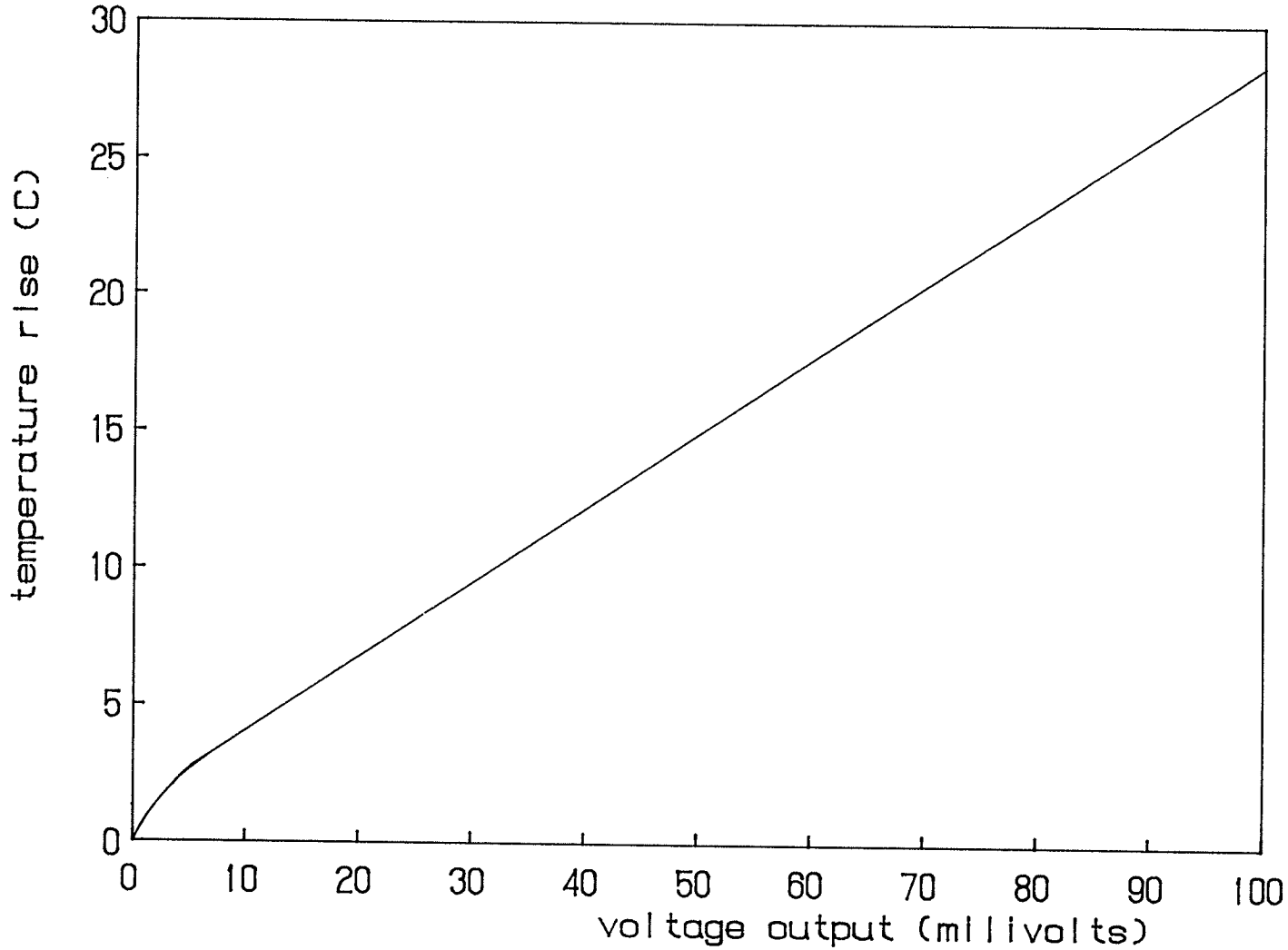

Figure 5.8 The calibration curve of the circuit of temperature measurement.

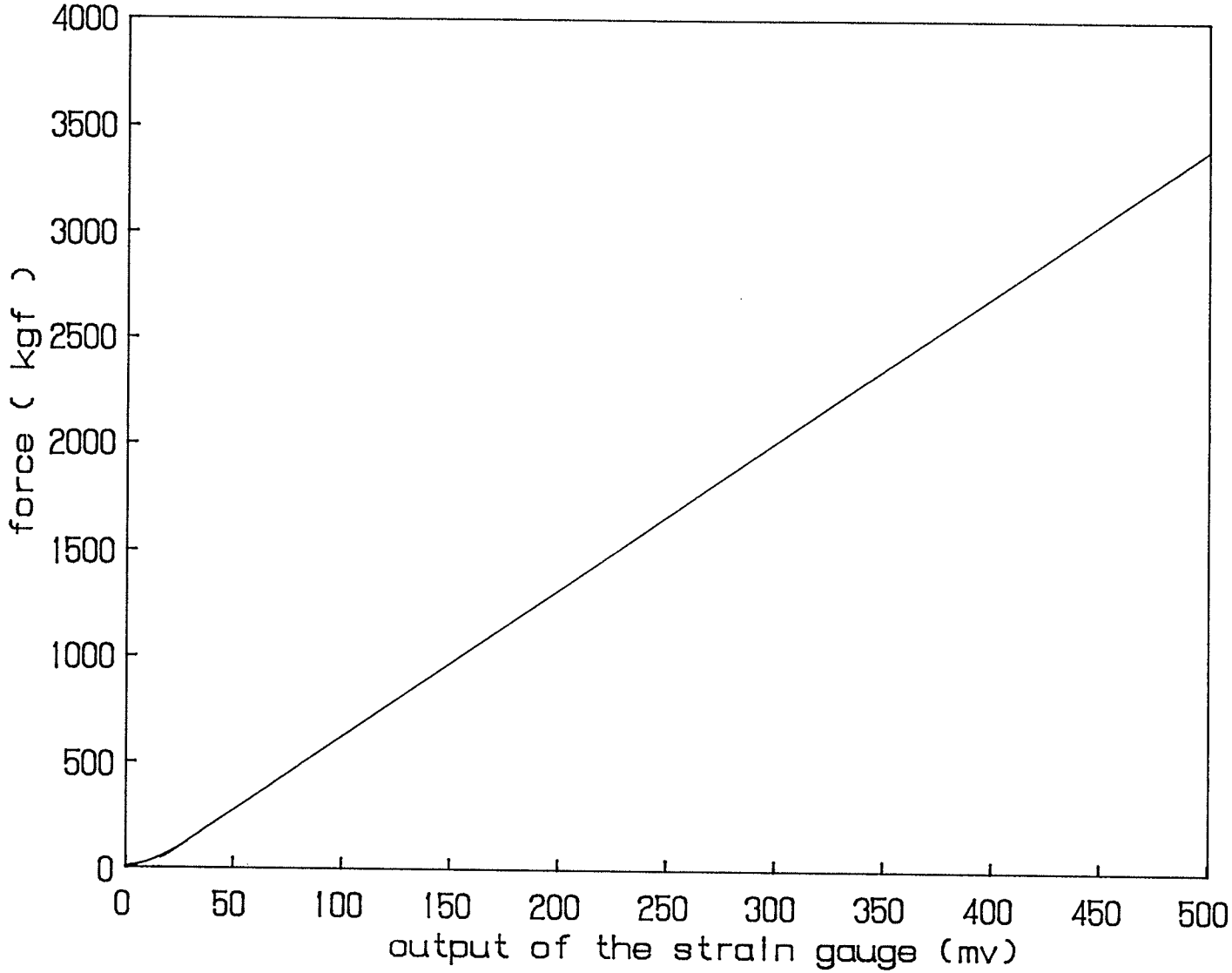

Figure 5.9 The calibration curve for impulsive force measurement.

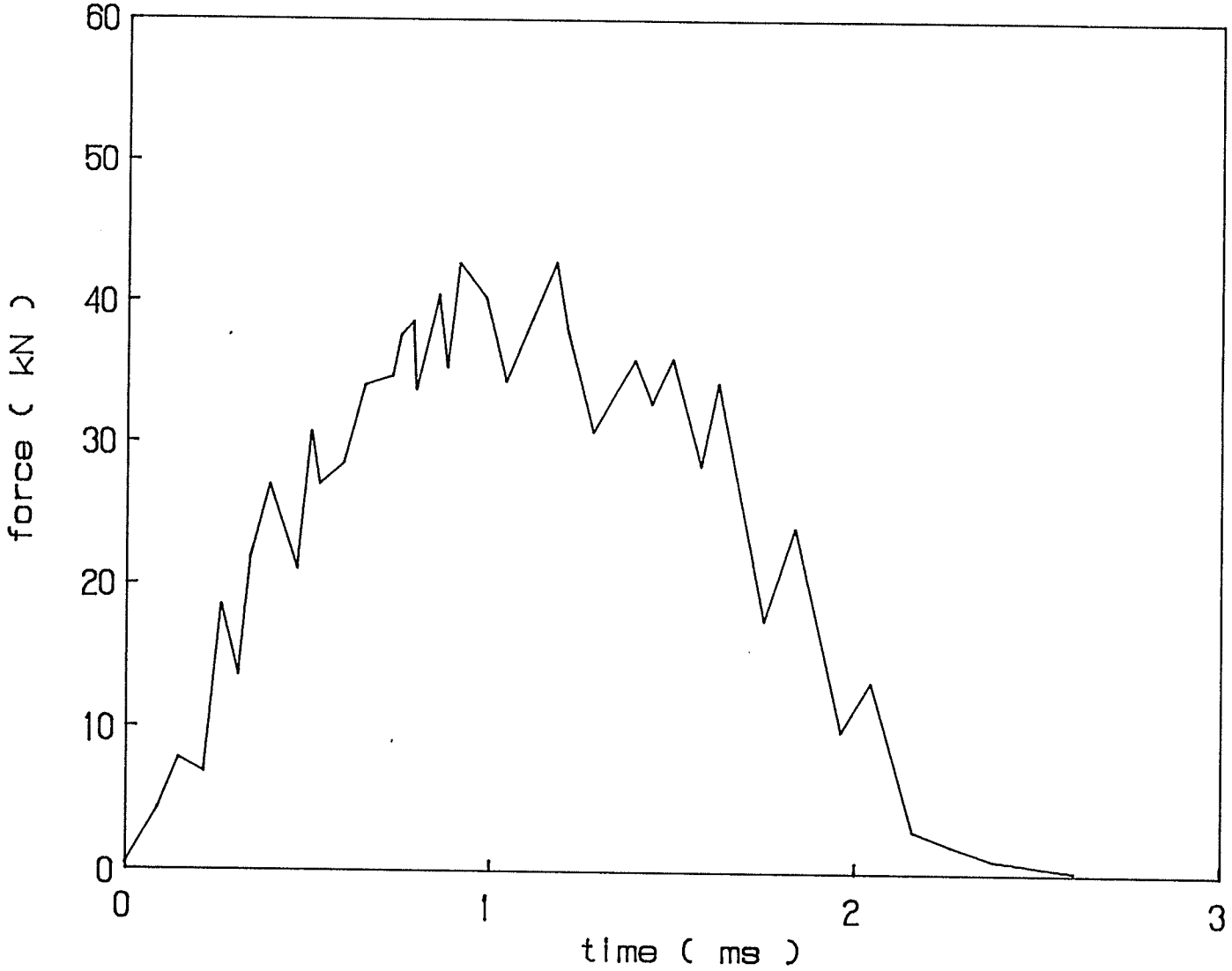

Figure 5.10 The impulsive force history.

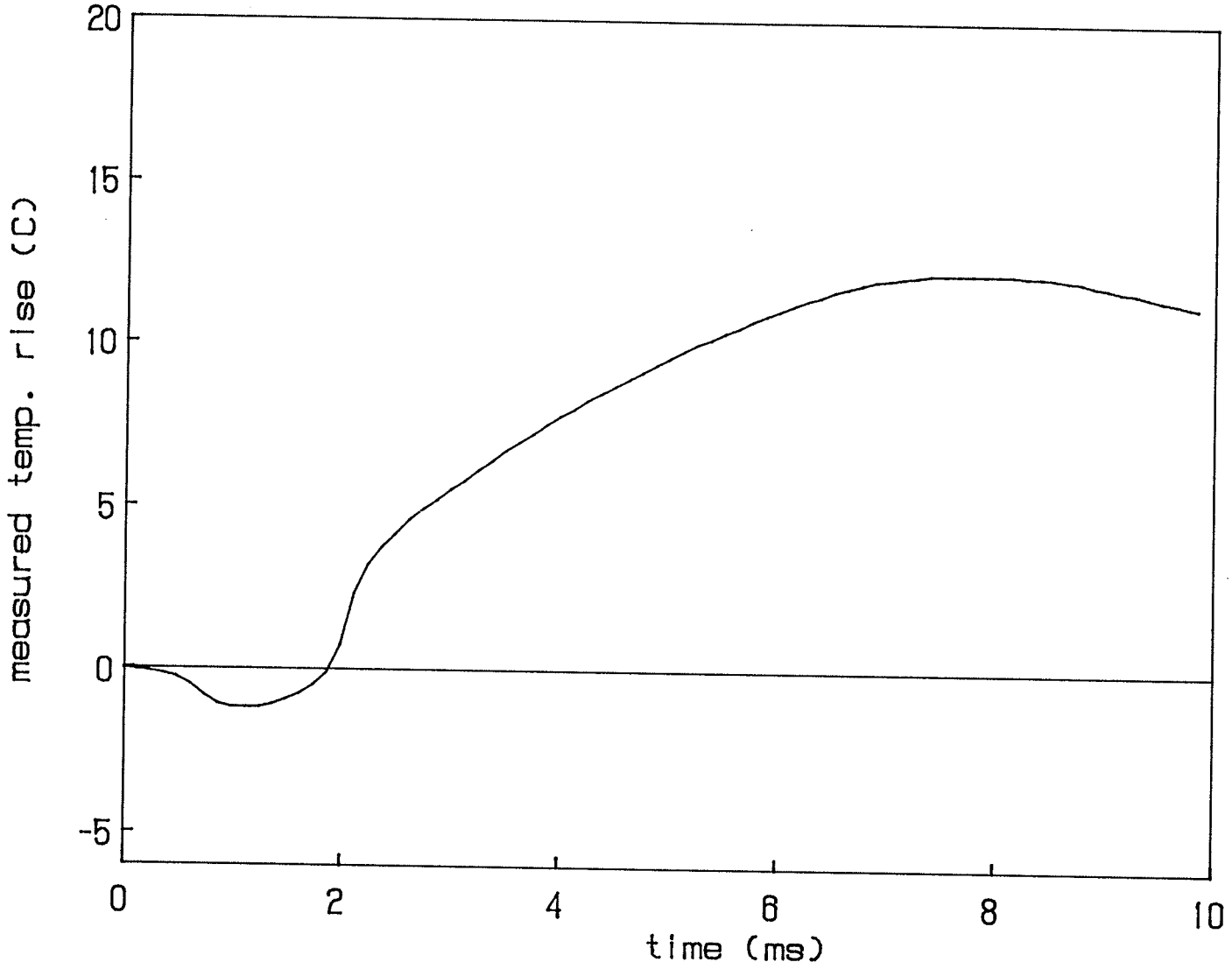

Figure 5.11 The temperature history at point A shown in Figure 5.1.

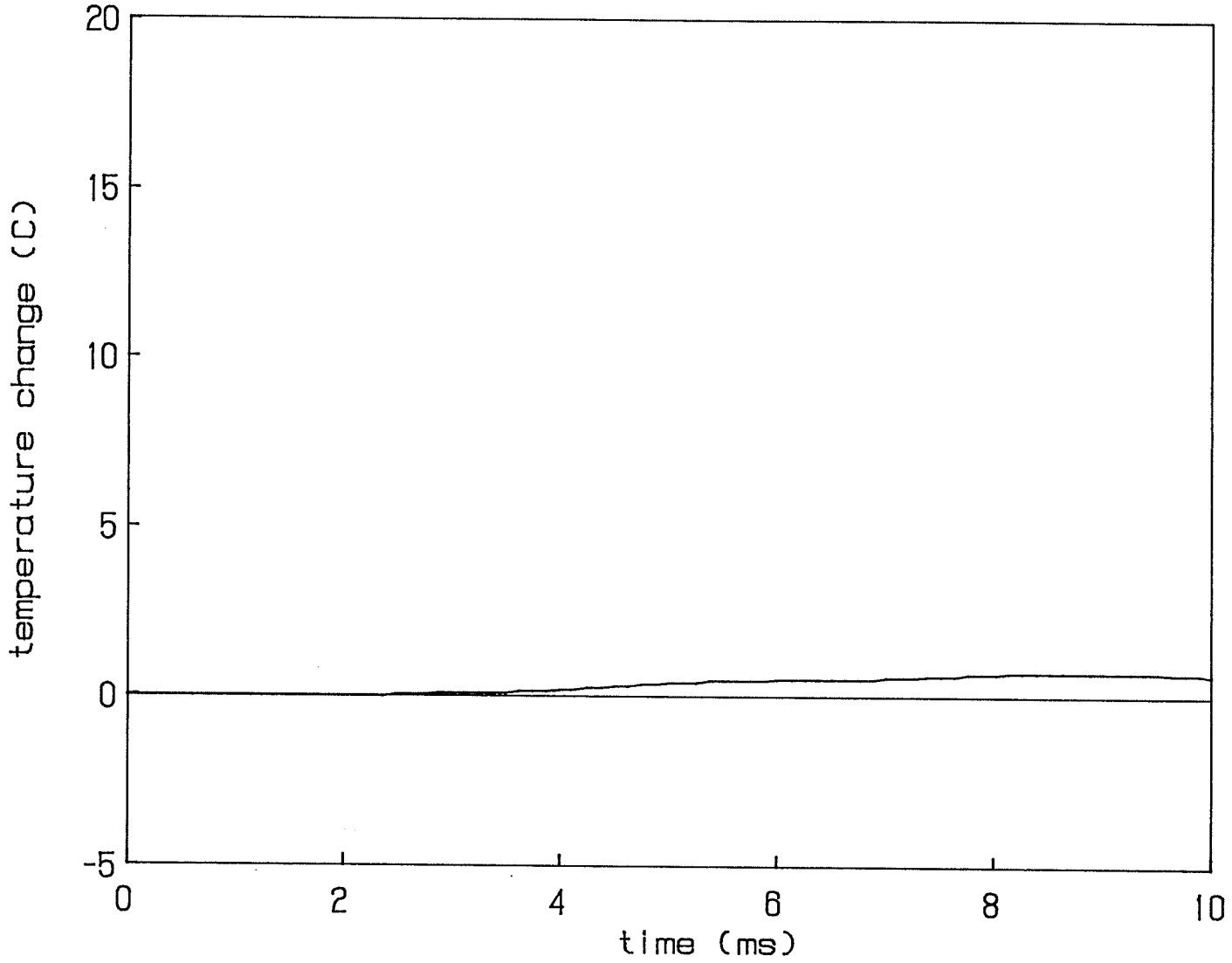

Figure 5.12 The temperature history at point B shown in Figure 5.1.

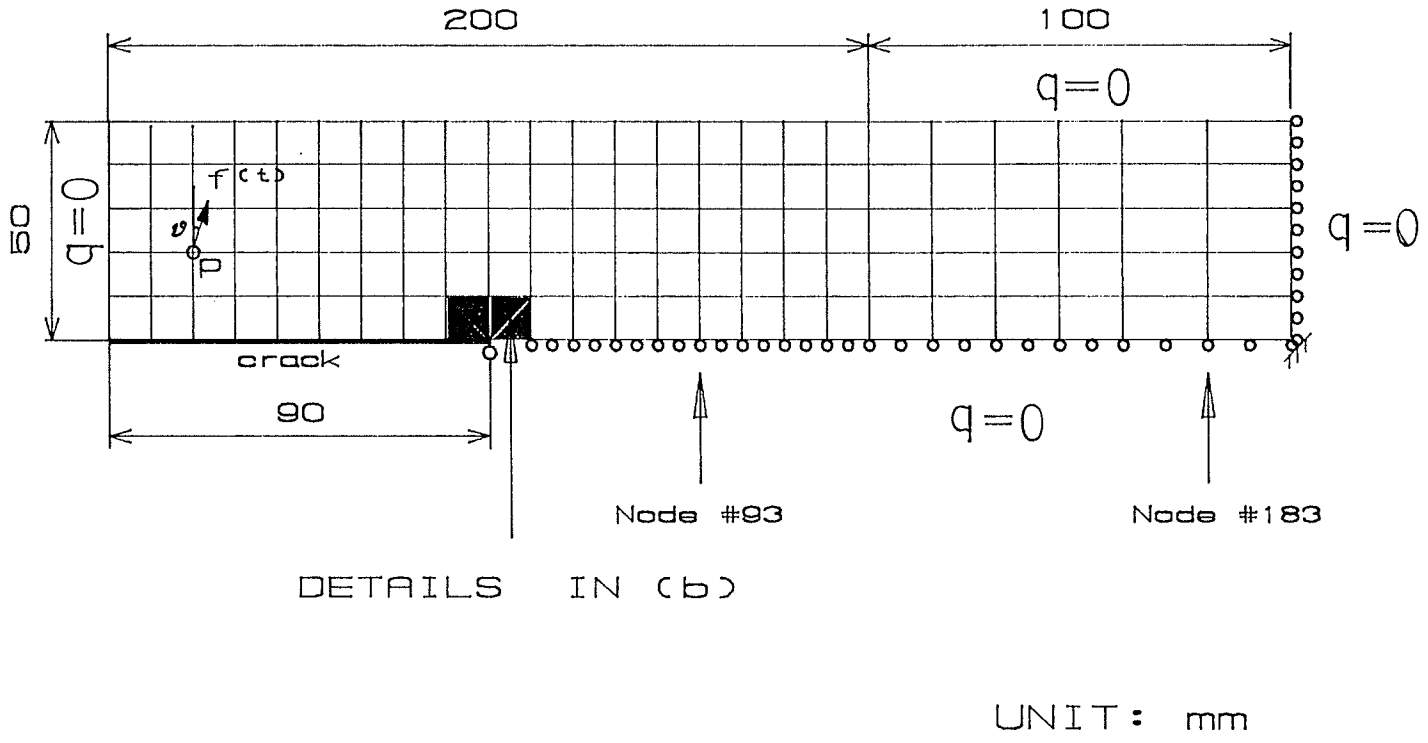

Figure 6.1(a) Finite element mesh: overall view.

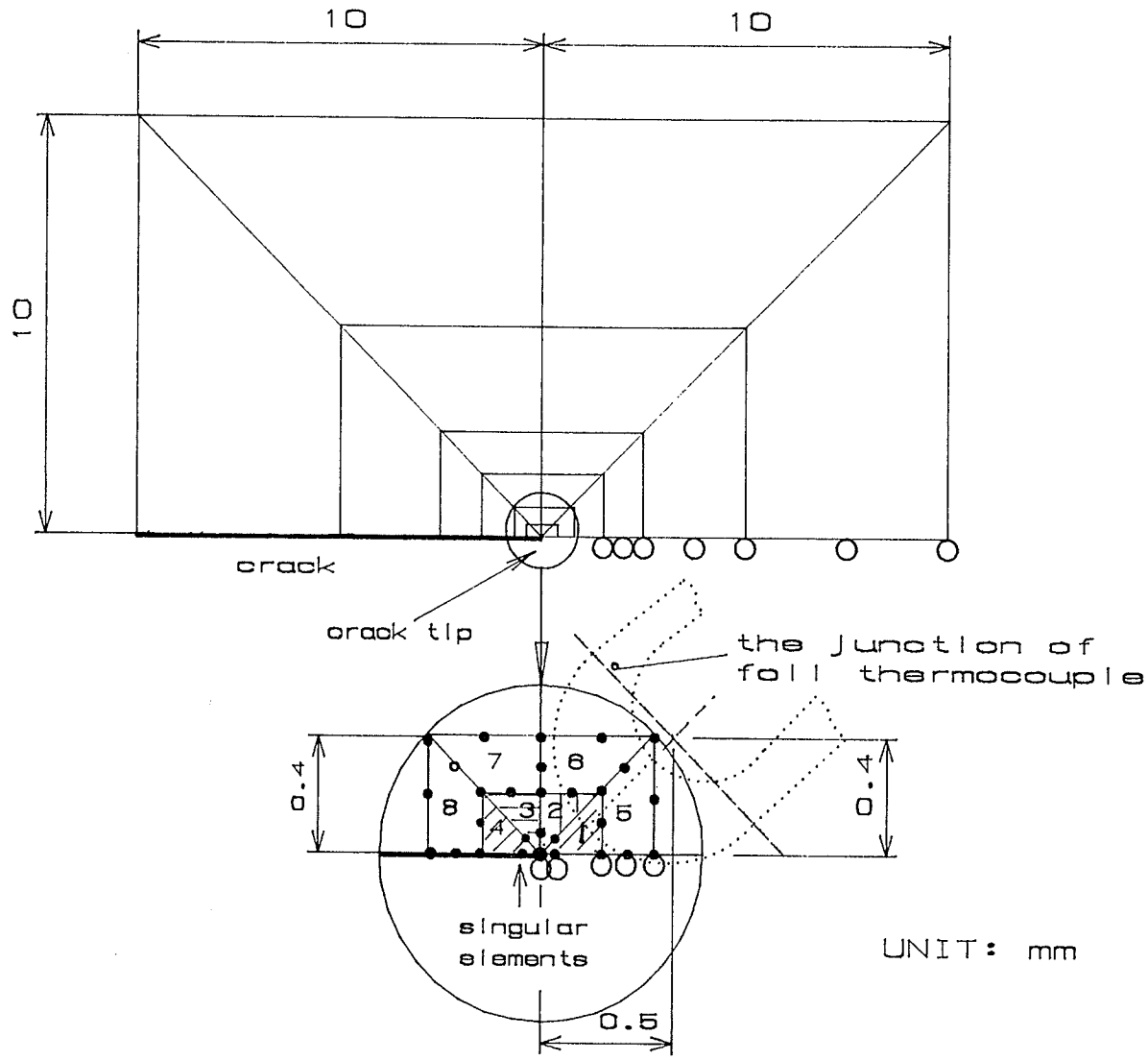

(b) Finite element mesh: crack tip region.

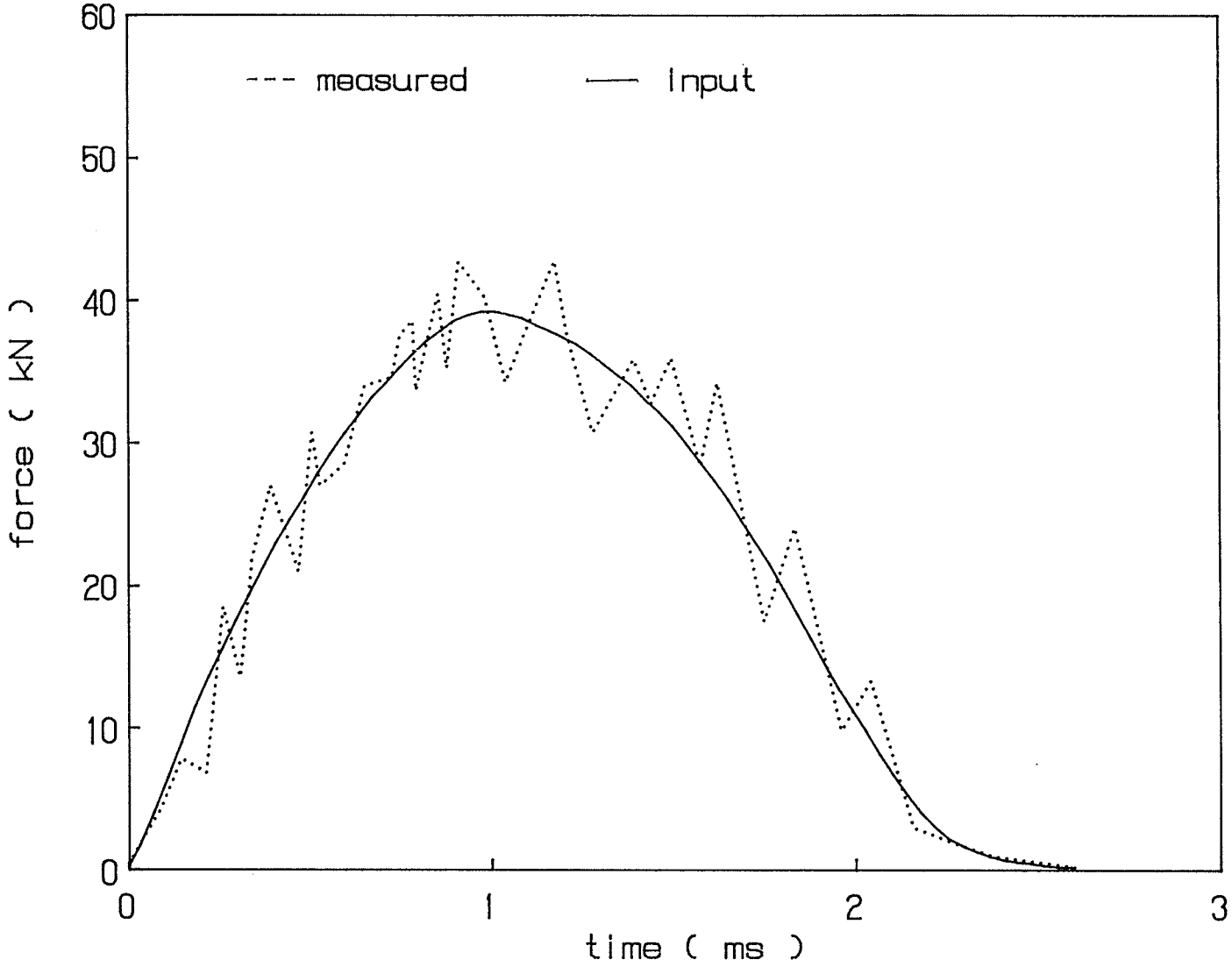

Figure 6.2 Input data for finite element analysis.

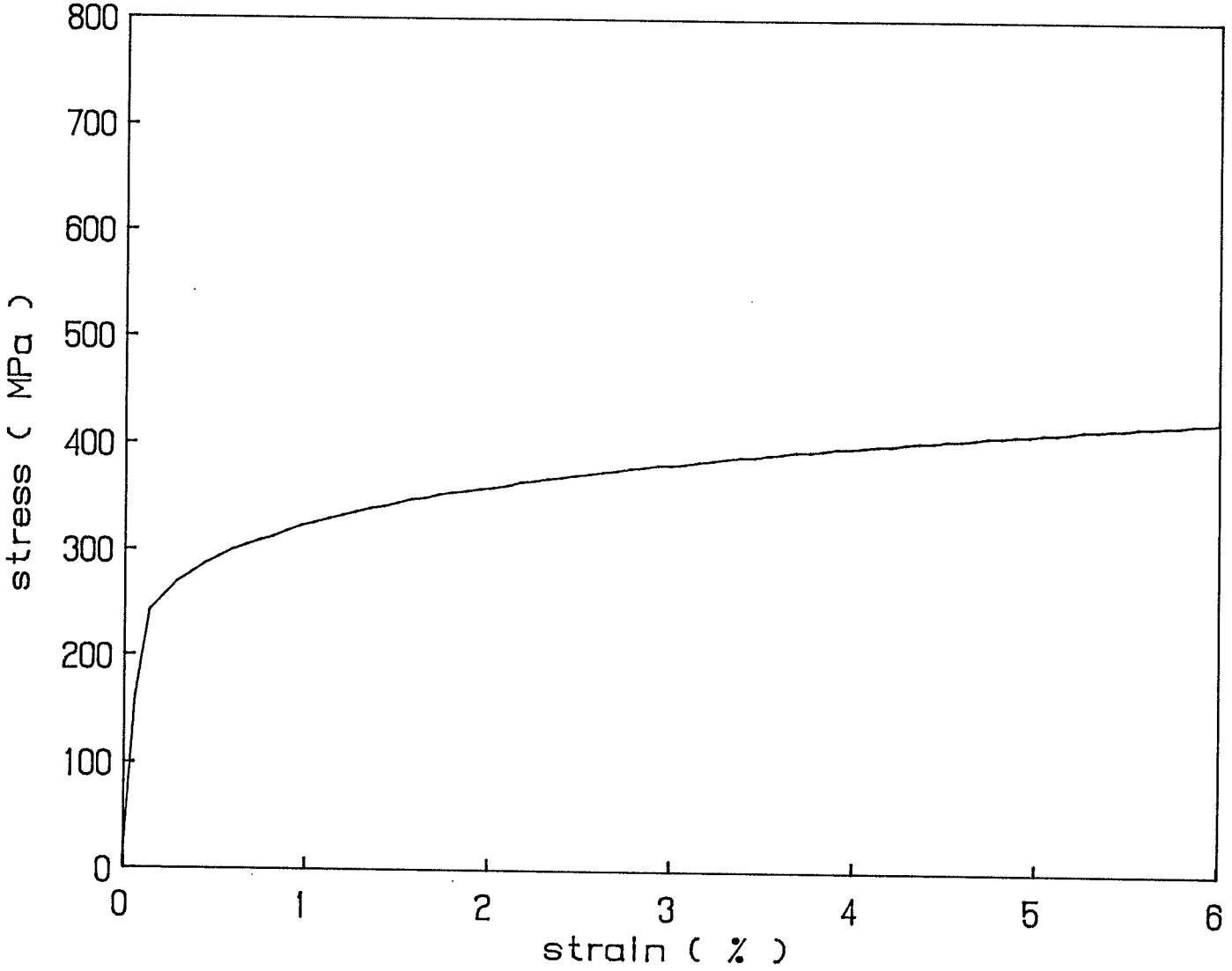

Figure 6.3 Uniaxial stress-strain curve of AISI 1018 steel.

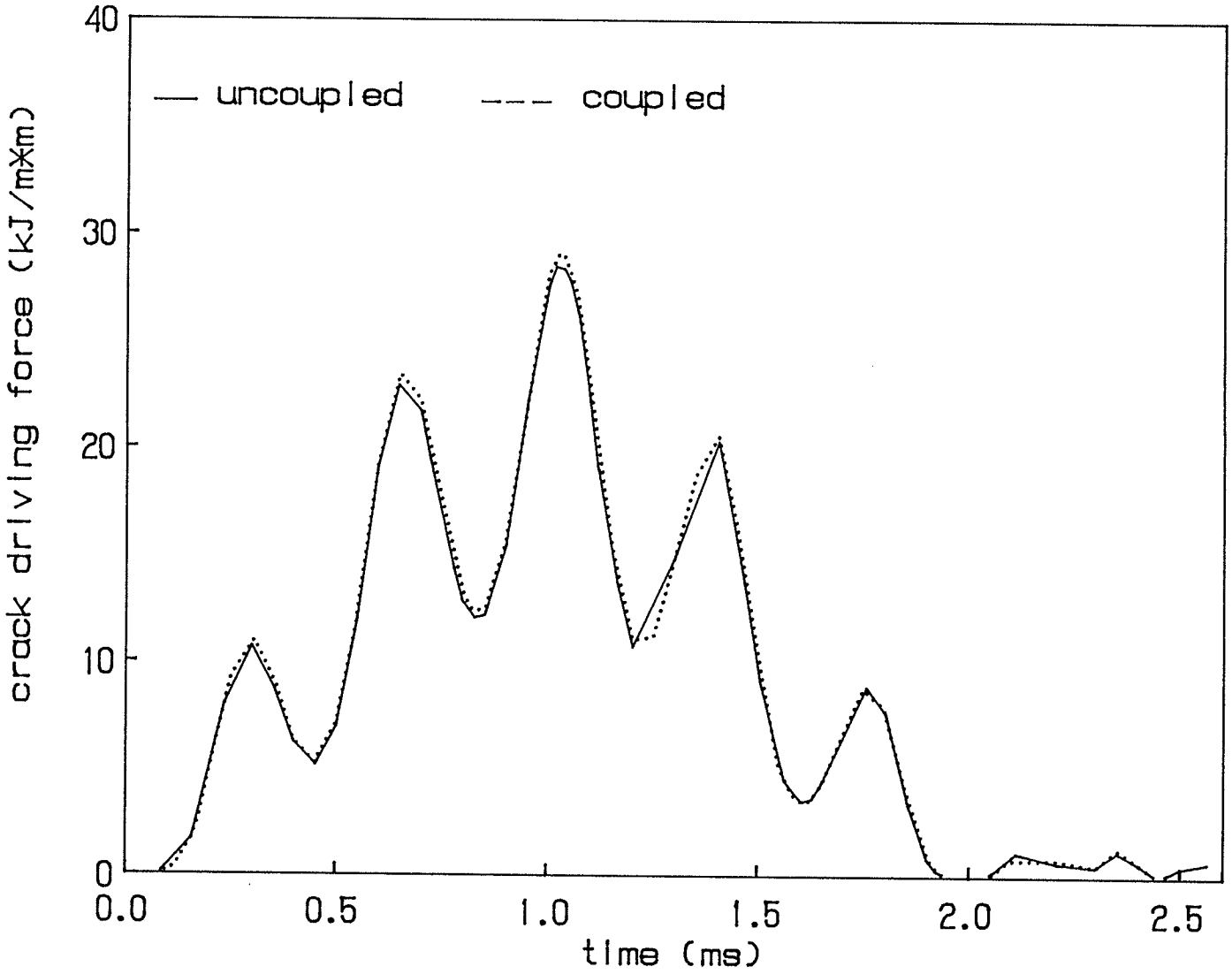

Figure 6.4 Crack driving force histories.

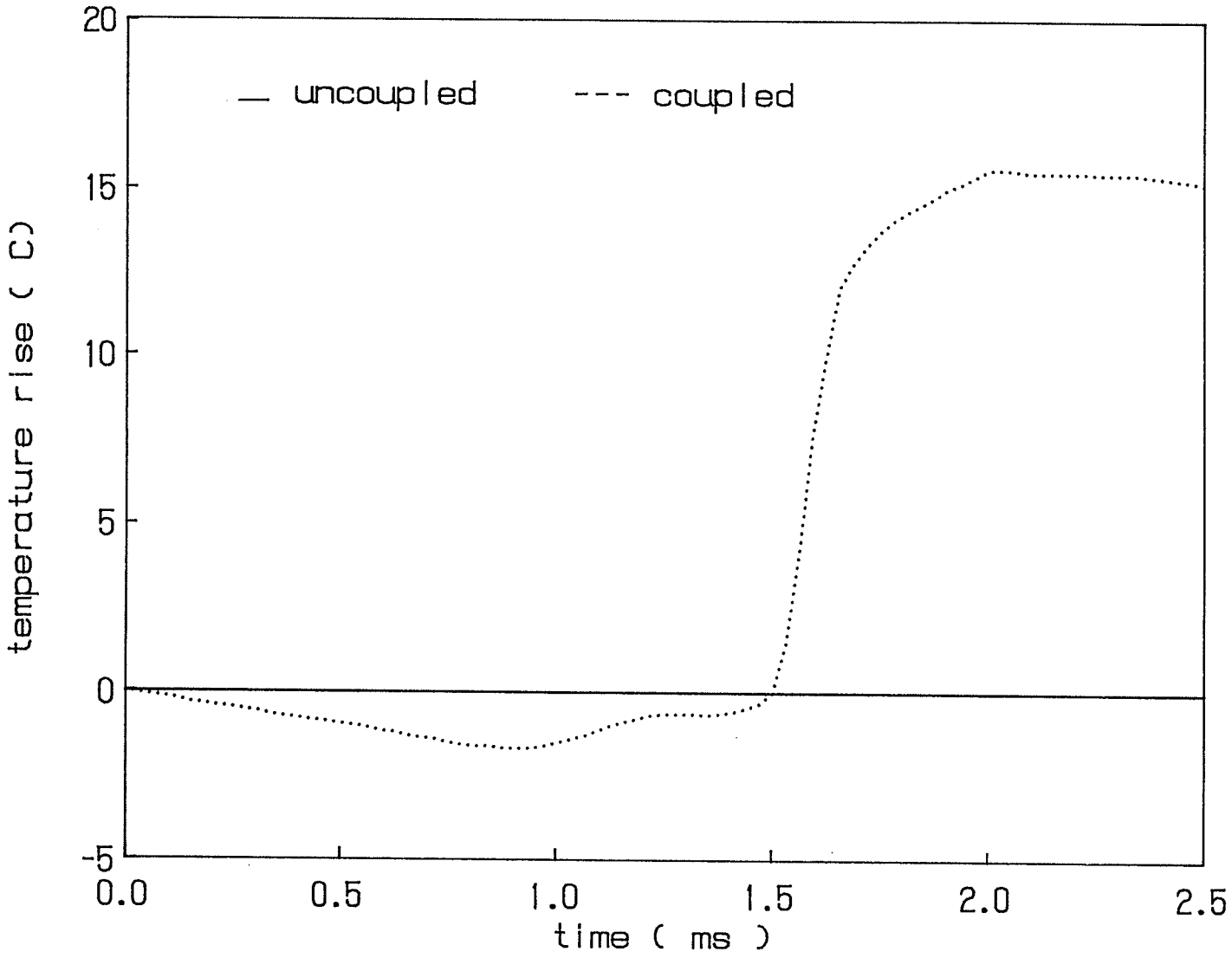

Figure 6.5(a) Temperature changes at the crack tip.

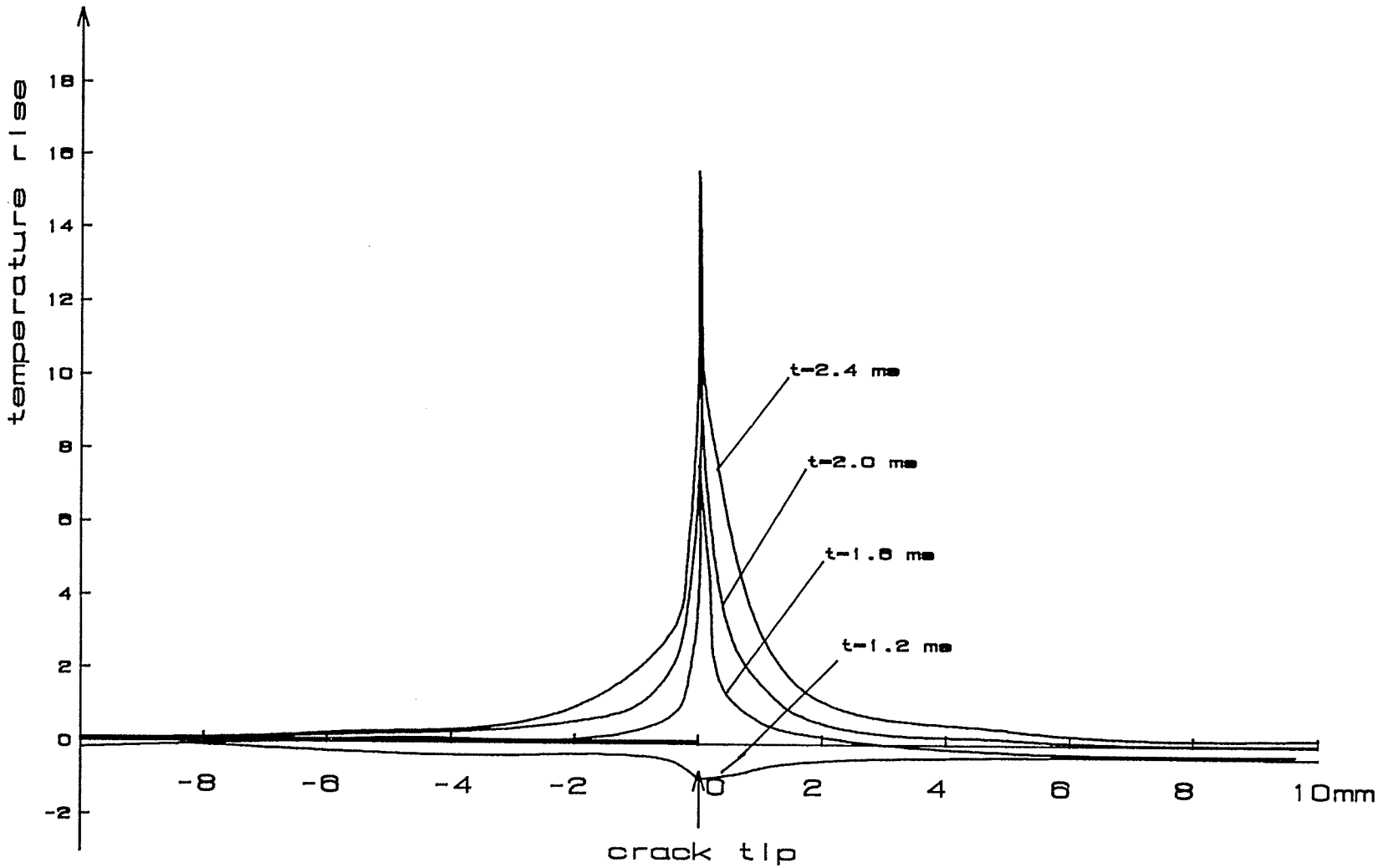

(b) Temperature distributions on the crack line.

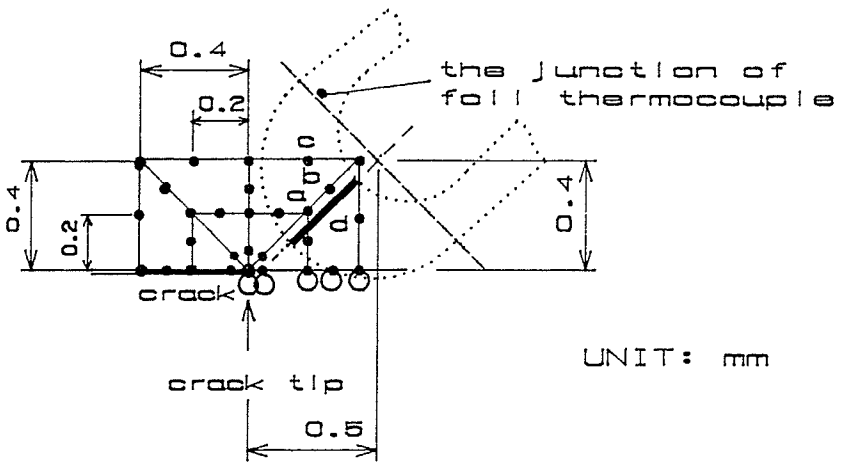

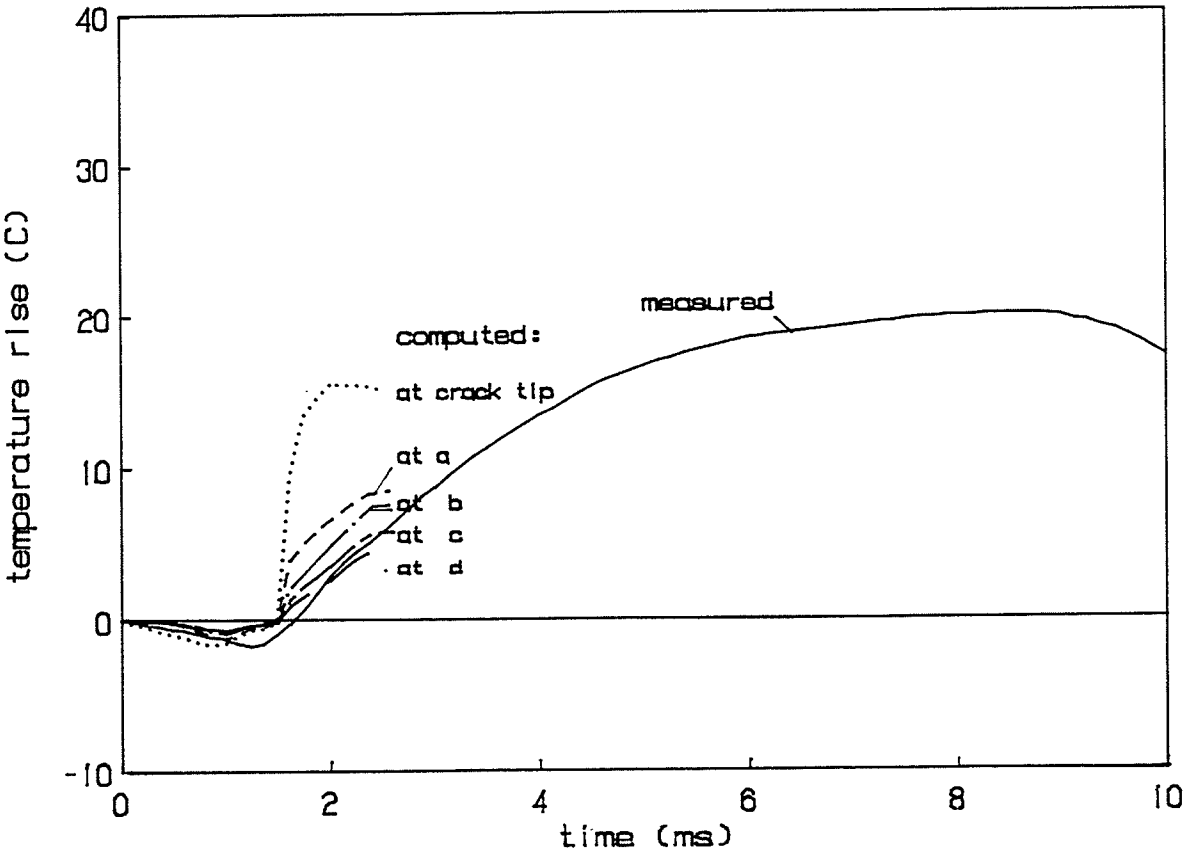

Figure 6.6 Comparison between temperature results of finite element analysis and measurement.

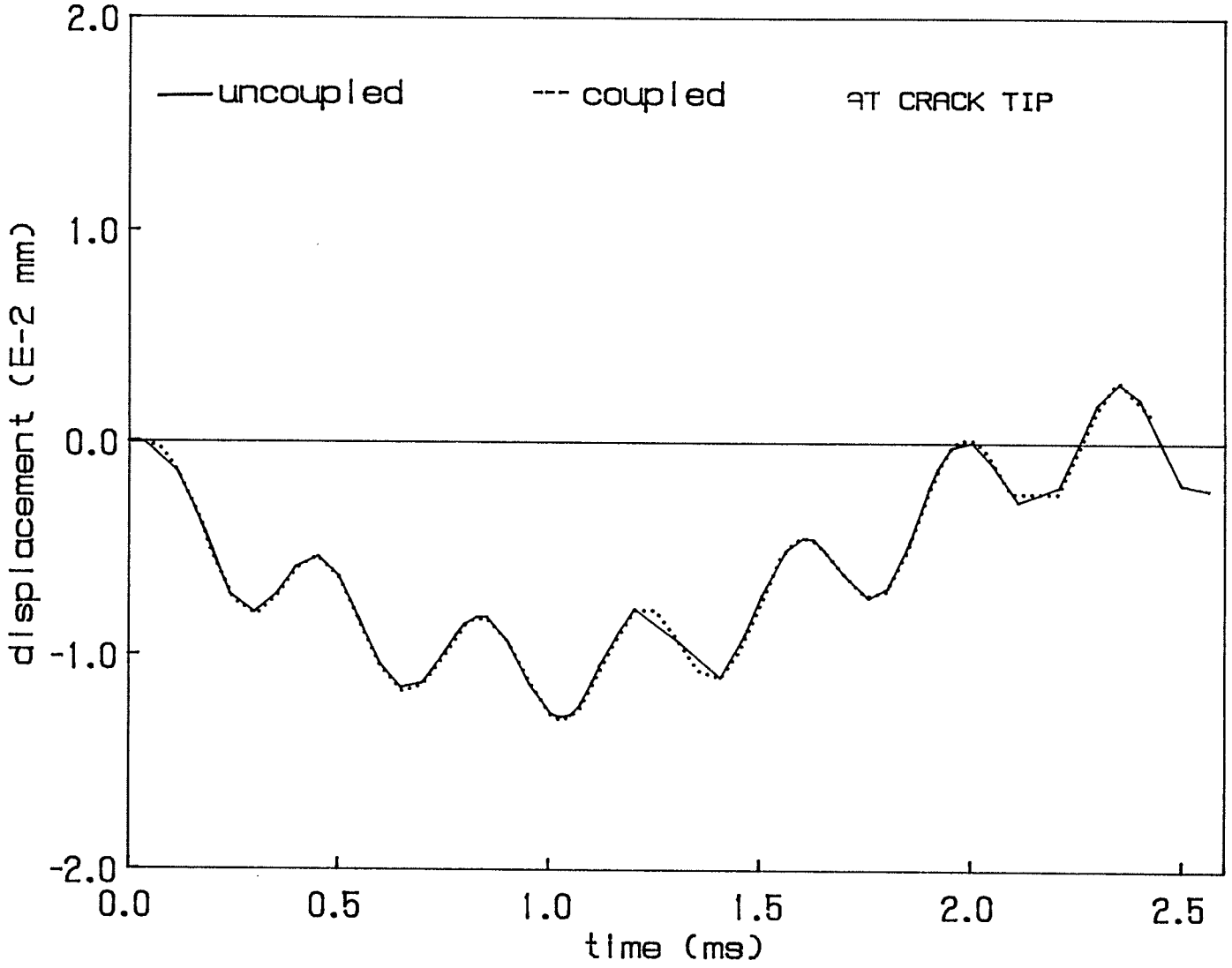

Figure 6.7 Displacement histories at the crack tip.

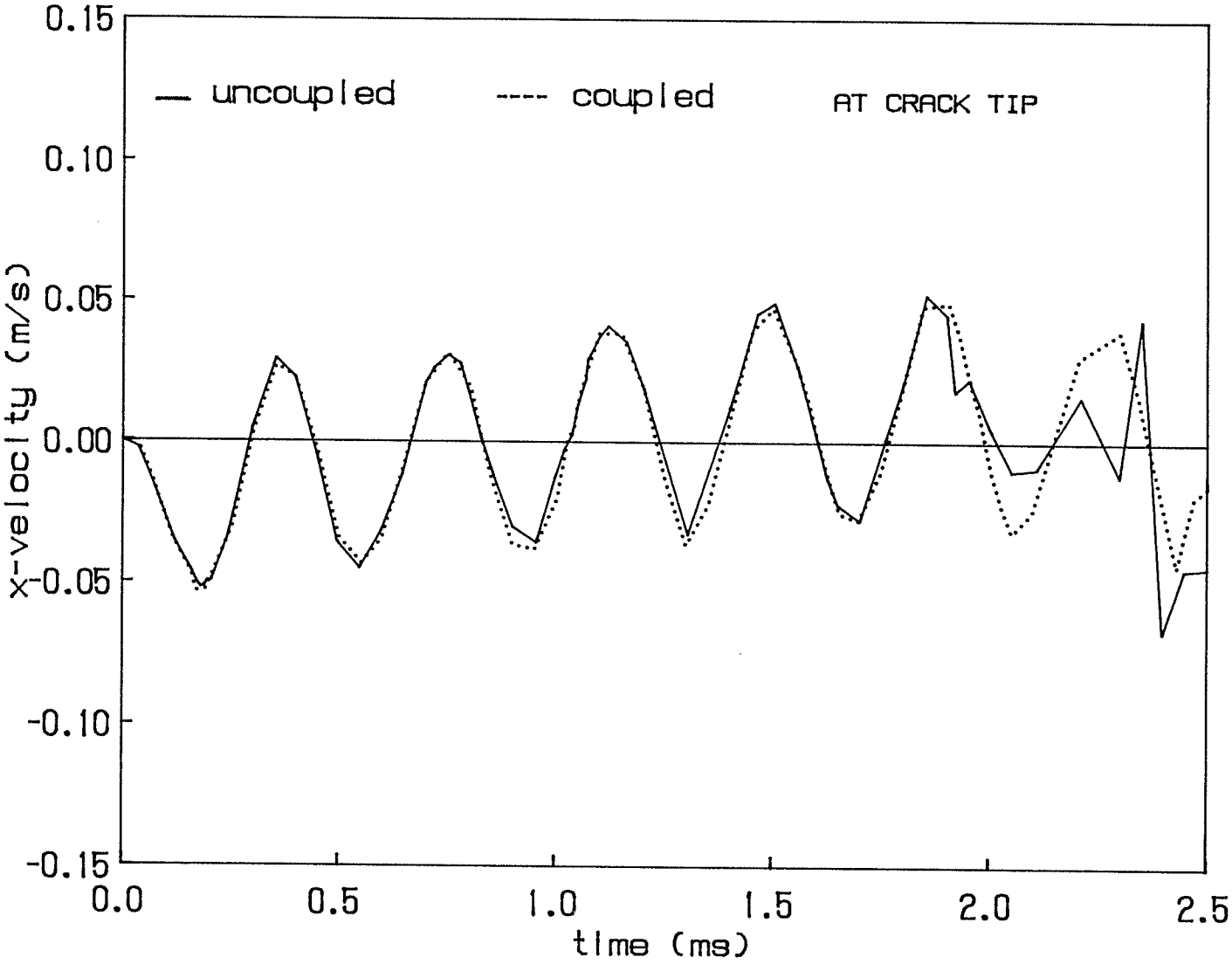

Figure 6.8 Velocity histories at the crack tip.

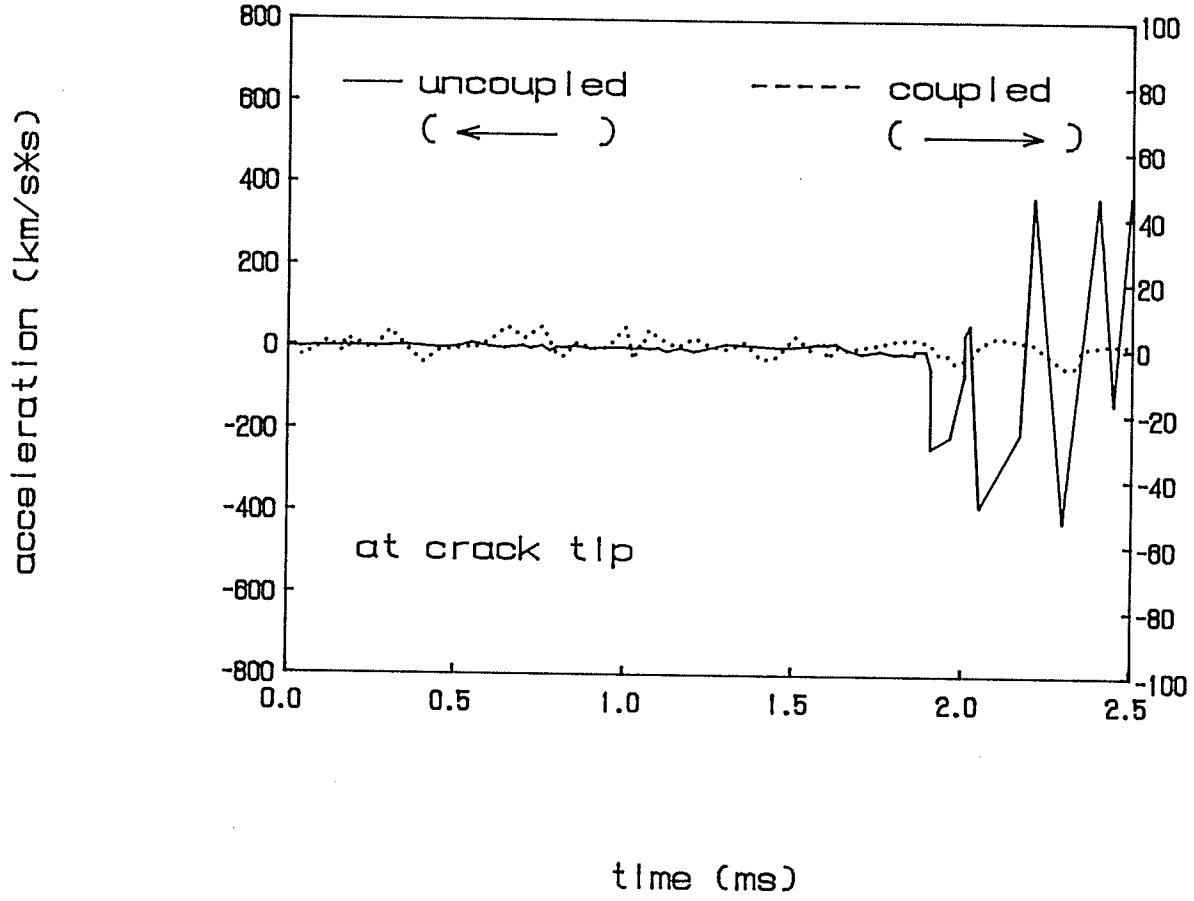

Figure 6.9 Acceleration histories at the crack tip.

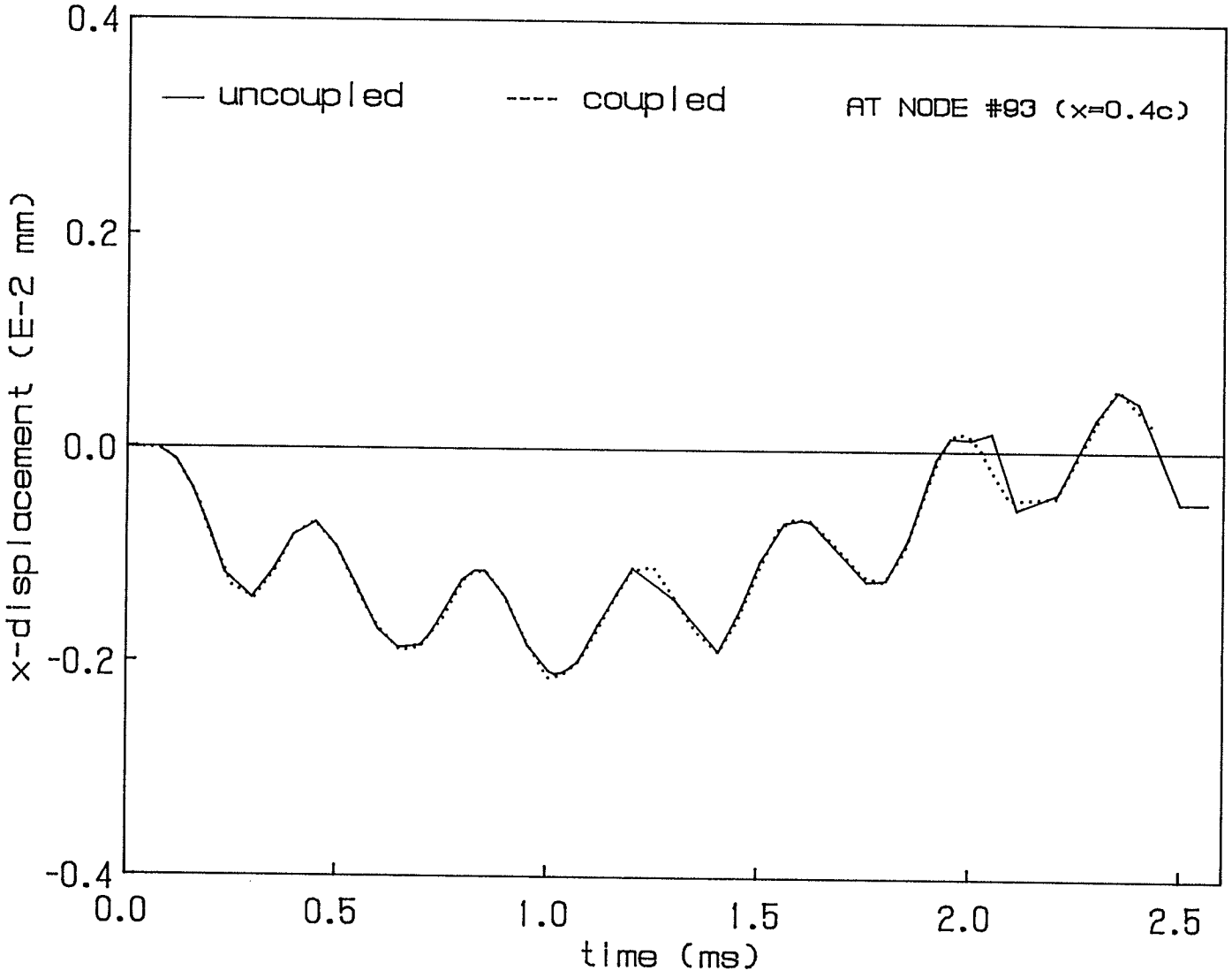

Figure 6.10 Displacement histories at the node #93 (x=0.4c_o)

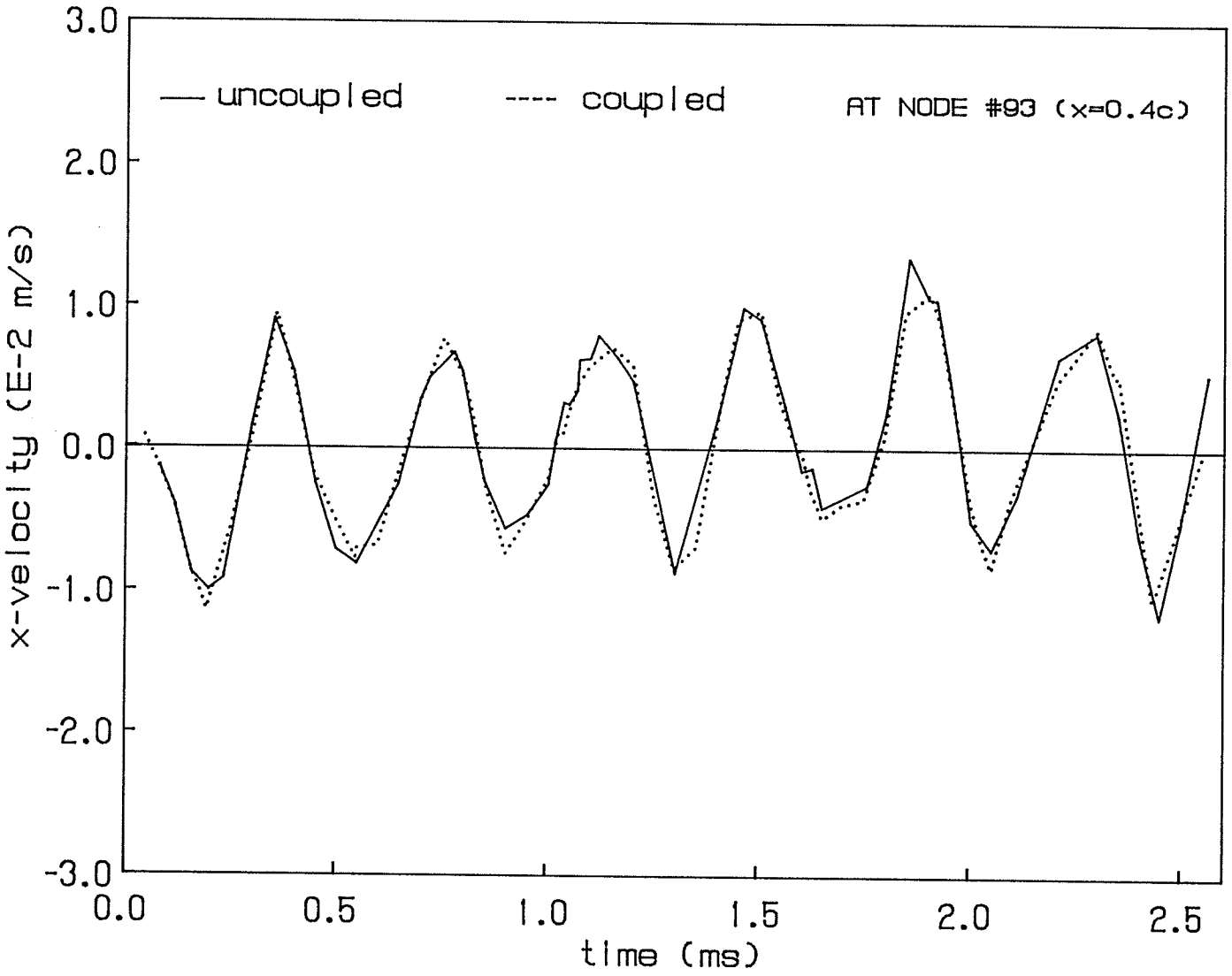

Figure 6.11 Velocity histories at the node #93 (x=0.4c_o)

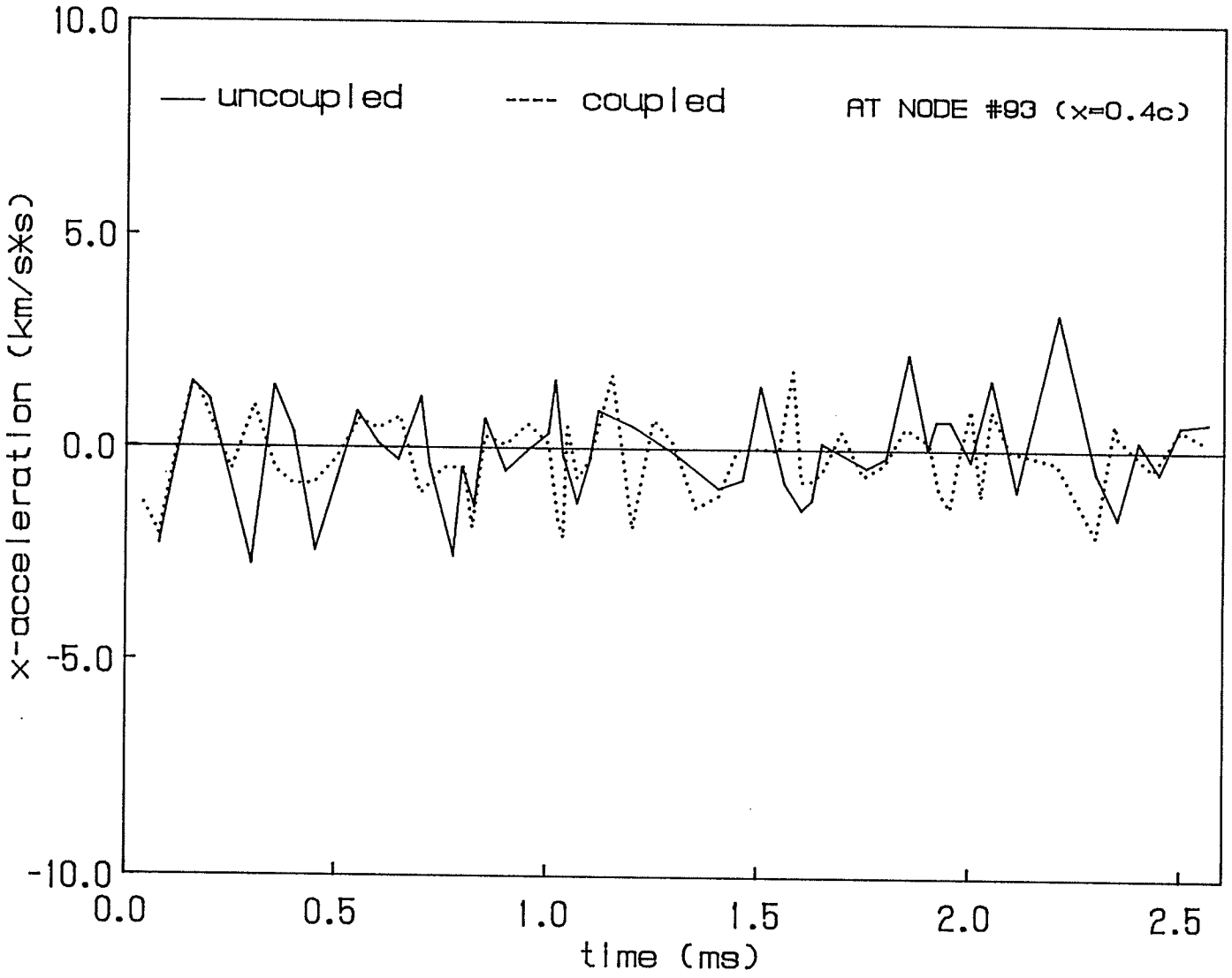

Figure 6.12 Acceleration histories at the node #93 (x=0.4c_o)

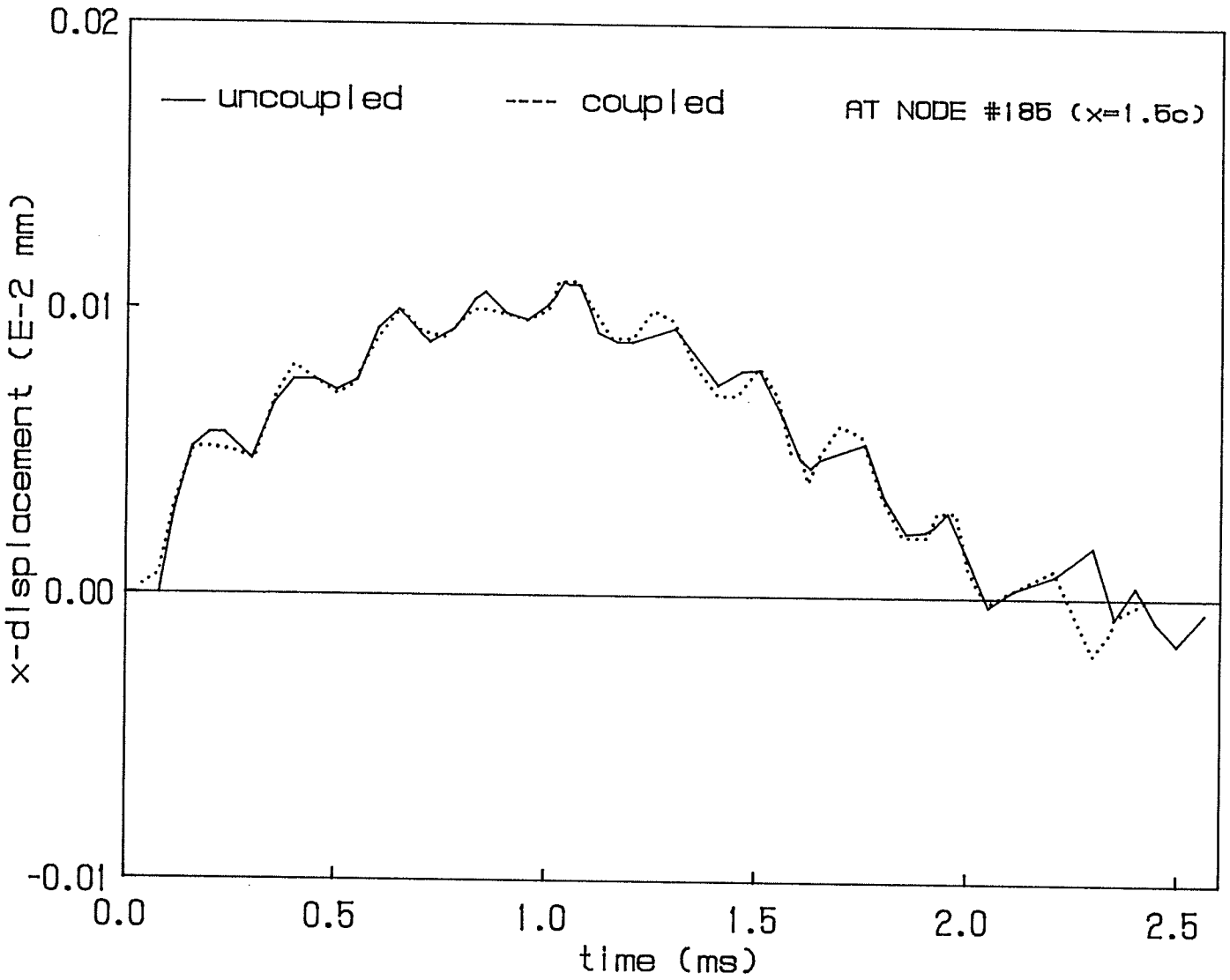

Figure 6.13 Displacement histories at the node # 185 (x=1.5c_o)

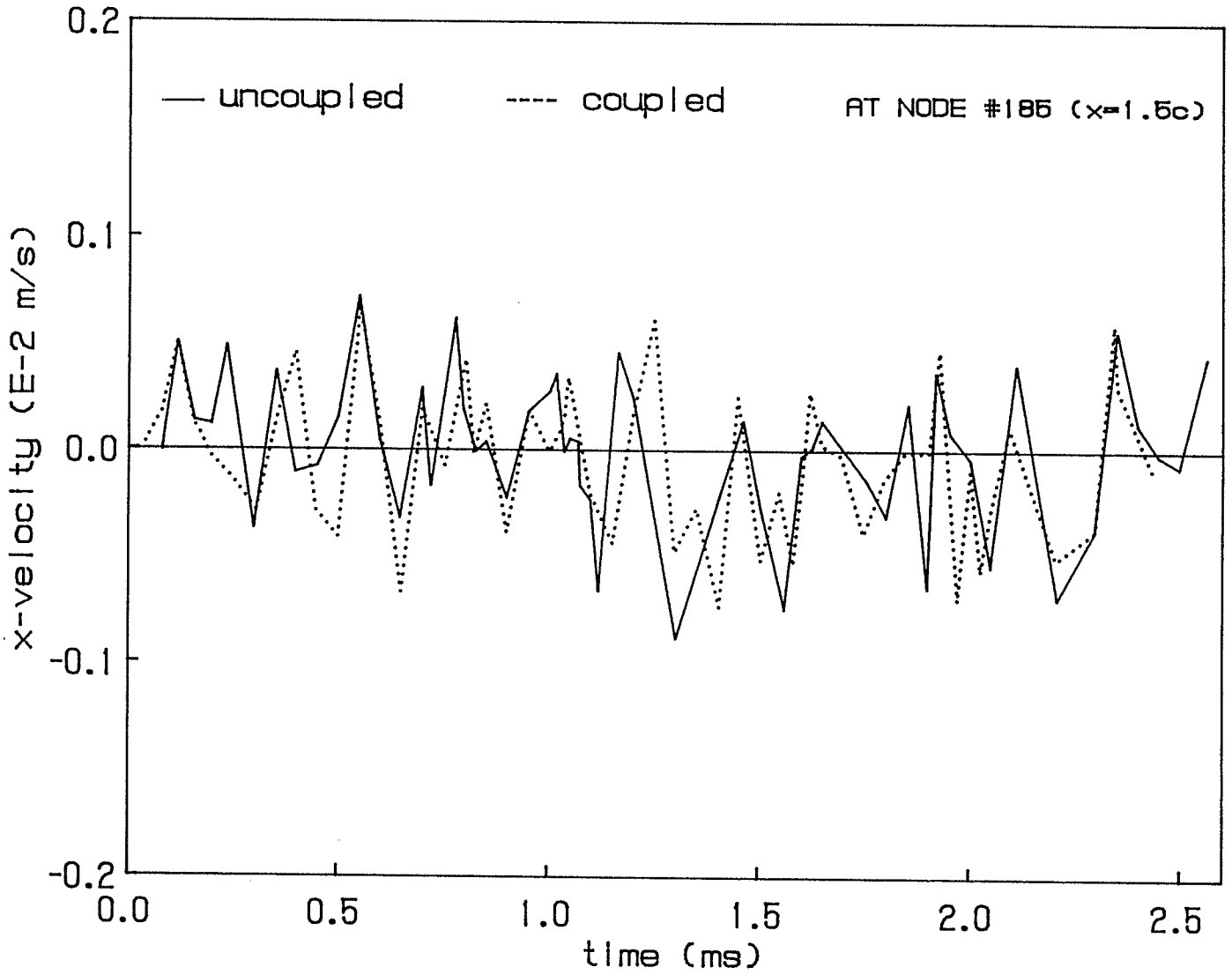

Figure 6.14 Velocity histories at the node # 185 (x=1.5c_o)

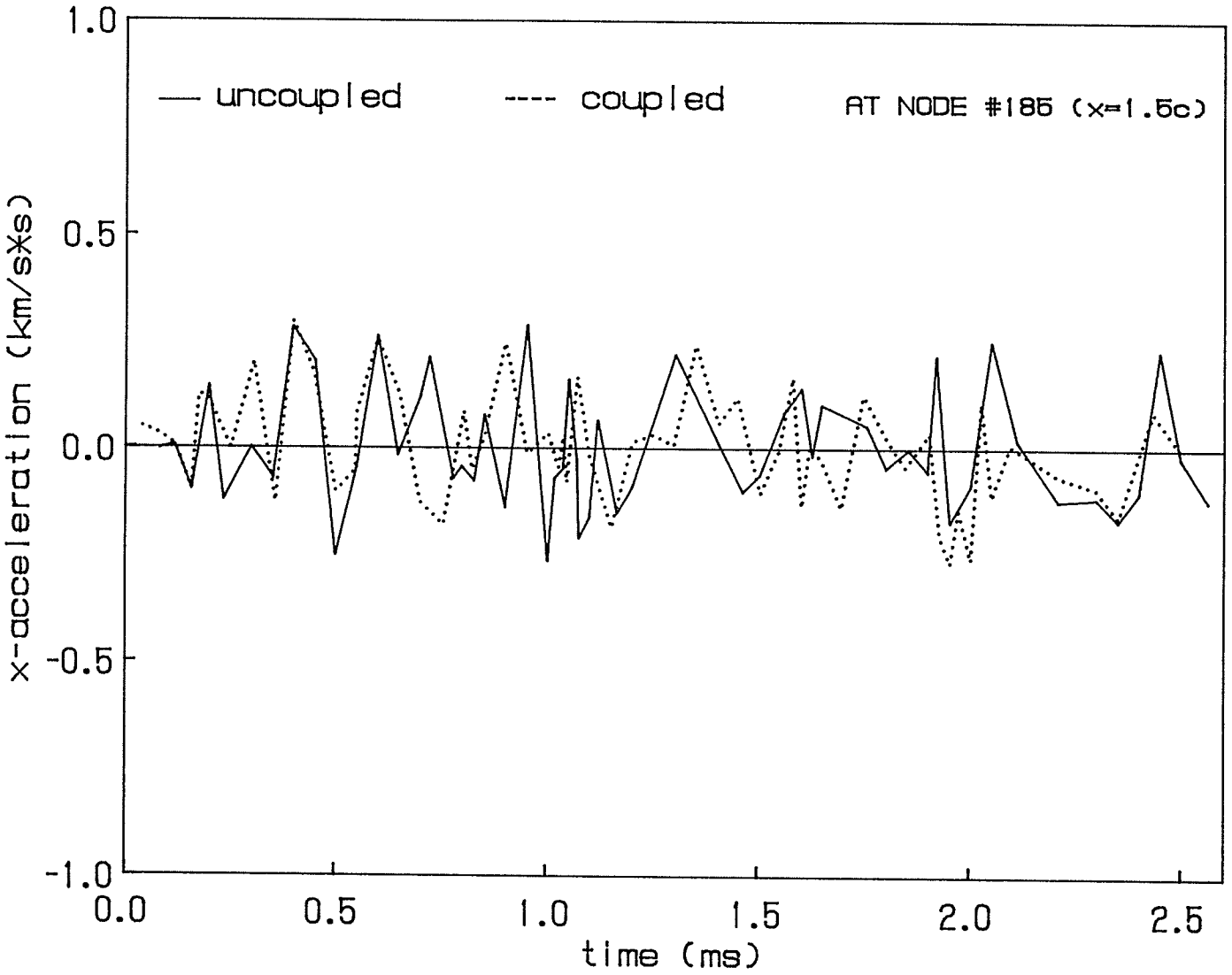

Figure 6.15 Acceleration histories at the node # 185 (x=1.5c_o)

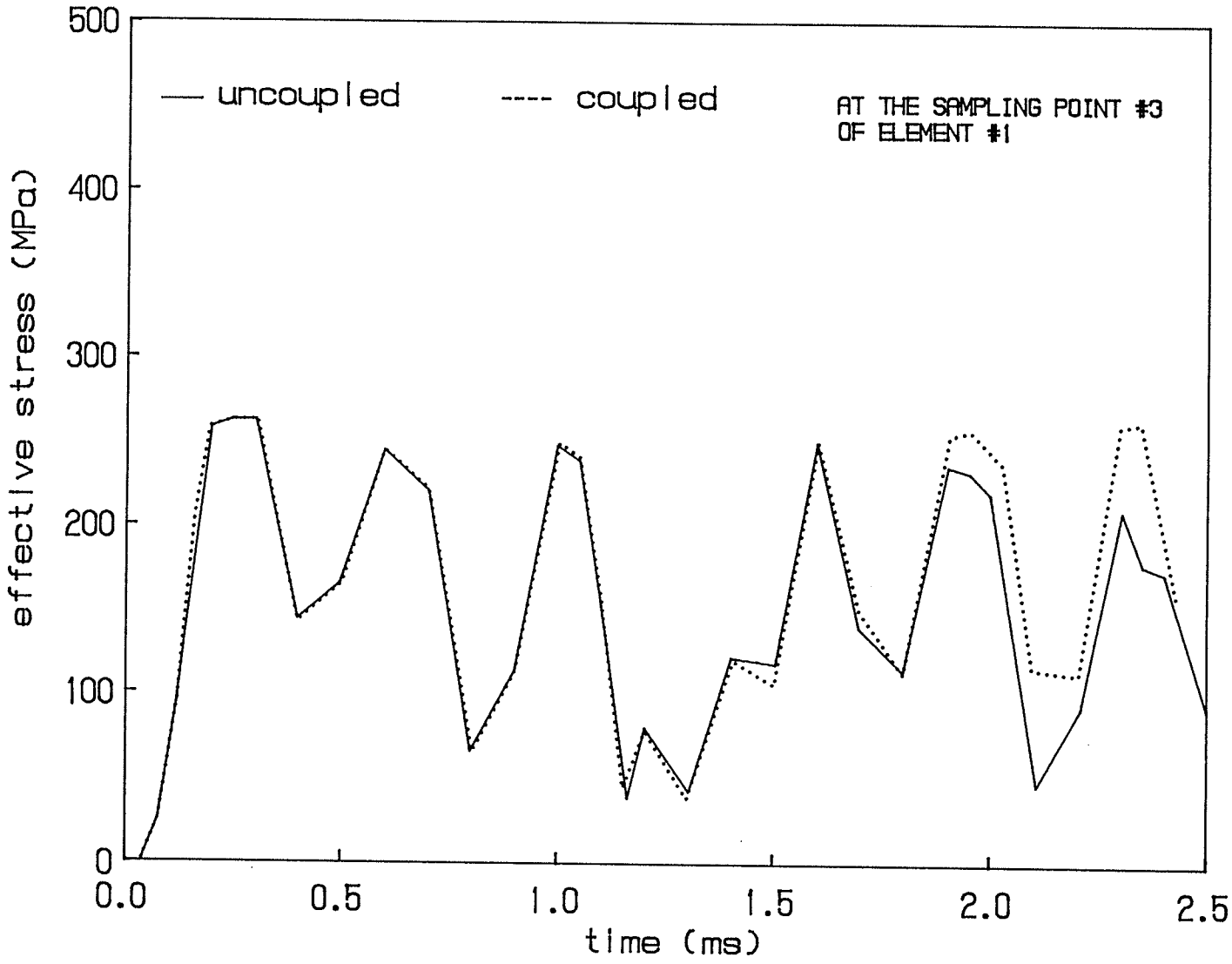

Figure 6.16 Effective stress at the sampling point # 3 of element # 1.

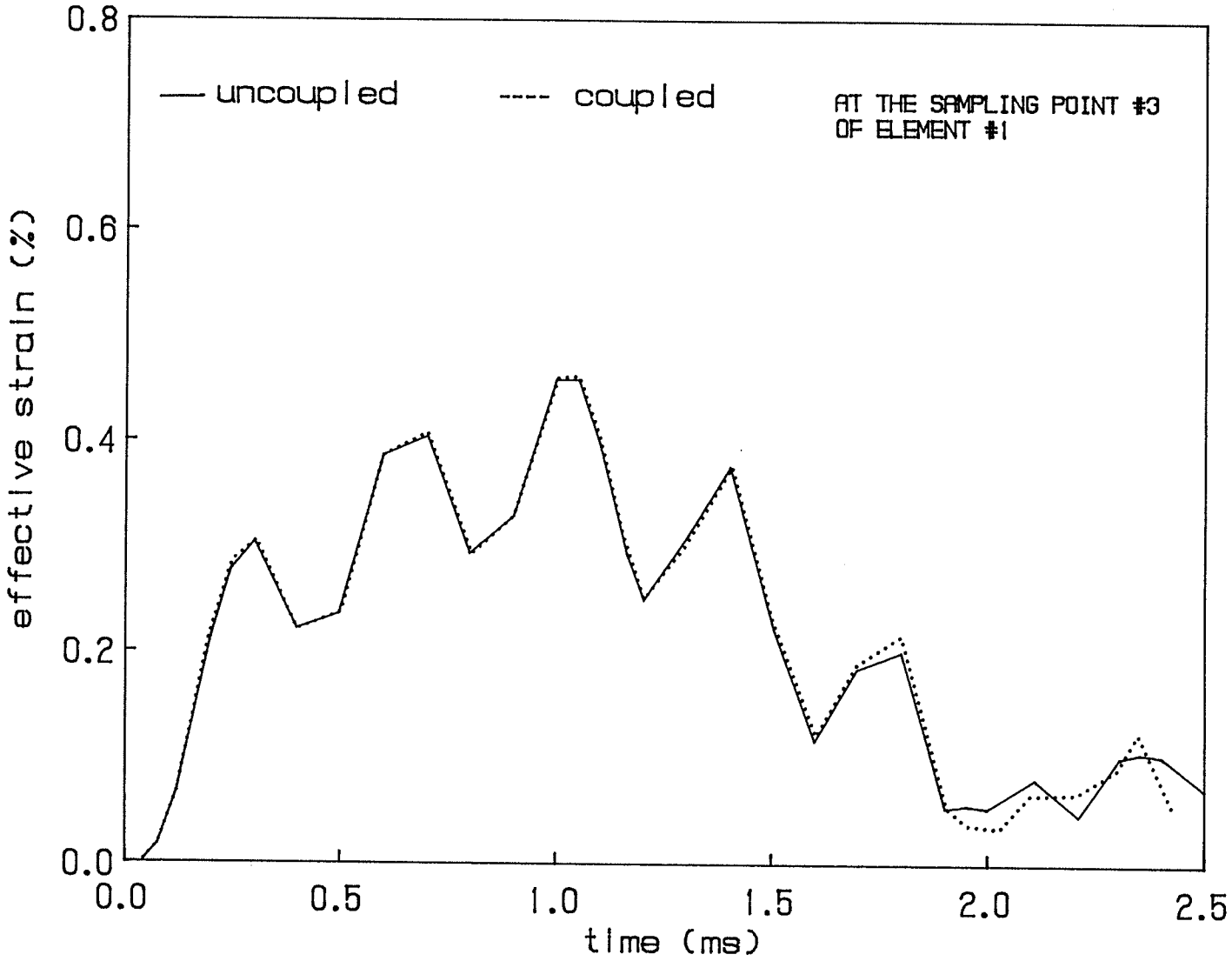

Figure 6.17 Effective strain at the sampling point # 3 of element # 1.

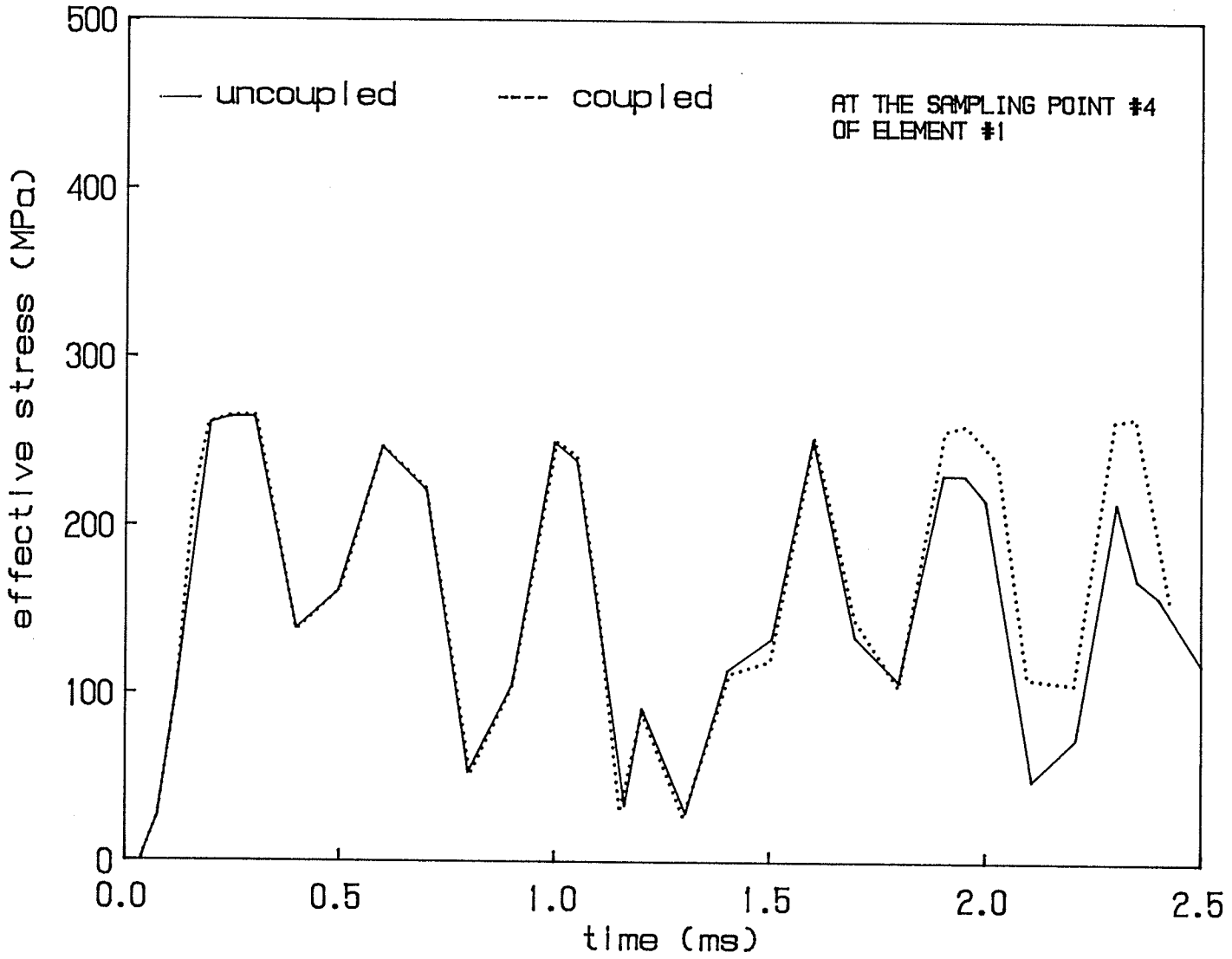

Figure 6.18 Effective stress at the sampling point # 4 of element # 1.

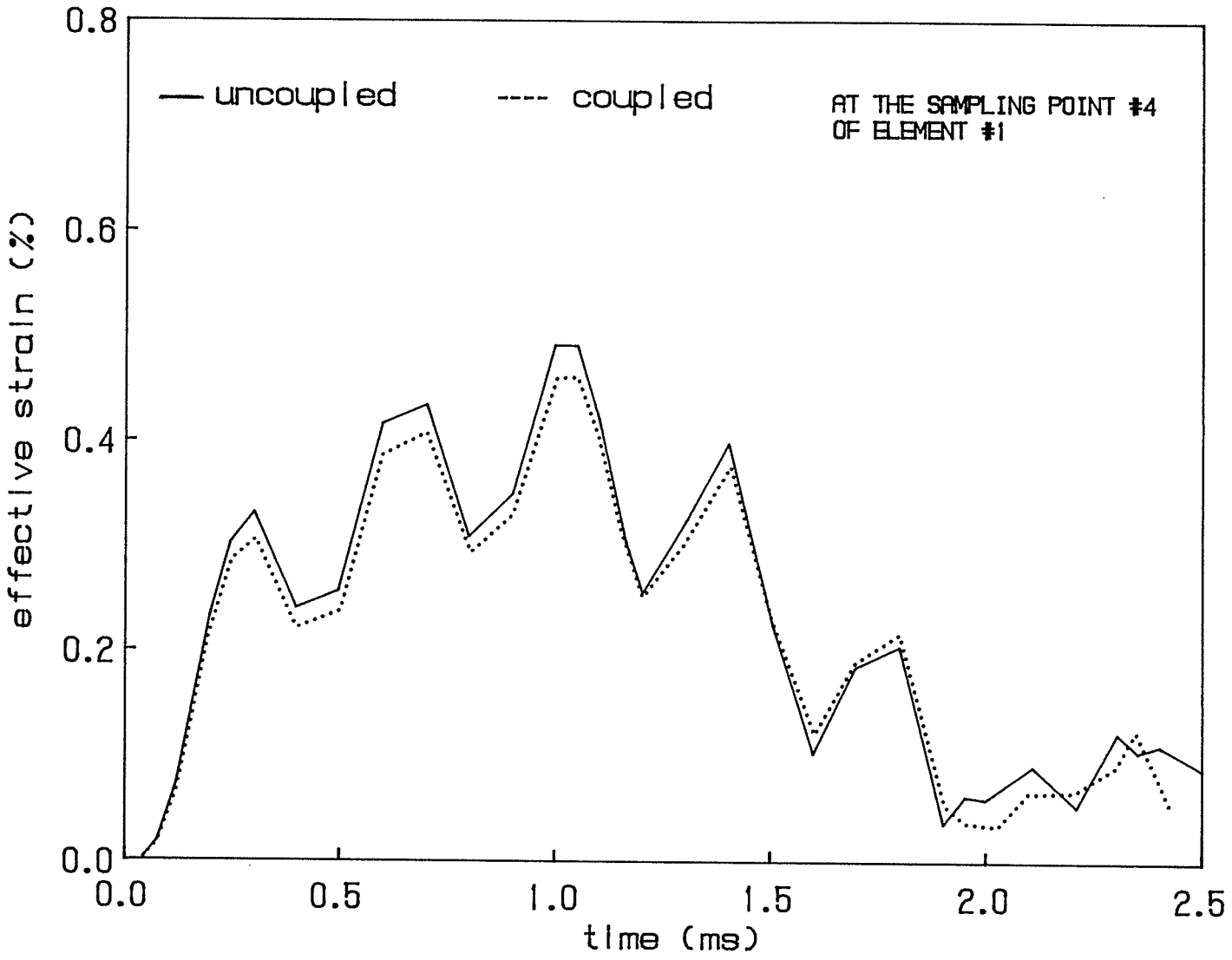

Figure 6.19 Effective strain at the sampling point # 4 of element # 1.

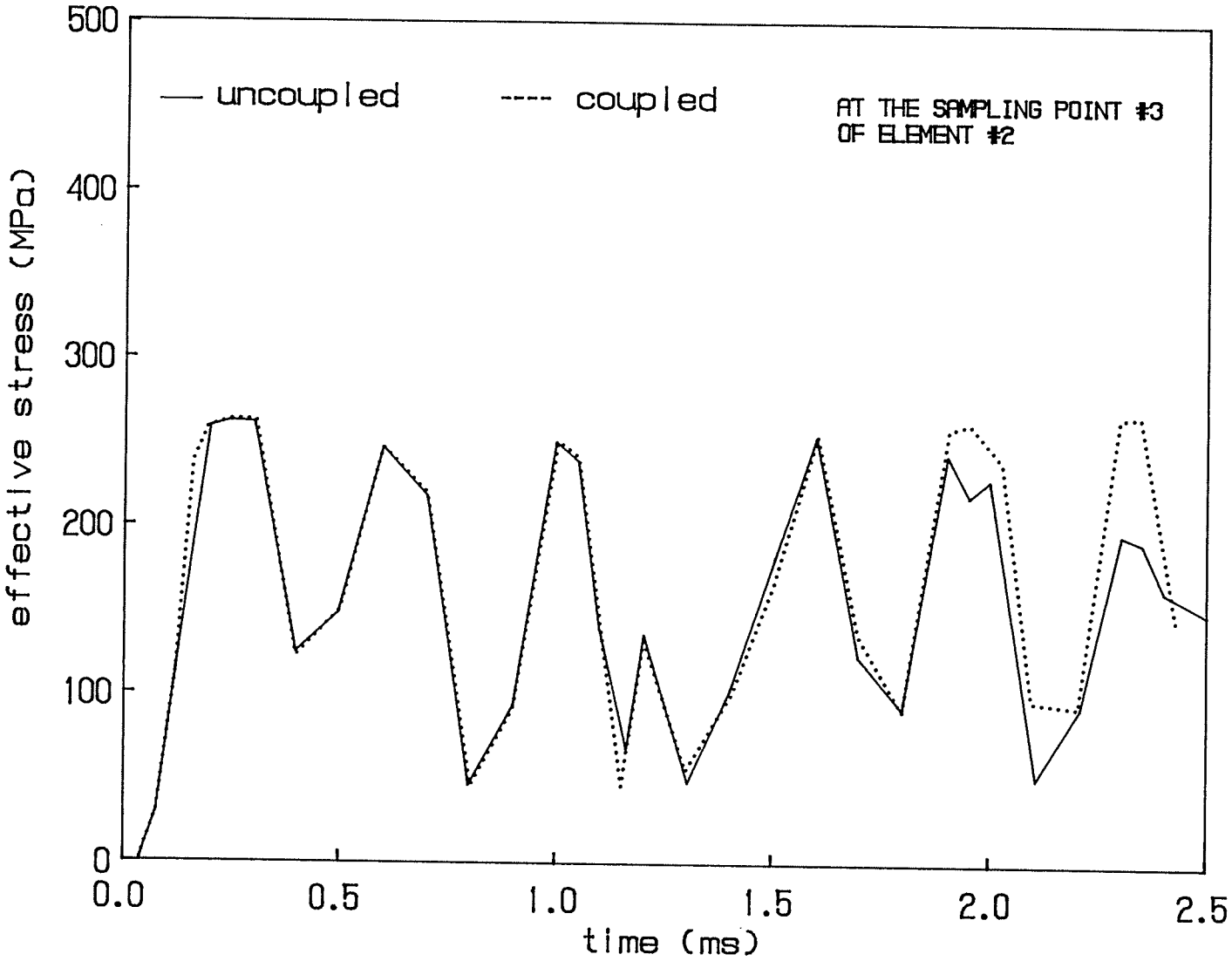

Figure 6.20 Effective stress at the sampling point # 3 of element # 2.

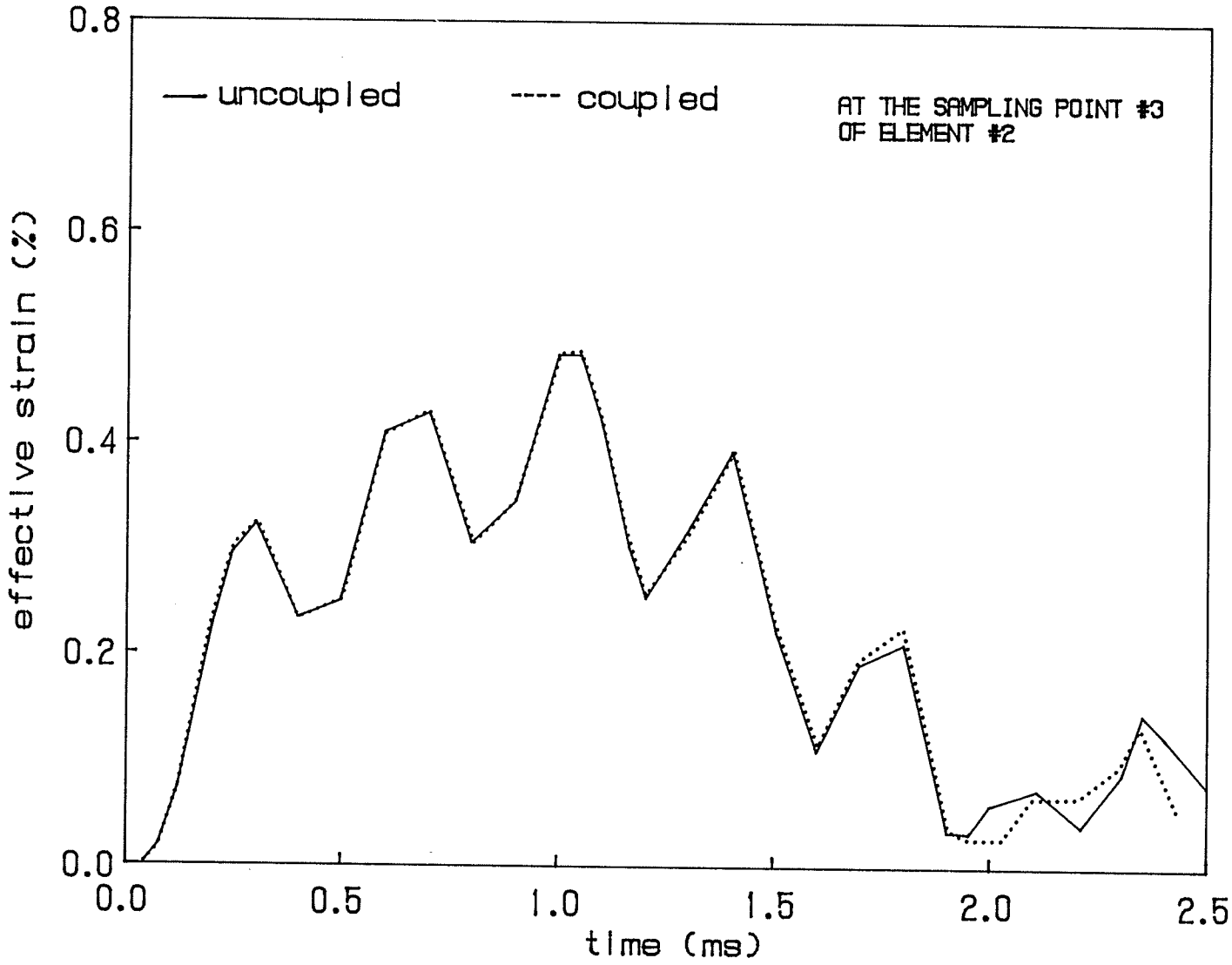

Figure 6.21 Effective strain at the sampling point # 3 of element # 2.

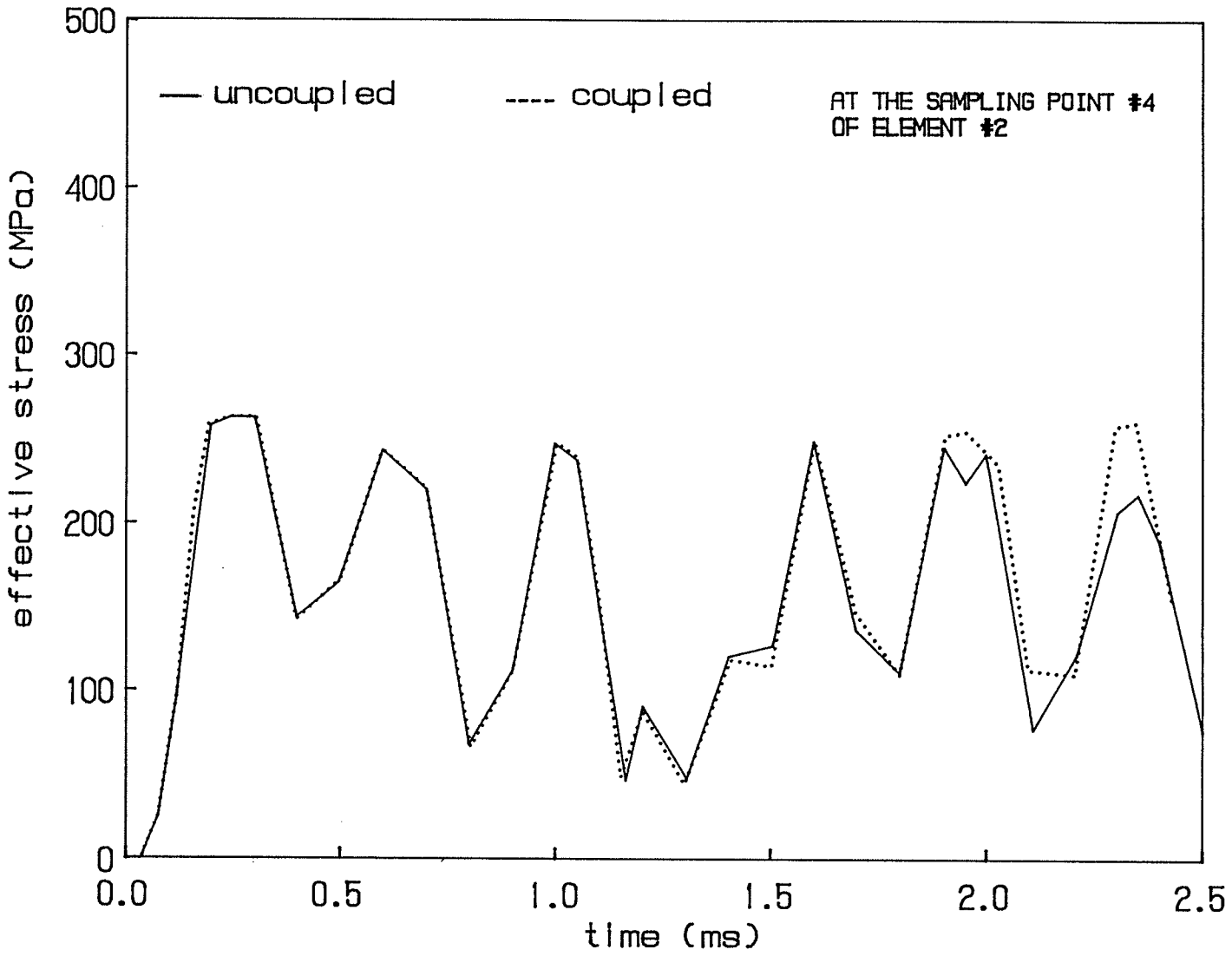

Figure 6.22 Effective stress at the sampling point # 4 of element # 2.

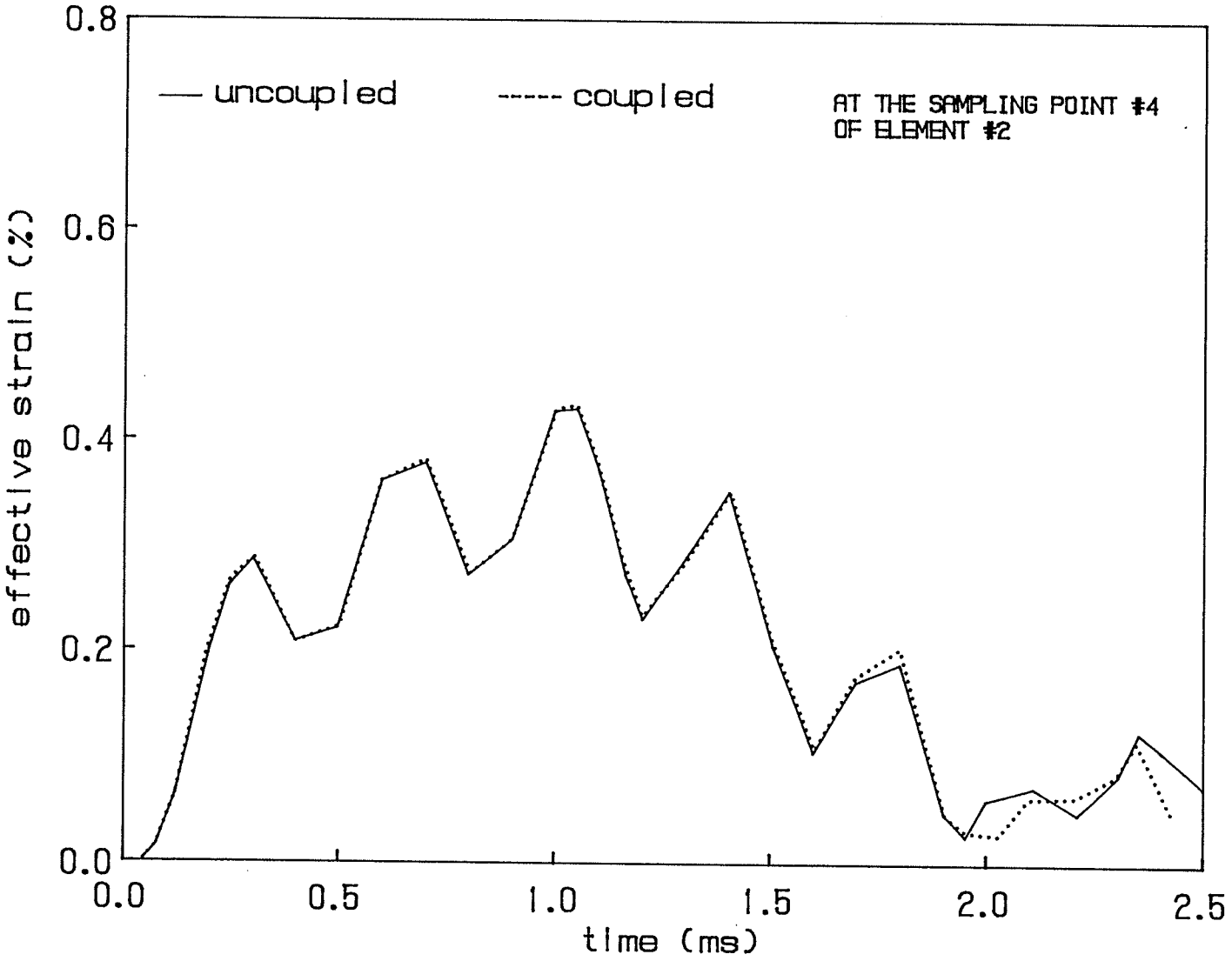

Figure 6.23 Effective strain at the sampling point # 4 of element # 2.

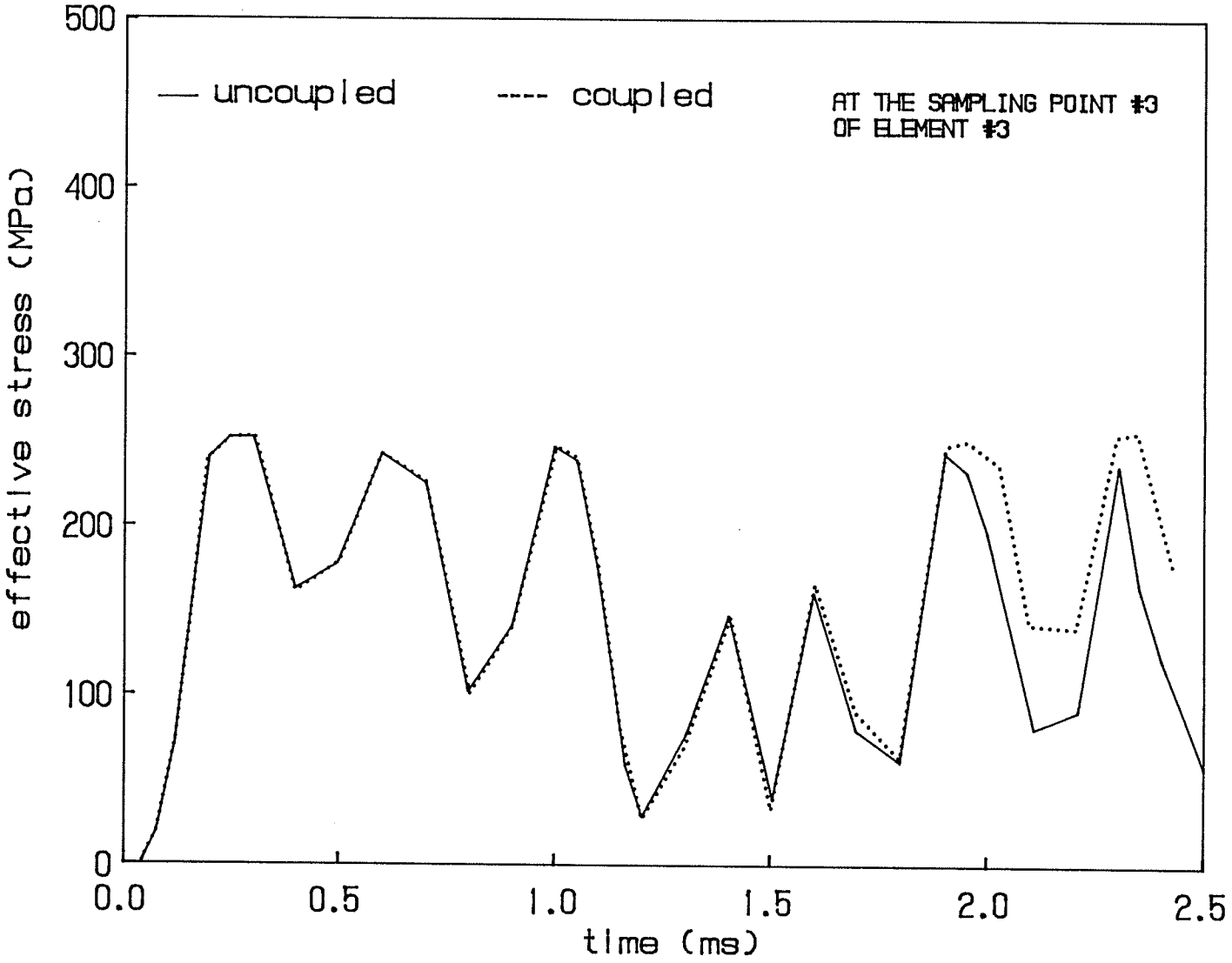

Figure 6.24 Effective stress at the sampling point # 3 of element # 3.

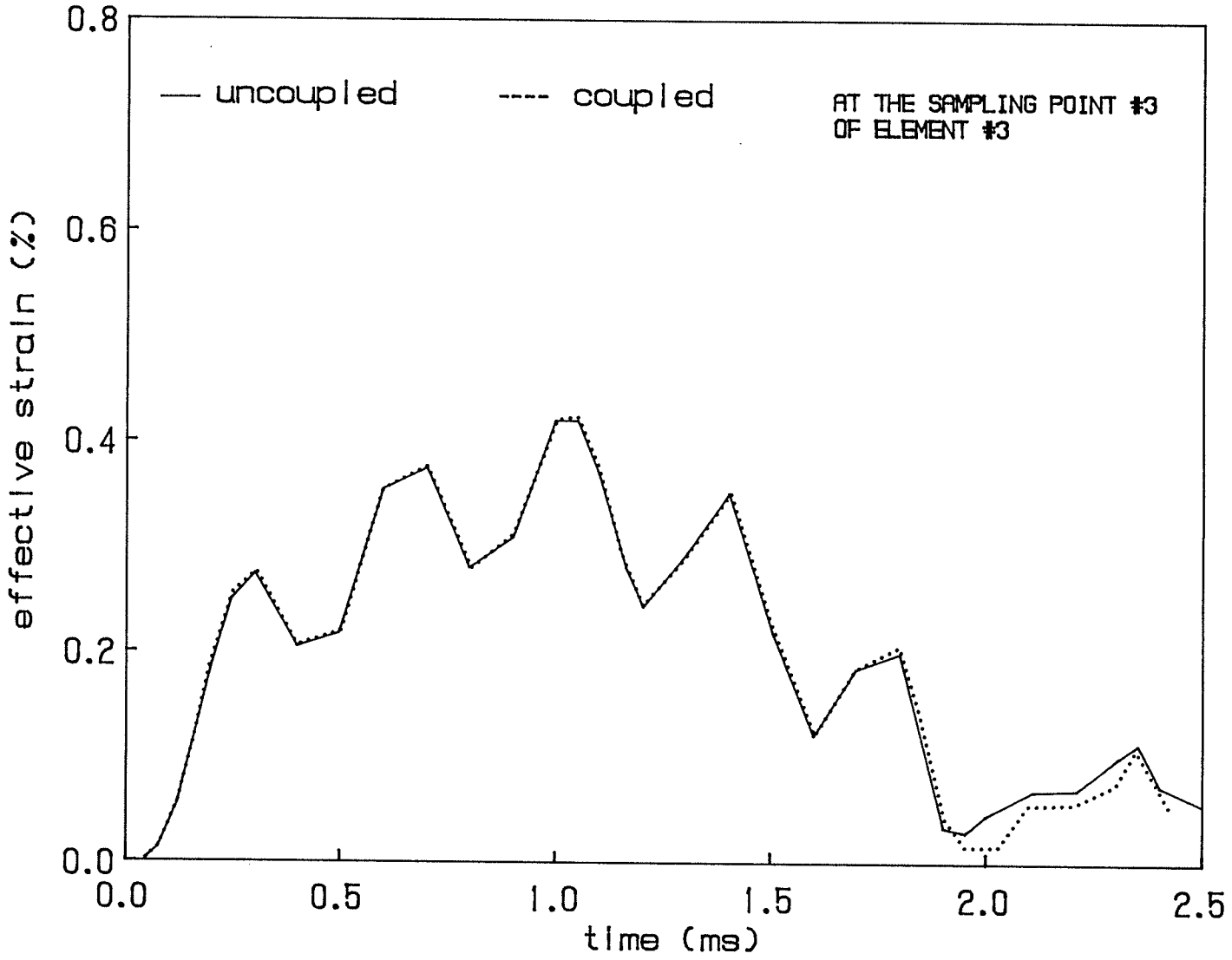

Figure 6.25 Effective strain at the sampling point # 3 of element # 3.

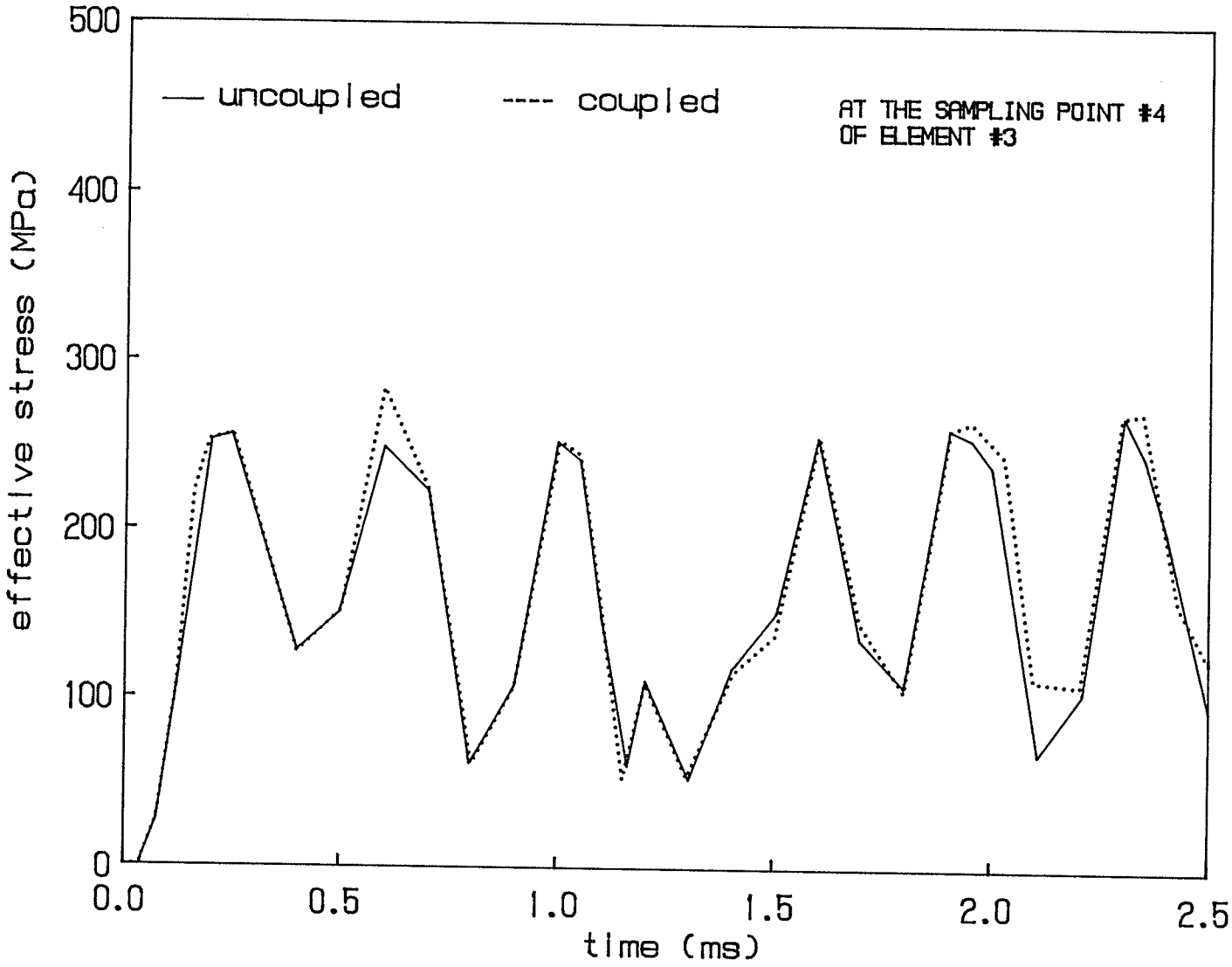

Figure 6.26 Effective stress at the sampling point # 4 of element # 3.

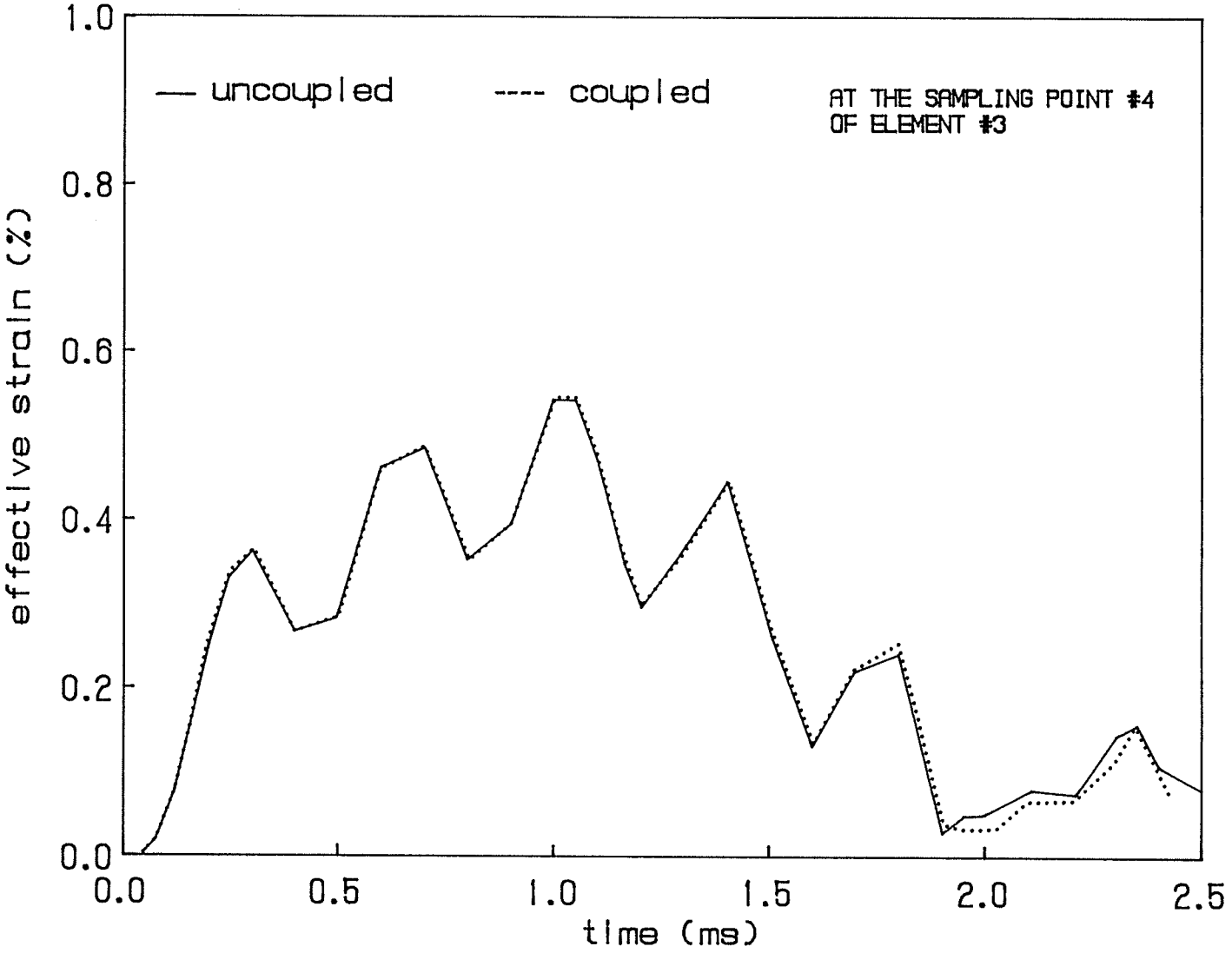

Figure 6.27 Effective strain at the sampling point # 4 of element # 3.

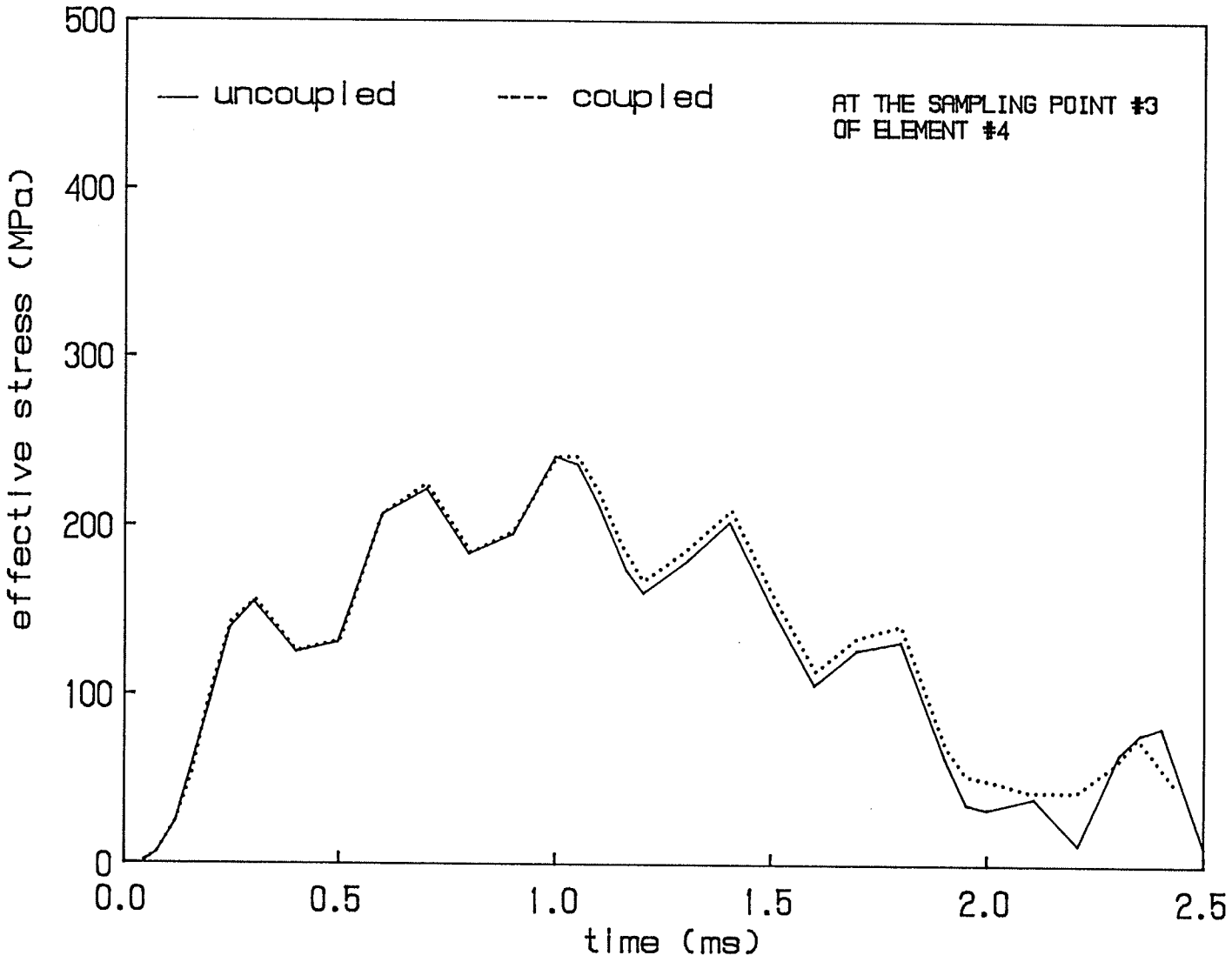

Figure 6.28 Effective stress at the sampling point # 3 of element # 4.

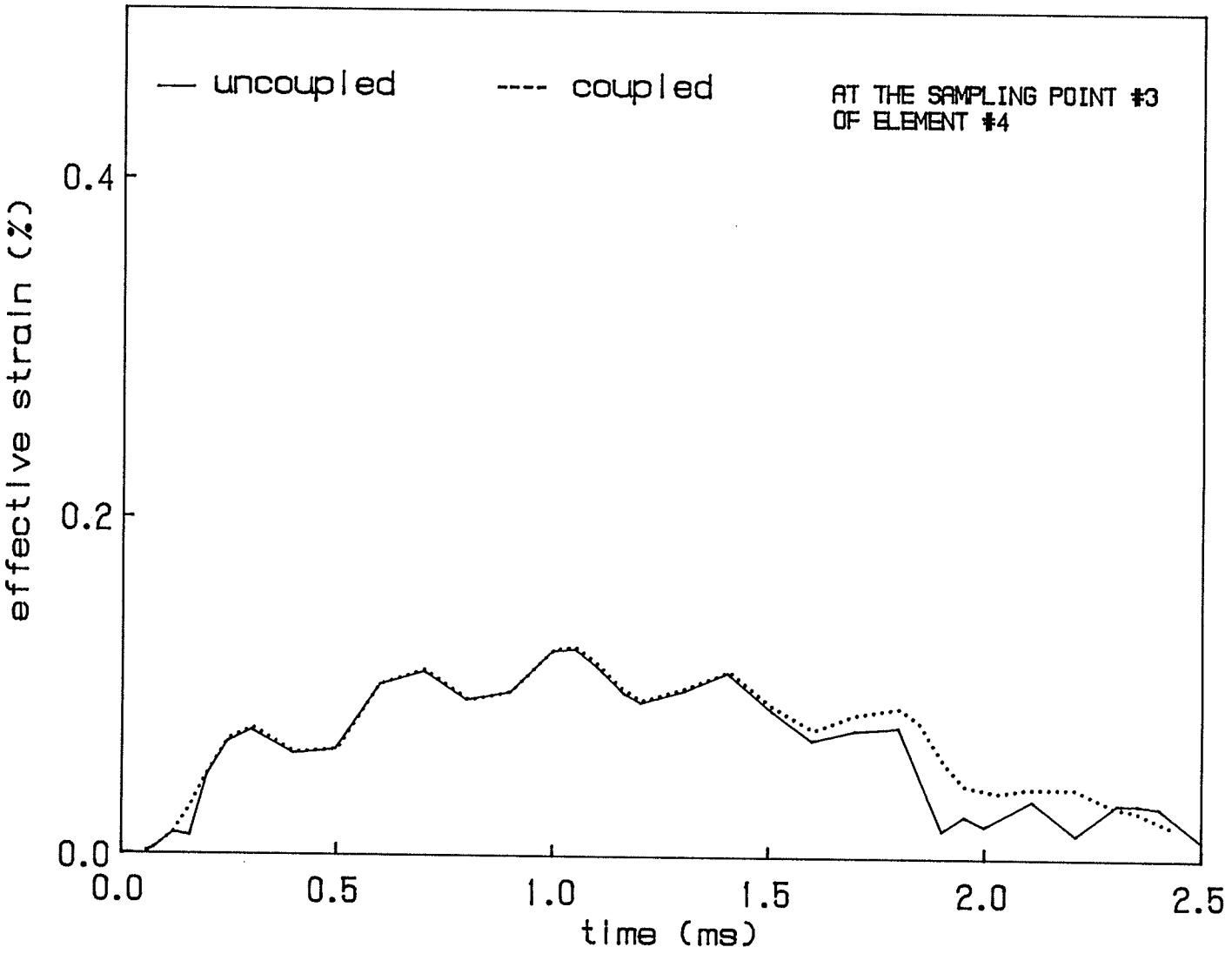

Figure 6.29 Effective strain at the sampling point # 3 of element # 4.

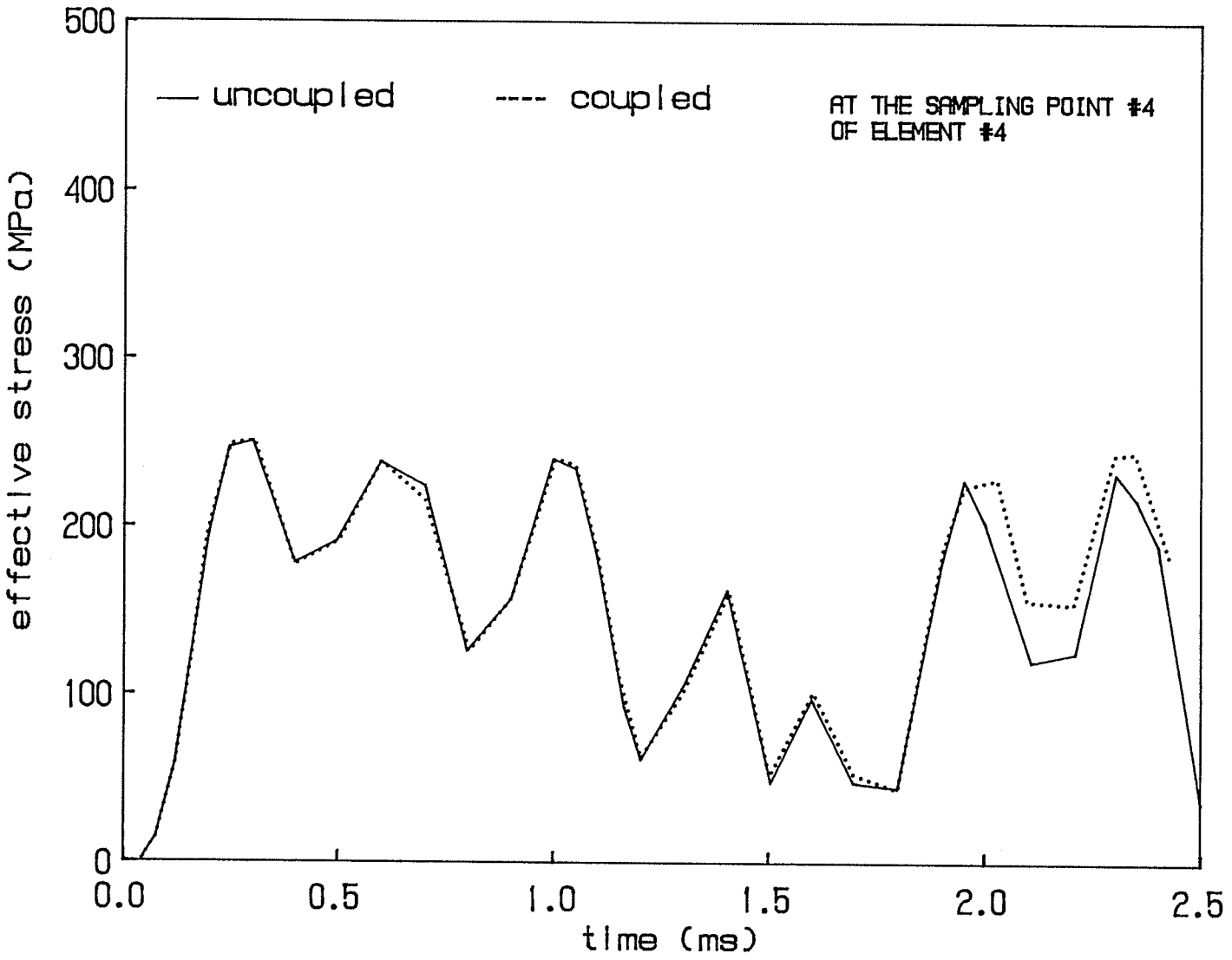

Figure 6.30 Effective stress at the sampling point # 4 of element # 4.

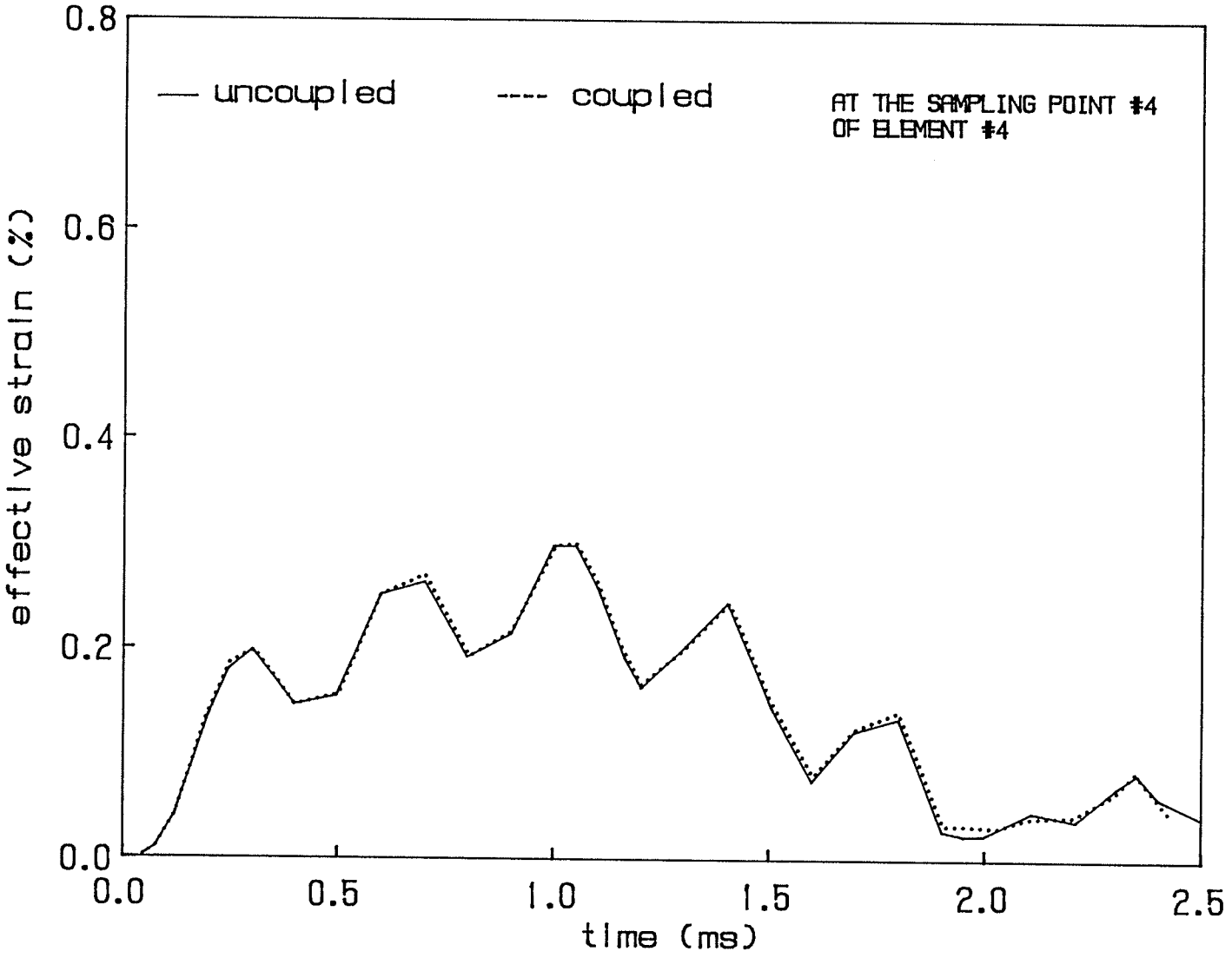

Figure 6.31 Effective strain at the sampling point # 4 of element # 4.

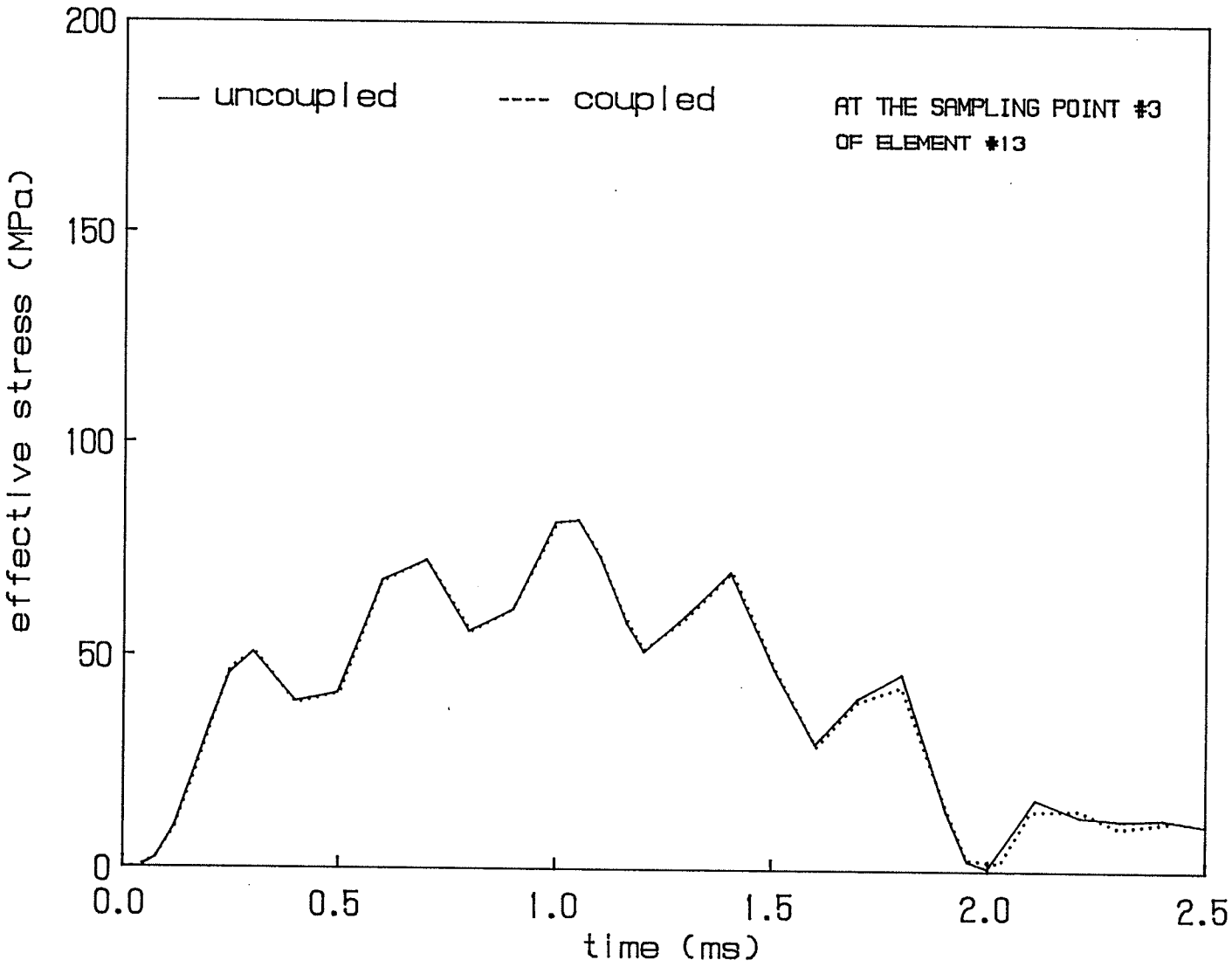

Figure 6.32 Effective stress at the sampling point # 3 of element # 13.

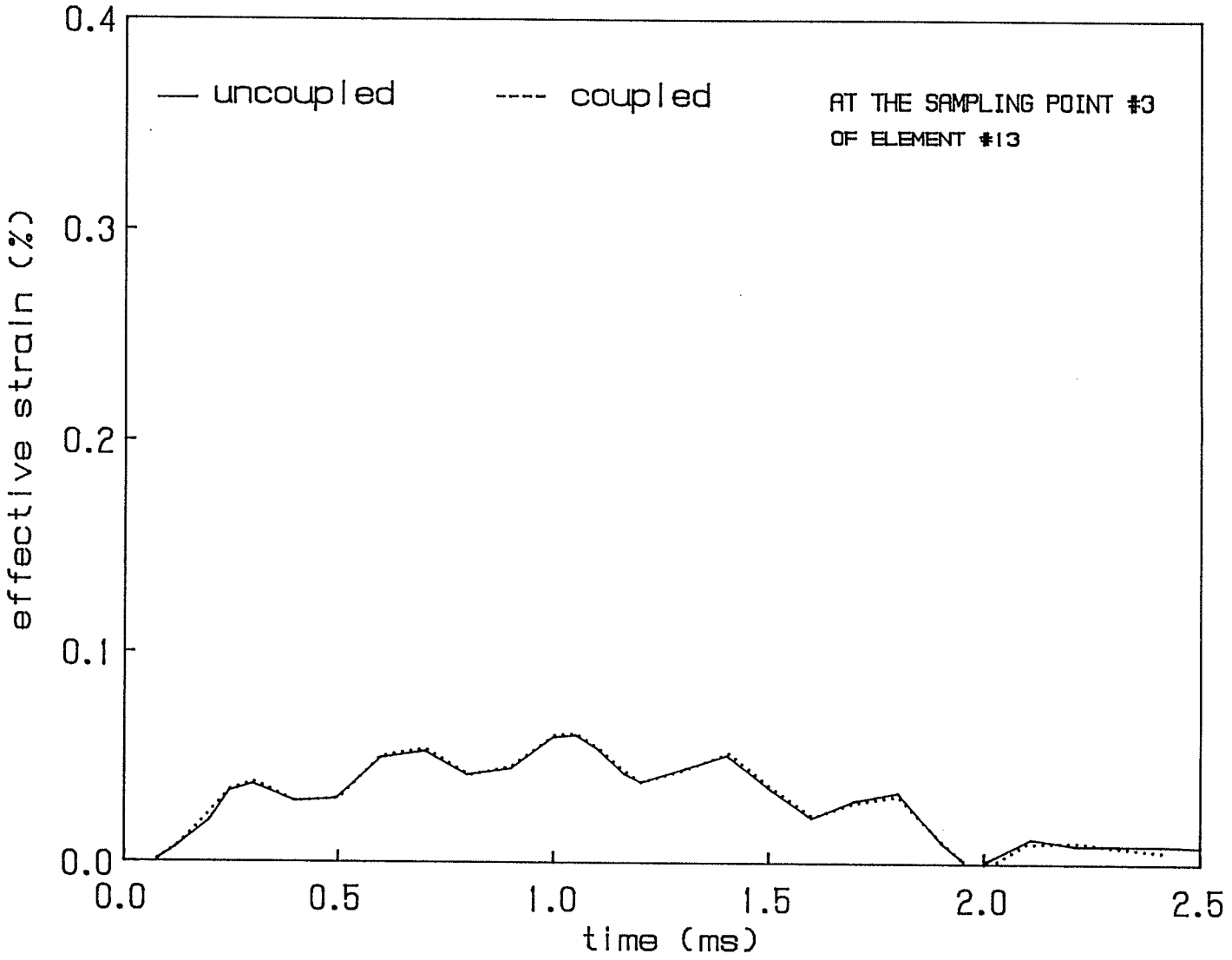

Figure 6.33 Effective strain at the sampling point # 3 of element # 13.

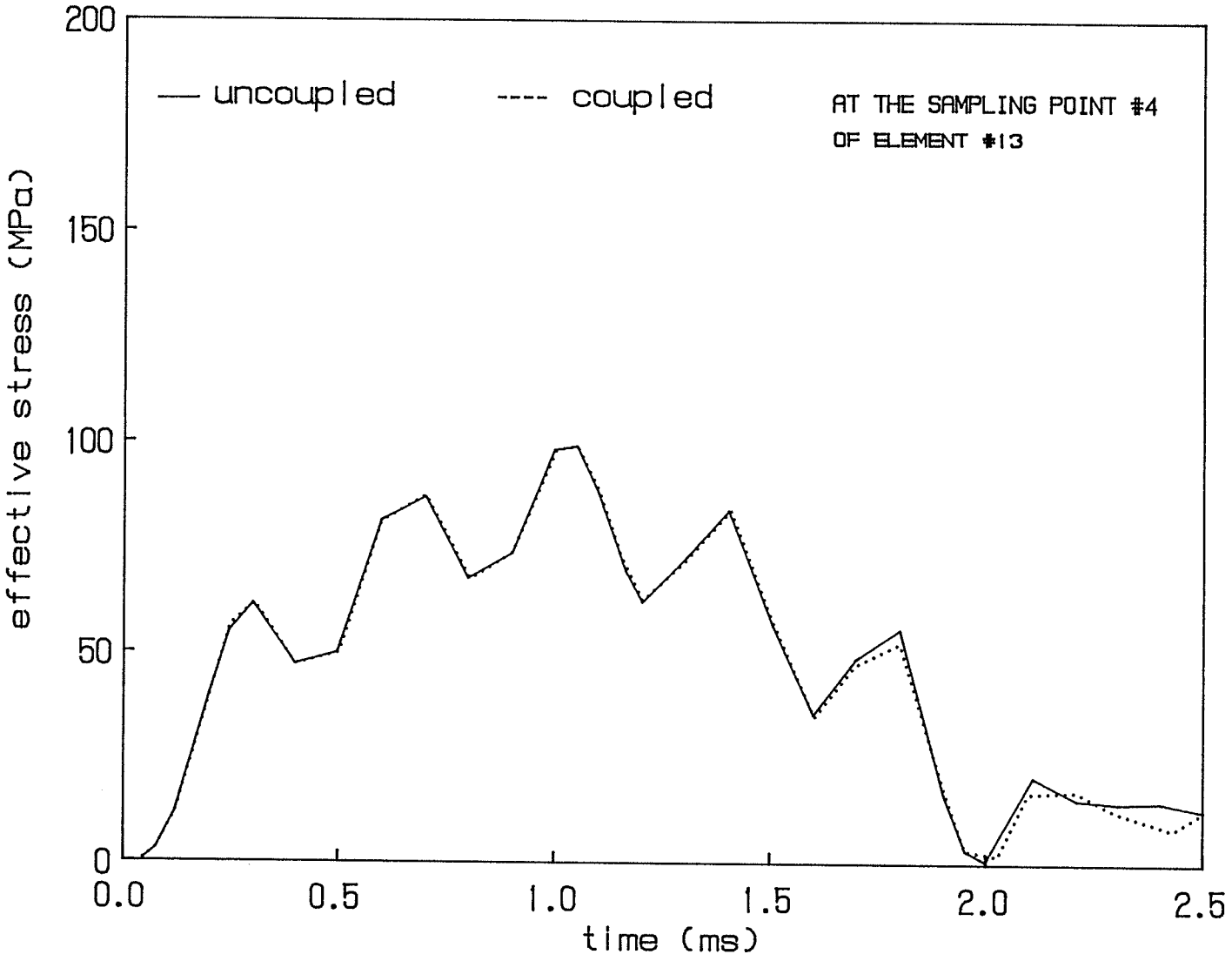

Figure 6.34 Effective stress at the sampling point # 4 of element # 13.

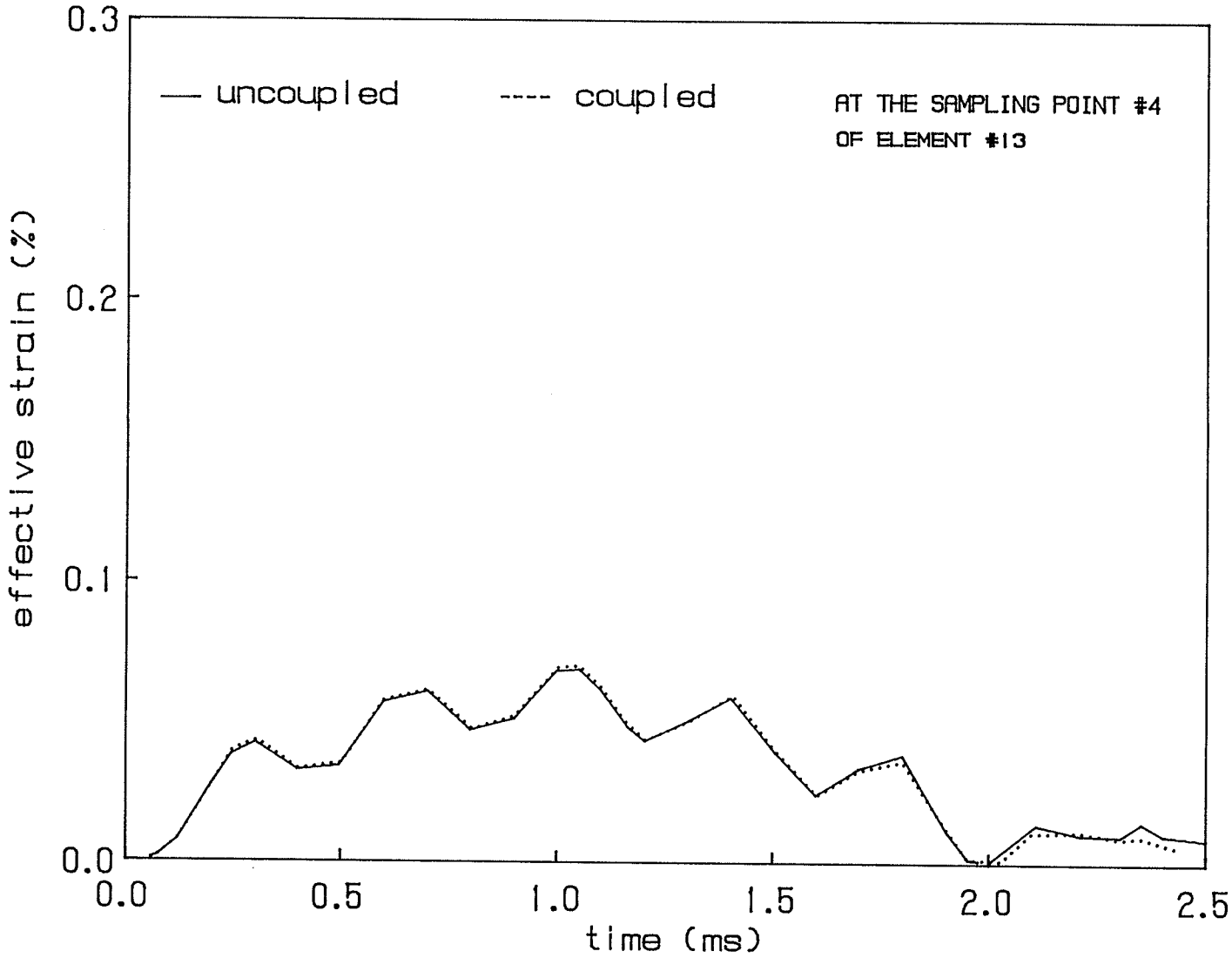

Figure 6.35 Effective strain at the sampling point # 4 of element # 13.

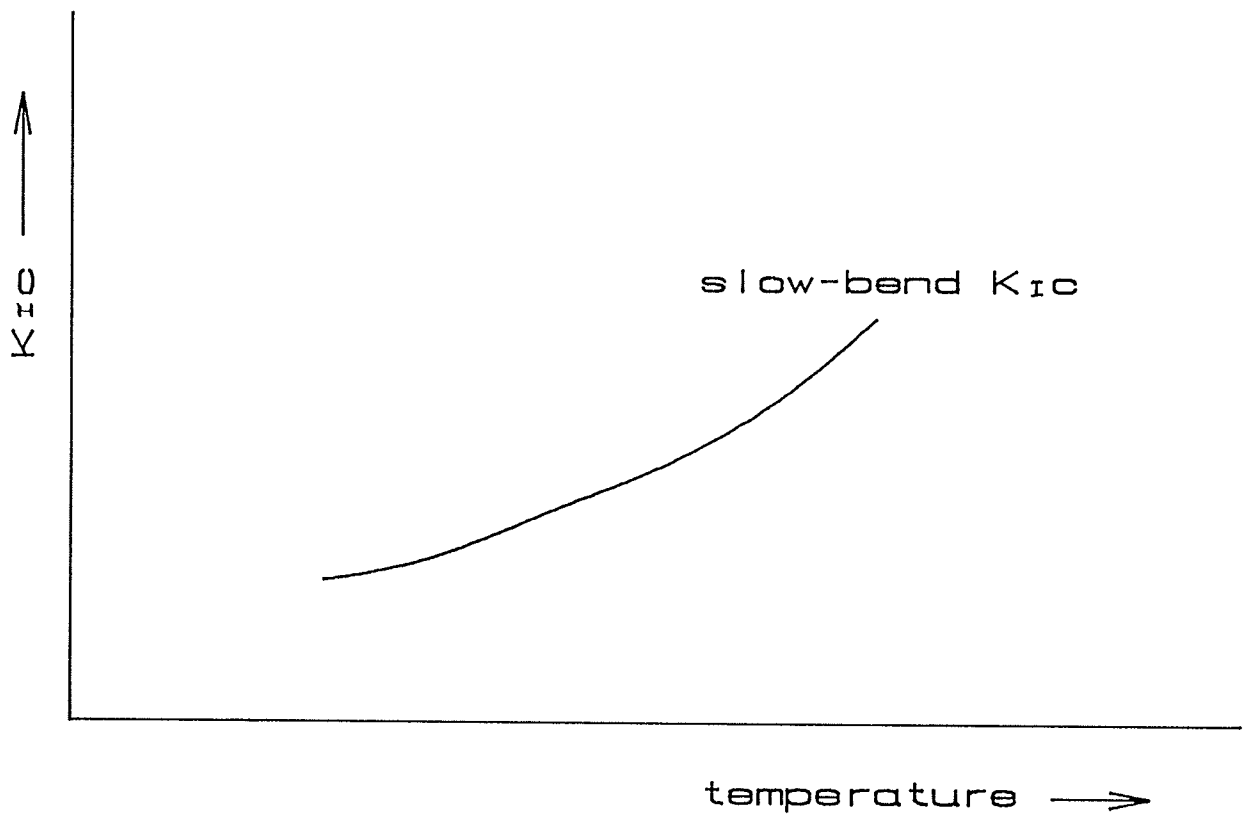

Figure 6.36 Effect of temperature on K_{Ic}.

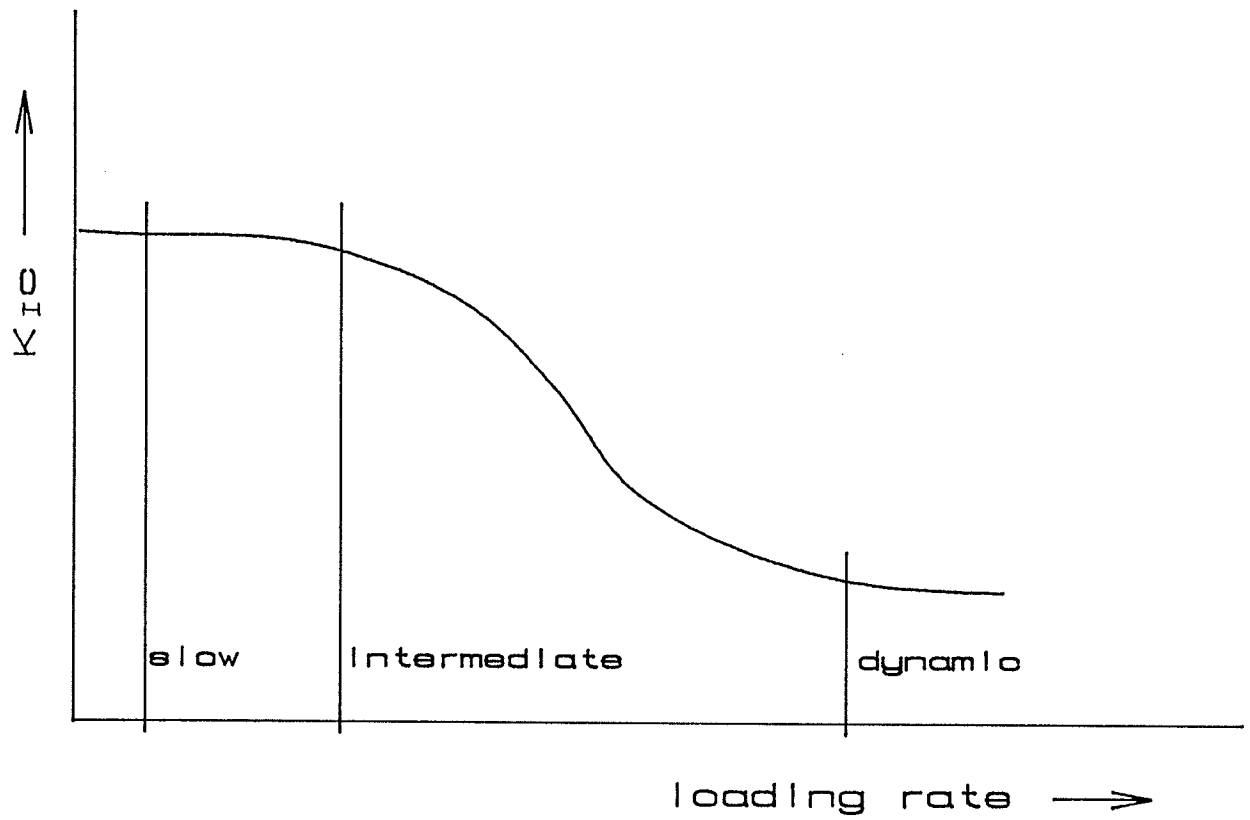

Figure 6.37 Effect of loading rate on K_{Ic}.

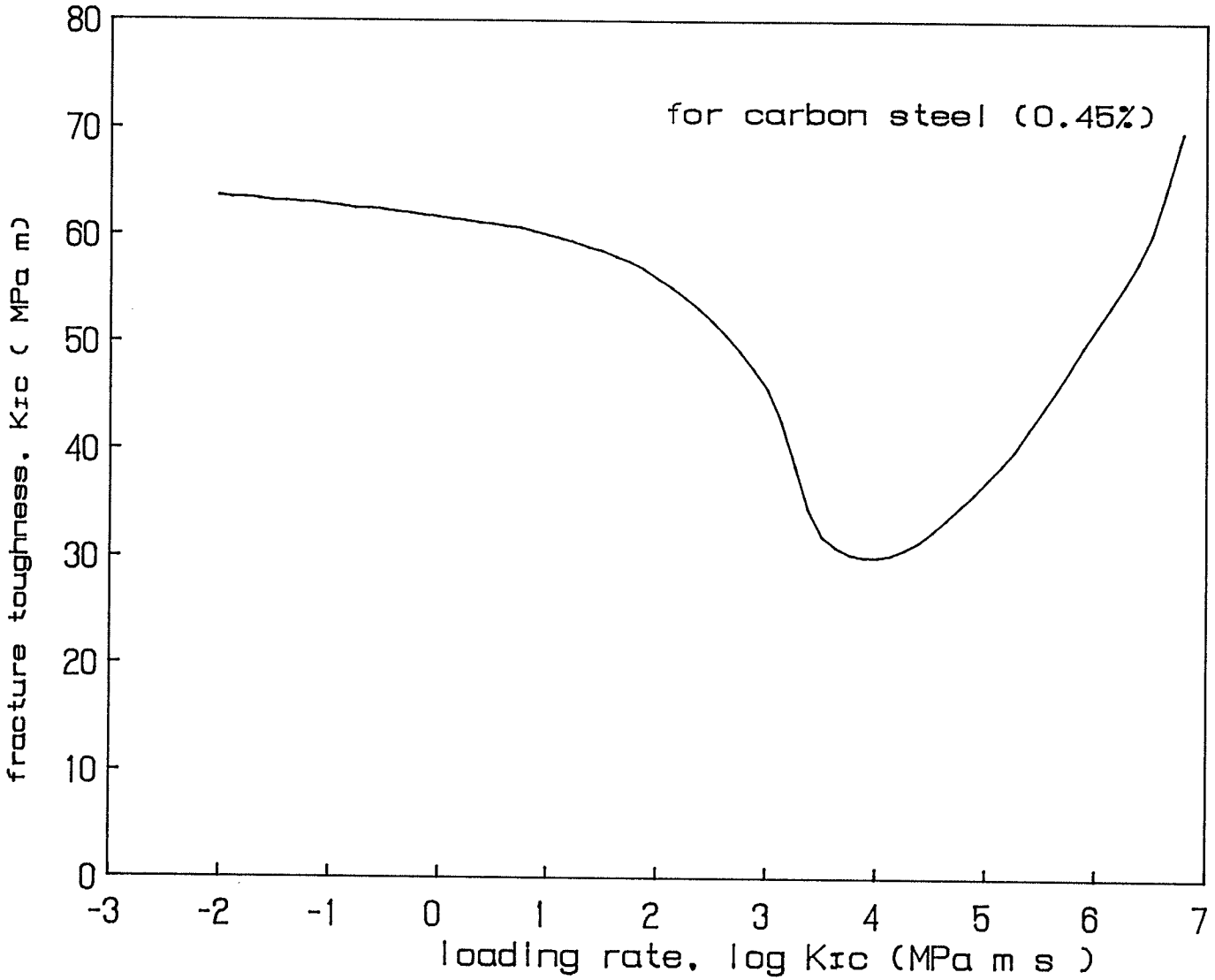

Figure 6.38 K_{Ic} - $\dot{K}_{Ic}$ curve by Klespaczko [95].

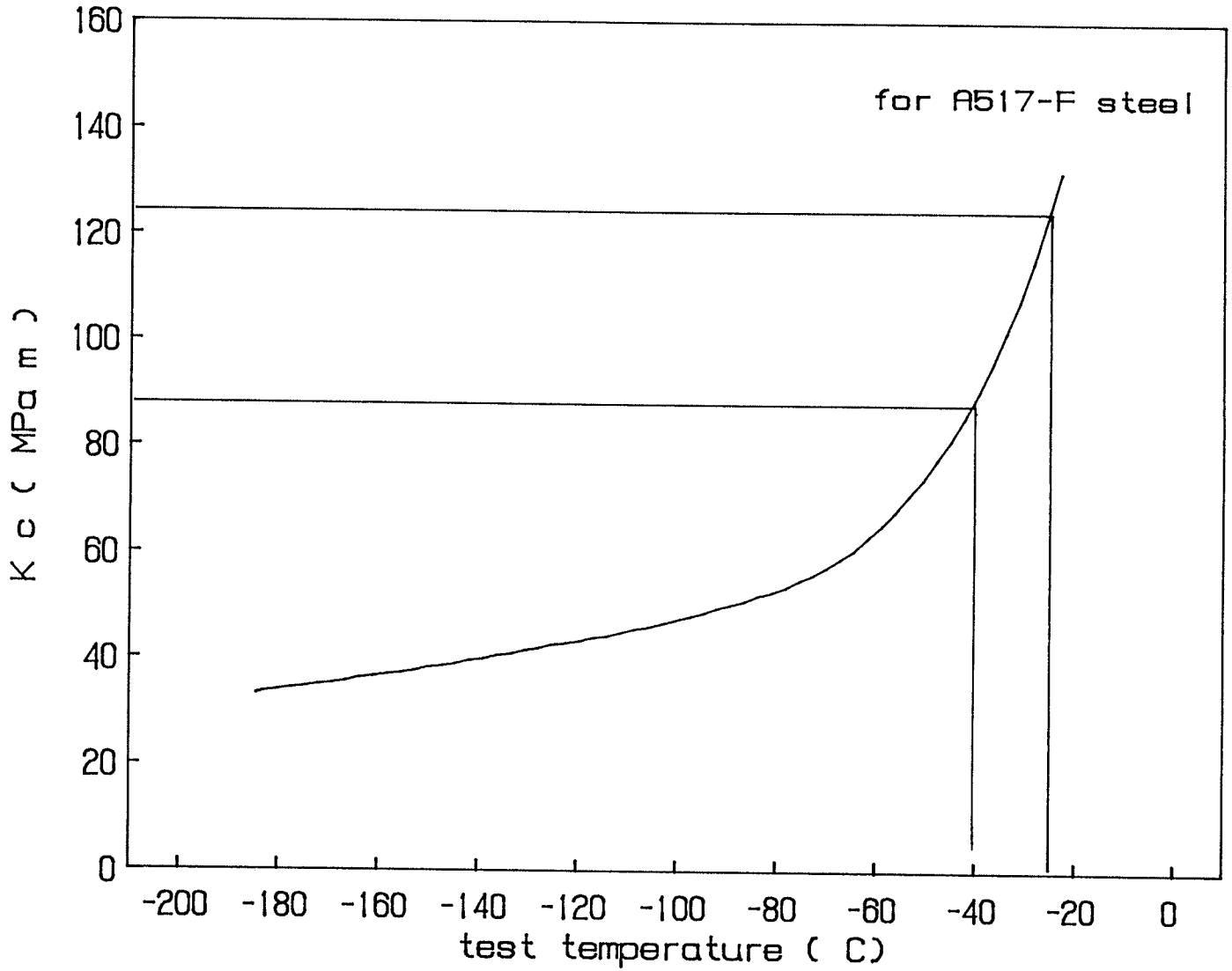

Figure 6.39 K_{Ic} - T curve of A517-F steel.

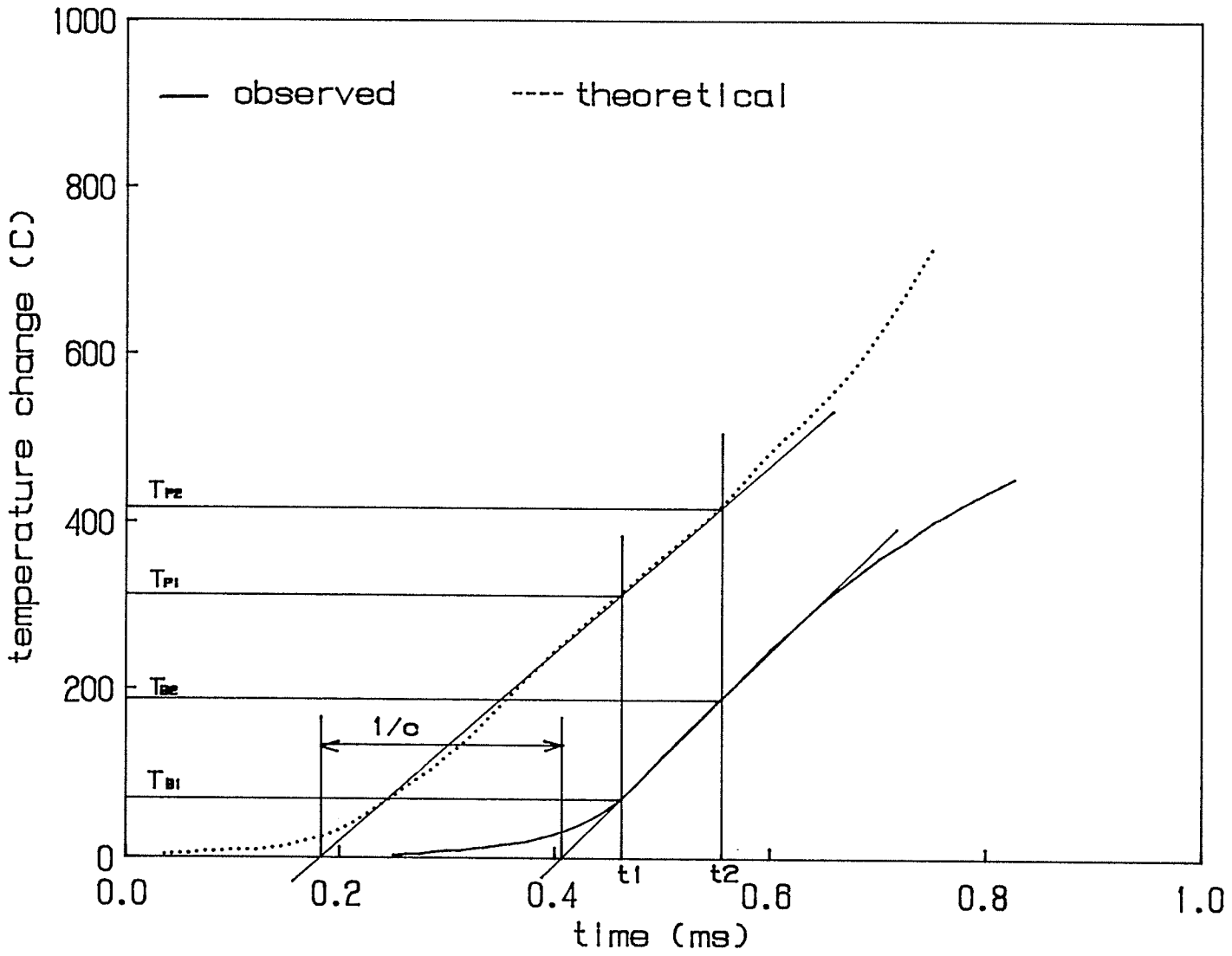

Figure B.1 Graphical determination of transfer function constants.

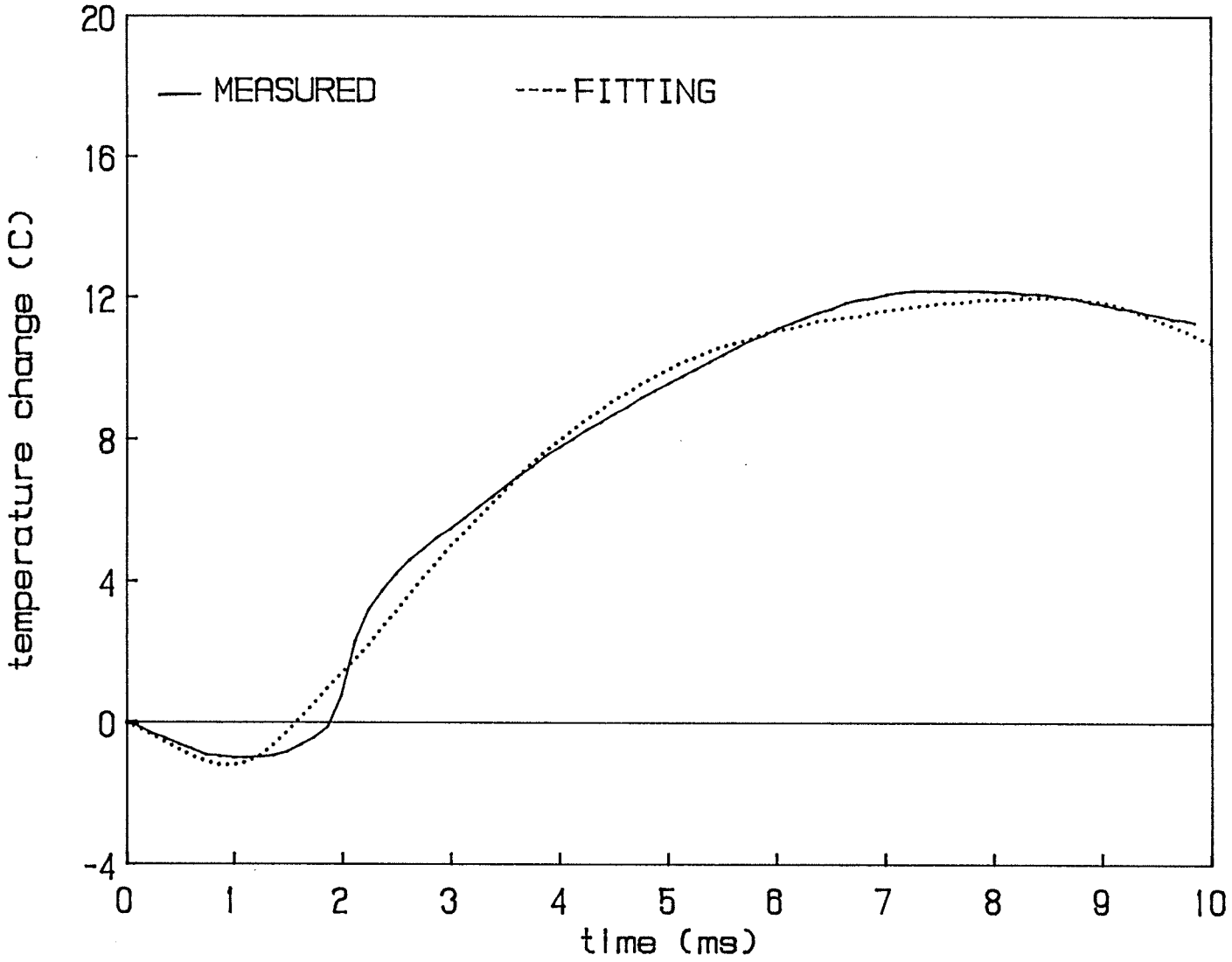

Figure B.2 Fitting the curve of measured temperature change.

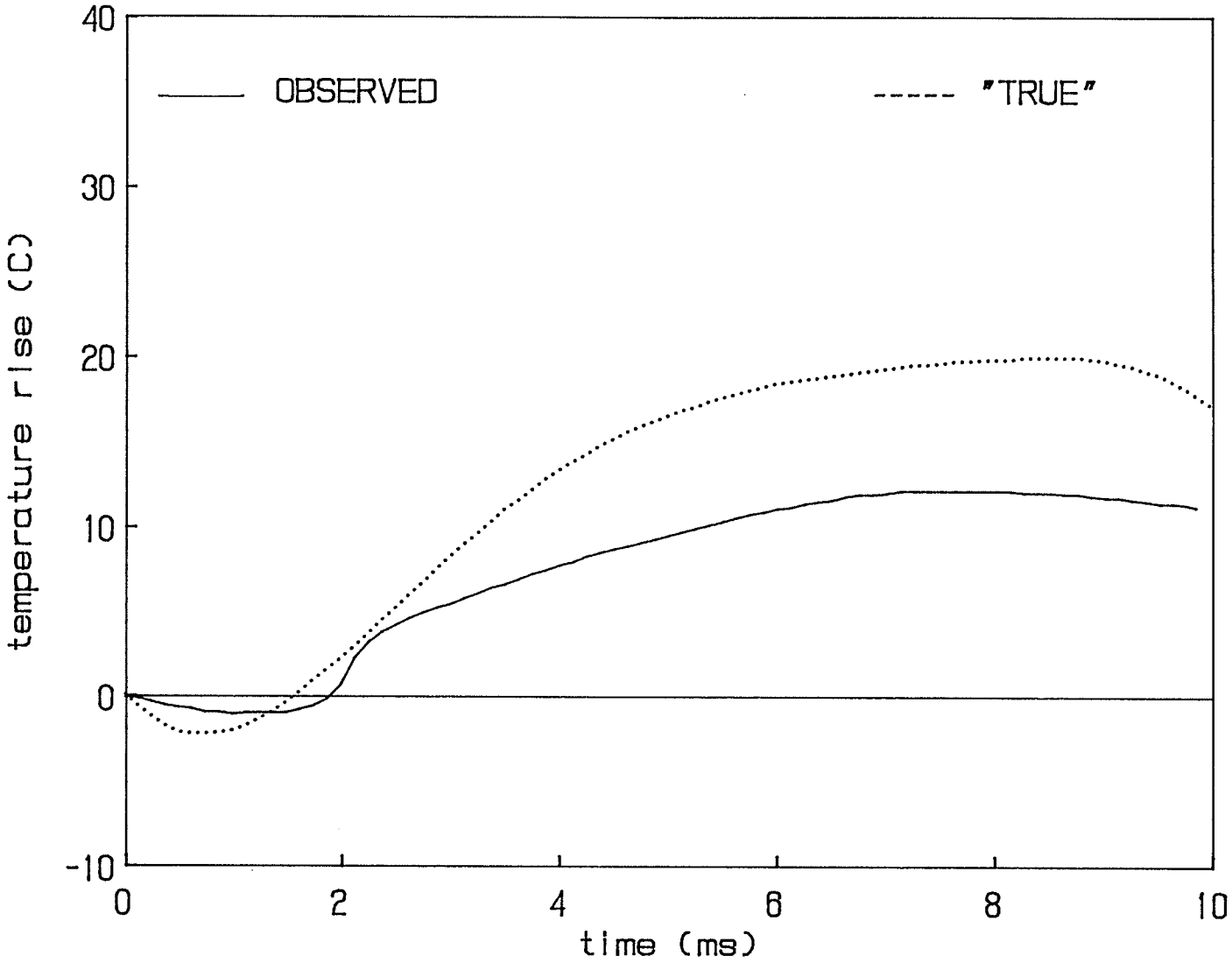

Figure B.3 Comparison between the "observed" and "true" temperature change histories.